Design, Fabrication, Modeling and Control of Artificial Muscle Actuated Wrist Joint System

Hou-Pin Yoong

A Thesis
In the Department
of
Mechanical, Industrial & Aerospace Engineering

Presented in Partial Fulfilment of Requirements
For the Degree of
Doctor of Philosophy (Mechanical Engineering) at
Concordia University
Montreal, Quebec, Canada

November 2018

©Hou-Pin Yoong, 2018

CONCORDIA UNIVERSITY

SCHOOL OF GRADUATE STUDIES

This is to certify that the thesis prepared

By: Hou Pin Yoong

Entitled: Design, Fabrication, Modeling and Control of Artificial Muscle Actuated Wrist Joint System

and submitted in partial fulfillment of the requirements for the degree of

Doctor Of Philosophy (Mechanical Engineering)

complies with the regulations of the University and meets the accepted standards with respect to originality and quality.

Signed by the final examining committee:

_____ Chair
Dr. Luis Amador

_____ External Examiner
Dr. Simon X. Yang

_____ External to Program
Dr. Chun Wang

_____ Examiner
Dr. Subhash Rakheja

_____ Examiner
Dr. Wen Fang Xie

_____ Thesis Supervisor
Dr. Chun-Yi Su

Approved by _____
Dr. Ali Dolatabadi, Graduate Program Director

March 8, 2019

_____
Dr. Amir Asif, Dean
Gina Cody School of Engineering and Computer Science

Abstract

Design, Fabrication, Modeling and Control of Artificial Muscle Actuated Wrist Joint System

Hou-Pin Yoong, Ph.D.
Concordia University, 2018

This research dissertation presents the design, fabrication, modeling and control of an artificial muscle (AM) actuated wrist joint system, i.e., a thermoelectric (TEM) antagonistically driven shape memory alloy (SMA) actuator, to mimic the muscle behavior of human beings. In the developed AM based wrist joint system, the SMA, exhibiting contraction and relaxation corresponding to its temperature, is utilized as the actuator in the AM. Similar to the nerve stimulation, TEM is introduced to provide heat stimulation to the SMA, which involves heating and cooling of the SMA.

SMA possesses superelastic behavior that provides a large force over its weight and effective strain in practical applications. However, such superior material has been underutilized due to its high nonlinear hysteresis behavior, strongly affected by the loading stress. Using the data obtained from the experiments, based on the Prandtl-Ishlinskii (PI) model, a Stress-Dependent Generalized Prandtl-Ishlinskii (SD-GPI) model is proposed, which can describe the hysteresis behavior of the SMA under the influence of various stresses. The parameters of the SD-GPI models at various stresses are obtained using a fitting function from the Matlab. The simulation results of the SD-GPI showed that prediction error is achieved at mean values of $\pm 2\%$ and a standard deviation of less than 7%. Meanwhile, the TEM model is also developed based on the heat balance theory. The model parameters are identified via experimental data using Range-Kutta fourth order integration equation and Matlab curve fitting function. The TEM model has shown a satisfactory temperature prediction. Then, by combining the obtained two models, an integrated model is developed to describe the

whole dynamics of the wrist joint system.

To control the SMA actuated wrist system, the SD-GPI inverse hysteresis compensator is developed to mitigate the hysteresis effect. However, such a compensator shows errors in compensating the hysteresis effect. Therefore, the inverse hysteresis compensator error and the system tracking error are analyzed, and the adaptive back-stepping based control approach is adopted to develop the inverse based adaptive control for the antagonistic AM wrist joint. Subsequently, a corresponding control law is developed for the TEM system to generate the required temperature obtained from the adaptive controller. Simulations verified the developed approach. Finally, experiments are conducted to verify the proposed system. Input sinusoidal signal with frequency 0.1rad/s and amplitude of ± 0.524rad ($\pm 30°$) is applied to the wrist joint system. Experimental results verified that the TEMs antagonistically driven SMA actuators for artificial muscle resembling wrist joint have been successfully achieved.

Acknowledgement

I would like to express my gratitude to everyone who supported me throughout my Ph.D. study. I am thankful for their inspiring guidance, invaluably constructive criticism and friendly advice during my research. First and foremost, I would like to especially thank my supervisor, Prof. Dr. Chun-Yi Su, for his insightful guidance, encouragement and support throughout my program and the thesis writing.

I would also like to thank the Ministry of Higher Education of Malaysia and University Malaysia Sabah for providing the scholarship for me to do my Ph.D. at Concordia University, Canada.

I would also like to thank my father, mother and siblings. My special thanks to my wife and my sons. It would not have been possible to accomplish my Ph.D. study without their love, encouragement and support.

Last but not least, I would like to thank my colleagues and friends: Prof. Dr. Yeo Kiam Beng, Dr. Zhi Li, Dr. Ying Feng, Dr. Yang Fan and Mr. Yap Wen Jun for their invaluable help.

Contents

List of Figures ix
List of Tables xvii
Nomenclature and Abbreviations xix
Chapter 1 Introduction **1**
1.1 AM Working Principles 2
1.2 Artificial Muscle Resembling Wrist Joint System 4
1.3 Shape Memory Alloy Materials 8
1.4 Working Principle of Shape Memory Alloy 8
1.5 Objectives and Contributions 11
1.5.1 Objectives of the Dissertation Research 11
1.5.2 Contributions of the Dissertation Research 12
1.6 Organization of the Thesis 13
Chapter 2 Artificial Wrist System Design, Fabrication and Implementation 15
2.1 Artificial Wrist Mechanical Design 16
2.1.1 System Requirement, Force Identification and Transmission Design . 16
2.1.2 Wrist System Design in 3D Environment 18
2.1.3 Nitinol Winding and Clamping System Design 23
2.1.4 Pre-load Mechanism Design 25
2.1.5 Liquid Cooling System Design 26
2.2 Artificial Wrist Fabrication and Assembly 27
2.2.1 Parts Fabrication 27

2.2.2 Artificial Wrist System Assembly and Calibration 28
2.2.3 Pre-load Calibration and Zero Position Calibration 29
Chapter 3 Literature Review **30**
3.1 SMA Configuration and AM System Models 30
3.1.1 Bias Spring Configuration AM System Model 31
3.1.2 Antagonistic SMA Pair Configuration AM System Model 33
3.2 Input-Output Characteristic of the SMA 34
3.2.1 Experimental Platform Setup 35
3.2.2 Input-Output Characteristic with Different Mechanical Loads 38
3.3 SMA Constitutive Models 40
3.3.1 SMA Phenological Models 43
3.3.2 SMA Combined Physical and Phenological Models 51
3.4 Control Systems 62
3.4.1 Direct Control System 64
3.4.2 Inverse-Based Control System 68
3.5 Summary and Outlook 78
3.5.1 SMA Constitutive Model 79
3.5.2 AM Control System 82
3.6 Concluding Remarks and Emerging Research Problems 86
Chapter 4 Systems Modeling and Verification **88**
4.1 Generalized Prandtl-Ishlinskii Shape Memory Alloy Hysteresis Model 88
4.1.1 Generalized Prandtl-Ishlinskii SMA Hysteresis Model Parameter Identification 90
4.1.2 Generalized Prandtl-Ishlinskii SMA Hysteresis Model Verification . . 93
4.2 Stress-Dependent Generalized Prandtl-Ishlinskii Shape Memory Alloy Hysteresis Model 99
4.2.1 Stress-Dependent Generalized Prandtl-Ishlinskii SMA Hysteresis Model Development 100

4.2.2 Stress-Dependent Generalized Prandtl-Ishlinskii Model Parameters Identification . . . 101
4.2.3 Stress-Dependent Generalized Prandtl-Ishlinskii Model Verification . 103
4.3 Thermoelectric Module and SMAs Heat Flow Model . . . 109
4.3.1 Thermoelectric Module and SMAs Heat Flow Experimental Setup . . 111
4.3.2 Heat Flow Model Parameters Identification and Verification . . . 115
4.4 Artificial Wrist joint Model . . . 121
4.5 Concluding Remarks . . . 123
Chapter 5 Control Development of Artificial Wrist System 124
5.1 Inverse-based Feedback Adaptive Control . . . 125
5.1.1 Inverse Stress-Dependent Generalized Prandtl-Ishlinksii Model . . . 125
5.2 Inverse Stress-Dependent Generalized Prandtl-Ishlinskii Model Parameters Identification and Model Verification . . . 127
5.2.1 Inverse Compensation Error . . . 132
5.2.2 Back-stepping Adaptive Control Design . . . 134
5.3 Concluding Remarks . . . 146
Chapter 6 Experiment 148
6.1 Artificial Wrist Experiment Platform Setup . . . 148
6.2 Experimental Result . . . 153
6.3 Discussion of Results . . . 160
6.4 Concluding Remarks . . . 162
Chapter 7 Conclusions and Future Work 163
7.1 Concluding Remarks . . . 164
7.2 Recommendations for Future Work . . . 166
Bibliography 168

List of Figures

1.1 Working principle of natural muscle and AM. 3
1.2 Artificially articulated system via SMA [1]. 5
1.3 Natural muscle and SMA as AM similarity. 6
1.4 Natural muscle wrist joint system and AM joint system. 7
1.5 The proposed concept for the wrist joint system. 7
1.6 Energy flow and molecular structure at deferent transition phase [2]. 9
1.7 SMA Young's modulus change versus temperature [3]. 10

2.1 (a) Initial concept, (b) Modified concept. 16
2.2 Simulated required force. 17
2.3 Completed Wrist joint design. 18
2.4 Exploded view for the Nitinol actuator. 20
2.5 Exploded view for the wrist transmission system. 21
2.6 Winding pattern for the Nitinol. 23
2.7 (a) Mounting the winding plates on the winding jig; (b) Winding the Nitinol wire on the winding plates. 23
2.8 (c) Removing the lock plates; (d) Transferring the winding to the clamp plates. 24
2.9 (e) Fastening the clamp plates by screws. 24
2.10 Realizing the conceptual design. 25
2.11 Schematic diagram of the liquid cooling system. 26
2.12 Cooler heat exchange plate design. 27
2.13 Nitinol installation. 28

2.14 Pre-load calibration for the wrist joint. 29

3.1 SMA configuration in articulated AM system. 31
3.2 Proposed experimental setup. 36
3.3 Experimental setup for hysteresis data acquisition. 37
3.4 Elongation of Nitinol #6 with response to input temperature with different loads. 38
3.5 Elongation of Nitinol #8 with response to input temperature with different loads. 39
3.6 Elongation of Nitinol #6 with response to input temperature under superelastic condition. 41
3.7 Elongation of Nitinol #8 with response to input temperature under superelastic condition. 42
3.8 Schematic structure of the Preisach model [4]. 44
3.9 Input, $v(t)$ variation to T plane translation [5]. 45
3.10 Play operator (a) PI model (b) GPI model [6]. 47
3.11 Comparison of GPI model with measured hysteresis loops of a SMA . 48
3.12 KP operator [7]. 49
3.13 Discretized Preisach plane [8]. 50
3.14 Schematic of Neural network inverse hysteresis and result of the inverse model [9]. 52
3.15 Phase change temperature under stress load [10]. 54
3.16 Strain-temperature loop for NiTi [10]. 55
3.17 Simulation of the minor loop in SMA hysteresis [11]. 56
3.18 Applied stress versus transition temperature. 57
3.19 Potential energy and shear length [12]. 58
3.20 Comparison of simulation of the minor loop and experimental result [13]. 62
3.21 Block diagram; a.)Direct control scheme and b.) Inverse-based control scheme. 63

3.22 PID control architectures. 65
3.23 Block diagram for Fuzzy PID controller. 66
3.24 Adaptive control block diagram [14]. 74
3.25 Reviewed SMA constitutive model. 79

4.1 GPI model constants a_i and b_i. 92
4.2 GPI model constants c_i, d_i, ρ, τ and c. 93
4.3 GPI loop at 650g load. 93
4.4 GPI model at 650g load. 93
4.5 GPI loop at 700g load. 94
4.6 GPI model at 700g load. 94
4.7 GPI loop at 750g load. 94
4.8 GPI model at 750g load. 94
4.9 GPI loop at 800g load. 94
4.10 GPI model at 800g load. 94
4.11 GPI loop at 850g load. 95
4.12 GPI model at 850g load. 95
4.13 GPI loop at 900g load. 95
4.14 GPI model at 900g load. 95
4.15 GPI loop at 950g load. 95
4.16 GPI model at 950g load. 95
4.17 GPI loop at 1000g load. 96
4.18 GPI model at 1000g load. 96
4.19 GPI loop at 1050g load. 96
4.20 GPI model at 1050g load. 96
4.21 GPI model error at 650g load. 97
4.22 GPI model error at 700g load. 97
4.23 GPI model error at 750g load. 97
4.24 GPI model error at 800g load. 97

4.25 GPI model error at 850g load. 97
4.26 GPI model error at 900g load. 97
4.27 GPI model error at 950g load. 98
4.28 GPI model error at 1000g load. 98
4.29 GPI model error at 1050g load. 98
4.30 SD-GPI loop at 650g load. 103
4.31 SD-GPI model at 650g load. 103
4.32 SD-GPI loop at 700g load. 104
4.33 SD-GPI model at 700g load. 104
4.34 SD-GPI loop at 750g load. 104
4.35 SD-GPI model at 750g load. 104
4.36 SD-GPI loop at 800g load. 104
4.37 SD-GPI model at 800g load. 104
4.38 SD-GPI loop at 800g load. 105
4.39 SD-GPI model at 800g load. 105
4.40 SD-GPI loop at 850g load. 105
4.41 SD-GPI model at 850g load. 105
4.42 SD-GPI loop at 900g load. 105
4.43 SD-GPI model at 900g load. 105
4.44 SD-GPI loop at 950g load. 106
4.45 SD-GPI model at 950g load. 106
4.46 SD-GPI loop at 1000g load. 106
4.47 SD-GPI model at 1000g load. 106
4.48 SD-GPI loop at 1050g load. 106
4.49 SD-GPI model at 1050g load. 106
4.50 SD-GPI error at 650g load. 107
4.51 SD-GPI error at 700g load. 107
4.52 SD-GPI error at 750g load. 107

4.53 SD-GPI error at 800g load. 107
4.54 SD-GPI error at 800g load. 107
4.55 SD-GPI error at 850g load. 107
4.56 SD-GPI error at 900g load. 108
4.57 SD-GPI error at 950g load. 108
4.58 SD-GPI error at 1000g load. 108
4.59 SD-GPI error at 1050g load. 108
4.60 Heat flow in the TEM-SMA system. 109
4.61 Temperature sensor placement to measure the Nitinol temperature. . 112
4.62 Experimental setup for TEM model verification. 112
4.63 Nitinol 1 temperature at 1/128Hz. 113
4.64 Nitinol 2 temperature at 1/128Hz. 113
4.65 Nitinol 1 temperature at 1/64Hz. 113
4.66 Nitinol 2 temperature at 1/64Hz. 113
4.67 Nitinol 1 temperature at 1/32Hz. 113
4.68 Nitinol 2 temperature at 1/32Hz. 113
4.69 Nitinol 1 temperature at 1/16Hz. 114
4.70 Nitinol 2 temperature at 1/16Hz. 114
4.71 Nitinol 1 temperature at 1/8Hz. 114
4.72 Nitinol 2 temperature at 1/8Hz. 114
4.73 Nitinol 1 temperature at 1/4Hz. 114
4.74 Nitinol 2 temperature at 1/4Hz. 114
4.75 Nitinol 1 temperature at 1/2Hz. 115
4.76 Nitinol 2 temperature at 1/2Hz. 115
4.77 Nitinol 1 temperature at 1Hz. 115
4.78 Nitinol 2 temperature at 1Hz. 115
4.79 TEM SMA heat model at 1/128Hz. 116
4.80 TEM SMA heat model at 1/128Hz. 116

4.81 TEM SMA heat model at 1/64Hz. 117
4.82 TEM SMA heat model at 1/64Hz. 117
4.83 TEM SMA heat model at 1/32Hz. 117
4.84 TEM SMA heat model at 1/32Hz. 117
4.85 TEM SMA heat model at 1/16Hz. 117
4.86 TEM SMA heat model at 1/16Hz. 117
4.87 TEM SMA heat model at 1/8Hz. 118
4.88 TEM SMA heat model at 1/8Hz. 118
4.89 TEM SMA heat model at 1/4Hz. 118
4.90 TEM SMA heat model at 1/4Hz. 118
4.91 TEM SMA heat model at 1/2Hz. 118
4.92 TEM SMA heat model at 1/2Hz. 118
4.93 TEM SMA heat model at 1Hz. 119
4.94 TEM SMA heat model at 1Hz. 119
4.95 TEM SMA heat model errors at 1/128Hz. 120
4.96 TEM SMA heat model errors at 1/64Hz. 120
4.97 TEM SMA heat model errors at 1/32Hz. 120
4.98 TEM SMA heat model errors at 1/16Hz. 120
4.99 TEM SMA heat model errors at 1/8Hz. 121
4.100 TEM SMA heat model errors at 1/4Hz. 121
4.101 TEM SMA heat model errors at 1/2Hz. 121
4.102 TEM SMA heat model errors at 1Hz. 121
4.103 Wrist joint system schematic drawing. 122

5.1 Wrist joint adaptive control system. 125
5.2 Hysteresis loop compensator at 650g load. 129
5.3 Inverse compensated result at 650g load. 129
5.4 Hysteresis loop compensator at 700g load. 130
5.5 Inverse compensated result at 700g load. 130

5.6 Hysteresis loop compensator at 750g load. 130
5.7 Inverse compensated result at 750g load. 130
5.8 Hysteresis loop compensator at 800g load. 130
5.9 Inverse compensated result at 800g load. 130
5.10 Hysteresis loop compensator at 850g load. 131
5.11 Inverse compensated result at 850g load. 131
5.12 Hysteresis loop compensator at 900g load. 131
5.13 Inverse compensated result at 900g load. 131
5.14 Hysteresis loop compensator at 950g load. 131
5.15 Inverse compensated result at 950g load. 131
5.16 Hysteresis loop compensator at 1000g load. 132
5.17 Inverse compensated result at 1000g load. 132
5.18 Hysteresis loop compensator at 1050g load. 132
5.19 Inverse compensated result at 1050g load. 132
5.20 Direct Adaptive controller conceptual design. 138
5.21 Adaptive controller simulation using Matlab Simulink. 139
5.22 Adaptive controller simulation result. 140
5.23 Schematic diagram of the single input current to control both sides temperatures for the TEM. 142
5.24 TEM control simulation with step inputs. 143
5.25 TEM control simulation with sinusoidal inputs. 144
5.26 Two layers of TEM control system schematic diagram. 145
5.27 Double layers TEM control simulation with step inputs. 145
5.28 Double layers TEM control simulation with sinusoidal inputs. 146

6.1 Artificial Wrist joint. 149
6.2 Wrist joint system experimental setup. 150
6.3 PID controller conceptual design. 151
6.4 PID controller system. 151

6.5 Inverse-based controller conceptual design. 152
6.6 Inverse-based controller system. 152
6.7 Wrist joint experimental result for inverse adaptive control, direct adaptive control and PID control system at load 100g. 153
6.8 Wrist joint experimental result for inverse adaptive control, direct adaptive control and PID control system at load 200g. 154
6.9 Wrist joint experimental result for inverse adaptive control, direct adaptive control and PID control system at load 300g. 154
6.10 Wrist joint experimental result for inverse adaptive control, direct adaptive control and PID control system at load 400g. 155
6.11 Wrist joint experimental result for inverse adaptive control, direct adaptive control and PID control system at load 500g. 155
6.12 Wrist joint experimental result for inverse adaptive control, direct adaptive control and PID control system at load 600g. 156
6.13 Inverse adaptive control, direct adaptive control system and PID control system error at load 100g. 157
6.14 Inverse adaptive control, direct adaptive control system and PID control system error at load 200g. 157
6.15 Inverse adaptive control, direct adaptive control system and PID control system error at load 300g. 158
6.16 Inverse adaptive control, direct adaptive control system and PID control system error at load 400g. 158
6.17 Inverse adaptive control, direct adaptive control system and PID control system error at load 500g. 159
6.18 Inverse adaptive control, direct adaptive control system and PID control system error at load 600g. 159

List of Tables

2.1 Artificial wrist parts list. 22

3.1 Summary of direct control systems for SMA or SMA actuated AM systems development. 83

3.2 Summary of inverse-based control systems for SMA or SMA actuated AM system development. 84

4.1 GPI model parameters a_i and b_i. 91

4.2 GPI model parameters c_i and d_i. 91

4.3 GPI model parameters ρ τ c and $J(T)$. 92

4.4 GPI model errors statistic (%). 99

4.5 SD-GPI model parameters s_{aij} and s_{bij}. 102

4.6 SD-GPI model parameters c_i, d_i, ρ, τ and c. 103

4.7 SD-GPI model 650g to 800g load error statistic (%). 108

4.8 SD-GPI model 800g to 1050g error statistic (%). 109

4.9 TEM and SMA heat flow model parameters. 116

4.10 TEM and SMA heat flow model errors statistic. 119

5.1 Linear regression parameters p_{ai} and p_{ci}. 127

5.2 Inverse model parameters for loads range from 650g to 850g. 128

5.3 Inverse model parameters for loads range from 850g to 1050g. 129

5.4 Model parameters used in the simulation. 138

5.5 Adaptive controller parameters. 139

6.1 Artificial wrist control parameters. 153

6.2 Control system error analysis. 161

Nomenclature and Abbreviations

Nomenclature

$v(t)$	system input
$u(t)$	system output
r	threshold of the hysteresis operator
$\mu(\cdot,\cdot)$	density function of the Preisach model
$\hat{\gamma}[v](t)$	relay operator
$F_r[v](t)$	play operator
$E_r[v](t)$	stop operator
Λ	upper limit of integration in the PI model
$p(r)$	density function of the PI model
$k_p\left[v,\xi_p\right](t)$	denotes the KP kernel
$P[v](t)$	Prandtl-Ishlinskii model
$\Psi[v](t)$	shift model
$\Psi_c[v](t)$	shift operator
$C_{pm}[0,T]$	space of monotone, continuous functions on $[0,T]$
I	current
I_ω	moment of inertia
R_I	equivalent resistor of TEM
D	Young's modulus of the SMA
D_m	Young's modulus of the SMA at pure martensite
D_a	Young's modulus of the SMA at pure austenite
M_s	martensite start temperature
M_f	martensite finish temperature
M_a	bounded aerodynamic moment
A_s	austenite start temperature
A_f	austenite finish temperature

E_m	elastic modulus of the SMA at pure martensite
E_a	elastic modulus of the SMA at pure austenite
Θ	thermoelectric tensor
Ω	phase transformation tensor
A_{wire}	SMA wire cross section area
M	external load
F	force
σ	stress
ε	strain
ε_{res}	residual martensite strain
ε_L	maximum recoverable strain
k_f	damping coefficient
Δ	shear length
C^A_{ijkl}	isotropic elastic stiffness tensor
$q(t)$	angular position
Θ^n	contraction in $C[0,T]$
$y_{p\gamma}$	SD-GPI model
$y^{-1}_{p\gamma}$	inverse of the SD-GPI model
p_0	initial loading curve
$\hat{p}(r)$	inverse initial loading curve
$p_0^{-1}(r)$	initial loading curve of the inverse PI model
ξ	volumetric function of martensite in SMA
ξ_A	residual martensite phase in SMA
z_1	transformed error
$V(t)$	Lyapunov function
ρ	TEM average density
C_p	TEM specific heat at constant pressure
α	Thompson coefficient

τ	thermal conductance
K_T	heat convection to the heat sink and fan
K_∞	room temperature

Abbreviations

AM	Artificial muscle
SMA	Shape memory alloy
TEM	Thermoelectric module
PI	Prandtl-Ishlinskii
KP	Krasnosel'skii-Pokrovkii
GPI	Generalized Prandtl-Ishlinskii
SD-GPI	Stress dependent generalized Prandtl-Ishlinskii
NN	Neural network
IPMC	Ionic polymer-metal composites
PID	Proportional-Integral-Derivative

Chapter 1

Introduction

Millions of years of adaptation and evolution had created the creatures on earth as living technology that is far more advanced than what we have understood. With just the tip of the iceberg of this natural knowledge, it already motivated many advanced human-made technologies. These natural technologies are not only around us; humankind is also part of them. Learning from the human wrist, this dissertation presents the design, fabrication, modeling and control for an antagonist pair of shape memory alloys (SMA) artificial muscle (AM) that resembled a wrist joint system. In search of a smart material that exhibits similar actuation like the muscle, shape memory alloy with the ability to contract and relax, and large strain appear to be compatible as an actuator in the AM. Moreover, by utilizing the superelastic behavior of the Nitinol (a type of SMA), the antagonistic AM can generate large strain for the artificial wrist joint to replicate human wrist movement. To generate the strain, the SMA AM has to undergo thermomechanical manipulation. Such manipulation can be achieved by using the thermoelectric module (TEM). When current is supplied to the TEM, it will generate one hot side and a cool side, and these can be reversed by reversing the current supplied. During cooling of the Nitinol, the other side of the TEM will generate excess heat. Therefore, a liquid cooling system learnt from the natural thermoregulation in animals is designed and implemented to remove the heat from the TEM and dissipate through an external radiator.

To achieve the implementation of an AM, the foundation of the AM is first laid down. The understanding of AM working principle is studied and presented in the next section. Because the core component of the AM system is the SMA actuator, an introduction on the SMA including SMA materials and the principle of the SMA actuator is given next. According to the literature, the study of hysteretic input and output responses of the SMA have been extensively investigated. However, the exploration of the stress-dependent hysteresis is very limited, and information reviewed is not substantial for this research. Therefore, an experimental platform has been established to study the SMA stress dependent behavior of the SMA wire. Different temperature input amplitudes and mechanical loads are subjected to the SMA to investigate thoroughly and fully understand the input-output behavior of the SMA actuator. Based on the experimental data collected, the type of SMA that is suitable for the AM and compatible with the TEM is identified.

The use of SMA has provided various advantages, and also challenges. The SMA nonlinear hysteresis behavior is complex and difficult to control. Furthermore, the wrist system is operating within the SMA superelastic range which is highly influenced by the stress; and the SMA temperature is controlled by using the TEM. With the combination of all these systems in the wrist system, it is extremely complex and difficult to control. Therefore, the understanding and modeling of the complete system are very crucial for predicting and achieving satisfactory control of the SMA actuated AM. Thus, system model development and control approaches are constituted as the main objective of this dissertation.

1.1 AM Working Principles

AM is an actuator system that can replicate natural muscle function where it will contract when subjected to a stimulant and relax when the stimulant is removed. Figure 1.1 shows the working principle of both the natural muscle and the AM. Various AM systems have been made by researchers which include conventional types such as the woven mesh pneumatic (McKibben) muscle [15] [16], electromagnetic array [17] and others. However, these AMs are

heavy or have power systems that are bulky and heavy.

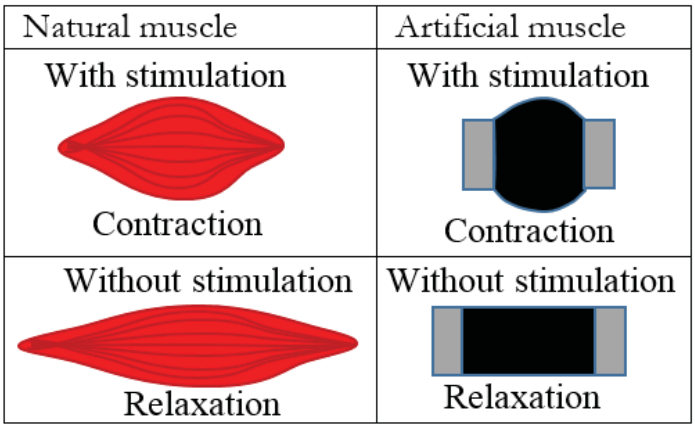

Figure 1.1: Working principle of natural muscle and AM.

To improve the power-to-weight ratio of the AM, various smart materials were considered for making the AM. These smart materials include the SMA, ionic polymer metal composite (IPMC) [18] [19], ferroelectric polymers such as polyvinylidene fluoride (PVDF) piezoelectric [20], [21], dielectric elastomers like plasticized poly vinyl chloride (PVC) gel [22] and others. AMs made from ionic polymer metal have a short life cycle, and the use of PVDF and PVC gel require very high activation voltage and actuation voltage, respectively. On the other hand, although SMA has high nonlinear and hysteretic behaviors, its high power-to-weight ratio and large effective strain are attractive features. These features are ideal for various applications such as aerospace, automobile, biomedical, and robotics, specifically in AM. AM plays a very important role in various areas, including exoskeleton, robotic prostheses, humanoids, bio-mimetic robotics and other applications. Researchers had been using SMA as an actuator; this can be observed in [23], [24], [25], [26] and others. These researchers are more focused on modeling and characterizing the SMA. Researches that focus on applying SMA as AM such as [27] and [28] are very limited. The limitation could be due to the lack of exploration on the stress-dependent hysteresis and the superelastic behavior of SMA. The AM functions can be realized by using SMA in various configurations as per Figure 1.2. However, among the configurations, the spiral and bending configurations do not satisfy the

working principle of AM. In terms of an active actuator, these antagonist SMA configurations can be further sub-grouped into a single actuator with spring return and double actuators system. Furthermore, the antagonistic SMA actuated AM system can also be sub-categorized into straight and shaped SMA type. Straight SMA actuator is made of single or multiple straight wires or flat bars as the actuator. Shaped SMA type actuator is made by annealing SMA into spring, snake, rectangular, ring wave or other shapes to increase the strain. The shaped SMA actuators are preferred for systems with low torque and large strain. The dynamic model of the deferent configurations of SMA actuated AM system can be generally grouped into the single actuator with spring return and double actuators. This is because the multiple SMAs dynamic model is in proportion to the single SMA system. Meanwhile, the shaped SMA actuator uses the spring Young's modulus in the form of a nonlinear hysteretic function derived from the SMA martensite to austenite fraction.

1.2 Artificial Muscle Resembling Wrist Joint System

The natural muscles are not able to extend by themselves. Therefore, the natural articulated system consists of an antagonizing pair of muscles. At the wrist joint, the extensor muscle contracts and the flexors muscle extends during extension. The muscle action is vice versa during flexion as shown in Figure 1.4. The contraction of natural muscles is a result of stimulation from the nerve system. Similar to the natural muscle, the SMAs are capable of contracting and extending with response to temperature stimulation as shown in Figure 1.3. Emulating the wrist, the SMA is configured in the antagonistic form to resemble an artificial wrist system as shown in Figure 1.4. In the antagonistic formation, when one of the SMA contracts the other extends. This leads to the implication that one of the SMA needs heating and the other needs cooling.

Generally, resistive heating is widely used to provide thermal stimulation to the SMA. This can be observed in [29], [30], [31], [32] and et al. This method is widely used due to controllability, and no extra heat generation element is needed. Other heating methods

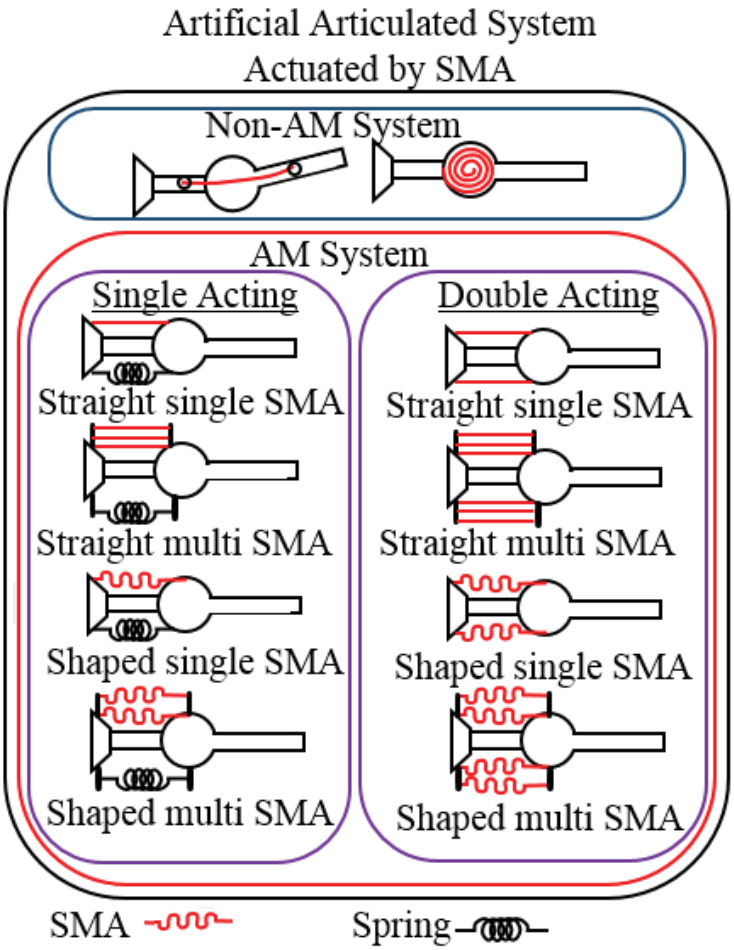

Figure 1.2: Artificially articulated system via SMA [1].

like convection through TEM, radiation through microwave or induction through magnetic wave had also been used, but these methods involve additional heating elements that could be bulky. However, heating is only half of the thermal control. Cooling of the SMA is also important in controlling the SMA. Passive cooling methods are too slow and uncontrollable in most of the SMA applications [33]. Therefore, active cooling methods are introduced. Non-controllable active cooling methods like immersion in a cooled liquid and fan cooling could contribute to large overshoot. Thus, controllable cooling methods like thermoelectric cooling and cools chip technology are preferred [26] [33]. To achieve heating and cool the antagonist SMA pair at the same time, TEM is proposed to heat and cool the SMA antagonistically. The Peltier effect exhibited by the TEM will act as a heat pump to pump the heat from one side of the TEM to the other side to heat the SMA via convection heating. The side that the heat is pumped away from will experience the cooling effect. Thus heating one side of the SMA and cooling the other side of the SMA yields contraction toward the heated side and results in joint moving to the heated side. The heat pump direction can be reversed by reversing the polarity of the supply current to the TEM. Consequently, the joint movement is in the opposite direction. The proposed concept for the artificial wrist joint is shown in Figure 1.5

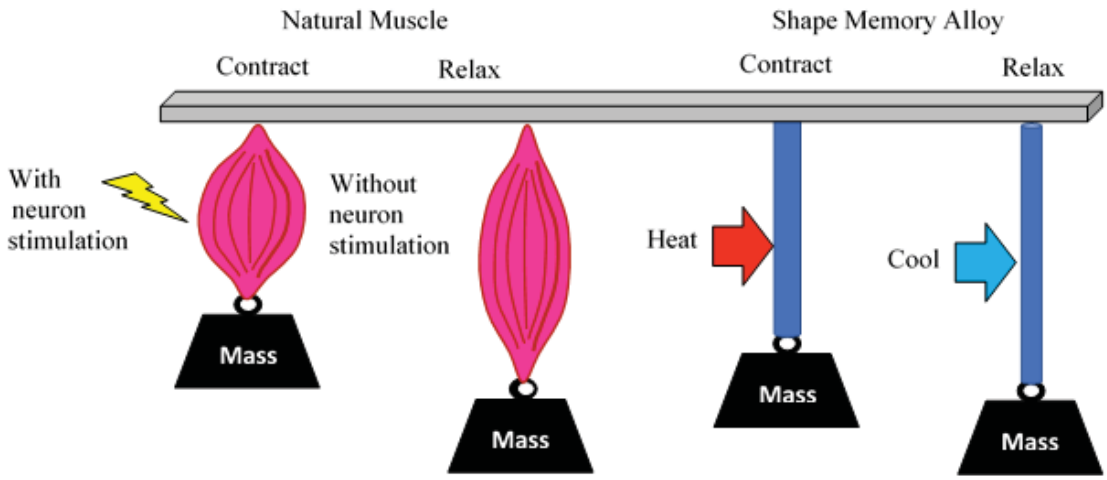

Figure 1.3: Natural muscle and SMA as AM similarity.

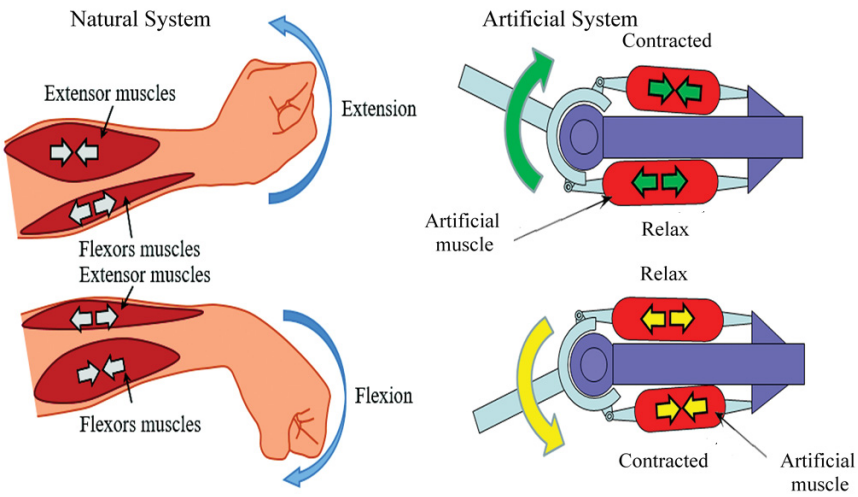

Figure 1.4: Natural muscle wrist joint system and AM joint system.

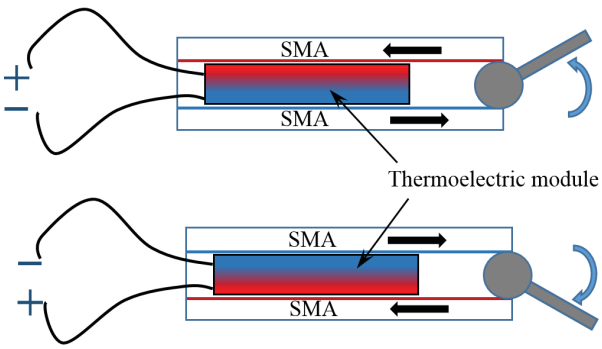

Figure 1.5: The proposed concept for the wrist joint system.

1.3 Shape Memory Alloy Materials

Shape memory alloy materials are a class of materials that can return to their pre-deformed shape when they are activated. SMA can be sub-classed into thermally activated and magnetically activated [34]. Thermally activated SMA is the sub-class of SMA that is of interest in this research. The phenomenon of the SMA materials that change their shape to the pre-programmed shape at the activation temperature is called shape memory effect [35]. Various SMA materials had been developed. A few of the widely used SMAs are made from a combination of nickel-titanium (NiTi), Copper-zinc-nickel (CuZnNi) and copper-aluminum-nickel (CuAlNi). Other SMAs with different combinations of metals have also been produced, but have not been widely explored because of high production costs, limited recoverable strain, narrow operating temperature range or slow response [36]. SMAs with Ni and Ti composition are also known as Nitinol. Nitinol was invented by Buehler and Wiley in 1961 [37] and became famous because of its properties. The Nitinol properties vary according to the nickel and titanium ratio.

The Ni and Ti ratio also affect the Nitinol transitional temperature of the memory-like behavior. The transitional temperature varies from -100 to 100°C depending on the composition of the Ni and Ti. The shape memory is programmed into the SMA by holding it in the desired shape and heating it to a temperature that ranges from 350 to 600°C [11], followed by a rapid cooling process. This heating and the rapid cooling process are called annealing. SMA that undergoes annealing will be able to perform shape memory effect.

1.4 Working Principle of Shape Memory Alloy

SMAs are solid state actuators that can convert heat input into corresponding mechanical output. This happens when the heat energy is absorbed by the SMA to restructure the molecular formation. At low temperature, the SMA is in the martensite phase with molecular structure in the form of the monoclinic lattice. SMA in this form has low stiffness, and the

shape is easily deformed. When the temperature increases up to the transition temperature, energy is absorbed to reform the SMA molecular structure into the austenite phase as shown in the upper curve in Figure 1.6. In the austenite phase, the molecular structure is in the form of a body-centred cubic (BCC) lattice. When the SMA is cooled down, as shown by the lower curve in Figure 1.6, the SMA changes from the austenite phase back to the martensite phase over an intermediate phase with rhombohedral lattice called the R-phase. However, the R-phase effect is normally small and often neglected [2], [11] [38].

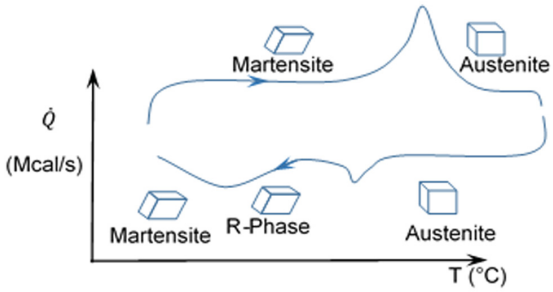

Figure 1.6: Energy flow and molecular structure at deferent transition phase [2].

The temperature induced martensite as described above is called the twinned martensite. In the twinned martensite, the monoclinic lattice structure is arranged in opposite directions at each layer. However, the SMA molecular structure is not only affected by the heat. When the applied stress is larger than the critical stress level, the monoclinic lattice structure at each layer will reorient to form aligned structure at all layers and form into de-twinned martensite. During the reorientation of the molecular structure, SMA can provide large strain up to about 8% [36] [38] [39]. The large strain behavior exhibited by the reorientation of the SMA molecular structure is also known as super-elasticity.

The phase transition cycle of SMA exhibits hysteresis behavior. This can be observed in the transition profile of Young's modulus at martensite to austenite and vice versa versus the temperature, as shown in Figure 1.7. The D_a, D_m, M_s, M_f, A_s and A_f represent Young's modulus at pure austenite, pure martensite, the temperature at martensite start, martensite complete, the temperature at austenite start and austenite complete respectively. Besides

that, the transition temperatures of M_s, M_f, A_s and A_f, also depend on the stress exerted on the SMA [3] [40] [41].

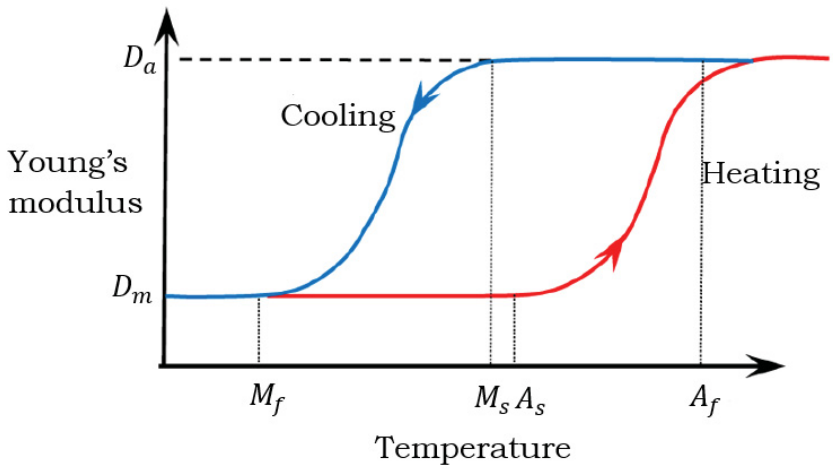

Figure 1.7: SMA Young's modulus change versus temperature [3].

The change of phase from martensite to austenite and vice versa under thermal stimulation is the most important property in the SMA materials. This property shows that the SMA in the austenite phase has a stiffness two to three times higher than in the martensite phase [2] [9] [42] [43]. The SMA in austenite phase will have higher stiffness. Thus, it will return to its memory shape when no load is applied to it. This thermomechanical behavior is the main reason that the SMAs are used as the actuator in the AM system. The increase of SMA stiffness is used to create a pulling force which functions as the linear actuator in the AM system. Furthermore, the thermally stimulated contraction in the SMA mimics the neuron-transmission stimulation in the natural muscle.

1.5 Objectives and Contributions

1.5.1 Objectives of the Dissertation Research

Due to the use of SMA as an actuator, the AM also exhibits hysteresis and nonlinearities behaviors. This makes the use of SMA as an actuator in the AM system very difficult. Therefore, this research dissertation aims to study and develop the model and control system for the TEM antagonistically driven SMA actuated AM wrist joint system.

The first objective is to formulate a mathematical model to describe input and output relation of the SMA complex hysteresis nonlinear phenomenon. In the literature, the phenological hysteresis models are the common approach used to describe the input and output behaviors of the SMA actuator. Due to the phenological hysteresis model being built without the knowledge of the SMA physical and mechanical principles, this approach only works under specific input conditions and mechanical load values. From the previous section, the hysteresis nonlinearity of the SMA behavior is influenced by the stress exerted on the SMA. Therefore, the phenological model will have to take into account the stress exerted on SMA to formulate the stress-dependent phenological hysteresis model with temperature and stress as inputs and Young's modulus as output.

Completing the SMA model, the complete joint system model can be developed by cascading the TEM model to the SMA model and finally to the joint mechanical dynamic model. The TEM input is the supply current, and the TEM provides the temperature on each side of the TEM as output. The temperature on each side of the TEM represents the amount of heat on the surface. This heat will be transferred into the SMA via convective heating. Considering the small volume of SMAs, a combined heat capacity of the TEM side ceramic material and SMAs is considered. Therefore, the temperature of each side of the TEM is used as the input temperature to the SMA model. The phenological SMA hysteresis models will take the temperature and stress as inputs and provide the resultant force acting on the joint shaft. With force acting on the joint shaft and the dynamic mechanical description,

the final joint angle can be yielded. Therefore, a comprehensive joint model considering the electric, thermomechanical and mechanical domain inside of the joint system as well as the interactions can be developed for the control system development.

The second objective is to develop a control system for position tracking to control the thermoelectric antagonistically driven SMA wrist joint. According to literature, many control approaches have been developed by researchers, such as sliding mode control, back-stepping control, and others. Among these control systems, back-stepping based prescribed adaptive control with the ability to guarantee the global stability of the closed-loop system, the transient and steady-state performance of the dynamic system is preferred. Due to the complexity of the joint model resulted from the SMA nonlinear hysteresis behavior, the control system development becomes very challenging. To overcome this problem, the feedforward inverse compensation approach is proposed to eliminate the nonlinear hysteresis that is caused by the SMA.

This research project is also part of the main research project to realize an artificial arm. From the main research project, the wrist joint system is required to achieve rotation angle of 60°, the rotation speed of 5° per second, tracking capability of tracking error less than 15% and load capacity of 1Kg at 0.09m from the joint axis.

1.5.2 Contributions of the Dissertation Research

According to the objectives mentioned before, the main contributions of the dissertation are highlighted as follows

- Experimental tests are conducted to study the input-output characteristics of Nitinol wire with a diameter of 0.25mm with various load conditions. Hysteresis loops with superelastic behavior within the temperature range of the TEM are identified. This information is crucial for defining the deferential force generated by the antagonist pair of SMAs to drive the wrist joint. At the same time, the super-elastic behavior provides large strain to achieve the required wrist joint rotation angle.

- From the critical load hysteresis loop that is exhibited by the Nitinol, a stress-dependent hysteresis model is developed using the Generalized Prandtl-Ishlinskii approach. The Stress-Dependent Generalized Prandtl-Ishlinskii (SD-GPI) provides the prediction of the Nitinol hysteresis under the influence of load and temperature. Meanwhile, the TEM model and the wrist joint dynamic model also have been developed. These models provide the complete simulation platform for the wrist joint system outcome prediction when subjected to a known input.

- Develop the inverse hysteresis compensator to mitigate the nonlinear hysteretic behavior of the Nitinol.

- From the estimated phenological hysteresis model, the inverse hysteresis model is derived. Therefore, some estimation errors are unavoidable. These estimation errors will cause compensation errors and translate into tracking error in the closed-loop system. Consequently, the wrist system error and the inverse compensator error are defined, and the back-stepping adaptive control approach is used to develop a controller to ensure the global stability of the wrist closed-loop tracking system is achieved. A stable TEM control system also has been developed using linearized feedback approach to bridge the gap between the controller and the TEM.

- A prototype is designed and developed to verify the wrist joint system and the controller. The experimental results from the prototype have confirmed the feasibility of the TEM antagonistically driven SMA wrist joint.

1.6 Organization of the Thesis

The dissertation is organized in the following way:

In Chapter 2, the physical hardware of this research is first shown to illustrate the completed outcome of this research. This chapter presented the realization of the wrist joint system, which first covered the design, fabrication and calibration of the wrist joint sys-

tem. The experimental platform is formed by connecting the calibrated wrist system to the instrumentation.

In Chapter 3, a comprehensive literature review is presented on the modeling and control of SMA in the aim of artificial muscle. A preliminary investigation of the SMA type Nitinol hysteresis behavior is presented to find consensus with the literature. The literature review covers the hybrid of physical and phenological hysteresis modeling method and the phenological hysteresis modeling method. Various control system and their advantages and disadvantages have also been covered in this chapter.

In Chapter 4, the development of SD-GPI model based on the GPI model that provides the Nitinol hysteresis prediction at various loading conditions is presented. The SD-GPI model is verified through numerical simulation. Following that, the TEM model also has been developed via experimental data. Meanwhile, the wrist system dynamic model also has been developed to provide a complete simulation platform for the wrist joint.

In Chapter 5, the development of the inverse compensator for the SD-GPI is first shown. Simulation results of the inverse compensator for the SD-GPI are presented. By defining the inverse compensator error and the wrist system dynamic error, the control system is developed based on the back-stepping adaptive control approach. The developed inverse based adaptive control system is verified numerically. To bridge the controller and the TEM, feedback linearized perfect controller is developed as a compensator to ensure the TEM produces the desired temperature.

In Chapter 6, the final result shows that the inverse based adaptive controller for the wrist joint system can track the desired input with errors of less than 10%. The result verifies the feasibility of TEM antagonistically driven SMA actuated wrist joint system.

Finally, Chapter 7 draws a conclusion and recommendations for further work.

Chapter 2

Artificial Wrist System Design, Fabrication and Implementation

The initial concept of the artificial wrist joint as referring to Figure 1.5, which consists of a pair of Nitinols attached to both ends of two chains to drive the sprockets. The Nitinols pair will sandwich a layer of TEM in between. Both sides of the Nitinols that are exposed will be covered with heat sinks, and cooling fans as shown in Figure 2.1 (a). The heat sinks and cooling fans are utilized to remove excess heat from the TEM. However, later in Chapter 5, it was discovered that the control system for the TEMs was unable to achieve good control of temperature on both sides. Accommodating this problem, two layers of TEMs are used, and only one side of the TEM will be in contact with the Nitinol to control the temperature. A heat sink system with minimum thickness is designed to remove the excess heat from both layers of the TEMs as shown in Figure 2.1 (b). If the heat sink is too thick, the pulley size will increase, and this will reduce the rotation angle, which leads to the need for a high transmission ratio to amplify the output angle. This will result in a very small output torque which is unable to achieve the wrist torque requirement. All the problems faced in the implementation and methods to overcome them are recorded in this chapter.

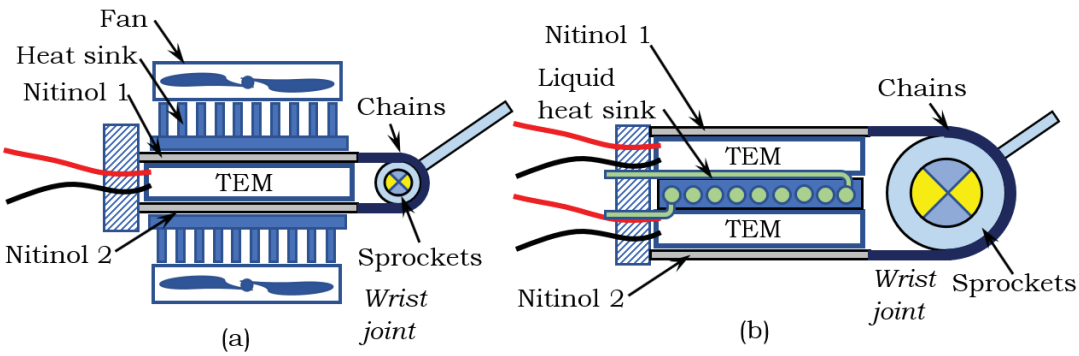

Figure 2.1: (a) Initial concept, (b) Modified concept.

2.1 Artificial Wrist Mechanical Design

The artificial wrist mechanical design includes the computation of the mechanical system requirement, actuation torque and transmission system; the mechanism to transform the AM linear movement to the wrist rotational movement; the Nitinol clamping mechanism; the pre-load mechanism; and the liquid heat sink system.

2.1.1 System Requirement, Force Identification and Transmission Design

The targeted angular velocity is 5° per second which is equivalent to 0.0873 rad per second. By considering a higher angular velocity at 0.1 rad per second, simulation is conducted to acquire the needed force at a horizontal position. At this position, the angular position is set as zero, and the gravity load is the highest. The simulation result yielded from the system model developed in Chapter 5 shown in Figure 2.2, indicates the required force is about 12 Kgf at the sprocket with a pitch diameter of 15.92mm. Referring to Figure 3.6 in Chapter 3, the working range of the Nitinol is between 0.70Kgf and 0.85Kgf. This means each Nitinol can contribute a maximum force of 0.15Kgf under the superelastic condition. To produce 12Kgf, 80 Nitinol wires are needed. Meanwhile, the elongation at the superelastic condition is

about 3.5 mm. Considering the effective elongation at 3mm, and the sprocket pitch diameter, the joint can achieve a rotation angle of 21.59°. To achieve 60°, a transmission with a step-up ratio of 3 (round up of 2.78) is required. Thus, to remain the same force at the end of the transmission, the required input force has to be multiplied by 3, which results in 36 Kgf or equivalent to 240 Nitinol wires. However, the TEM surface is only 40mm by 40mm. It can only accommodate up to a maximum 160 of wires of 0.25mm diameter. A 2.5mm space at the edge is voided to avoid the uneven temperature distribution near the edge of the TEM. With using only the 35mm width, a total of 140 Nitinol wires can be fitted on the TEM. Based on the TEM limitation, the TEM antagonistic driven SMA wrist joint is built using only 140 Nitinols wires on each side of the TEM layers. This provides maximum ability to carry a 0.6Kg load at the palm instead of the 1Kg.

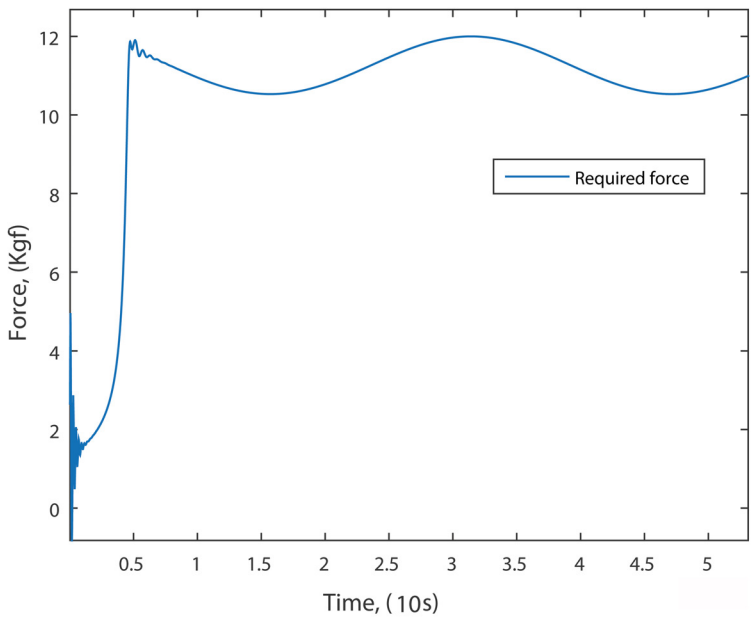

Figure 2.2: Simulated required force.

2.1.2 Wrist System Design in 3D Environment

The AM wrist system design is developed in the 3D environment using AutoCAD software. The completed wrist design 3D drawing is shown in Figure 2.3.

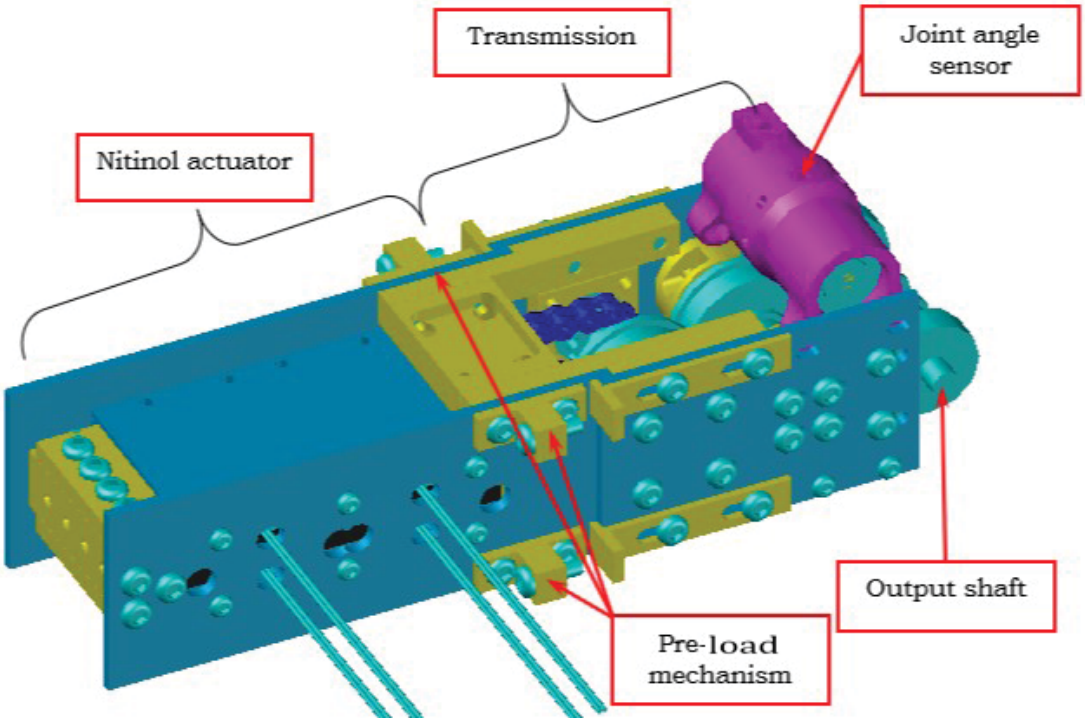

Figure 2.3: Completed Wrist joint design.

The wrist system comprises the Nitinol actuator and the transmission system. The exploded view drawings of these systems are shown in Figures 2.4 and 2.5, respectively. In the Nitinol actuator section, the TEMs are arranged side by side on both sides of the liquid cooling system. The Nitinol wires are laid on top of the TEMs with one end fixed onto the base clamp plate and the other end onto the chain link clamp plate. The chain link clamp plate connects the Nitinol to two chains that drive the sprockets. Meanwhile, to hold all the components together, two sides plates are designed on both sides of the Nitinol actuator to provide structural support. The Nitinol cover plates are included in the design to protect the Nitinol and avoid heat loss.

The pre-load sliders are designed to connect the Nitinol actuator to the transmission system and to allow the transmission system to slide during the pre-load calibration. Four pre-load adjusters are used to push the transmission system away and create pre-loaded stress on the Nitinol wires. Pre-load holders are designed and placed at the stress loading point on the transmission side plates to reinforce the transmission structure during the pre-load process. The transmission ratio is achieved using chains and sprockets in two stages of 1.5 and 2, respectively. The used of chain and sprocket system not only provides high loading ability but also provides backlash free and easy assembly. Bearings are installed at all the joints to reduce friction. A sensor holder is designed to hold the angular sensor together with the timing pulley. Another timing pulley is attached to the output shaft and connected to the angular sensor to provide angular feedback to the control system.

The main components are labeled in the drawing and listed in Table 2.1. Various materials and fabrication methods are adopted in the wrist design. Most of the components are designed to be fabricated by milling and lathe machine. Meanwhile, 3D printing technology using polylactic acid (PLA) material also has been adopted to fabricate a complex part that does not sustain large load such as the sensor holder.

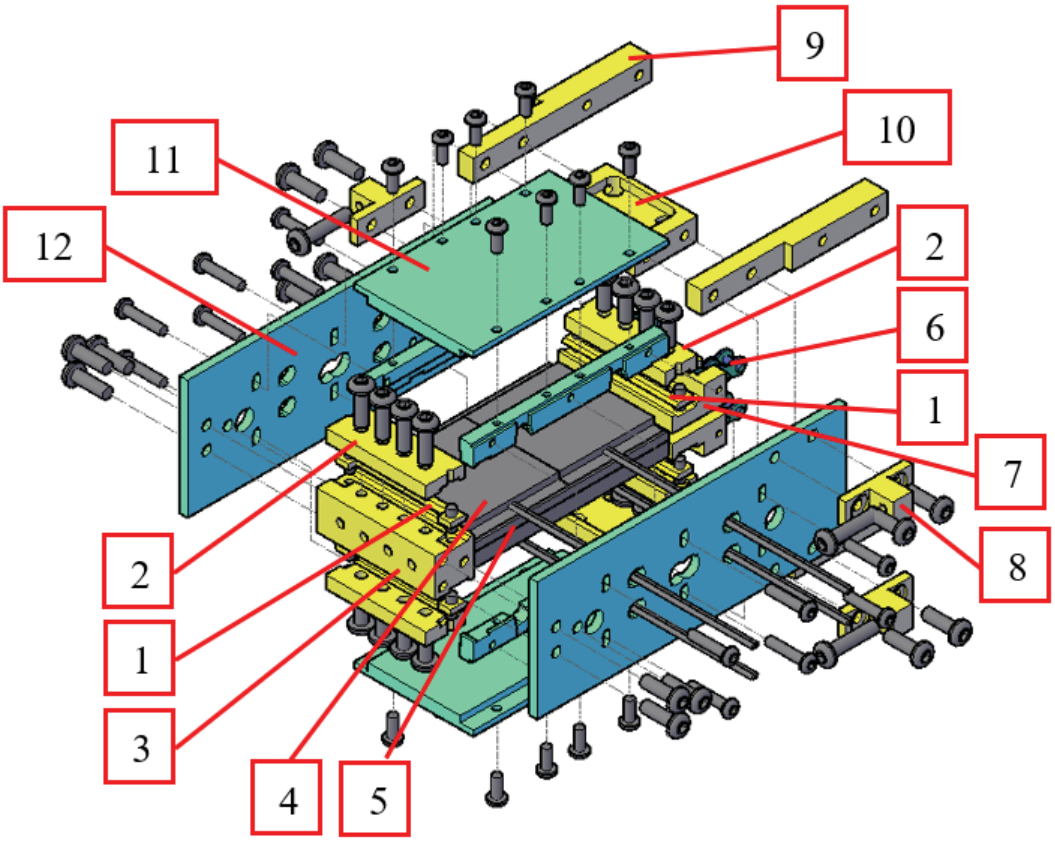

Figure 2.4: Exploded view for the Nitinol actuator.

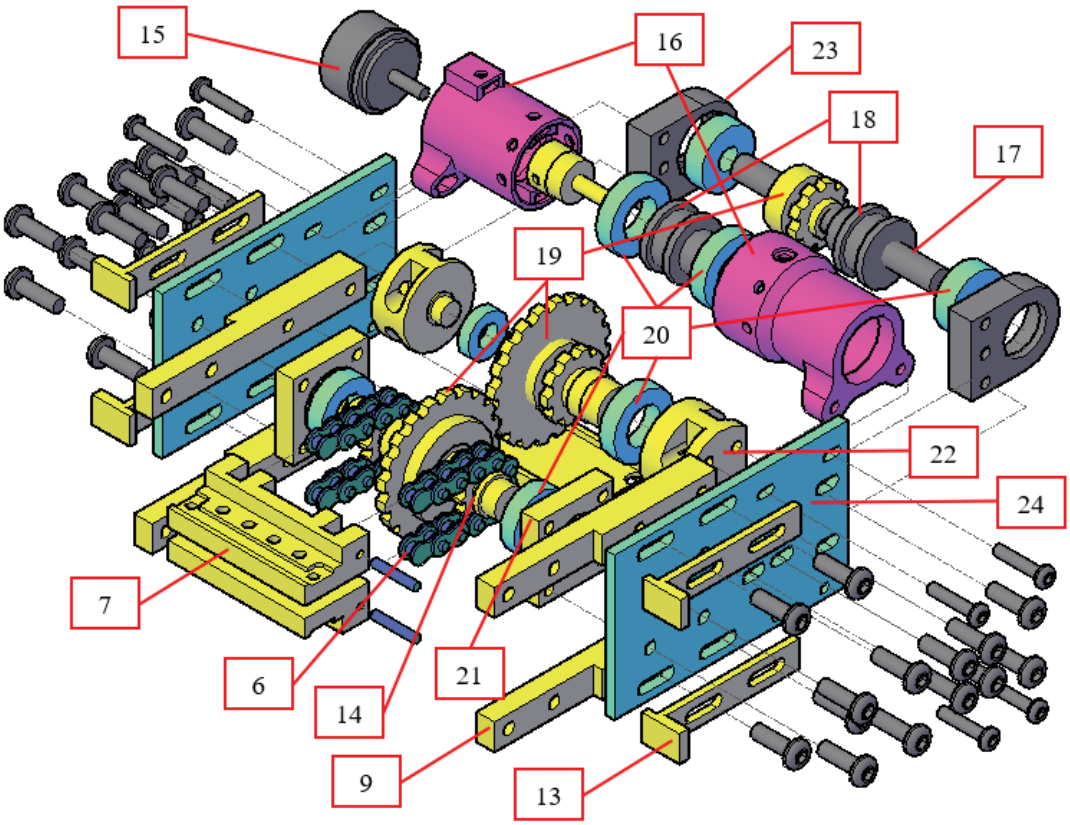

Figure 2.5: Exploded view for the wrist transmission system.

Table 2.1: Artificial wrist parts list.

No.	Description	Material	Quantity
1.	Nitinol winding plate	Brass	4
2.	Nitinol top clamp plate	Brass	4
3.	Nitinol base clamp plate	Brass	1
4.	TEM	Thermocouple	4
5.	Liquid cooling system	Aluminum	1
6.	Chain	Steel	2
7.	Nitinol chain link clamp plate	Brass	2
8.	Pre-load adjuster	Brass	4
9.	Pre-load slider	Brass	4
10.	Center reinforcement bracket	Brass	2
11.	Nitinol cover plate	Aluminum	2
12.	Actuator side plate	Aluminum	2
13.	Pre-load holder	Brass	4
14.	Pre-loading sprocket	Brass	2
15.	Angular sensor	Potentiometer	1
16.	Sensor holder	PLA	1 set
17.	Output shaft	Stainless steel	1
18.	Timing pulley	Aluminum	2
19.	Transmission sprocket	Brass	1 lot
20.	Bearing	Steel	8 (various size)
21.	Fix bearing holder	Brass	2
22.	Adjustable bearing holder	Brass	2
23.	Output shaft bearing holder	Aluminum	2
24.	Transmission side plate	Aluminum	2

2.1.3 Nitinol Winding and Clamping System Design

Each AM consists of 140 Nitinol wires. The Nitinols are bundled by winding it on two winding plates and fixed in between the brass clamp plates at both ends to form an 83mm exposed center length. A custom made jig is designed to assist the winding of the Nitinol wires. Figure 2.7 (a) illustrates how the winding jig holds the winding plates apart. The Nitinol is first wound onto a spool that fits into the jig; then the Nitinol wires are transferred onto the winding plates according to the winding pattern shown in Figure 2.6. Figure 2.7 (b) shows how the Nitinol winding process is achieved using the winding jig.

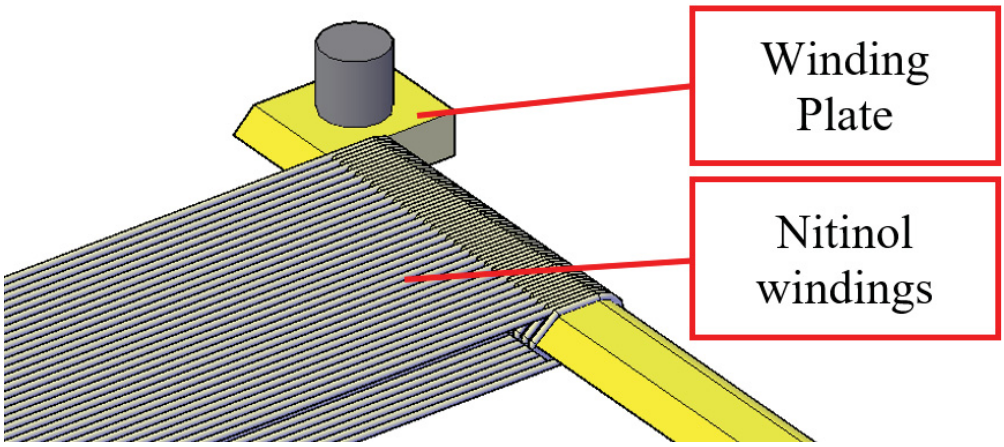

Figure 2.6: Winding pattern for the Nitinol.

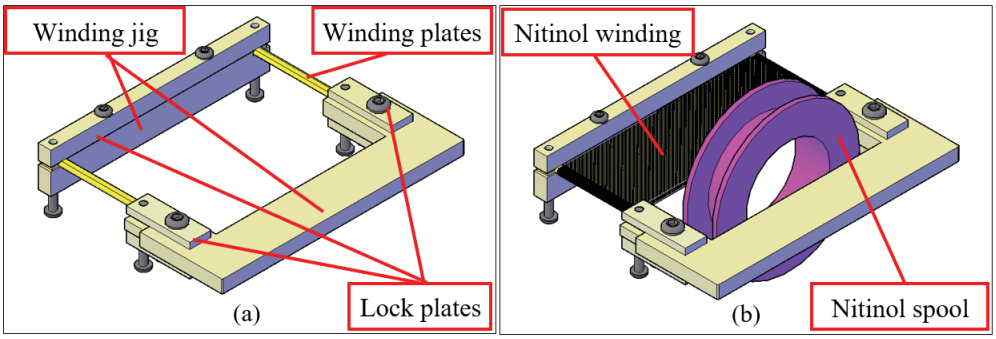

Figure 2.7: (a) Mounting the winding plates on the winding jig; (b) Winding the Nitinol wire on the winding plates.

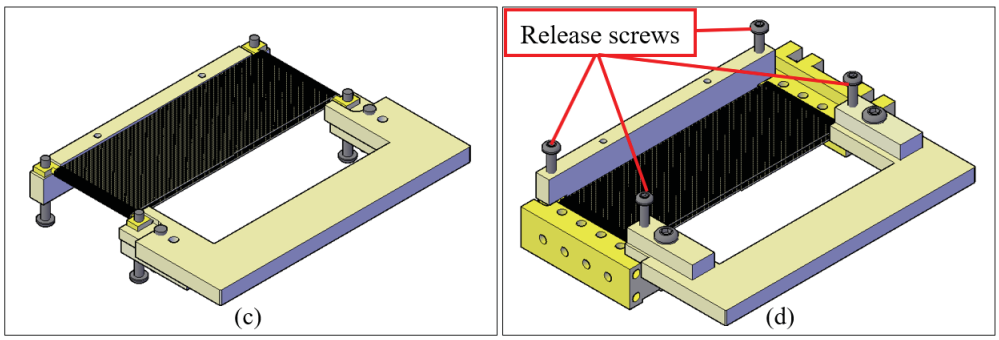

Figure 2.8: (c) Removing the lock plates; (d) Transferring the winding to the clamp plates.

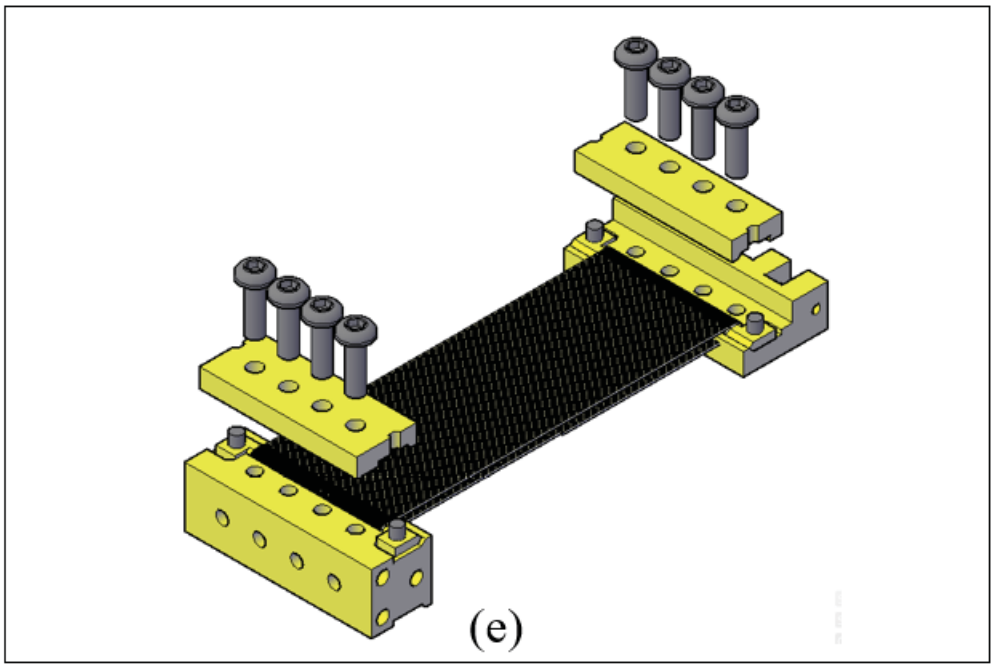

Figure 2.9: (e) Fastening the clamp plates by screws.

After the winding process is completed, the lock plates are then removed as shown in Figure 2.8 (c). Then, the jig with the winding is flipped over and installed onto the base clamp plate and the chain link clamp plate. By tightening the release screws simultaneously as shown in Figure 2.8 (d), the jig will release the winding plates onto the clamp plates. The Nitinol windings are then fastened on the clamp plates using the Nitinol top clamp plates and screws, as shown in Figure 2.9 (e). After both bundles of Nitinols are installed on the

base clamp plate, the chain link clam plates are then attached to the chains as shown in Figure 2.10.

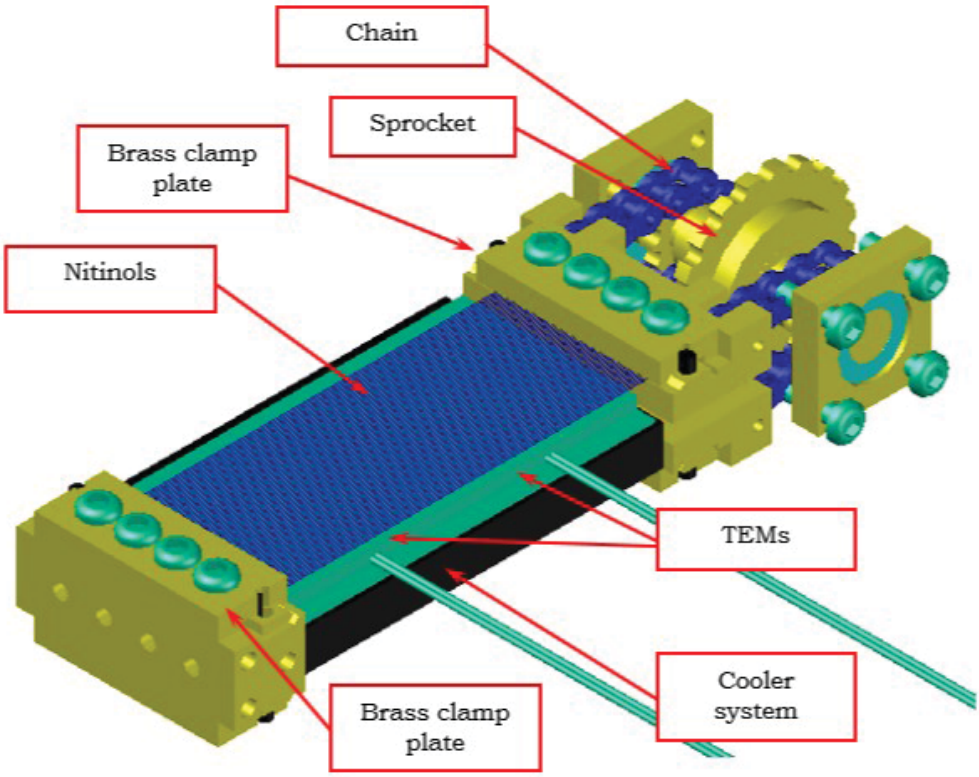

Figure 2.10: Realizing the conceptual design.

2.1.4 Pre-load Mechanism Design

Pre-loading mechanism is designed to calibrate the Nitinol to its superelastic behavior. Figure 2.3 shows the pre-load adjustors mounted at both sides of the Nitinol actuator. Four screws are tighten concurrently to push the transmission system evenly away and create constant stress on the Nitinol. When the applied stress achieves critical stress, the Nitinol will exhibit superelastic behavior. The critical stress calibration is discussed in a later section.

2.1.5 Liquid Cooling System Design

The next challenge is to propose the heat sink system that can fit in between the TEMs and yet accommodate the sprocket diameter. The initially proposed system was to use a thin-fin forged aluminum heat sink with model number APF40-40-10CB and thermal resistance of 2.5°C per Watt. However, this heat sink module cannot be fitted into the space between the TEMs. Therefore, a liquid cooling system with an external radiator for computer heat sink is modified to solve the space limitation. The schematic design of the heat sink for the TEM is shown in Figure 2.11. The liquid cooling system from GameStorm, model MaelStom 120T with a 12V 120mm diameter cooling fan is used. The heat removing capability of the liquid cooling system is unavailable. The radiator size of 154×120×22mm has more surface area compared to four thin-fin forged aluminum heat sinks. This shows that the liquid cooling system has sufficient heat sink capability.

The heat transfer contact surface of the GameStorm liquid cooling system is attached to the pump and cannot be fitted in between the TEMs. A special heat exchange plate is designed and fabricated to fit in between the TEMs to replace the existing heat transfer system. The heat exchanger is designed as per Figure 2.12, and another top piece with mirrored liquid channel pattern is joint to the bottom piece using the epoxy compound. To further ensure the cooling capability, heavy-duty radiator coolant from NASA brand with the mixture of one part coolant with three parts of water is used as the cooling liquid.

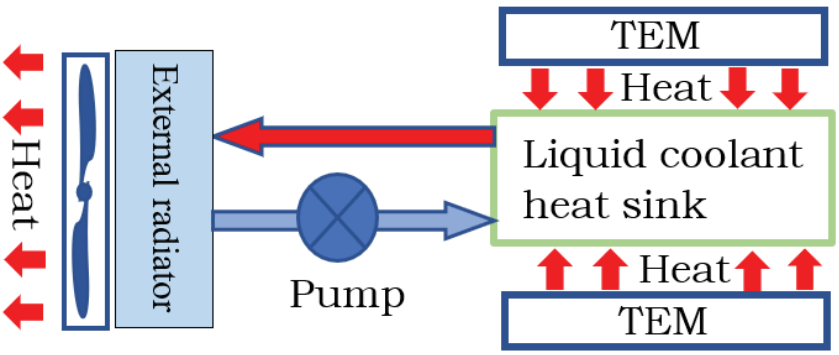

Figure 2.11: Schematic diagram of the liquid cooling system.

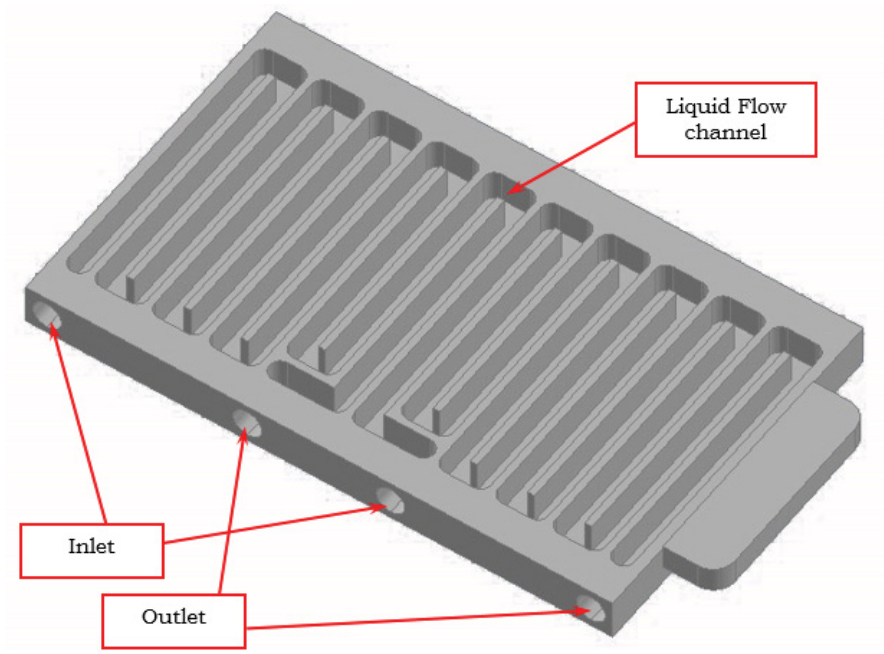

Figure 2.12: Cooler heat exchange plate design.

2.2 Artificial Wrist Fabrication and Assembly

This section compiles the description of work done in wrist parts fabrication, the sequence in assembling the parts, and method in calibrating the wrist joint.

2.2.1 Parts Fabrication

Detailed drawing of each part is produced using AutoCAD software for fabrication. Brass and alloy aluminum are used for most of the parts to reduce fabrication time and weight of the wrist. Most of the parts are manually fabricated using milling and lathe machine equipped with a digital scale with resolution up to 0.01mm. Parts with complex design are fabricated using a 3D printer with PLA. All fabricated parts are deburred and cleaned before assembly.

2.2.2 Artificial Wrist System Assembly and Calibration

The wrist assembly starts with the Nitinol winding as described in section 2.1.3. The clamped Nitinol wires are then installed onto the TEMs that sandwich the heat exchange plate as shown in Figure 2.13. The side plates are installed consequently to provide support to the base clamp plate. A thin layer of heat conductive paste is applied evenly on the TEMs to provide better heat convection. Temperature sensors are inserted on top and under the Nitinol wires before the Nitinol top plates are installed. Subsequently, the pre-load sliders, pre-load adjusters and the center reinforcement brackets are installed.

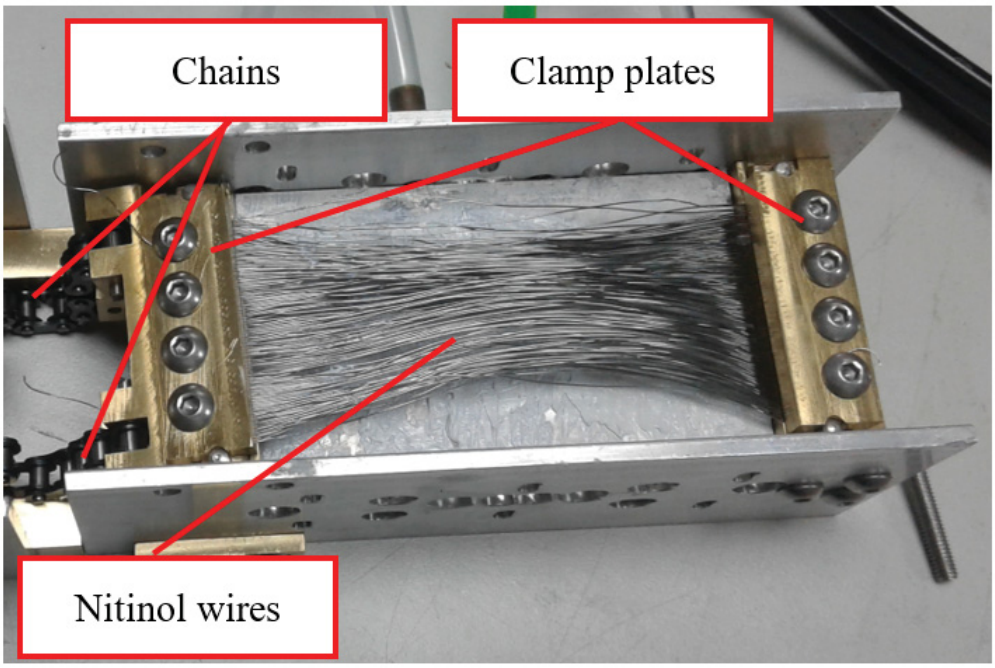

Figure 2.13: Nitinol installation.

The transmission system is then assembled according to Figure 2.5 and attached to the pre-load sliders. The use of the chain system provides a detachable segment that can be easily installed compared to a timing belt that is in a loop form. The external pump, radiator system and electronic devices are then attached to the wrist joint system.

2.2.3 Pre-load Calibration and Zero Position Calibration

The assembled wrist joint system is calibrated for the pre-loading. Figure 2.14 shows the pre-load mechanism used to calibrate the pre-load position. From the relaxed position, the pre-load screws are adjusted to stretch the Nitinol wires. At the same time, the input temperature is set to vary from 20°C to 76°C, and the rotation angle of the output shaft is observed. The transmission system will be fixed at the pre-load slider once the largest angular rotation is observed. The calibration procedure sets the Nitinol wires to the critical stress level within the temperature range from 20°C to 76°C. This enabled the Nitinol wires to yield full hysteresis loop recovery at load ranging from 0.70Kgf to 0.85Kgf. If the stress is lower than the critical load, the superelastic will not happen, and if the load is more than the critical load, the Nitinol cannot recover to the martensite phase.

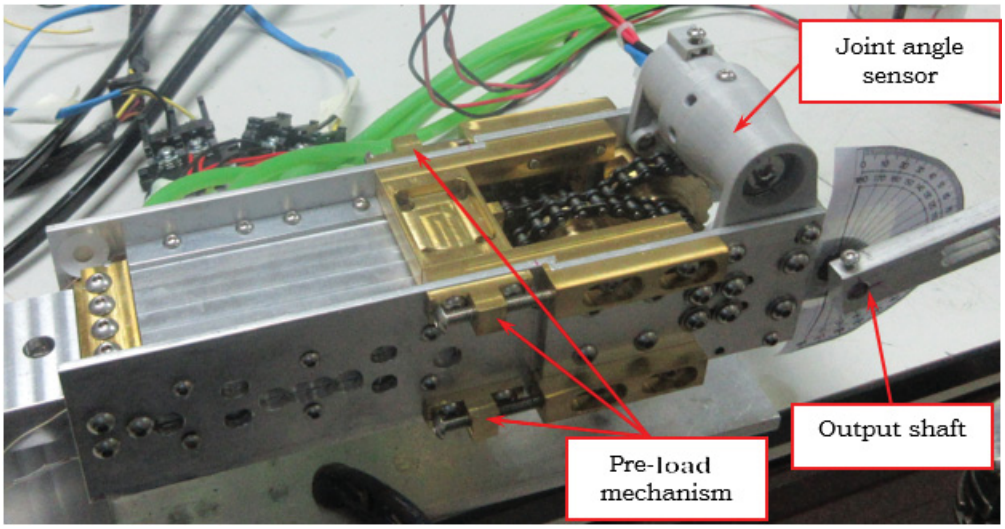

Figure 2.14: Pre-load calibration for the wrist joint.

Once the movement of the joint is calibrated to the optimum angle range, the angular sensor is attached to the joint system, and zero calibration is performed both physically and through the software. The angular sensor is a high accuracy potentiometer that is used to feedback the angular position to the control system.

Chapter 3

Literature Review

The primary search objective is planned towards the information on SMA actuated AM and system with similar functions. The general working principle of the SMA and AM is discussed in Chapter 1. Thus this Chapter will cover the primary search in the area of AM system configuration, SMA hysteresis modeling, SMA constitutive modeling, and control system. The preliminary investigation of SMA type Nitinol is also presented here to show the concurrence and deficiency of the literature to this research.

3.1 SMA Configuration and AM System Models

Generally, articulated AM systems are grouped into single acting and double acting as shown in Figure 1.2. These can be realized through the bias spring configuration and antagonistic configuration, respectively. Figure 3.1 shows the two typical configurations of the articulated artificial muscle systems and the equivalent schematic systems. The bias spring configuration uses only one actuator as the artificial muscle, and the bias movement is countered by a spring. This configuration needs a much higher strength actuator to handle the working load and the load from the bias spring at the same time. Such configuration is normally applied in a system that has priority actuation in a single direction. For example, human

fingers are mainly used for gripping material. The inward actuation of the finger has more priority than the outward actuation. The development of the control system for the bias spring configuration system is normally easier. This is because only one actuator will be controlled. However, some natural articulated systems need bi-directional actuation. For example, the human arm needs to perform the pull and push movement. In such a system, the antagonistic pair actuation configuration is preferred. The SMA pair can be of the same size or different, depending on the application. The antagonistic pair configuration system consists of the coupling of two actuators with highly nonlinear and hysteresis behaviors. Therefore, the control system development for such a system will be more challenging.

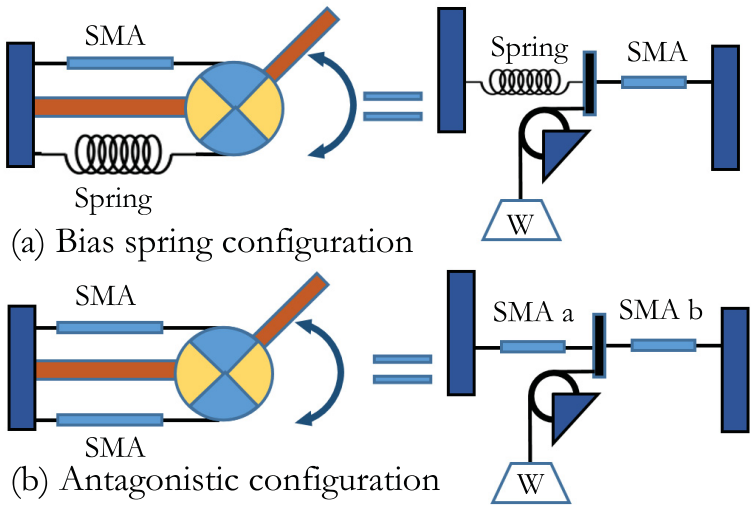

Figure 3.1: SMA configuration in articulated AM system.

3.1.1 Bias Spring Configuration AM System Model

Based on the concept of solid to solid phase change and the thermomechanical point of view, the constitutive model of SMA was introduced by [10] and [44] as Equation 3.1

$$\dot{\sigma} = D\dot{\varepsilon} + \Theta\dot{T} + \Omega\dot{\xi}, \tag{3.1}$$

where σ is the stress, and the constants D, Θ and Ω are Young's modulus, thermoelastic tensor, and phase transformation tensor, respectively. The variables ε, T and ξ are the SMA

strain, SMA temperature, and volumetric function of the martensite in SMA, respectively. The accent dot represents the time rate. Authors of [40] used the quasi-static assumption to combine the bias spring effect into the SMA constitutive Equation 3.1 yielding Equation 3.2.

$$\left(1 + \frac{A_{wire}D}{kL}\right)\dot{\sigma} = \Theta\dot{T} + \Omega\dot{\xi}. \tag{3.2}$$

The external load M is included in the system as shown in Figure 3.1(a) as the following equation

$$\sigma_0 A_{wire} = F_s + M, \tag{3.3}$$

where F_s is the spring force, which can be derived as spring force Equation 3.4.

$$FA_{wire} = kL(\varepsilon_{res} - \varepsilon), \tag{3.4}$$

where ε_{res} is the residue martensitic strain. Equation 3.2 is also the general stress-temperature relation that can be written as

$$\sigma - \sigma_0 = \Omega'(\xi - \xi_0) + \Theta'(T - T_0), \tag{3.5}$$

where

$$\Theta' = \frac{\Theta}{1 + \frac{A_{wire}D}{kL}} \quad and \quad \Omega' = \frac{\Omega}{1 + \frac{A_{wire}D}{kL}}, \tag{3.6}$$

and A_{wire} and L are the SMA wire cross-section area and length, respectively. Due to the initial martensite fraction residue, if the SMA temperature is not over the initial temperature T_M, the stress of the SMA remains as initial stress, σ_0. When the temperature of the SMA is heated over T_M the stress temperature relations are given by [40] and [3] as follows:

$$\sigma = \begin{cases} \Theta'(T - T_M) + \sigma_0 & T_M \leq T \leq A_s^m \\ \Theta'(T - A_s^m) + \Omega'(\xi - \xi_0) + \sigma_{As} & A_s^m \leq T \leq A_f^m \\ \Theta'(T - A_f^m) + \sigma_{Af} & A_f^m \leq T. \end{cases} \tag{3.7}$$

By including the initial stress, the austenite start temperature and the corresponding stress are modified as

$$\begin{cases} A_s^m = \frac{C_a A_s - \Theta' T_M + \sigma_0}{C_A - \Theta'} \\ \sigma_{As} = \Theta'(A_s^m - T_M) + \sigma_0. \end{cases} \tag{3.8}$$

During the cooling process, the stress temperature relation is given by [40] as

$$\sigma = \begin{cases} \Theta'(T - T_c) + \sigma_c & T_c \leq T \leq M_s^m \\ \Theta'(T - M_s^m) + \Omega'(\xi - \xi_c) + \sigma_{Ms} & M_s^m \leq T \leq M_f^m \\ \Theta'(T - M_f^m) + \sigma_{Mf} & M_f^m \leq T, \end{cases} \tag{3.9}$$

where σ_c, T_c and ξ_c are the initial conditions for the cooling process. However, Equations 3.5 to 3.9 are not rate dependent and may not be useful in dynamic modeling. Meanwhile, Equation 3.2 can be rewritten as a function in terms of strain ε and strain rate $\dot{\varepsilon}$ that relate to the angular displacement θ and angular velocity $\dot{\theta}$ as

$$h(\theta, \dot{\theta}) = g(\varepsilon, \dot{\varepsilon}), \tag{3.10}$$

which can be used in the control development such as the sliding mode control development [45].

In [46] the bias spring effect is combined in the form of resultant strain as per Equation 3.55, where the spring constant is embedded in parameters b_1, b_2, and b_3. Authors also combine Equation 3.55 into a single polynomial as Equation 3.56 to allow continuous differentiation, which is used by [13] in the control system development.

3.1.2 Antagonistic SMA Pair Configuration AM System Model

The antagonistic SMA configuration is also called the differential configuration. As per Figure 3.1 (b) the SMAs are labeled as "a" and "b". Under the condition of both SMAs having the same material, the initial condition can be written as Equation 3.11 for SMA"a" and SMA"b", respectively. In this section, the parameters for SMA"a" and SMA"b" are labeled with their superscript "a" and "b", respectively.

$$\begin{cases} \xi_0^a = 0, \ \xi_0^b = \frac{\varepsilon_{res}}{\varepsilon_L} \\ \sigma_0^a = 0, \ \sigma_0^b = \frac{W}{s} \\ \varepsilon_0^a = 0, \ \varepsilon_0^b = \varepsilon_{res}, \end{cases} \tag{3.11}$$

where ε_L is the maximum recoverable strain. From the constitutive equation, Equation 3.1, the antagonistic SMA configured AM system can be defined in the rate form as

$$\begin{cases} \dot{\sigma}^a = D\dot{\varepsilon}^a + \Omega\dot{\xi}^a + \Theta\dot{T}^a \\ \dot{\sigma}^b = D\dot{\varepsilon}^b + \Omega\dot{\xi}^b + \Theta\dot{T}^b. \end{cases} \tag{3.12}$$

The SMA"a" and SMA"b" will achieve an equilibrium condition when

$$\begin{cases} L_a\dot{\varepsilon}^a = -L_b\dot{\varepsilon}^b \\ a_s^a\sigma^a = a_s^b(\sigma^b - \sigma_0^b). \end{cases} \tag{3.13}$$

Therefore, the system governing equation can be written as

$$[L_a(\dot{\sigma}^a - \Omega\dot{\xi}^a - \Theta\dot{T}^a)] + [L_b(\dot{\sigma}^b - \Omega\dot{\xi}^b - \Theta\dot{T}^b)] = 0. \tag{3.14}$$

Meanwhile, the deferent of stress rate can be obtained from Equation 3.12, and integrating the deferent of stress rate yields

$$(\sigma^a - \sigma^b) = \int f(\dot{\varepsilon}^a, \dot{\xi}^a, \dot{T}^a, \dot{\varepsilon}^b, \dot{\xi}^b, \dot{T}^b)dt. \tag{3.15}$$

Equation 3.15 can be utilized in Equation 3.99 for control system development in [30] and [47].

3.2 Input-Output Characteristic of the SMA

The hysteretic behavior exhibited by the SMA is normally described as the output Young's modulus with response to the input temperature at a fixed load. At varying load conditions the phase transition temperature increases with respect to the increase of load. Earlier researcher such as [3], [10], [11], [12], [13], [24], [26], [41], [44], [46], [48], [49], [50], [51], [52], [53], [54], [55], [56], [57], [58], [59] and [60] have proposed various constitutive models to model the SMA hysteresis. Although these constitutive models include the stress dependency in the hysteresis model, their models are unable or too complex to yield the inverse model for the hysteresis behavior. The inverse model is an important component to mitigate the hysteresis effect. Overcoming the limitation of these constitutive models, invertible phenological model

was developed by [4], [5], [6], [7], [8], [31], [61], [62], [63], [64], [65], [66], [67], [68], [69], [70], [71], [72], [73], [74] and [75] under a fixed load condition. Unfortunately, the model developed under the fixed load condition becomes inaccurate in the system with load variance such as in this research application. To the best of the author's knowledge, there is no study on the stress-dependent invertible SMA model up to date. This motivates the investigation to develop the stress-dependent hysteresis model using invertible phenological approach for the SMA in this research. Before further discussion on the SMA constitution model, a preliminary experiment is setup to investigate the stress-dependent characteristic of the SMA.

3.2.1 Experimental Platform Setup

An experimental platform is designed and setup to measure the SMA strain versus the temperature. The vertical loading method is proposed by hanging the load at the lower end of the SMA with the other end fixed to a rigid beam. TEMs are used to heat and cool the SMA. A computer with control software such as Matlab is proposed to control the TEM via data acquisition (DAQ) dSPACE control board. The control signal is amplified to supply driving power to the TEMs. Heat is transferred from the TEMs to the SMA via convective heating assisted with thermal paste. The SMA temperature and elongation are measured with the temperature sensor and displacement sensor, respectively. The measured data are recorded via the same DAQ system for further analysis. The proposed system is shown in Figure 3.2.

SMA with transition temperature close to room temperature is selected to reduce excessive heating and cooling during operation and to dispense with intensive insulation on the system. The transition temperature also has to be in the TEM operation range. Based on this constraint, SMA models Nitinol #6 and Nitinol #8 from Fort Wayne Metals with A_f 40 to 80°C, and 22 to 40°C, respectively are proposed for investigation. In realizing the proposed experimental setup, sensors and equipment systems are carefully selected to reduce errors

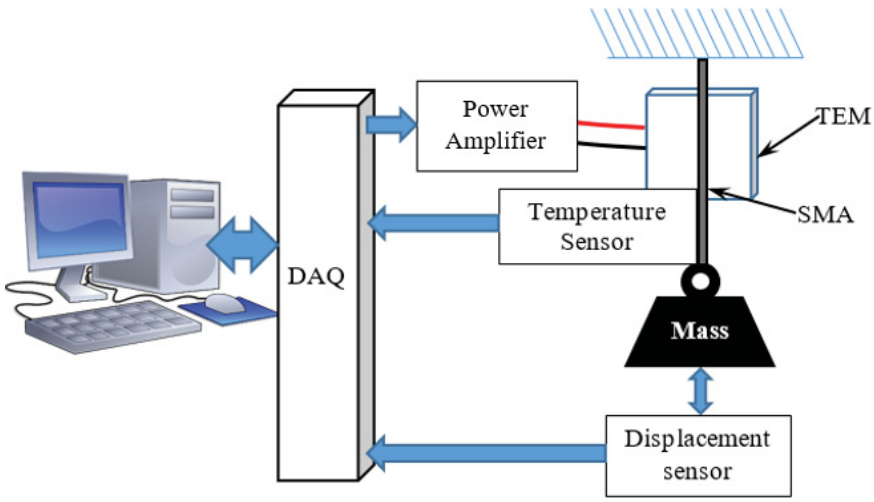

Figure 3.2: Proposed experimental setup.

caused by physical friction, time delay, and signal noise. The experimental platform hardware comprises a SMA wire, a non-contact displacement sensor, a power amplifier, a mass, two thermoelectric modules, two temperature sensors, a cooling fan, and dSPACE control board. The following provides detailed information on the experimental platform materials, and the physical setup is shown in Figure 3.3.

- The SMA wire with 0.25mm diameter, 120mm length, made by Fort Wayne Metals is used. To achieve a fast response, the smallest industrial standard diameter at 0.25mm is selected. The effective initial length is 80mm, in which a 20mm length at each end of the SMA is used for gripping.
- The Non-contact displacement sensor (Brand: Keyence, Model: LK031) is employed to measure the SMA elongation. The LK031 is able to measure up to 1μm accuracy. Non-contact sensor is selected to avoid additional friction in the system.
- The H-bridge, 20A, 5V to 28V power amplifier model: RB-Rop-05 amplifies the pulse width modulation signal to drive the TEM.
- Loading mass.

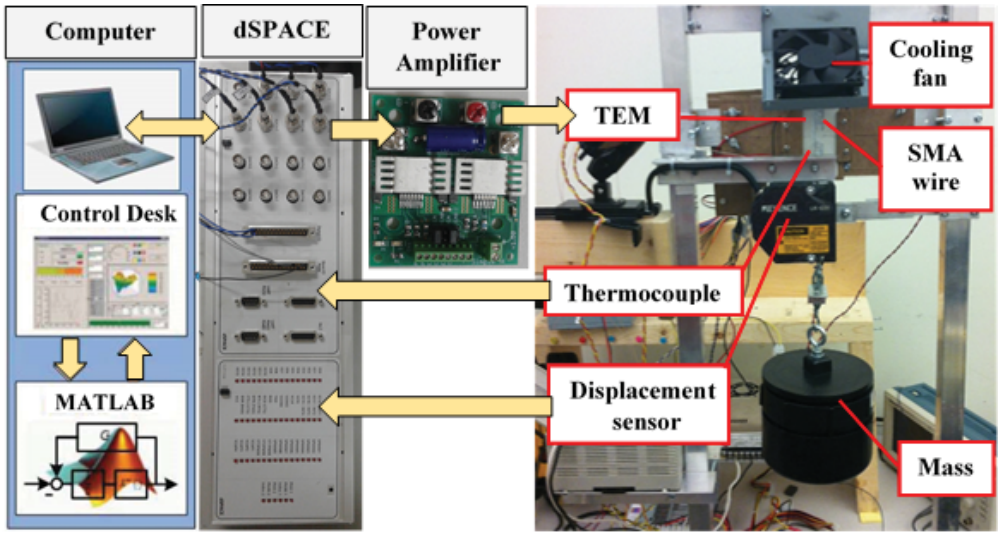

Figure 3.3: Experimental setup for hysteresis data acquisition.

- Two high heat pumping TEMs series: UT15,200,F2,4040 from Laird Technology are employed to heat and cool the SMA.
- Two K-type thermocouple temperature sensors (Brand: Omega, Model: 5TC-TT-K-40-36) with 0.08mm diameter wire are used to detect the SMA temperature. The temperature sensor has a response time of less than 0.25s and is connected to the dSPACE via TX93A temperature transmitter from the same manufacturer.
- The 65mm diameter, 12V cooling fan is used as an active cooling system for the SMA.
- The control board (Brand: dSPACE, Model: DS1104) provides 16-bits analog-to-digital converters (ADC) input channel and digital-to-analog converter (DAC) output channel. The inputs are connected to the displacement sensor and temperature sensor to record the sensors signals. The output channel is connected to the power amplifier to drive the TEMs for heating the SMA.

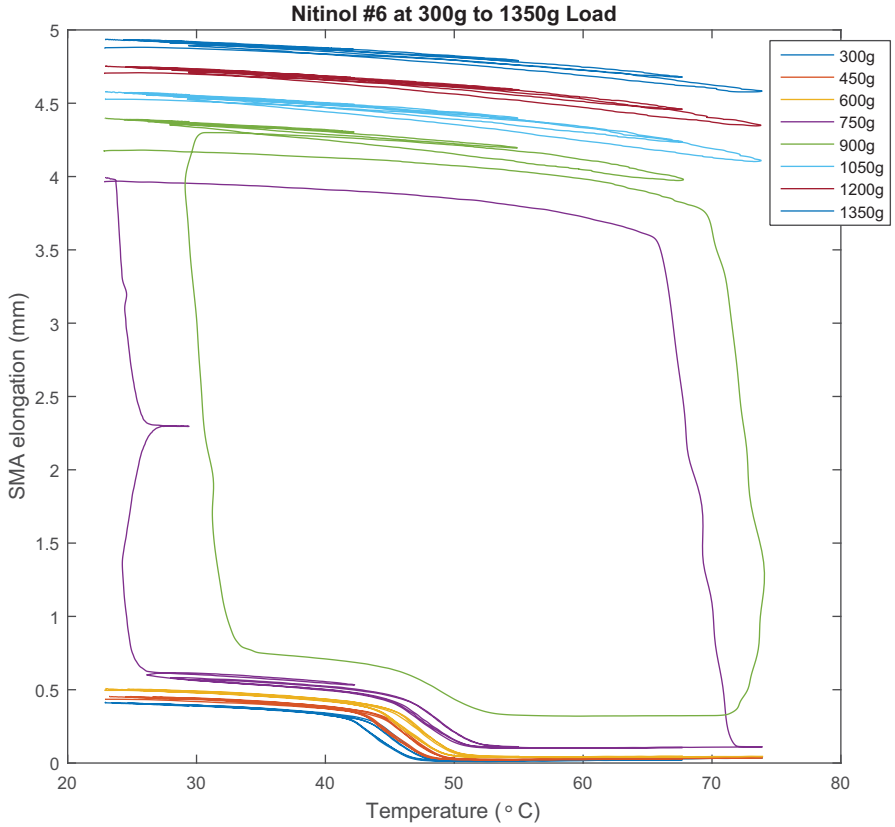

Figure 3.4: Elongation of Nitinol #6 with response to input temperature with different loads.

3.2.2 Input-Output Characteristic with Different Mechanical Loads

A decaying sawtooth signal with a 4×10^{-3}Hz frequency and decaying rate of -1×10^{-3} is subjected to the SMA. The initial amplitude is set at 78°C, slightly below the TEM maximum temperature of 80°C. The elongation of the SMA under load variations is measured and recorded. Figures 3.4 and 3.5 show the elongation as the output response of Nitinol #6 and Nitinol #8, respectively to the input temperature under load variation of 150g each step.

Figure 3.4 shows the elongation of the SMA with responses to the applied load starting from 300g to 1350g with a step of 150g. The hysteresis loops for 300g to 600g load show small strain variation between the martensite and austenite phase with an elongation difference of about 0.33mm. The A_f and the M_f take place in between 41 to 54°C with an increase

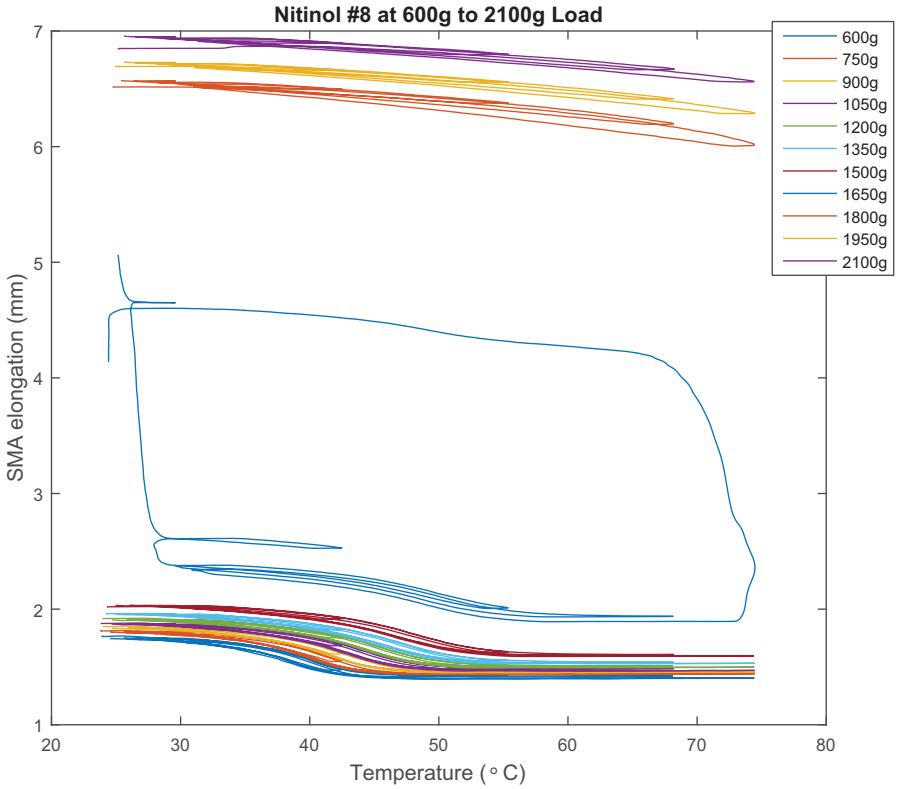

Figure 3.5: Elongation of Nitinol #8 with response to input temperature with different loads.

of about 1°C for each 150g load increase. A large strain with a difference of about 3.5mm elongation in between the martensite and austenite phase is observed in the hysteresis loop between 750g to 900g load. This shows the superelastic behavior at the critical load. At the superelastic condition, the hysteresis effect becomes more distinct, where the transition temperature is about 45°C apart. Hysteresis loop from 1050g and above show small strain difference between the phases. This is due to the transition temperature being higher than the input temperature.

Similar trends are observed in Figure 3.5. For Nitinol #8, the critical load is between the 1500g to 1800g load, which is 1000g higher than Nitinol #6. The transition temperature is about 49°C apart.

Large strain at superelasticity of the SMA provides useful strain for realizing the AM. Therefore, a more refined experiment is carried out on both the Nitinol #6 and Nitinol #8 at the superelastic load range. A smaller load step of 50g is applied to study the hysteresis loop under superelastic conditions. The results of the experiment are shown in Figures 3.4 and 3.5.

More numbers of complete hysteresis loops are observed in Figure 3.6 compared to Figure 3.7 due to the higher transition temperature of Nitinol #8 that is not achievable by the TEM. Based on this limitation, the Nitinol #6 is a better choice than Nitinol #8. The smaller gap of the transition temperature of Nitinol #6 is allowing it to achieve the desired temperature by the TEM in a shorter time. Based on this initial finding, Nitinol #6 is identified as the SMA material for this study. Further in this thesis, Nitinol is refers to Nitinol #6; otherwise, it is specified.

3.3 SMA Constitutive Models

Generally, there are three groups of SMA constitutive models. One group uses the finite element method, which is mainly for simulation and analysis, as reported in [76], [77], [78]

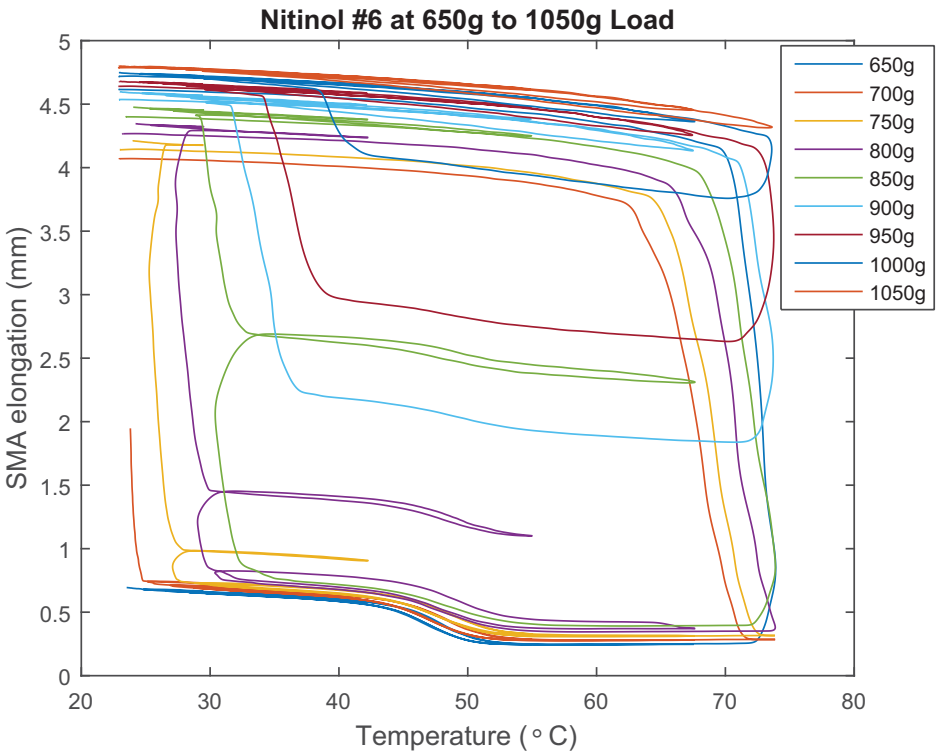

Figure 3.6: Elongation of Nitinol #6 with response to input temperature under superelastic condition.

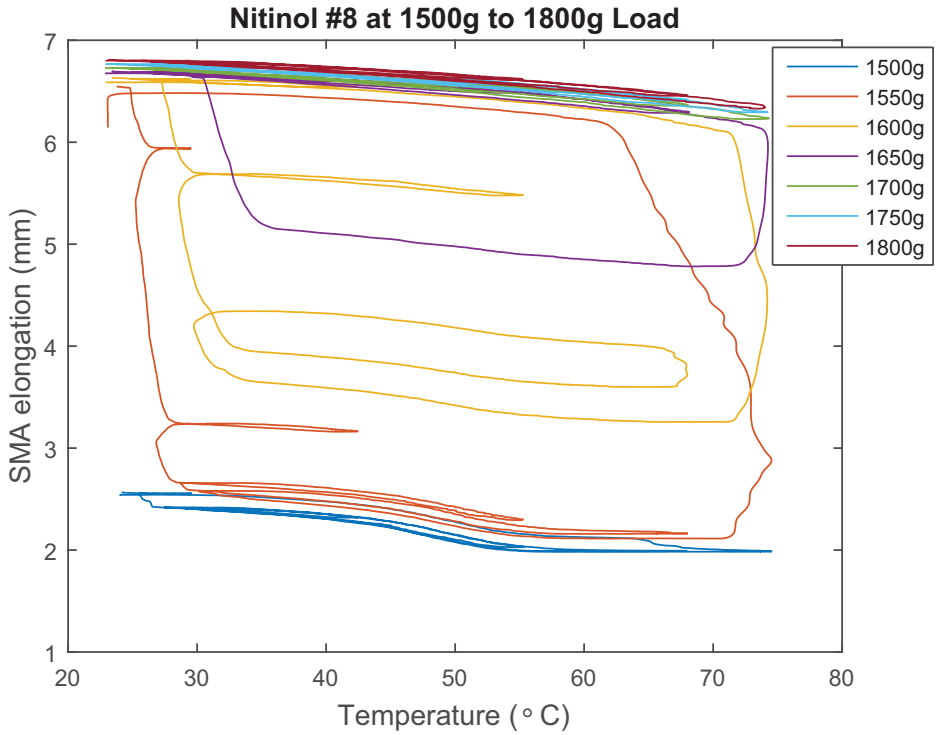

Figure 3.7: Elongation of Nitinol #8 with response to input temperature under superelastic condition.

and [42]. This group of models is not discussed here. The second group of SMA constitutive models are derived from the solitary phenological method. Meanwhile, the third group of models are the analytical models, which are derived from combining physical and phenological modeling method. The second and third group of models are of interest in this review because these models could be utilized to develop a real-time control system. In the solitary phenological method, the system models are obtained by analyzing the system output and mathematically modeled the system concerning the system input under various conditions. On the other hand, the combined method models such as the stress-strain behavior in Tanaka model [48]are derived via the physical method. Meanwhile, the SMA thermomechanical behavior that relates the Young's modulus to the temperature or amount of molecular structure in the martensite and austenite phase is modeled via the phenological method.

3.3.1 SMA Phenological Models

The nonlinear and hysteresis behaviors of SMA are observed in the transformation kinetics, which is defined by the molecular phase fraction of the SMA subjected to stress and temperature. These nonlinear and hysteresis behaviors are difficult to be modeled via the physical approach. Therefore some researchers use the solitary phenological method to mathematically model the SMA output with the corresponding input via the mathematical model.

Preisach Model

The Preisach hysteresis model was first developed to model ferromagnetic material. However, researchers found that the Preisach model can also be used to model various hysteresis effects, such as piezo and SMA. Many researchers have successfully applied the Preisach method on SMA hysteresis modeling, among them being [4], [5], [61], [62], [63] and [64]. The main concept of the Preisach model is that the system output is a parallel summation of the activated continuum weighted hysteresis operators $\gamma_{\alpha\beta}$. Each of these operators is controlled

by a pair of α and β switches, which is the increase and decrease switching values of input, respectively. Each of the operators $\gamma_{\alpha\beta}$ is also assigned with a weight function $\mu(\alpha, \beta)$ called the Preisach function. The general Preisach model is written as

$$y(t) = \int\int_{\alpha \geq \beta} \mu(\alpha, \beta)\gamma_{\alpha\beta}[u(t)]d\alpha d\beta. \tag{3.16}$$

Equation 3.17 is the switching mechanism for the operator.

$$\gamma_{\alpha\beta} = \begin{cases} +1 \ for \ \ (\beta, \alpha) \in S^{+}(t) \\ -1 \ for \ \ (\beta, \alpha) \in S^{-}(t), \end{cases} \tag{3.17}$$

where $S^{+}(t)$ and $S^{-}(t)$ are the two domains in the Preisach plane T. The line separating the two domains is called the memory interface, $L(t)$. Figure 3.8 shows the schematic structure of the Preisach model. The output value $u_{\alpha\beta}$ can be obtained from the experimental result. At

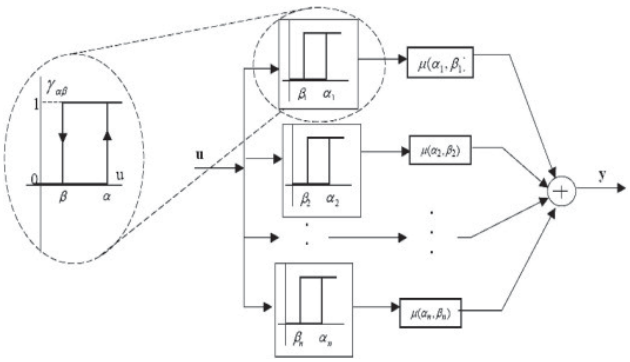

Figure 3.8: Schematic structure of the Preisach model [4].

first, uniformly dividing the T plane to a finite vertical and horizontal line. Each intersection of the line is a point, represented by (β_j, α_i), where the β is the vertical decreasing line, and α is the horizontal increasing line. Let $v(t)$ be the input of the system, the output at each $u(\alpha_i, \beta_j)$ is recorded by increasing the $v(t)$ to a α_i and decreasing the $v(t)$ to a β_j point with $\alpha_i \geq \beta_j$. Figure 3.9 shows the staircase like $L(t)$ when $v(t)$ goes through the major loop and the first-order decreasing curve (FOD). By recording all the values for the output at (α_i, β_j) points, an upwards triangular matrix of $u(\alpha, \beta)$ can be obtained. Connecting all the FOD points forms a FOD surface. A smooth FOD surface can be defined by the least squares

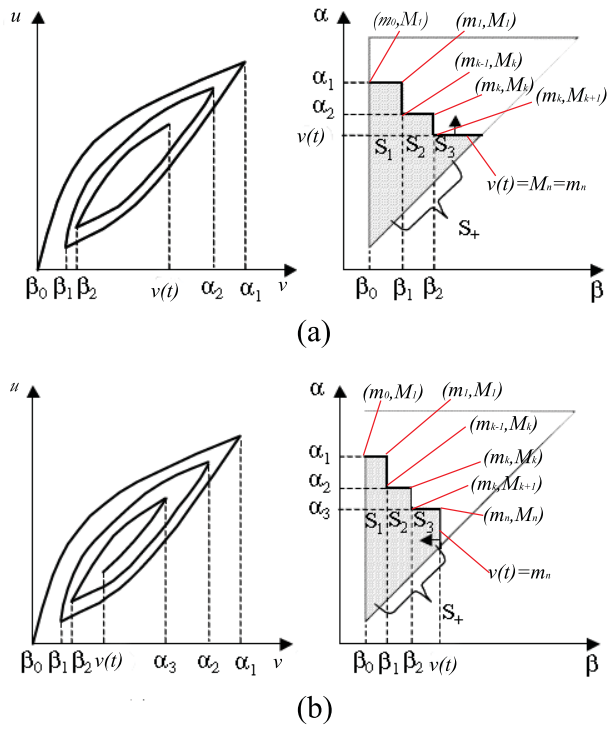

Figure 3.9: Input, $v(t)$ variation to T plane translation [5].

method or interpolation method. This will provide a continuous FOD surface. Each increase and a decrease of $v(t)$ will form a trapezoid, such as S_1, S_2 and S_3 in Figure 3.9 (b). If the last variation of $v(t)$ is an increment, it will end with a triangle as shown in Figure 3.9 (a). By noting the memory point at the $L(t)$ as $(m_0, M_1) \rightarrow (m_1, M_1) \downarrow (m_1, M_2) \ldots (m_{k-1}, M_k) \rightarrow (m_k, M_k) \downarrow (m_k, M_{k+1}) \ldots (m_n, M_n) \downarrow v(t) = m_n$, as shown in Figures 3.9 (a) and (b), the output $u(t)$ is defined as Equation 3.18 by [62]. Details of the equation can be referred to [62].

$$u(t) = \sum_{k=1}^{n} (u_{M_k m_k} - u_{M_k mk-1}) + u^{-}. \tag{3.18}$$

From the FOD surface recursive equation and Equation 3.18, the continuous hysteresis output can be generated with a given continuous time input.

Generalized Prandtl-Ishlinskii (GPI) Model

The conventional Prandtl-Ishlinskii (PI) model uses linear play operators, which leads to the limitation of symmetric hysteresis prediction. However, the SMA is known to inherent asymmetric hysteresis behavior. Therefore, the Generalized Prandtl-Ishlinskii (GPI) hysteresis model has been proposed by many researchers, such as [6], [31], [65], [66], [67], [68] and [69] in modeling the SMA hysteresis effect. In the GPI model, the generalized play operator is a nonlinear operator that will result in asymmetric hysteresis loop prediction. Figure 3.10 (a) shows the PI operator and (b) shows the GPI operator. The curves γ_l and γ_r are the continuous envelope function for the increase and decrease input-output relationship, respectively, where $\gamma_l \leq \gamma_r$. For a given input temperature $T(t) \in C_m[0, t_E]$, the generalized play operator can be written as

$$\begin{aligned} F_{lr}^{\gamma}[T](0) &= f_{lr}^{\gamma}(T(0), 0) = w(0); \\ F_{lr}^{\gamma}[T](t) &= f_{lr}^{\gamma}(T(t), F_{lr}^{\gamma}[T](t_i)); \\ &\quad for\ t_i < t \leq t_{i+1}\ and\ 0 \leq i \leq N-1, \end{aligned} \tag{3.19}$$

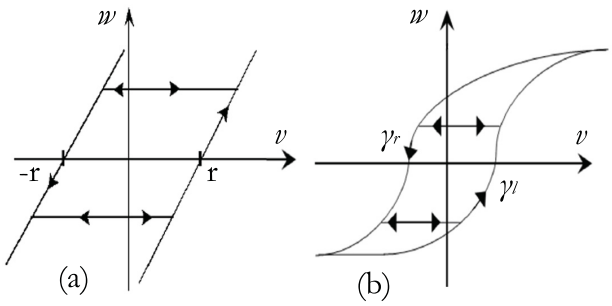

Figure 3.10: Play operator (a) PI model (b) GPI model [6].

where $f_{lr}^{\gamma}(T,w) = max\,(\gamma_l(T) - r, min\,(\gamma_r(T) + r, w))$. With the generalized play operator $F_{lr}^{\gamma}[T](t)$, the SMA hysteresis $y_{p\gamma}(t)$ in the form of a fraction of martensite or stress can be written as

$$y_{p\gamma}(t) = p_0\gamma(T) + \int_0^R p(r)F_{lr}^{\gamma}[T](t)dr. \tag{3.20}$$

[6], [66], [67], [68], and [69] have used the hyperbolic-tangent envelope function for the generalized play operator and the non-memory function, $p_0\gamma(T)$. Equations 3.21 and 3.22 show the adoption of hyperbolic-tangent function in the GPI model.

$$\begin{aligned} \gamma_r(T) &= a_0 tanh(a_1T + a_2) + a_3, \\ \gamma_l(T) &= b_0 tanh(b_1T + b_2) + b_3, \end{aligned} \tag{3.21}$$

$$\gamma(v) = \begin{cases} c_0(tanh(c_1T + c_2)) + c_3 & for\ \dot{T} \geq 0, \\ d_0(tanh(d_1T + d_2)) + d_3 & for\ \dot{T} < 0. \end{cases} \tag{3.22}$$

The density function is given as

$$p(r) = \rho e^{-\tau r}, \tag{3.23}$$

moreover, the threshold function can be chosen as

$$r_j = cj \quad j = 1, 2, 3 \ldots, n. \tag{3.24}$$

where a_i, b_i, c_i, d_i $(i = 0, 1, 2, 3)$, ρ, τ and c are constants that form the vector X, which will be identified from the experimental data via the minimization error squared function that is

given by:

$$J(X) = \sum_{i=1}^{M} (y_{p\gamma}(i) - y_m(i))^2 \tag{3.25}$$

where y_m is the measured displacement of the SMA, M is the number of data points used, and J is the total error from the regression. Figure 3.11 shows the simulated and measured major and minor hysteresis loop of a SMA presented by [6].

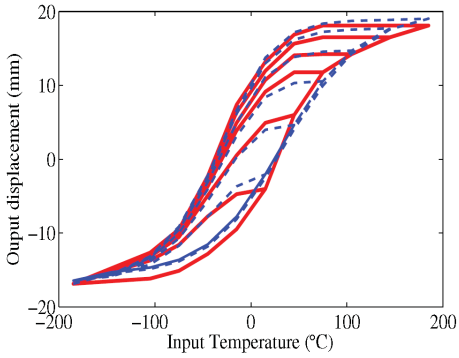

Figure 3.11: Comparison of GPI model with measured hysteresis loops of a SMA

Krasnoselskiiand Pokrovskii (KP) Model

Krasnoselskiiand Pokrovskii (KP) model uses a continuous operator called the KP kernel instead of the discontinuous operator in the Preisach model. The use of the KP model in SMA hysteresis modeling can be observed in [7], [8], [70], [71], [72], [73], [74], and [75]. The KP kernel is a continuous function consisting of minor loops within the major loop on the Preisach plane. By considering P as the Preisach plane, the following can be defined

$$P = p(\alpha, \beta) \in R^2 : V^- \leq \alpha \leq \beta \leq V^+ - a, \tag{3.26}$$

where V^+ and V^- are the positive and negative saturation value of input $v(t) \in [V^-, V^+]$, respectively. a is a positive rise constant of the kernel. The KP kernel function for a given point $p(\alpha, \beta)$ is shown by Equation 3.27

$$k_p(v, \xi_p) = \begin{cases} max\{\xi_s, r(v-\alpha)\} & for\ \dot{v} \geq 0, \\ min\{\xi_s, r(v-\beta)\} & for\ \dot{v} \leq 0, \end{cases} \tag{3.27}$$

where the ξ_s is the memory term that will be updated every time the $\dot{v}$ changes sign. The kernel active functions $r(v-\alpha)$ and $r(v-\beta)$ form the envelope of the hysteresis. The width of the envelope is governed by the α and β, while the transform slope from -1 to 1 is defined by the rise constant, a, as shown in Figure 3.12. The ridge function $r(x)$ in Equation 3.27 is given as

$$r(x) = \begin{cases} -1 & x < 0 \\ -1 + 2\frac{x}{a} & 0 \leq x \leq a \\ 1 & x > a. \end{cases} \tag{3.28}$$

The integral form of the KP hysteresis model can be written as

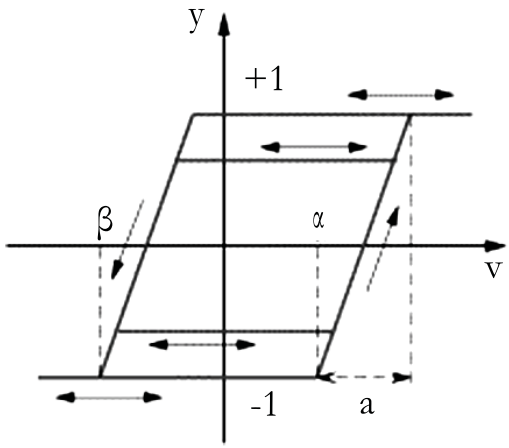

Figure 3.12: KP operator [7].

$$y_{kp}(t) = \int\int_P k_p(v(t), \xi_s)\mu(\alpha, \beta)d\alpha d\beta. \tag{3.29}$$

The integral form of the KP model consists of double-integrable, which is difficult for implementation. Therefore, the numerical implementation is achieved via parameterizing the KP

model by uniformly dividing the Preisach plane, as shown in Figure 3.13. The Preisach plane is divided into $l \times l$ line, and the number of cells is $N = 0.5(l+2)(l+1)$. A large l will provide a near to integral model, but this also increases the computational cost. Therefore, the number of l has to be optimized according to the computational cost without compromising model accuracy.

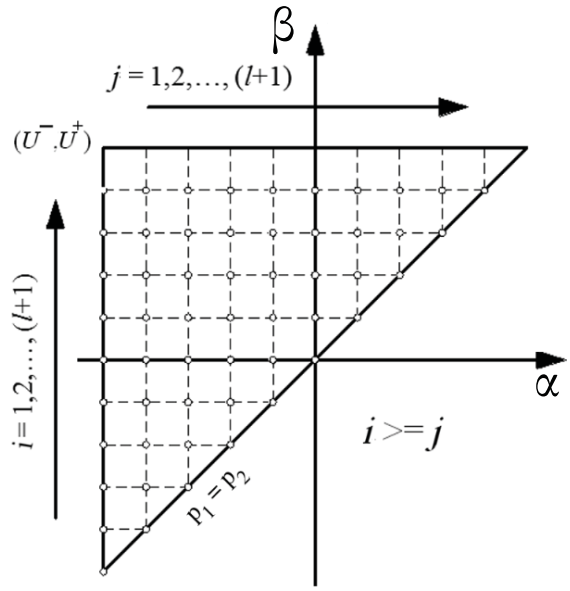

Figure 3.13: Discretized Preisach plane [8].

The coordinates (V_i, V_j) start from the lower-left node and can be defined as

$$(v_i, v_j) = (V^- + (i-l)\Delta v,\ V^- + (j-1)\Delta v, \tag{3.30}$$

where $i \leq j$, and $i, j = 1, 2, \ldots, l+1$, and $\Delta v = (V^+ - V^-)/l$. The rise constant, a, is selected as δv to have a smooth transition from one cell to another in the Preisach plane, P. For $a < \Delta v$ it could cause discontinuity, and for $a > \Delta v$ it could overlap. In the discrete form, the KP hysteresis effect can be considered as the lumped effect of all the nodes at the lower-left node of the cell. The lumped KP model can be written as follows:

$$y_{kp}(t) = \sum_{i=1}^{l+1} \sum_{j=1}^{i} k_{p_{ij}}(t)\rho_{ij} + d(v(t)), \tag{3.31}$$

where the $k_{p_{ij}}$ and ρ_{ij} are the KP kernel and the lumped density associated with the lower-left node at coordinate (v_i, v_j), respectively. Equation 3.31 can be written in the vector form as

$$y_{kp}(t) = \Upsilon^T K + d(v(t)), \tag{3.32}$$

where $K^t = [k_{p_{11}}, k_{p_{21}}, k_{p_{22}}, k_{p_{31}}, k_{p_{32}}, k_{p_{33}}, \ldots, k_{p_{(l+1)(l+1)}}] \in R^N$ and
$\Upsilon^T = [\rho_{11}, \rho_{21}, \rho_{22}, \rho_{31}, \rho_{32}, \rho_{33}, \ldots, \rho_{(l+1)(l+1)}] \in R^N$
are the kernel vector and density vector, respectively [8].

Neural Network Hysteresis Model

Neural network (NN) has been used in [9] and [79] to model the SMA hysteresis and inverse hysteresis. The network is designed to accept two inputs, the displacement as an input voltage and the direction of the displacement, which is labeled as 'tag'. The NN undergoes a training process with low-frequency input of voltage ranging from 0.4 to 2.6 V. The same data is also used in training the inverse hysteresis NN model. Based on the accuracy and training time of the network, an optimized NN consisting of four layers of neurons was proposed. The network has two hidden layers. The first layer has four 'tansig' and the second layer has five 'tansig'. The NN hysteresis model can also predict the asymmetric hysteresis loop. Figure 3.14 (a) and (b) show the schematic of the NN inverse model and the result of the inverse model, respectively.

3.3.2 SMA Combined Physical and Phenological Models

Several combined method models among many constitutive models will be reviewed and presented in this paper, including the commonly used Tanaka model [48] and [49], Müller model [52] and [53], Boyd-Lagoudas model [57] and [59], and Ivshin-Pence model [60].

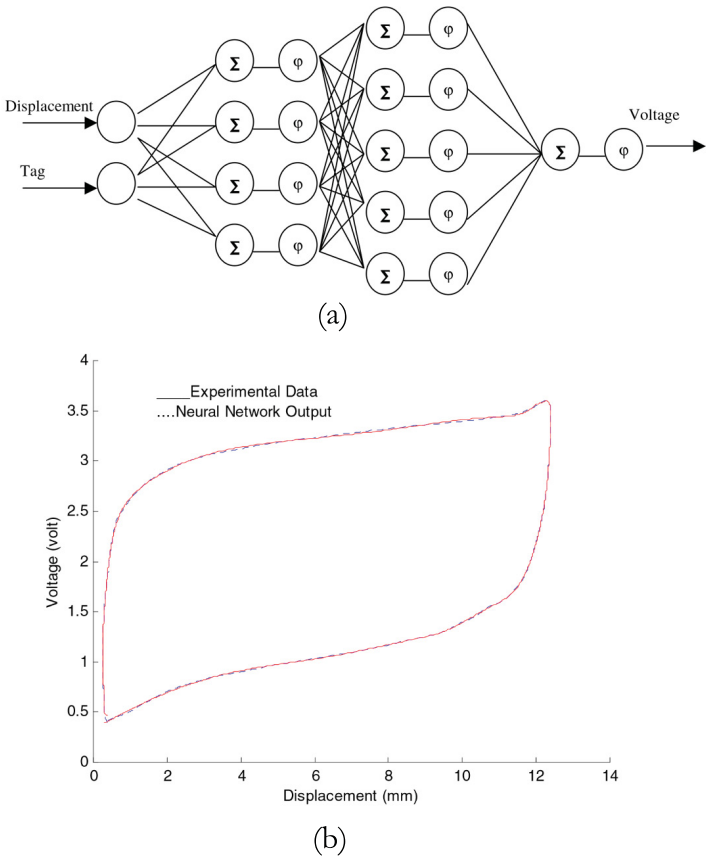

Figure 3.14: Schematic of Neural network inverse hysteresis and result of the inverse model [9].

Tanaka's Model

Tanaka's contribution to the constitutive model can be observed starting from [48] and [49]. Based on the concept of solid to solid phase change and the thermomechanical point of view, the constitutive model of SMA was introduced by [10] and [44] as Equation 3.1. This model has been widely used by researchers such as [3], [11], [24], [26], [50], [51] and others.

Later Tanaka's constitutive equation has also been written as Equation 3.33 by [41].

$$\sigma - \sigma_0 = D(\varepsilon - \varepsilon_0) + \Theta(T - T_0) + \Omega(\xi - \xi_0), \tag{3.33}$$

where the subscript "0" denotes the initial condition at each change of phase transformation direction. The Young's modulus D and the phase transformation tensor Ω are functions of the volumetric function of the martensite in the SMA, ξ. Their relationships are described in Equations 3.34 and 3.35.

$$D(\xi) = D_A + \xi(D_A - D_M). \tag{3.34}$$

$$\Omega(\xi) = -D\varepsilon_{res}, \tag{3.35}$$

where the D_A, D_M and ε_{res} are the austenite Young's modulus, martensite Young's modulus, and residual strain, respectively. Tanaka modeled the hysteresis behaviors of the temperature to the volumetric function of the martensite in the SMA using a phenological method. He and his colleagues proposed an exponential hysteresis model to describe the transformation kinetic for the constitutive model of SMA in [10] and [44]. By examining the transformation kinetics of the SMA under a uniaxial tensile stress load, σ, the M_s, M_f, A_s, and A_f vary with proportion to σ. Figure 3.15 shows the relation of stress to temperature, which can be obtained experimentally. The explicit forms of the volume fraction of the martensite, ξ, from martensite to austenite (forward) and from austenite to martensite (reverse) are given as Equations 3.36 and 3.37, respectively

$$\begin{aligned} &\xi = exp\left[b_A c_A(A_s - T) + b_A\sigma\right], \\ &b_A c_A(A_s - T) + b_A\sigma \leq 0. \end{aligned} \tag{3.36}$$

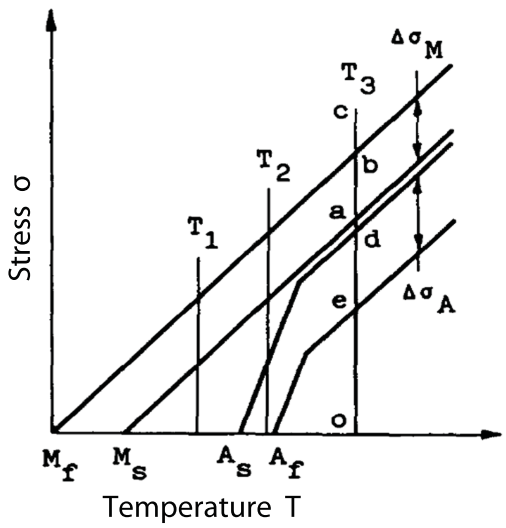

Figure 3.15: Phase change temperature under stress load [10].

$$\begin{aligned} &\xi = 1 - exp\left[b_M c_M (M_s - T) + b_M \sigma\right], \\ &b_M c_M (M_s - T) + b_M \sigma \leq 0, \end{aligned} \tag{3.37}$$

The forward and reverse transformation lines can be defined at $\xi = 0$ and $\xi = 1$ as

$$\begin{aligned} &\sigma = c_A (T - A_s), \xi = 1, \\ &\sigma = -2(ln10)/b_A + c_A (T - A_s), \xi = 0. \end{aligned} \tag{3.38}$$

and

$$\begin{aligned} &\sigma = c_M (T - M_s), \xi = 0, \\ &\sigma = -2(ln10)/b_M + c_M (T - M_s), \xi = 1. \end{aligned} \tag{3.39}$$

The experimental values of the transformation lines can be used to determine the parameter values for b_M, b_A, c_M and c_A. Figure 3.16 shows the strain-temperature numerical simulation for NiTi SMA using the exponential hysteresis model developed by Tanaka. Tanaka's hysteresis model has also been used in [26], [80], [81], [82] and by other researchers.

Similar to Tanaka, Ikuta and colleagues also proposed a set of exponential phase transformation models to describe the SMA hysteretic behavior [11]. The proposed model consists of the residual of martensite fraction when the phase change is in the opposite direction.

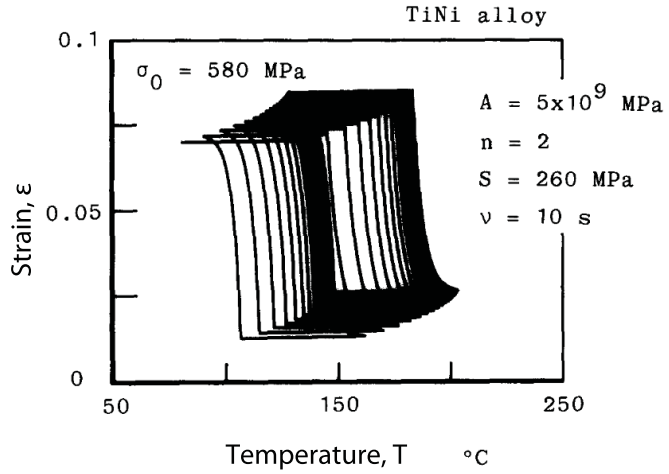

Figure 3.16: Strain-temperature loop for NiTi [10].

Ikuta's forward and reverse phase transformation models are shown in Equations 3.40 and 3.41, respectively. The ξ_M is the residual martensite fraction when reverse transformation changes to forward transformation, and the ξ_A is the residual austenite fraction when forward transformation changes to reverse transformation.

$$\xi = \frac{1-\xi_A}{1+exp\left[\frac{6.2}{M_f-M_s}(T-\frac{M_s+M_f}{2})\right]} + \xi_A, \tag{3.40}$$

$$\xi = \frac{\xi_M}{1+exp\left[\frac{6.2}{A_f-A_s}(T-\frac{A_s+A_f}{2})\right]}. \tag{3.41}$$

Adding the residual martensite fraction allows the model to simulate the minor hysteresis loop. Figure 3.17 shows the simulation of the minor loop with Ikuta Hysteresis model. The Ikuta hysteresis model has been used by [26], [82] and other researchers.

Following Ikuta, Liang and Rogers proposed a cosine function hysteresis model via phenomenology observation to describe the martensite fraction in the SMA [3]. Since the commercially available SMAs mostly have $As < Ms$, the Liang-Roger hysteresis model was therefore formulated based on this assumption. The hysteretic phase transformation models are described in Equations 3.42 and 3.44 as forward and reverse phase transformations,

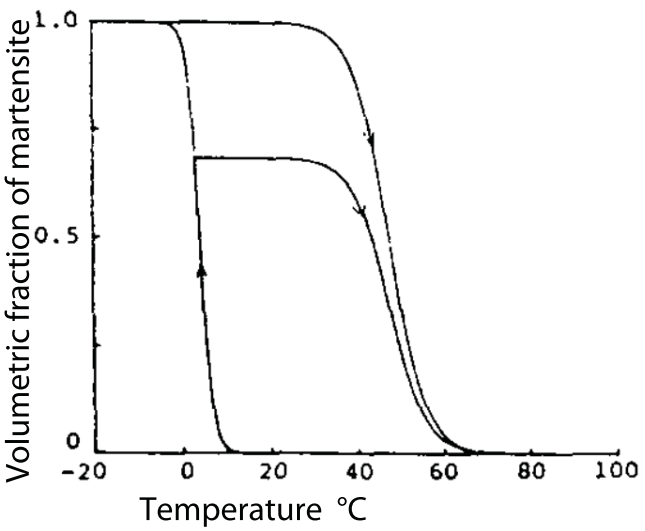

Figure 3.17: Simulation of the minor loop in SMA hysteresis [11].

respectively.

$$\xi = \frac{\xi_M}{2}(\cos[a_A(T - A'_s) + b_A\sigma] + 1) \tag{3.42}$$

$$\begin{cases} 1 & T < A_s \\ \xi & A'_s > T > A'_f \\ 0 & T > A_f \end{cases} \tag{3.43}$$

where for $C_A(T - A_f) < \sigma < C_A(T - M_s)$, $A'_f = A_f + \frac{\sigma}{C_M}$, $A'_s = A_s + \frac{\sigma}{C_A}$, $a_A = \frac{\pi}{A_f - A_s}$, $b_A = \frac{-a_A}{C_A}$, $C_A = \frac{\sigma}{A'_f - A_f}$.

$$\xi = \frac{1 - \xi_A}{2}\cos[a_M(T - M'_F) + b_M\sigma] + \frac{1 + \xi_A}{2} \tag{3.44}$$

$$\begin{cases} 1 & T < M_f \\ \xi & M'_f > T > M'_s \\ 0 & T > M_s \end{cases} \tag{3.45}$$

where for $C_M(T - M_s) < \sigma < C_M(T - M_f)$, $M'_f = M_f + \frac{\sigma}{C_M}$, $M'_s = M_s + \frac{\sigma}{C_M}$, $a_M = \frac{\pi}{M_s - M_f}$, $b_M = \frac{-a_M}{C_M}$, $C_M = \frac{\sigma}{M'_f - M_f}$. The Liang-Roger model also included the stress-induced phase transition effect. The shift of the phase transition start and finish temperatures due to the external stress are shown in Figure 3.18. C_A and C_M are obtained from experiments, and [3]

also reported that C_A is equal to C_M. The Liang-Roger Hysteresis model has been widely

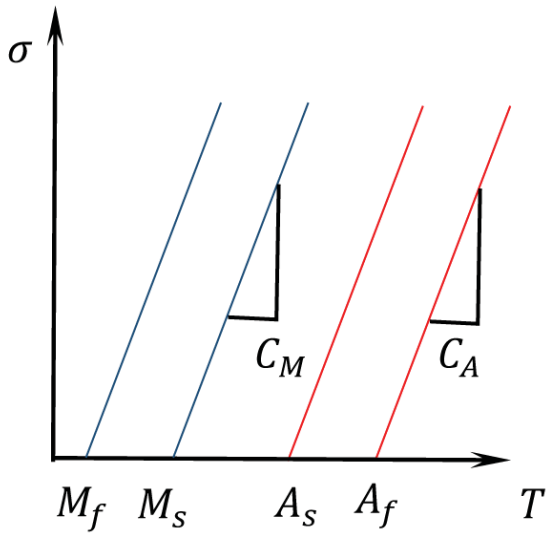

Figure 3.18: Applied stress versus transition temperature.

used by researchers, as seen in [24], [29], [41], [50], [83], [84], [85], and others.

Müller's Model

Müller and colleagues in [12], [52], [53], [54] and [55] proposed a model describing the deformation of the SMA in-plane strain subject to loading and temperature that was prescribed as a function of time. Müller's model was based on the idea that the martensite and austenite phase are separated by potential barriers. This model was characterized by the shape memory metallic lattice in three equilibrium configurations as the martensitic twins, $M_\pm$ and the austenite, A. The $M_\pm$ were treated as a sheared version of A with a shear length of $\Delta = \pm J$. Figure 3.19 (a), shows the potential energy, and Φ corresponds to the shear length. The potential energy profile shows two stable minima for the martensitic twins and metastable minima for the austenite. The minima are separated by the potential barriers with the magnitude of $\Delta = \pm s$. When a shear load P is subjected to the lattice, the potential energy of the particle will be distorted as shown in Figure 3.19 (b). This additional

shear load causes the minima for the martensitic twins and the potential barriers to change. Based on the idea described above, if the lattice is subjected to shear stress τ the resulting

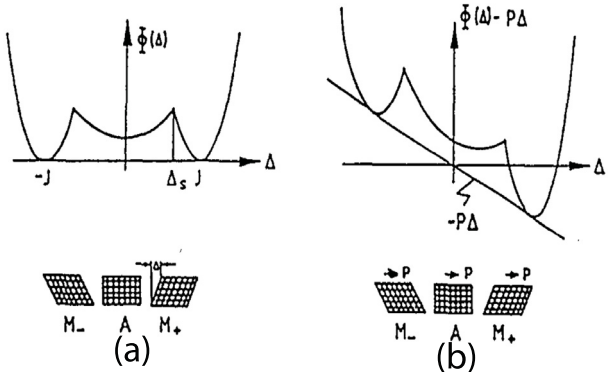

Figure 3.19: Potential energy and shear length [12].

deformation of the lattice is ε, and is defined as

$$\begin{aligned}\varepsilon = x^{-}\frac{\int_{-\infty}^{m_L}\Delta e^{-\Phi(\Delta,\tau)/kT}d\Delta}{\int_{-\infty}^{m_L}e^{-\Phi(\Delta,\tau)/kT}d\Delta} + x^{0}\frac{\int_{m_L}^{m_R}\Delta e^{-\Phi(\Delta,\tau)/kT}d\Delta}{\int_{m_L}^{m_R}e^{-\Phi(\Delta,\tau)/kT}d\Delta} \\ +x^{+}\frac{\int_{m_R}^{\infty}\Delta e^{-\Phi(\Delta,\tau)/kT}d\Delta}{\int_{m_R}^{\infty}e^{-\Phi(\Delta,\tau)/kT}d\Delta}.\end{aligned} \tag{3.46}$$

where Δ is shear length and T is temperature; and x^{-}, x^{0}, and x^{+} are the fractions of particles in phase M_{-}, A and M_{+}, respectively; and (m_L, m_R), $(-\infty, m_L)$ and $(m_R, +\infty)$ are the shear range of the phase M_{-}, A and M_{+}, respectively. Based on the free energy hysteresis modeling approach, the fractions of particles in the phases are governed by a set of probability functions for the occurrence of particles at shear length Δ and temperature T. The sum of the fractions of particles must fulfill $x^{-} + x^{0} + x^{+} = 1$. The deformation model also has been revised by [56] and reformulated as

$$\varepsilon = x_M^{-}(\varepsilon_M^{-} - \varepsilon_A) + \varepsilon_A + x_M^{+}(\varepsilon_M^{+} - \varepsilon_A). \tag{3.47}$$

where the $\varepsilon_\alpha(\sigma, T)$ is the stress-strain relation that is described by Equation 3.48

$$\varepsilon_\alpha = \begin{cases} \frac{\tau}{K_M} + J \\ \frac{\tau}{K_A} \\ \frac{\tau}{K_M} - J, \end{cases} \tag{3.48}$$

where $x_M^{\pm}$ is the phase fraction that is similar to the fraction of particles that is governed by the transition probabilities.

Boyd-Lagoudas's Model

Inspired by Tanaka, Boyd and Lagoudas proposed a 3-D constitutive model to describe the SMA behavior. The general stress-strain relation with defined temperature is defined as Equation 3.49 in [57], [59].

$$\sigma_{ij} = C_{ijkl}(\varepsilon_{kl} - \varepsilon_{kl}^t - \alpha_{kl}\Delta T), \tag{3.49}$$

where C_{ijkl}, ε_{ij} and ε_{ij}^t are the effective elastic stiffness, total infinitesimal strain, and transformation strain, respectively. $\Delta T = t - T^0$ where T^0 is the stress-free reference temperature. The effective elastic stiffness was defined using similar methods in the Tanaka model as per Equation 3.34 as

$$C_{ijkl} = C_{ijkl}^A + \xi(C_{ijkl}^A + C_{ijkl}^M), \tag{3.50}$$

where C_{ijkl}^A and C_{ijkl}^M are the isotropic elastic stiffness tensor at austenite and martensite phase, respectively. Similar methods have also been observed in [58] and [59]. The hysteresis behavior was modeled in the volumetric function of the martensite, ξ which was obtained from Tanaka exponential model as per Equations 3.37 and 3.36.

Ivshin-Pence's Model

Ivshin-Pence's model is considering the micro-scale level, where the strain is directly related to the fraction of molecular structure phases. Instead of using the martensite fraction, the austenite fraction α is used, where $\alpha = 1 - \xi$. Therefore, the overall strain in the phase mixture ε can be written as Equation 3.51 [60].

$$\varepsilon = (1 - \alpha)\varepsilon_M(T, \sigma) + \alpha\varepsilon_A(T, \sigma), \tag{3.51}$$

where the stress-strain responses with thermal expansion are defined as

$$\begin{aligned}\varepsilon_A(T,\sigma) &= \sigma/E_A + \epsilon_A(T-T_0)\\ \varepsilon_M(T,\sigma) &= \sigma/E_M + \delta + \epsilon_M(T-T_0),\end{aligned} \tag{3.52}$$

where E_A and E_M are the elastic modulus of the pure phases, ϵ_A and ϵ_M are the corresponding thermal expansion coefficients, and δ is the transformation strain from austenite to the martensite phase. Ivshin-Pence's Model was later adopted by [28]. By changing the phase fraction to austenite fraction, Equations 3.51 and 3.52 can be combined and rewritten as Equation 3.53.

$$\sigma = \left[\frac{\xi}{D_M} + \frac{1-\xi}{D_A}\right]^{-1}(\varepsilon - \xi\varepsilon_L), \tag{3.53}$$

where ε_L is the residual plastic strain. Similar to Tanaka's method, the hysteresis model in Ivshin-Pence's Model was developed via the phenological approach with the exponential function.

Dutta-Ghorbel's Model

Dutta and Ghorbel proposed a constitutive model based on the lumped parameter system in [13] and [46]. Assuming there is no effect of stress to the phase transition temperature, the resulting tensile stress σ is contributed by the two phases based on the martensite fraction. Therefore, in Dutta-Ghorbel's model, σ is given as Equation 3.54:

$$\sigma = (1-\xi)\sigma_a + \xi\sigma_m, \tag{3.54}$$

where ξ_a and ξ_m are the stress obtained from the stress-strain characteristics at the austenite and martensite phase, respectively. The martensite fraction describing the SMA hysteresis was developed using the phenological approach in the form of a differential equation. Meanwhile, the strain is solved in quadratic form as Equation 3.55

$$\varepsilon = \begin{cases} \varepsilon_0 - \frac{d_1}{2c_1} - \frac{\sqrt{d_1^2-4c_1e_1}}{2c_1}, if 0 \le \varepsilon < \varepsilon_m^y \\ \varepsilon_0 - \frac{d_2}{2c_2} - \frac{\sqrt{d_2^2-4c_2e_2}}{2c_2}, if \varepsilon_m^y \le \varepsilon < \varepsilon_m^d, \\ \varepsilon_0 - \frac{d_3}{2c_3} - \frac{\sqrt{d_3^2-4c_3e_3}}{2c_3}, if \varepsilon_m^d \le \varepsilon. \end{cases} \tag{3.55}$$

where c_i, d_i, and $e_i (i = 1, 2, 3)$ are quadratic solutions [13]. For simulation purposes, Dutta and Ghorbel further approximated the strain with a polynomial in ξ to provide a continuously differentiable strain model. Equation 3.56 shows the polynomial form of the strain as

$$\varepsilon = \varepsilon_0 + k_1\xi + k_2\xi^2 + k_3\xi^{50}, \tag{3.56}$$

where k_1, k_2 and k_3 are obtained by using Matlab's curve fitting toolbox. Dutta and Ghorbel proposed a Duhem differential hysteresis model based on the phenomenological approach in [13] [46]. The hysteresis model describes the fraction of martensite as

$$\begin{cases} \frac{d\xi}{dT} = \begin{cases} \frac{h_-(T)+\xi-1}{h_+(T)-h_-(T)} g_+(T), \dot{T} \geq 0 \\ \frac{h_+(T)+\xi-1}{h_-(T)-h_+(T)} g_-(T), \dot{T} < 0 \end{cases} \\ \xi(0) = 1, \end{cases} \tag{3.57}$$

where the slope function is a Gaussian probability density function that is characterized by the mean μ and variance υ defined as

$$g_{+/-}(T) = \frac{1}{\varsigma_{+/-}\sqrt{2\pi}} exp\left[-\frac{(T-\mu_{+/-})^2}{2\varsigma_{+/-}^2}\right], \tag{3.58}$$

where the subscripts $+$ or $-$ denote the increasing or decreasing curves, respectively. The major loop function is then given as

$$h_{+/-}(T) = \frac{1}{2}\left[1 + erf\left(\frac{T-\mu_{+/-}}{\varsigma_{+/-}\sqrt{2}}\right)\right]. \tag{3.59}$$

In the Dutta-Ghorbel hysteresis function, the minor loop is achieved by multiplying a scaling constant in Equation 3.58. This is similar to incorporating residual martensite fraction in the Ikuta and Liang-Roger hysteresis model. The result of the simulation of the minor loop of the Dutta-Ghorbel hysteresis model with comparison to the experimental result is shown in Figure 3.20.

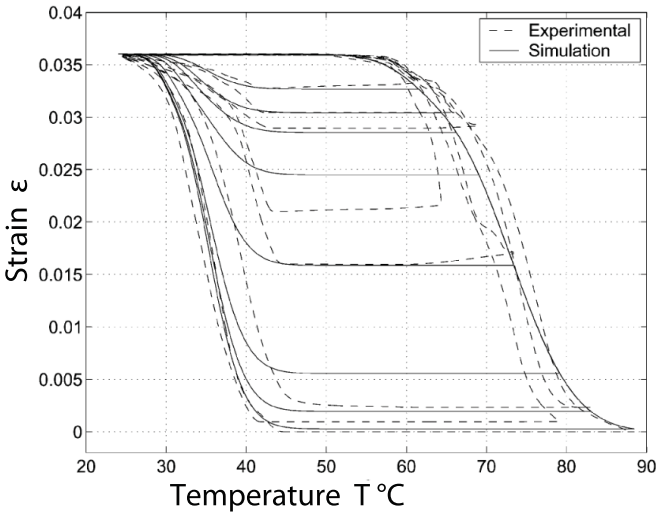

Figure 3.20: Comparison of simulation of the minor loop and experimental result [13].

3.4 Control Systems

The highly nonlinear and hysteretic behaviors of SMA have made the control system a challenge in driving the SMA as the actuator in the AM. Control methods range from the basic Proportional-Integral-Derivative (PID) control to nonlinear control, and fuzzy control has been adopted by researchers in controlling the SMA actuator. In the controller development, the aim is to achieve high accuracy, good stability, and low computational cost. However, to develop a good controller for the system with hysteresis such as the SMA, the right combination of the control scheme and modeling method also play an important role. The control scheme can generally be categorized into the direct control system and inverse-based control system as shown in Figures 3.21 (a) and (b), respectively. Direct control scheme deals with the hysteretic SMA behavior directly to obtain the desired output. Meanwhile, the inverse-based control system consists of inverse hysteresis compensator to eliminate the hysteresis effect. By eliminating the hysteresis effect, the complexity in designing the controller can be reduced.

Within the two control schemes reviewed, i.e., modeless approach and model-assisted approach, control methods have also been observed. The modeless approach controllers

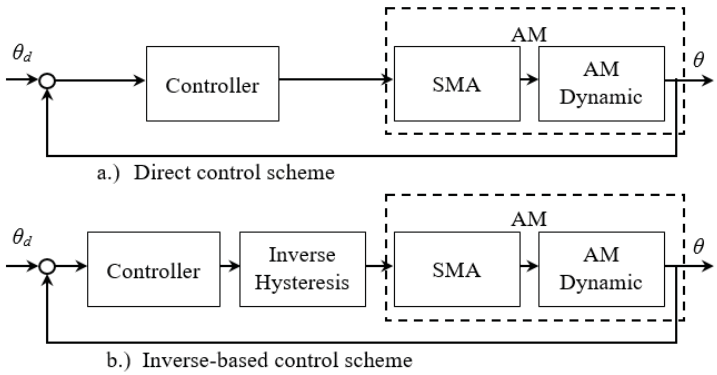

Figure 3.21: Block diagram; a.)Direct control scheme and b.) Inverse-based control scheme.

generate output solely based on the system feedback. Often these modeless controllers need intensive tuning due to the lack of information about the system. The development of such controllers is simple, but the results are normally limited in terms of accuracy and response time. Meanwhile, the system's mathematical models can be physically derived or obtained phenologically to assist the development of the model-based controller. Physically derived analytical models provide a detailed contribution of each physical parameter in the system. This knowledge could be important for the development of a good controller. However, the hysteresis behavior, as exhibited by the SMA, is difficult to be modeled via the physical model. Therefore, many researchers turn to use phenological approaches to model SMA hysteresis. The adoption of modeling approach has a direct impact on the type of control scheme used. This can be observed mainly in the model-based control such as the inverse-based control scheme where the construction of SMA inverse hysteresis model is required.

The following discussions of the SMA actuated AM control systems are sectioned, based on the control scheme of a direct control system and inverse-based control system approach. Categorizing the control system into these two main groups shows the significant contribution of the inverse based control scheme and direct control scheme in terms of control performance. Another important aspect is the matching of the modeling method and control scheme. In the review, some authors adopted modeling method that cannot be used in their control scheme, so the author ends up using non-model based control scheme.

3.4.1 Direct Control System

The direct control systems are designed to directly handle the SMA system including hysteresis behavior. It can be assisted with the SMA constitution model or without any predefined information such as typical modeless PID approach found in [85], [86] and [87]. Other more advanced modeless controllers such as the variable structure controller are presented in [29] and [83]. The model-assisted controllers are also observed in direct control scheme, such as the sliding mode control (SLC) presented by [45] and [26].

Proportional-Integral-Derivative (PID) Control System

The use of PID controls has been observed in [85], [86] and [87]. The PID controllers are used to generate a pulse-width-modulation (PWM) signal to control the power lever feeding to the SMA. The inputs of the PID controller are the sum of the input-output error, integral of the error, and rate of the error with each at a constant gain. The PWM input, which is in the percentage of 0 to 100%, is written as Equation 3.60 in [85].

$$PWM = K_P \Delta\theta + K_V \Delta\dot{\theta} + K_I \int \Delta\theta dt, \tag{3.60}$$

where $\Delta\theta$ is the feedback value minus the desired value, also known as the error. The K_P, K_I and K_V are the proportional, integral, and derivative gains, respectively. Two control architectures have been observed in the antagonistic configuration, [87] using overall feedback and individual SMA feedback loop together, while [86] using only the overall feedback loop in their PID control system. Figure 3.22 shows the overall feedback loop and the SMA individual feedback loop. The PID system development is easy because no detailed knowledge of the system is needed for the control system development. The only tedious work is the tuning of the PID gains to obtain good output performance. Meanwhile, the PID control systems also have limited ability in highly nonlinear systems, especially when uncertainty is added into the system. This can be observed in [87], where the system response time increases with the increase in load. The fixed gain in the PID control system is not robust

enough to deal with the nonlinearity and uncertainty in the AM system.

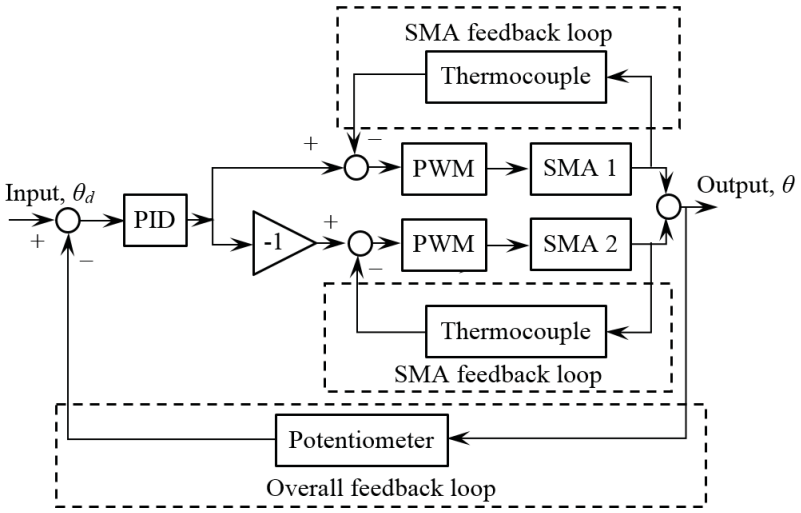

Figure 3.22: PID control architectures.

Fuzzy-PID Controller

PID controller limitation relies on the fixed PID gains. If the gains can be tuned perpetually in real-time speed, the PID can become adaptive. However, the model-based tuning method can be difficult to develop. Therefore, without any modeling, [88] fuzzy logic was used to tune the PID gains online.

The use of fuzzy in PID gains tuning shows some improvement on the response-time and steady-state error. Similarly, a fuzzy self-tuning PID controller was developed by [89] to control the SMA actuator. Figure 3.23 shows a similar block diagram used by [88] and [89]. The fuzzy PID system shows improvement in the SMA control compared to the conventional PID, in terms of the steady-state error and the response time. However, the system has not been tested at varying load conditions, to show the ability of the fuzzy PID controller in dealing with uncertainty and disturbance.

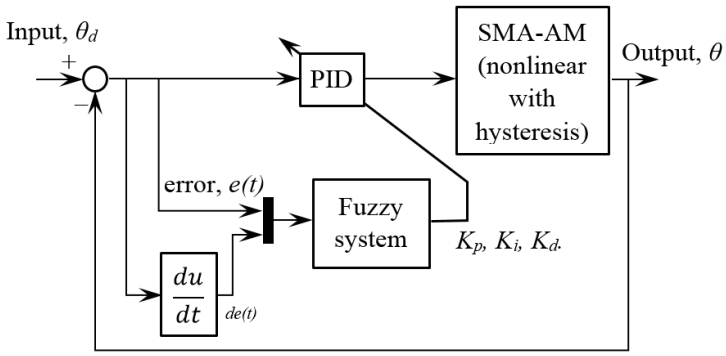

Figure 3.23: Block diagram for Fuzzy PID controller.

Variable Structure Control

Non-model based variable structure control (VSC) system is used to direct control of the SMA system. These have been observed in [29], [83] and [90]. Authors have developed a three links robot arm and model it using the Tanaka constitutive model, Equation 3.1. The SMA hysteresis effect is modeled via the phenological approach as a sinusoidal function as shown in Equations 3.42 to 3.44. The robot system model resulted in a nonlinear state equation with a state vector as per Equation 3.61.

$$x = [q_1 \; q_3 \; \dot{q}_2 \; \dot{q}_3 \; T_2 \; T_3 \; \sigma_2 \; \sigma_3 \; \xi_2 \; \xi_3]^T, \tag{3.61}$$

where the q is the joints angular; T is the SMA temperature; σ is the stress, and ξ is the fraction of martensite for the respective joints. The nonlinear state equation can be referred to in [83]. However, the inability to form the inverse of the state equation, caused the authors to limit to non-model based control. The output angular position of the robot joints are measured by sensors, and the position errors are yielded by subtracting the desired inputs. The position errors are used in the sliding surfaces with errors gains, λ_{P_i}. Subsequently, the velocity of the position errors are obtained through numerical differentiation and added to the sliding surfaces with velocity gains,λ_{V_i} as the speed regulator. Integral tracking errors with integral gains, λ_{I_i} are also added to the sliding surfaces to reduce steady-state errors.

The sliding surface equation for each joint is shown in Equation 3.62.

$$s_i = \lambda_{P_i}\tilde{q}_i + \lambda_{V_i}\dot{\tilde{q}}_i + \lambda_{I_i}\int_0^t \tilde{q}dt, \quad \tilde{q}_i = q_i - q_{d_i}, \quad i = 2, 3. \tag{3.62}$$

$$u = \begin{cases} u_{high} & if \ \frac{s_i}{\phi_i} < -1 \\ s_i & if \ -1 < \frac{s_i}{\phi_i} < 1 \\ u_{low} & if \ \frac{s_i}{\phi_i} > 1. \end{cases} \tag{3.63}$$

Boundary layers, ϕ_i are added to the controller for reducing overshoot as shown in Equation 3.63. Although time-consuming tuning process has been performed, the non-model based VSC system still exhibits some chattering.

Sliding-Mode Control System

Sliding mode control approaches are applied to control SMA. These can be observed in several publications such as [26] and [45]. In [45], Tanaka model, Equation 3.1 and the cosine hysteresis model, Equations 3.42 to 3.44 are adopted in the modeling of the SMA bias spring system. As per Figure 3.1 (a), the SMA bias spring system, Equation 3.10 and system dynamic are defined as

$$J\ddot{q} + c\dot{q} + [\tau_g(q) + \tau_s(q) = \tau_w(\sigma), \tag{3.64}$$

where τ_w, τ_g and τ_s are the torque generated by SMA, gravitational load and bias spring, respectively. Equation 3.64 can be further simplified as Equation 3.65 as below

$$J\ddot{q} + h(q, \dot{q}) = \tau_w(\sigma), \tag{3.65}$$

where $h(q, \dot{q})$ is the function of a combination of torsional damping, torque from the gravitational load and bias spring. $\tau_w(\sigma)$ is the torque from the SMA. Combining Equations 3.65 and 3.64, the desired SMA torque to drive the AM system can be defined as

$$\tau_w(\sigma) = I_e[\ddot{q}_d - \lambda\dot{e}] + h(q, \dot{q}) + Ksat(s), \tag{3.66}$$

where λ is a constant and θ_d is the desired angular position, K is a control gain, and $sat(s)$ is the saturation term. The saturation term is applied to ensure the trajectory converges. From Equation 3.66, the desired stress, σ_d is computed and substituted into the PI controller to define the input voltage as

$$V(t) = K_P(\sigma - \sigma_d) + K_I \int_0^t (\sigma - \sigma_d)dt, \tag{3.67}$$

The result of applying the sliding-mode controller in controlling the SMA shows better rise time, settling time, and less overshoot. However, the authors noted that large errors in the damping estimation would result in a poor tracking performance.

3.4.2 Inverse-Based Control System

Inverse-based control system requires the inverse hysteresis compensator to eliminate the hysteresis effect. The inverse hysteresis compensator can be developed from the SMA hysteresis model or using modeless estimation. Recently, invertible phenological hysteresis model has been adopted frequently to facilitate the construction of the inverse hysteresis compensator.

Feedforward and Feedback Control System

The modeless PID controller can be improved by introducing the SMA model as a feedforward compensator. In [91], authors used the modified Tanaka model, Equation 3.33 and combined with Preisach hysteresis model, Equations 3.16 and 3.17 in modeling the SMA actuator with bias spring configuration. At very a low speed of PWM input variation, the dynamic components of the system have a negligible effect. Therefore, the steady-state nonlinear output can be considered as only the hysteresis effect. Using Equations 3.16 and 3.17, the hysteresis model is obtained by authors in the form of PWM as input and force as output. With the Preisach model, the inverse model can be obtained and included in the PID controller as an inline compensator for the SMA system. The feedforward compensator developed from the inverse model overcomes the nonlinearity and hysteresis of the SMA

system. This can provide a near linear system for the PID controller, which resulted in the control improvement and works in a larger range of input without re-tuning the PID gains.

Meanwhile, [46] used the Dutta and Ghorbel model, Equations 3.54 to 3.56 with the differential hysteresis model, Equations 3.57 to 3.59 to model the SMA actuator with bias spring configuration. To avoid dividing by zero, a small constant δ is added to the inverse hysteresis model. This is to ensure that the $h_-(T) + R_m - 1$, $h_+(T) + R_m - 1$, and $g_{+/-}(t)$ are not zero, as shown in Equation 3.68.

$$\begin{aligned} \frac{dT}{d\xi} &= \begin{cases} \frac{h_+(T)-h_-(T)}{h_-(T)+\xi-1+\delta} \cdot \frac{1}{g_+(T)+\delta}, \dot{\xi} < 0 \\ \frac{h_-(T)-h_+(T)}{h_+(T)+\xi-1-\delta} \cdot \frac{1}{g_-(T)+\delta}, \dot{\xi} \geq 0. \end{cases} \\ T(0) &= T_{amb}, \end{aligned} \tag{3.68}$$

However, the addition of δ will lead to an error. Although there is an error in the inverse hysteresis compensator, the use of it as the feedforward component in the proportional-derivative (PD) control system resulted in better tracking errors compared to the PID modeless control system.

In [69], authors consided the GPI hysteresis model as per Equations 3.19 to 3.25 in developing the control system for a single SMA wire with the fixed load. From the GPI model, the inverse GPI hysteresis model can be obtained as Equation 3.69.

$$T(k) = \begin{cases} \gamma_l^{-1}\{\frac{1}{p_0}v(k) + \Sigma_{j=0}^{N}\hat{p}_j F_{\hat{r}_j}[v](k)\}, \ \dot{v} \geq 0 \\ \gamma_r^{-1}\{\frac{1}{p_0}v(k) + \Sigma_{j=0}^{N}\hat{p}_j F_{\hat{r}_j}[v](k)\}, \ \dot{v} \leq 0 \end{cases} \tag{3.69}$$

where the parameters $\hat{p}_j$ and $\hat{r}_j$ are shown in Equations 3.70 and 3.71

$$\hat{p}_j = -\frac{p_j}{(\sum_{i=0}^{j} p_i)(\sum_{i=0}^{j-1} p_i)}, \ (j = 1, 2, ..., N \tag{3.70}$$

$$\hat{r}_j = \sum_{i=0}^{j} p_i(r_j - r_i), \ (j = 0, 1, ..., N \tag{3.71}$$

The GPI inverse hysteresis model is applied in the feedforward compensator with the PI controller to compensate for the hysteresis effect. As the exact inverse models are available,

the controller shows a significant improvement in accuracy compared to the PID controller.

Similarly, [4] and [69] only consided the SMA hysteresis nonlinearity in the controller development for a single SMA wire with fix loading condition. Authors used the Preisach hysteresis model, Equations 3.16 to 3.18 and a fuzzy inference for interpolation in between the switching points. The fuzzy inference is to provide better accuracy even at the fewer switching points. The inverse model provides the amount of current needed to heat the SMA while corresponding to the desired input displacement. The inverse Preisach fuzzy model can be referred to in [4]. Meanwhile, the inverse model is used as a feedforward between the input and the SMA plant. At the same time, the Preisach hysteresis model is placed parallel to the SMA plant. The difference between the SMA plant and the model yielded the disturbance subjected to the SMA and the modeling error. The implementation of Preisach inverse and forward model with the fuzzy inference showed better accuracy in the position control. In [63], the authors used the same method in defining the forward and inverse hysteresis model as [4]. However, the controller development is slightly different, [63] used only the inverse Preisach model with the PID controller. The resulting controller showed the ability to eliminate the hysteresis behavior of the SMA. Besides, it is foreseen that the controller developed by [63] has less ability to eliminate disturbance and perform position tracking as there is no ability to detect disturbance compared to the controller developed by [4]. Even though, the PID controller can be improved with the implementation of model reference as feedforward compensator, the ability of the controller to deal with external disturbance and uncertainty is still lacking. The need for controllers such as adaptive and robust controller to deal with the external disturbance and uncertainty is necessary.

Inverse-Based Sliding Mode Control

In [26], authors only consided the hysteresis behavior of the SMA via the Ikuta exponential hysteresis model as Equations 3.40 and 3.41 in controlling the SMA wire displacement with

a fixed load attached at the end. Through algebraic manipulation on the thermal model, Equation 3.88 and the Ikuta exponential hysteresis model, the dynamic phase transformation can be written as

$$\dot{\xi} = f_{\xi}(\xi) + b_{\xi}(\xi) \cdot u. \tag{3.72}$$

The detail of f_{ξ} and $b_{\xi}(\xi)$ can be referred to in [26]. Under the assumption that the SMA wire has no thermal expansion and residual stress; and the martensite stress will be higher than its elastic limit. Equation 3.34 can yield the approximation of stiffness coefficient, K as

$$K = [(1-\xi) \cdot D_A] \cdot \frac{A_{wire}}{l_0}, \tag{3.73}$$

where A_{wire} and l_0 are the SMA wire cross section area and SMA wire initial length, respectively. From Equation 3.73, the SMA actuator system dynamic can be written as

$$I_e\ddot{x} + c\dot{x} + \frac{K_0(1-\xi)}{n^2}x = -m_L g + \frac{K_0(1-\xi)}{n}\Delta, \tag{3.74}$$

where $K_0 = D_A A_{wire}/l_0$ and $\Delta = 0.04 l_{max}$, l_{max} is the maximum length at martensite phase. The ξ cannot be measured, so authors proposed a quasi-static approximation at $\dot{x} = \ddot{x} = 0$ which gives

$$\hat{\xi} = 1 - \frac{m_L g}{K_0(\frac{\Delta}{n} - \frac{x}{n^2})}. \tag{3.75}$$

Differentiating Equation 3.74 and combining with Equation 3.72 yield the following state equation

$$\dddot{x} = f(x) + b(x) \cdot u, \tag{3.76}$$

with $x = [\xi \ x \ \dot{x} \ \ddot{x}]^T$, and detail of $f(x)$ and $b(x)$ can be referred to [26]. The control input $u = i^2$ is written as

$$u = \frac{1}{\hat{b}(x)}\big(- \hat{f}(x) + \dddot{x}_d - 2\lambda\ddot{\tilde{x}} - \lambda^2\dot{\tilde{x}}\big) - K_{SM} sat(s/\phi), \tag{3.77}$$

where $s = \ddot{\tilde{x}} + 2\lambda\ddot{\tilde{x}} - \lambda^2\dot{\tilde{x}} \cdot \hat{f}(x)$ and $\hat{b}(x)$ are the best approximation of the model, and the cut-off frequency of the closed-loop system, ϕ is the boundary layer thickness to eliminate chattering, and K_{SM} is the control gain. The result from the controller shows the system is

able to produce a similar result with and without thermoelectric cooling and with a ±20% load variation. However, chattering has been observed in the result.

Adaptive Control System

Adaptive control systems are observed in [14], [71], [72] and [73]. Authors used the model reference control approach for the fixed load SMA in the bias spring configuration system. By using the KP hysteresis modeling technique as per Equations 3.29 to 3.32 the SMA actuator is modeled with the temperature as input and Young's modulus as output. The SMA KP model is assumed to include thermal expansion and residual strain effect. The bias spring system is phenologically modeled in the form of the transfer function. The estimation of Equation 3.32 can be rewritten as

$$\hat{y} = \hat{H}(T) = \hat{\Upsilon}^T K(T), \tag{3.78}$$

the error between Equation 3.32 and Equation 3.78 is $e = y - \hat{y} = (\Upsilon^T - \hat{\Upsilon}^T K(T))$. A normalized estimation error is proposed by authors as Equation 3.79 to ensure the signal is bounded.

$$\varepsilon_n = \frac{(T - \hat{T})}{m^2} = \frac{\tilde{\Upsilon}^T F(T)}{m^2}, \tag{3.79}$$

where $\tilde{\Upsilon} = \Upsilon - \hat{\Upsilon}$ and the normalizing signal is defined as

$$m^2 = 1 + n_s, \quad n_s = K(T)^T K(T), \tag{3.80}$$

m^2 is designed by authors to be always larger than zero by considering the quadratic cost function as

$$J(\hat{\Upsilon}) = \frac{\varepsilon^2 m^2}{2} = \frac{[y - \hat{\Upsilon}^T K(T)]^2}{2m^2}. \tag{3.81}$$

To minimize the trajectory of the cost function, the gradient is defined as

$$\dot{\hat{\Upsilon}} = -\Gamma \nabla J(\hat{\Upsilon}), \tag{3.82}$$

where $\Gamma = \Gamma^T > 0$ is the adaptive gains matrix. Then the gradient of $J(\hat{\Upsilon})$ is defined as

$$\nabla J(\hat{\Upsilon}) = -\frac{[y - \hat{\Upsilon}^T K(T)]K(T)}{m^2} = -\varepsilon_n K(T), \tag{3.83}$$

which yields the adaptive law as

$$\dot{\hat{\Upsilon}} = \Gamma \varepsilon_n K(T). \tag{3.84}$$

Based on the Υ, the parameters estimation are ensured to be bounded in some set Q by defining the parameter projection as

$$Q = \hat{\Upsilon} \in \Re^n : p(\hat{\Upsilon}) \leq 0, \tag{3.85}$$

where $p(\hat{\Upsilon})$ is a vector of constraint equation on $\hat{\Upsilon}$. The adaptive law of Equation 3.84 is rewritten as

$$\dot{\hat{\Upsilon}} = \begin{cases} \Gamma \varepsilon_n K(T) \quad if \quad \hat{\Upsilon} \in interior(Q) \\ \qquad\qquad\qquad or \quad \hat{\Upsilon} \in boundary(Q) \\ \qquad\qquad\qquad and \quad [\Gamma \varepsilon_n K(T)]^T \nabla p \leq 0 \\ \Gamma \varepsilon_n K(T) - \Gamma \frac{\nabla p \nabla p^T}{\nabla p^T \Gamma \nabla p} \Gamma \quad if \quad otherwise. \end{cases} \tag{3.86}$$

With the known maximum value of the output, y_{max} the upper bound of Q can be set as $max(\Upsilon_i) = y_{max}$. The Q can be defined as

$$Q = \Upsilon \in \Re^n : u_{max} - \Upsilon_i \leq, \quad i = 0, 1, 2, ..., n. \tag{3.87}$$

The input current is controlled to create resistive heating, and the SMA temperature was modeled by authors as Equation 3.88

$$\dot{T} = -\alpha(T - T_\infty) + \beta u, \tag{3.88}$$

where α and β are the lump parameters for heat transfer and material property, respectively. u is current input square, i^2. By defining $\bar{T} = T - T_\infty$ and assuming the environment temperature T_∞ is constant, then the SMA temperature model can be redefined as follows

$$\dot{\bar{T}}_m = -\alpha_m \bar{T} + \beta_m r_T. \tag{3.89}$$

The control law is given by [71] as

$$u = -k * \bar{T} + L * r_T, \tag{3.90}$$

where r_T is the control signal $k* = (\alpha_m - \alpha)/\beta$ and $L* = \beta_m/\beta$, in which the α_m and β_m are the reference model parameters. The adaptive control algorithm achieves control by integrating Equation 3.89 to obtain the estimated temperature, $\hat{T}$. Then u is generated to force the $\hat{T}$ to follow the desired temperature, T_d. Which the T_d is obtained from the KP hysteresis inverse model. The overall control block diagram is shown in Figure 3.24. The

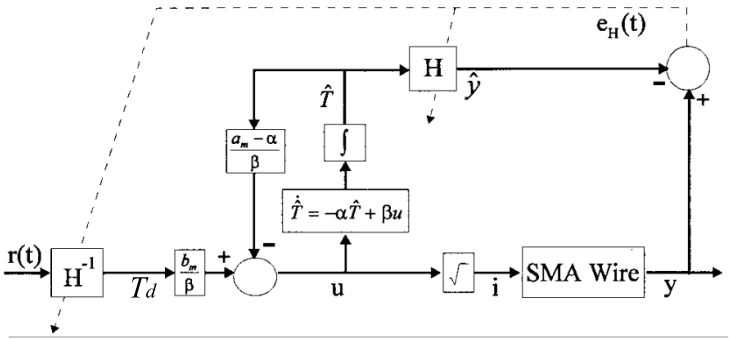

Figure 3.24: Adaptive control block diagram [14].

estimated temperature $\hat{T}$ and the estimated displacement $\hat{y}$ are adaptively updated. The result of the adaptive control with the exact inverse hysteresis model shows good adaptation of the system where it can be operated in air or fluid cooling environment with a good tracking capability [73].

Robust Control System

The applications of the robust control system in controlling the antagonistic SMA actuated AM systems are observed in [6] and [92]. Authors utilized the GPI model, Equations 3.19 to 3.25 in modeling the hysteresis effect of the SMA. The GPI model parameters are obtained under a fixed load condition with the voltage as input and displacement as output. In the

controller design, authors only consided a single SMA in the actuator system with a second-order differential system. The system is similar to Figure 3.1(b), and the system dynamics is given as

$$J\ddot{q} + \rho\dot{q} + k_s r_{pulley}^2 q = k_c r H(\tilde{T}(t)) - M_a, \tag{3.91}$$

where r_{pulley} is pulley radius, q is the pulley rotation angle, J is the effective moment which combines moment of the pulley and the flap, ρ is damping coefficient, and M_a is the bounded aerodynamic moment on the flap. k_s and k_c are the SMA stiffness constant and the SMA force constant. Equation 3.91 is then written as a second-order system as

$$\ddot{q}(t) + 2\xi_d\omega_n\dot{q} + \omega_n^2 q(t) = w(t) + d(t), \tag{3.92}$$

where ξ_d and ω_n are the dynamic parameters,$w(t)$ is the control input and $\theta(t)$ system output, $d(t)$ is a bounded perturbation term to address the disturbance, parametric uncertainty, measurement error and others. Including the thermal expansion of the SMA in the GPI model, the input $w(t)$ can be replaced by the SMA hysteresis and nonlinear behavior as per Equation 3.20, the system dynamics can then be defined as

$$\begin{aligned} &\ddot{x}(t) + 2\xi_d\omega_n\dot{x} + \omega_n^2 x(t) = p_0 v(t) + \\ &\int_0^R p(r) F_{lr}^{\gamma}[v](t)dr + d(t). \end{aligned} \tag{3.93}$$

The bounded $d(t)$ is denoted by D and it is assumed to be known. The control objective is to force the output, $x(t)$ to follow a desired trajectory path, $x_d(t)$ as $x(t) \to x_d(t)$ as $t \to \infty$. The system can be rewritten as Equation 3.94 by defining $x_1 = x$, $x_2 = \dot{x}$

$$\begin{aligned} \dot{x}_1 &= x_2 \\ \dot{x}_2 &= p_0 v(t) + \int_0^R p(r) F_{lr}^{\gamma}[v](t)dr - 2\xi_d\omega_n\dot{x} \\ &\quad -\omega_n^2 x(t) + d(t). \\ y &= x_1 \end{aligned} \tag{3.94}$$

The tracking error, $\tilde{x}$ is defined as

$$\tilde{x} = x - x_d. \tag{3.95}$$

The control law for the second-order SMA actuator system is defined as

$$v(t) = sgn(s_\varepsilon)(\phi(x,t) - v_0), \tag{3.96}$$

where

$$\phi(x,t) = \frac{-\beta}{q_{min}+\eta}(|\lambda(\dot{x}_1 - \dot{x}_d)| + |2\xi_d\omega_n x_2 \\ +\omega_n^2 x_1 + \ddot{x}_d| + D), \tag{3.97}$$

with $\beta > 1$.

Simulation result from the control system shows that the GPI model is effective in predicting the major and minor hysteresis loop. The development of the robust control system with the incorporation of the GPI model has shown to be effective in tracking control without the construction of the inverse hysteresis model.

Lyapunov Function Control System

In [30] and [47], the inversion-based controllers have been developed to control the antagonistic configured SMA actuated AM system. The Tanaka constitutive model, Equation 3.1 and the deferential of cosine hysteresis model, Equations 3.42 to 3.44 are used in formulating the hysteretic behavior of the SMA. The AM system used resistance heating to drive the SMA. Therefore, the SMA current heating model as per Equation 3.88 is utilized. The input to the model is the current square, $u = i^2$. Substituting the deferential of Equations 3.42 to 3.44 and Equation 3.88 into Equation 3.1 yields the following equation.

$$\dot{\sigma}_i = \frac{\Omega\xi_{iT}(T_i,\xi_i) + \Psi}{i - \Omega\xi_{i\sigma}(T_i,\sigma_i)}\beta_i i_1^2 + \frac{D}{i - \Omega\xi_{i\sigma}(T_i,\sigma_i)}\dot{\varepsilon}_i - \frac{\Omega\xi_{iT}(T_i,\sigma_i) + \Psi}{i - \Omega\xi_{i\sigma}(T_i,\sigma_i)}\alpha_i(T_i - T_\infty), \tag{3.98}$$

where $i = 1, 2$ for SMA 1 and SMA 2, respectively. Due to the two wires pulling in opposite directions the strain rates are $\dot{\varepsilon}_1 = -\dot{\varepsilon}_2$. The resultant force from the two SMAs can be written as

$$y = (f_1 - f_2)r_{pulley} = (\sigma_1 - \sigma_2)A_{wire}r_{pulley}, \tag{3.99}$$

where r_{pulley} is the pulley radius. Equation 3.99 is then differentiated and substituted into Equation 3.98 and yields the following simplified equation form.

$$\dot{y} = hu + g\dot{\sigma}_1 + d, \tag{3.100}$$

Detail of h, g, and d can be referred to [30]. Supposingly, substituting $u = h^{-1}(v - g\dot{\varepsilon}_1 - d)$ and $v = \dot{y}_d + k_e(y_d - y)$ will yield a controller that guarantees the error will be diminished exponentially, where $k_e > 0$. However, the h, g and d are complicated functions that may not be measurable or formulate their inverse. Therefore, [30] proposed an estimation parameter, $\hat{h}$ for h and the control input can be defined as

$$u = \hat{h}^{-1}v, \tag{3.101}$$

and Equation 3.100 is written as

$$\dot{y} = v + (h\hat{h}^{-1} - 1)v + g\dot{\varepsilon}_1 + d, \tag{3.102}$$

with v as

$$v = \dot{y}_d + k_e(y_d - y) + v_a, \tag{3.103}$$

where v_a is a time-varying term to compensate the error between $\hat{h}$ and h, and neglecting the g and d term. Combining Equations 3.102 and 3.103 yields the following equation

$$\dot{y} = \dot{y}_d + k_e(y_d - y) + (h\hat{h}^{-1} - 1)v + g\dot{\varepsilon}_1 + d + v_a. \tag{3.104}$$

Authors defined the disturbance term as

$$\Delta = (1 - h\hat{h}^{-1})v - g\dot{\varepsilon}_1 - d, \tag{3.105}$$

that should be compensated by v_a as

$$\dot{e} + k_e e = \Delta - v_a, \tag{3.106}$$

If $v_a = \Delta$, the error, e will approach zero exponentially. Else if $v_a \simeq \Delta$, high k_e value is selected to reduce the error and maintain robustness and stability. To make sure there exists a v_a that cancels Δ, $v_a = \Delta$ is substituted into Equations 3.103 and 3.105 and via algebraic manipulation, solution for v_a can be obtained as

$$v_a = \frac{1 - h\hat{h}^{-1}}{h\hat{h}^{-1}}(\dot{y}_d + k_e e) - \frac{g\dot{\varepsilon}_1}{h\hat{h}^{-1}}, \tag{3.107}$$

h is a part of the physical model of the SMA system that is nonzero, and same for $\hat{h}$ is a nonzero control parameter. Therefore, there are no singularities in v_a. The inversion-based control system is able to achieve small tracking errors while maintaining stability.

Neural Network Control System

NN control systems are considered as the model-based controller. This is because the NN models are trained based on the real response of the SMA system. This is similar to the phenological methods to model the hysteresis by using various functions to mimic the hysteresis as close as possible. [9] and [79] have used the NN based inverse hysteresis compensator in the controller for the SMA with bias spring configuration. The detail of the NN model has been discussed in the SMA Phenological Model Section. The inverse hysteresis NN is obtained by training the NN with the inverse hysteresis value obtained from the physical experiment. The NN system is easy to develop with the commercially available computational software. However, the number of neurons and the number of layers of the neuron could affect the accuracy of the hysteresis prediction. The result from the use of NN inverse control has shown the ability of the AM control system to track an input with sufficient accuracy.

3.5 Summary and Outlook

The use of SMA as the actuator in AM is becoming more realistic, especially with the rapid development of SMA modeling and control techniques. This survey has put together the path of the SMA development to the application as the actuator for the AM system, particularly in the field of modeling and control development. The contributions of the modeling method and control development techniques to the realization of SMA as the actuator for AM are very important and undeniable.

3.5.1 SMA Constitutive Model

In summary, the SMA constitutive model reviewed in this paper can be listed as in Figure 3.25. The SMA constitutive model review here can be divided into two groups based on their modeling approach. The SMA model derived from phenological approach is getting more popular due to their effectiveness in modeling various hysteresis and nonlinear effects. On the other hand, the SMA model derived from combining physical and phenological approach such as the Tanaka model has been widely used due to its simplicity.

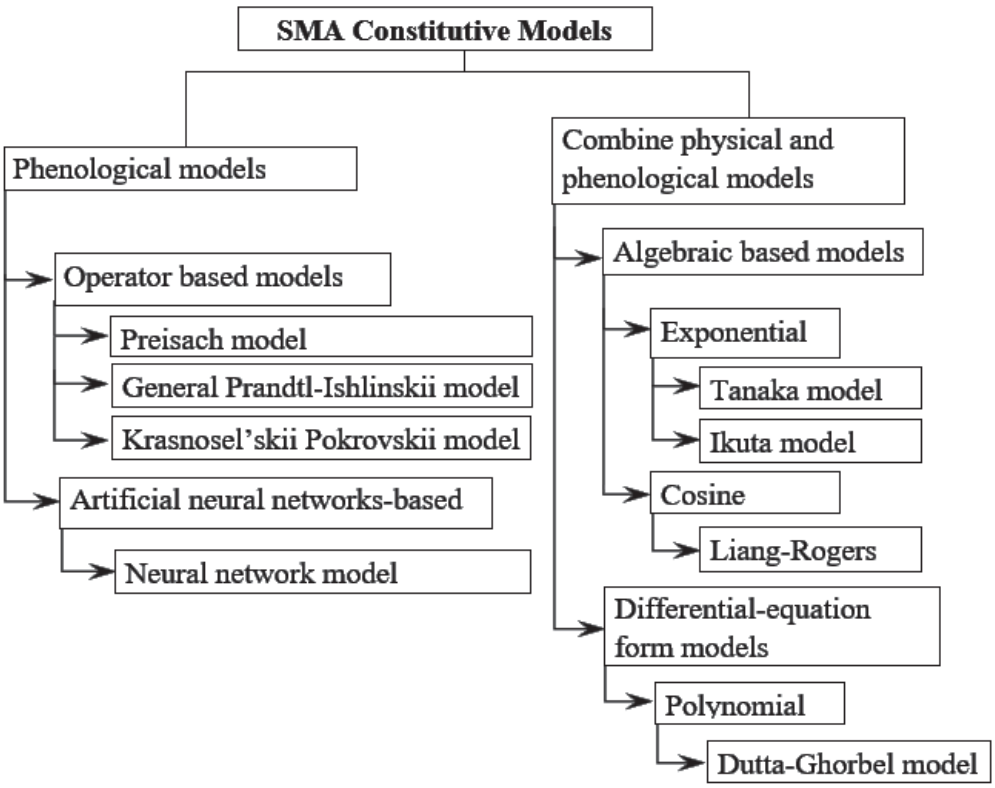

Figure 3.25: Reviewed SMA constitutive model.

Among the constitutive models, most of the combined physical and phenological models relate the stress that acting on the SMA to the SMA hysteresis behavior. For example, Tanaka's work as shown in Figure 3.16 showed the effect of stress on the hysteresis loop, is similar to the hysteresis loop for loads range from 300g to 600g in Figure 3.4 and loads range

from 600g to 1500g in Figure 3.5. The similar concept that explains the shift of hysteresis loop caused by the applied stress observed in Müller and colleagues, Boyd-Lagoudas, Ivshin-Pence and Dutta-Ghorbel work is in line with the example above. This is in agreement with part of the experiment findings. However, the modeling of superelastic behavior exhibited by the Nitinol #6 and Nitinol #8 beyond the loads of 600g and 1500g, respectively is not observed in any of the literature.

In the phenological modeling approach, the stress-dependent and the superelastic hysteresis for SMA are not observed. The phenological approaches show good accuracy and ability to yield the inverse model for hysteresis compensation. Especially the GPI model that can model the asymmetric hysteresis exhibited by the SMA. Thus, exploring the GPI model to include the stress dependency and the superelastic behavior will provide a high impact to the research area in SMA.

SMA Phenological Models

Operator based hysteresis and nonlinear models have gained popularity because of their simplicity and effectiveness in modeling various hysteresis effects. The Preisach model is simple, but the accuracy improves with the increasing number of FOD points. On the other hand, the GPI model has provided a promising model in predicting the asymmetric SMA hysteresis effect. GPI model is also simple, and inverse models are available. Another reviewed model is the KP model, which can provide smooth transitions among the hysteresis loop. However, the accuracy increases with the computational cost. The use of NN as the hysteresis model has also been observed. The NN is trained for the forward and inverse hysteresis based on experimental data. The NN hysteresis model technique is capable of modeling symmetric and asymmetric hysteresis. However, only the major loop modeling is observed in [79]. The training for minor hysteresis loop has not been observed. To include minor hysteresis loops in the NN might lead to additional neuron layers, which could lead to a more complex system and more computational cost.

The operator based hysteresis model in [79] does not include the stress effect in the hysteresis model. The stress effect is a very important component in the hysteresis modeling for the AM system that generally deals with dynamic loading. Each of the hysteresis model has its advantages and disadvantages, and the adoption of the model is very much dependent on the application. For example, if one only needs to simulate the hysteresis effect, then the Tanaka-liked based models are preferred due to their simplicity. However, in the case of developing the control system, the operator-based models are preferred due to the invertible ability.

SMA Combined Physical and Phenological Models

The constitutive model that has been used the most is the Tanaka model. The reason that the Tanaka model has been widely used is that the model is simple and able to capture all the necessary parameters of the SMA. The Tanaka model also has the flexibility to combine with any other phenological hysteresis modeling method. Meanwhile, the Müller model is based on the idea that the fraction of the martensite and austenite phase is separated by a potential energy barrier where the phase transition is governed by a probability function. Müller model is more complex and difficult to apply when it comes to the development of the control system and stability analysis. One also has to consider the computational cost-effectiveness when applying the Müller model in the real-time implementation. With inspiration from Tanaka, Boyd and Lagoudas introduced their 3-D constitutive SMA model based on the elastic stiffness of SMA. The Boyd-Lagoudas model can be described as the 3-D version of the Tanaka model. However, in most of the SMA applications, a single dimension model is sufficient. Looking from a simplicity point of view, the Ivshin-Pence model is also simple. Although the model was first introduced using the austenite fraction instead, it is easily converted to the martensite fraction. The Ivshin-Pence model provides the stress-strain relation compared to the Tanaka model, which provides the rate relation of the stress-strain. Therefore, in the dynamic modeling environment, the Tanaka model could

be more accurate compared to the Ivshin-Pence model [93]. Based on the same principle used by Tanaka, the mechanical properties of the SMA are contributed by the fraction of the mix martensite and austenite phase. The above algebraic based models are simple and include stress-induced hysteresis, but they are difficult to implement in the control system development. This is due to their inability or the difficulty to produce an analytical inverse model for hysteresis compensation. Meanwhile, Dutta-Ghorbel model can yield the inverse model and allows for the computation of a continuously differentiable strain. However, the Dutta-Ghorbel model is formulated based on the assumption that there is no effect of stress on the phase transition temperature. Therefore, the accuracy of the Dutta-Ghorbel model under large load conditions may not be accurate. Furthermore, to prevent the inverse models from dividing to zero, an additional parameter is added, and this leads to some errors.

3.5.2 AM Control System

Tables 3.1 and 3.2 show the summary of various control systems developed by researchers to control the SMA in actuating the AM or with similar function.

Controlling the SMA actuated AM directly involves the construction of a controller that deals with the hysteresis system without compensating the hysteresis behavior of the SMA. Typically the modeless PID controller is simple, but it is very limited in dealing with the highly nonlinear and hysteresis SMA actuated AM system. The tuning of the PID gains is tedious, yet it will not guarantee good control performance through the whole operation range. To overcome this issue, the fuzzy system is introduced to continuously tune the gains based on the system's nonlinear output. Although the fuzzy system can improve the PID controller by tuning the PID based on the nonlinearity of the system, the fuzzy system is not able to respond to external disturbance. Meanwhile, the modeless VSC is more effective in responding to the external disturbance. This is because the VSC captures the error and error rate, with both included as part of the control variables. However, the lack of

Table 3.1: Summary of direct control systems for SMA or SMA actuated AM systems development.

Direct Control			
Control	Model	Configuration	Result
PID	Transfer function [87], Tanaka [85], modeless [86]	Antagonistic	Unable to respond to the load uncertainty
VSC	Tanaka [83] [29]	Bias spring	Exhibit chattering
Fuzzy PID	Tanaka [88], modeless [89]	Antagonistic [88], single wire [89]	Improvement steady state error and response time
Sliding mode	Tanaka [45]	Bias spring [45]	Improved controller response. But, poor damping estimation result in poor tracking performance [45].

information about the system, the control structure cannot change smoothly between the control structures. A boundary layer is introduced to smoothen the transition between the control structure. However, it leads to another problem of the steady state error. Up to this point, one can see that the inclusion of the system model in the controller is very important. Although the models are not perfect, the models can provide a prediction that is close enough for the controller to respond effectively.

Similar to the VSC, the sliding-mode controller is also effective in controlling the nonlinear SMA actuated AM system. In the review, the sliding-mode control is used in both the direct control scheme and inverse-based control scheme. Under the direct control scheme, authors use the Tanaka constitutive and cosine hysteresis model as a forward prediction via sliding-mode control to obtain the desired torque. An additional PI controller is used to generate

Table 3.2: Summary of inverse-based control systems for SMA or SMA actuated AM system development.

Inverse-Based Control

Control	Model	Configuration	Result
Feedforward and Feedback	Modify Tanaka + Preisach [91], Dutta Ghorbel [46], GPI [69]	Bias spring [91] [46], single wire [69]	Able to eliminate hysteresis behavior
Adaptive	KP [14] [73] [71] [72]	Antagonistic [71], Bias spring [14], Single wire [73] [72]	Good tracking capability in versatile environment.
Robust	GPI [6] [92]	Antagonistic [92], Single wire [6]	Effective in tracking control.
Sliding mode	Tanaka-Ikuta [26]	Single wire [26]	Able to handle load variation, but exhibits chattering [26].
Lyapunov function	Tanaka [30] [47], NN [79] [9]	Antagonistic [30] [47], Bias spring [79] [9]	Good stability and tracking ability.

the control input from the desired torque and feedback torque. Because the sliding-mode scheme is applied to yield the desired SMA stress instead of input for the entire system, the control system is unable to eliminate the nonlinear hysteresis problem from the SMA.

The inverse-based control scheme involves the development of hysteresis compensator to cancel the hysteresis behavior exhibited by the SMA. Without the hysteresis effect, the SMA actuated AM system behaves like a linear system, and PID control is known to be very effective in linear systems. The feedforward functions are the inverse hysteresis or nonlinear functions to linearize the SMA actuated AM system. Simple and invertible hysteresis models

such as the Preisach, GPI, and KP model are very useful in feedforward control strategies. However, getting the inverse models of the SMA hysteresis and the AM system non-linear model depend on the modeling method adopted. For example [4], [63], [69], and [91] have chosen modeling methods that can provide an accurate inverse model of the system. Therefore, the development of the feedforward control can be done successfully. Meanwhile, [46] chose a modeling method that will yield an inverse model with an error. Although the resulting control system is better than the PID controller, there is an error that cannot be avoided.

The improved PID systems have shown their ability to control the bias spring SMA configuration in the AM. However, the improved PID control method only applies to fixed load experiments. The ability to deal with complex nonlinear and uncertainty of the real world loading are still doubtful. Examples of AM systems that deal with uncertainty are such as the antagonistic configuration of SMA, the cooling environments that have liquid and gas phase (for amphibious robot), working with the unknown workload and others. Under such uncertain conditions, a more advanced nonlinear controller is necessary to overcome the uncertainty and ensure the stability of the system. Nonlinear controllers, like the adaptive controller and robust controller, have shown a better capability of handling the uncertainty. Using the invertible modeling method with the adaptive control strategy, [73] has successfully controlled the SMA actuated AM system in diverse environmental conditions. Meanwhile, with the use of GPI hysteresis model, [6], [92] and [94] have successfully developed a robust controller to control the antagonistic SMA actuated AM system. Due to the involvement of a system model and error dynamic in the controller design, the control systems can respond to various disturbances and uncertain conditions.

In the review, most of the authors that used inverse-based control scheme are adopting a modeling method that can yield inverse hysteresis model. However, some author used approximation value in replacing the inverse hysteresis effect. This can be observed in [26] where authors used the Ikuta exponential hysteresis model approach which resulted in difficulties to obtain the inverse model. Therefore, the martensite fraction had to be

approximated. The result from the parameter approximation shows that the system is not sensitive to external disturbance and chattering is also observed.

Another example can be seen in the Lyapunov function control system development. In [30] and [47], authors used the cosine hysteresis model which is difficult to yield the inverse model. Therefore, authors have to use parameter estimation to replace the non-invertible model. Although the inverse-based controller developed by [30] and [47] showed good tracking error, the control development is complicated due to the non-invertible and complex system model resulting from adopting the cosine hysteresis modeling approach.

The ability and advantages of the control system ranging from PID control to a nonlinear control approaches have been presented. One very important finding in the literature reviews is that the key to the success of control development is subjected to the modeling approach. Many authors are not concerned about the compatibility of the control strategy and the system modeling approach. This can be observed in research works presented in [26], [29], [30], [45], [47] and [83], where authors have developed models for the system, but the developed models are unable to be utilized in the development of the control system. Authors either switch to non-model based control or use the approximation in the controller. This will lead to the compromise of controller ability or complexity in the controller development.

3.6 Concluding Remarks and Emerging Research Problems

The review is in agreement with the stress-dependent hysteresis of the SMA in the preliminary experiment results, where the similar stress dependent model had been observed in the combined physical and phenological model. However, the superelastic behavior observed in the preliminary experiment was not found in any of the literature. Thus, the exploration of SMA superelastic behavior using a phonological approach is of importance.

Besides, the review also found that the adoption of modeling approach is very important during the control system development. A model-based control system generally performs much more effectively than modeless control. However, about half of the controller development in this review has the problem of matching the modeling approach and the control scheme. Therefore, the modeling approach and the control scheme have to be wisely selected through this research.

Additionally, through the literature review, few emerging research problems on SMA actuated AM system are found. These include: 1) phenological stress dependent hysteresis modeling and inverse model construction for the SMA; 2) the development of a robust or adaptive controller for the antagonistic configuration SMA actuated AM system based on the SMA stress dependent hysteresis model; 3) conducting stability analysis of the controller for the antagonistic configuration SMA actuated AM system.

Chapter 4

Systems Modeling and Verification

In Chapter 3, various existing hysteresis modeling methods have been reviewed and discussed. Among them, the GPI model having advantages over other modeling approaches due to its ability to model asymmetric hysteresis behavior and analytical inverse model can be obtained to mitigate the effects of the SMA hysteresis nonlinearity. The first section of this Chapter demonstrates the capacity of GPI model in predicting the SMA hysteresis behavior at various load conditions. The preliminary data in Chapter 1 shows agreement with [3] and [40] where the SMA transition temperature varies according to the applied stress. However, the invertible phenological model with stress-dependent characteristic has not been observed. Therefore, a Stress-Dependent GPI model is proposed to describe the Nitinol hysteresis behavior under stress variations. To complete the modeling of the wrist joint system, the TEM model and the wrist dynamic model are also developed.

4.1 Generalized Prandtl-Ishlinskii Shape Memory Alloy Hysteresis Model

GPI model as per Equations 3.19 to 3.24 in Chapter 3 is utilized in predicting the Nitinol hysteresis nonlinearity as shown in Figure 3.6. Equation 3.20 also can be written in numerical

form as per Equation 4.1.

$$y_{p\gamma}(t) = p_0\gamma(T) + \sum_{j=1}^{n} p(r_j)F^{\gamma}_{lr_j}[T](t), \tag{4.1}$$

where n is the number of generalized play operators. The discrete form of the GPI model is used for the numerical computation during GPI parameter fitting.

To obtain the GPI parameters from the fitting function, the Nitinol hysteresis loop shape had to be adjusted to match the GPI play operator shape. In general, Nitinol has shown contraction behavior when heated over the transition temperature which is also known as negative induced strain. This causes the Nitinol hysteresis loop to have a horizontal mirrored orientation to the GPI play operator as per Figure 3.10. The hysteresis value is subtracted from a constant which is larger than the maximum strain to reorient the hysteresis loop. This produces a mirror of the hysteresis loop that matches to the GPI operator. The Nitinol experimental measured displacement is defined as y_{N6}, and the mirrored hysteresis loop is defined as y_m. The mathematical representation of the mirror process can be written as Equation 4.2.

$$y_m = k_f - y_{N6}. \tag{4.2}$$

The constant, k_f is defined at 6mm since the maximum hysteresis value is less than 5mm as per Figure 3.6. Another way to correct the hysteresis loop orientation is to alter the parameters' signs in the play operator functions of the GPI model. However, this is more complicated compared to mirroring the Nitinol hysteresis loop along the horizontal. Furthermore, the strain can be recovered by the same Equation 4.2 by switching the y_m and y_{N6}. The reorientation of the hysteresis loop was not observed in any published articles. Other researchers could have use deferent reference positions during the data measurement, in which the data obtained is orientation with the play operator.

4.1.1 Generalized Prandtl-Ishlinskii SMA Hysteresis Model Parameter Identification

After reorientation of the hysteresis loop, the model parameters a_i, b_i, c_i, d_i $(i = 0, 1, 2, 3)$, ρ, τ and c can be identified using Matlab lsqcurvefit() function by the minimization of error squared function as per Equation 3.25. Due to a large number of model parameters, there are many possible local optimum solutions. Therefore, the starting points selection is crucial for achieving the best local optimum. The method to obtain the initial point was not mentioned in any of the published papers. To overcome this, a systematic method in identifying the GPI model parameters using Matlab is proposed. The proposed method separates the curve fitting process into three stages by first fitting the memory curve that involves the preliminary identification of parameters a_i, b_i, ρ, τ and c for the summation part, and ignoring the $p_0\gamma(T)$ in Equation 4.1. The initial values of a_i and b_i are obtained based on the saturation value of the parabolic tangent, $tanh()$ function. At maximum temperature, $\gamma_r(T)$ and $\gamma_l(T)$ are equal to maximum strain, and at minimum temperature, $\gamma_r(T)$ and $\gamma_l(T)$ are equal to the minimum strain at maximum temperature. With this, the initial values of a_i and b_i can be obtained and the values of ρ, τ and c are equated to 0.1. Set the initial values into the Matlab lsqcurvefit() function and repeat the process until a local minimum is achieved. The preliminary parameters obtained in the first stage are used in the second stage as initial values. The initial values of c_i and d_i are also defined using the same method as the a_i and b_i based on the $tanh()$ function saturation. In the second stage, the parameters identified in the first stage are fixed. Using the same function of lsqcurvefit(), the value of c_i and d_i can be identified when the lsqcurvefit() function achieves local minimum. For the final stage, all parameters pre-identified in the first and second stage are used as initial values in the lsqcurvefit() function and continue to iterate until the function achieves local minimum condition. The final values of the GPI model parameters and the least square error $J(T)$ are shown in Tables 4.1 to 4.3. n value shows a very small improvement in error beyond $n = 15$. Besides that, $n = 15$ showed acceptable accuracy in modeling the Nitinol hysteresis.

Table 4.1: GPI model parameters a_i and b_i.

Load	a_0	a_1	a_2	a_3	b_0	b_1	b_2	b_3
650g	51.0249	0.3260	-24.1350	46.4954	75.5864	1.8889	-43.0755	-29.3174
700g	13.0535	0.2504	-17.0276	36.5160	29.7906	0.9093	-20.6438	14.2003
750g	14.4445	0.2867	-19.9362	38.2133	13.5110	1.2686	-32.9130	33.9629
800g	29.9294	0.1779	-13.1168	53.2837	15.3133	1.2140	-34.4942	37.4424
850g	36.3054	0.1933	-14.6169	59.4939	12.2908	1.4726	-44.7955	35.3045
900g	36.4567	0.2765	-21.5099	59.3167	3.6740	0.4237	-14.4475	26.4354
950g	91.9085	0.2893	-23.1274	114.7249	14.4426	0.2286	-9.5034	37.1770
1000g	124.6829	0.2819	-23.6714	147.5849	5.8886	0.2194	-9.4957	28.7565
1050g	41.6176	0.0142	-4.2494	64.5277	15.0431	0.0160	-3.8359	37.9034

Table 4.2: GPI model parameters c_i and d_i.

Load	c_0	c_1	c_2	c_3	d_0	d_1	d_2	d_3
650g	-29.8407	-0.1888	8.5775	375.2065	-30.0396	-0.1932	8.6998	375.3413
700g	-6.5062	-0.2026	9.6819	-50.9852	-6.5179	-0.2130	9.7377	-50.9754
750g	-6.1313	-0.2770	13.2732	-44.5758	-6.1311	-0.2850	13.2741	-44.5753
800g	-3.2149	-0.2593	12.7136	-19.7034	-3.2147	-0.2685	12.7153	-19.7025
850g	-1.7137	-0.0969	4.5924	-16.3713	-1.7137	-0.0970	4.5924	-16.3713
900g	-0.5225	-0.0800	4.1149	-18.5873	-0.5233	-0.0847	4.1308	-18.5868
950g	-0.6397	-0.0801	4.0371	-22.9332	-0.6410	-0.0841	4.0373	-22.9326
1000g	-0.2626	-0.0793	4.0308	-26.3554	-0.2638	-0.0834	4.0356	-26.3551
1050g	-10.6968	0.9290	-11.5754	-25.9048	-0.0013	-0.1557	12.3271	-36.5858

Table 4.3: GPI model parameters ρ τ c and $J(T)$.

Load	ρ	τ	c	$J(T)$
650g	0.0053	0.1525	0.3634	21.6703
700g	0.0286	0.6866	0.2453	10.4530
750g	0.0298	6.2695	0.0302	138.3143
800g	0.0489	10.1125	0.0335	80.7545
850g	0.1061	14.7604	0.0365	55.4026
900g	0.3301	28.3763	0.0240	13.9073
950g	0.2577	33.2333	0.0176	21.2868
1000g	0.5961	77.3561	0.0076	16.3969
1050g	3.6259	33.8717	0.0143	0.1651

Figures 4.1 and 4.2 show the changes of GPI model parameters fitted for each hysteresis curve under various load conditions using the GPI modeling approach.

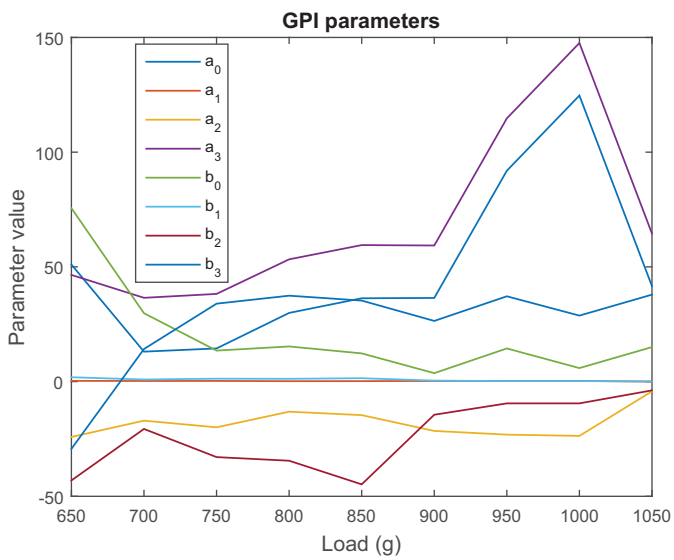

Figure 4.1: GPI model constants a_i and b_i.

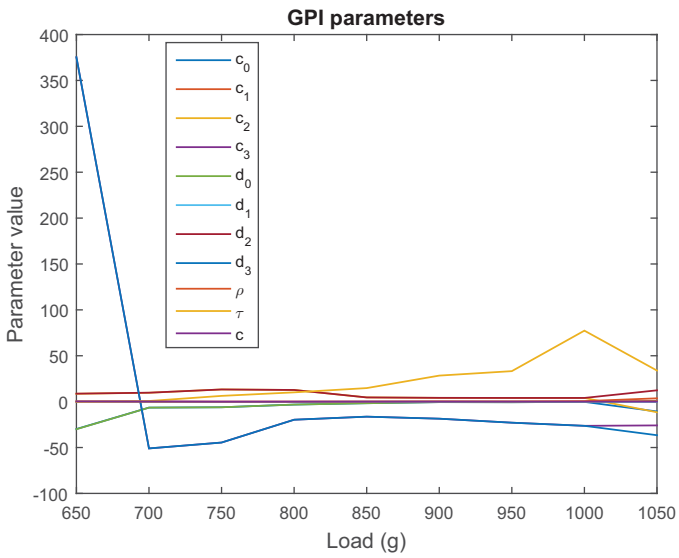

Figure 4.2: GPI model constants c_i, d_i, ρ, τ and c.

4.1.2 Generalized Prandtl-Ishlinskii SMA Hysteresis Model Verification

The experimental data of Nitinol hysteresis and the GPI models are shown in Figures 4.3 to 4.20. Both the hysteresis profile with elongation versus the temperature and time are illustrated to verify the effectiveness of the GPI modeling approach.

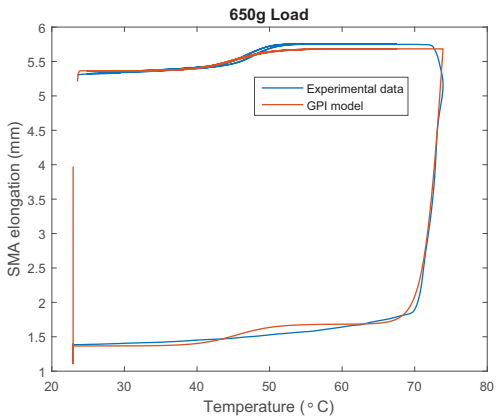

Figure 4.3: GPI loop at 650g load.

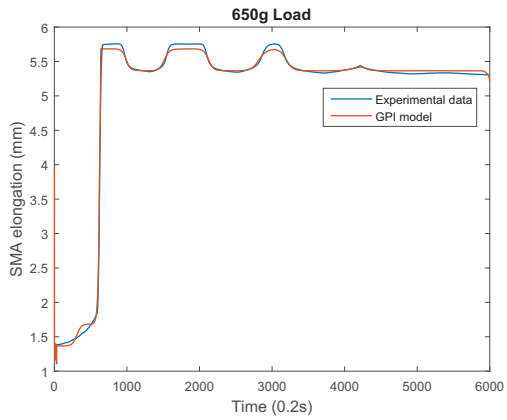

Figure 4.4: GPI model at 650g load.

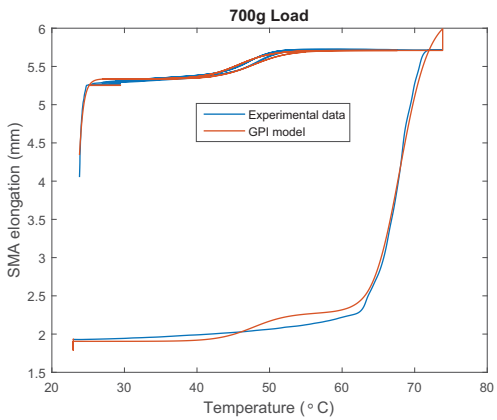

Figure 4.5: GPI loop at 700g load.

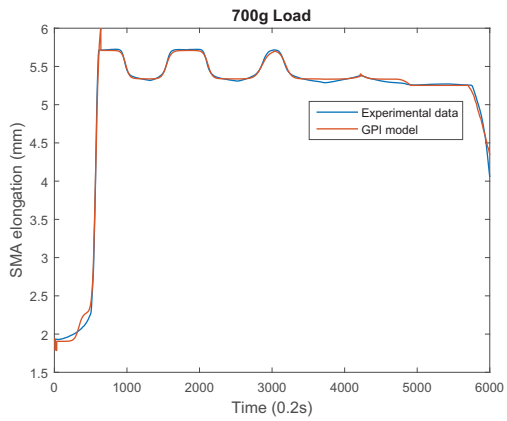

Figure 4.6: GPI model at 700g load.

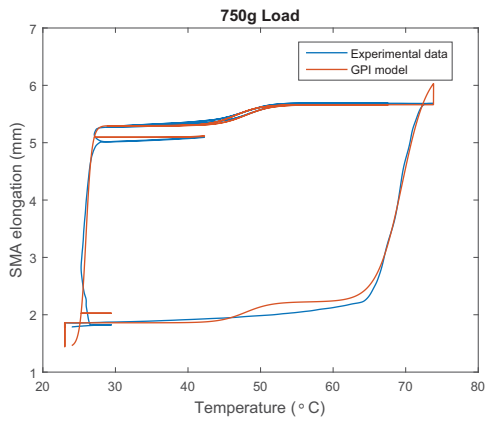

Figure 4.7: GPI loop at 750g load.

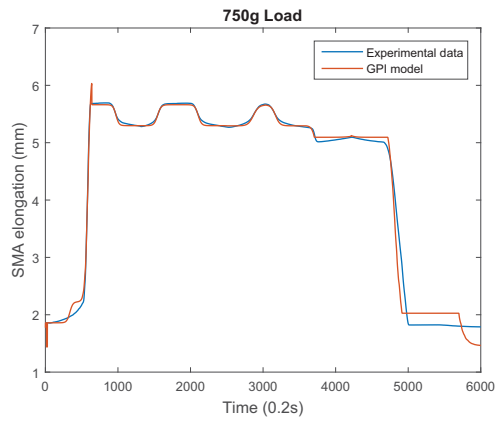

Figure 4.8: GPI model at 750g load.

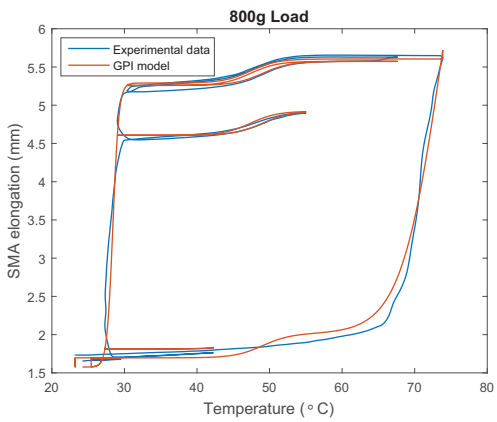

Figure 4.9: GPI loop at 800g load.

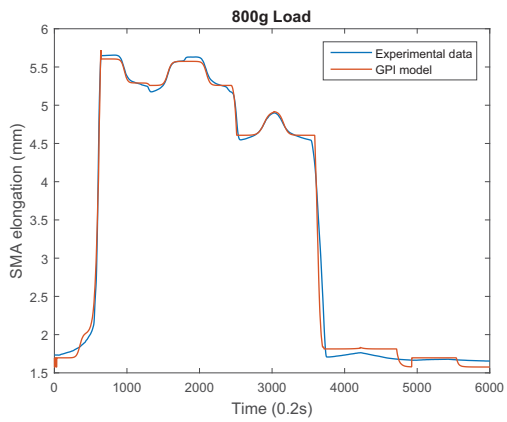

Figure 4.10: GPI model at 800g load.

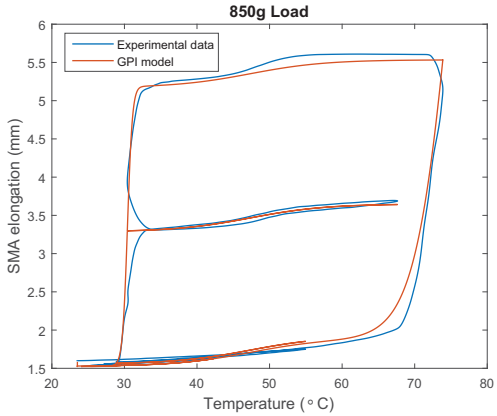

Figure 4.11: GPI loop at 850g load.

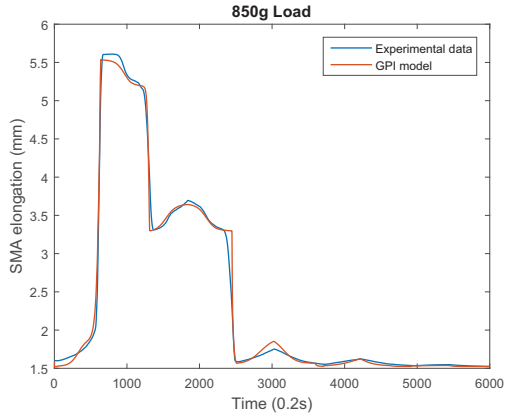

Figure 4.12: GPI model at 850g load.

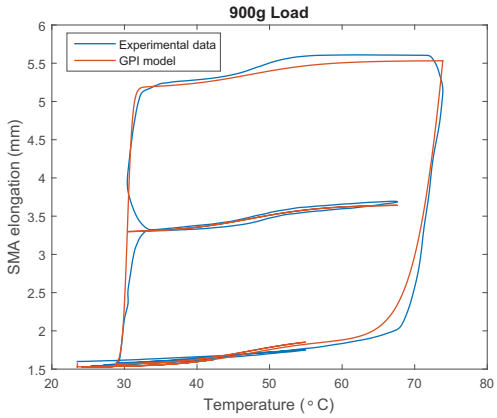

Figure 4.13: GPI loop at 900g load.

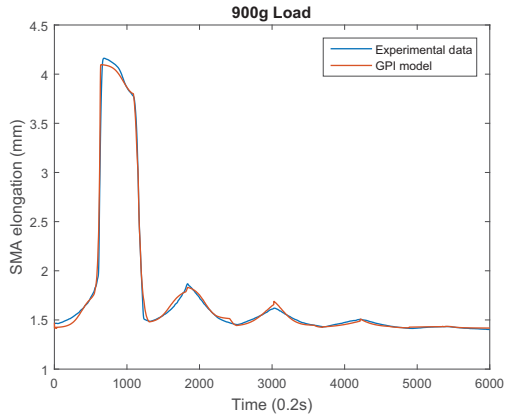

Figure 4.14: GPI model at 900g load.

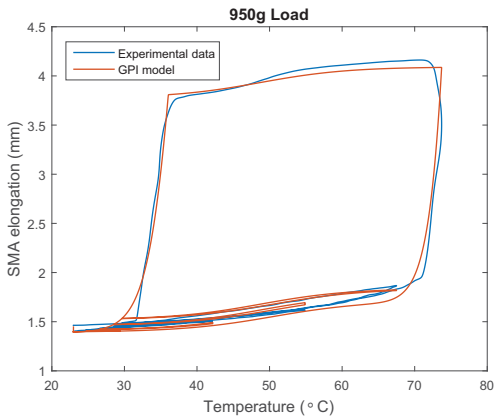

Figure 4.15: GPI loop at 950g load.

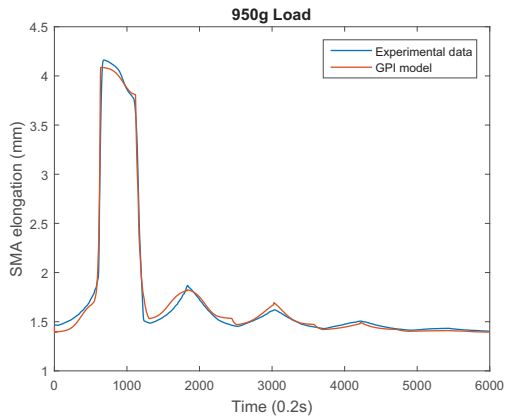

Figure 4.16: GPI model at 950g load.

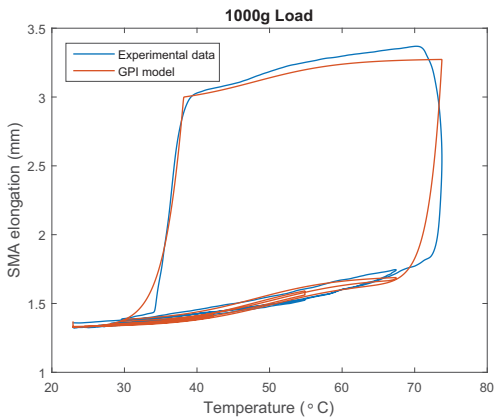

Figure 4.17: GPI loop at 1000g load.

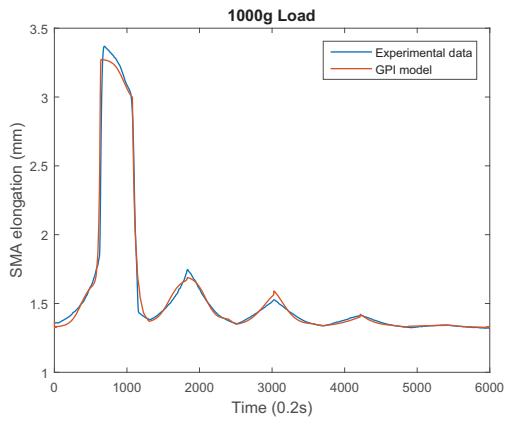

Figure 4.18: GPI model at 1000g load.

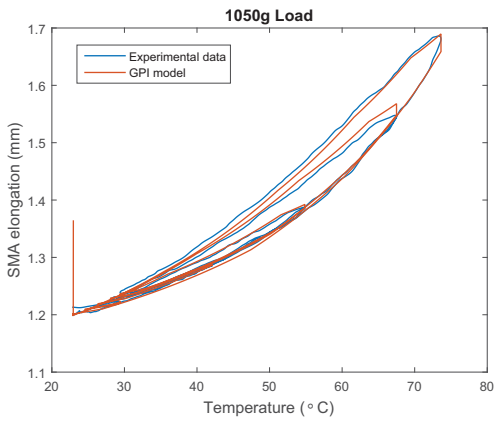

Figure 4.19: GPI loop at 1050g load.

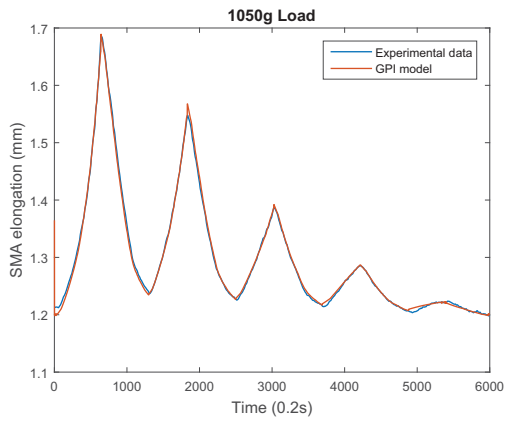

Figure 4.20: GPI model at 1050g load.

Further error analysis is conducted to study the accuracy of the GPI model. The error is computed using Equation 4.3

$$e_{mT} = \frac{100(y(T) - y_{p\gamma}(T))}{MAX_y - MIN_y}, \tag{4.3}$$

where $y(T)$ and $y_{p\gamma}(T)$ denote the experimental data and the GPI model value, MAX_y and MIN_y are the maximum and minimum values of the experimental data. Figures 4.21 to 4.29 show the error distribution for the GPI models under various load conditions. The statistics of the GPI model errors are also obtained and shown in Table 4.4.

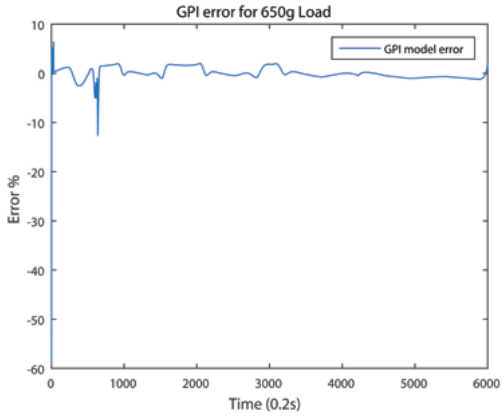

Figure 4.21: GPI model error at 650g load.

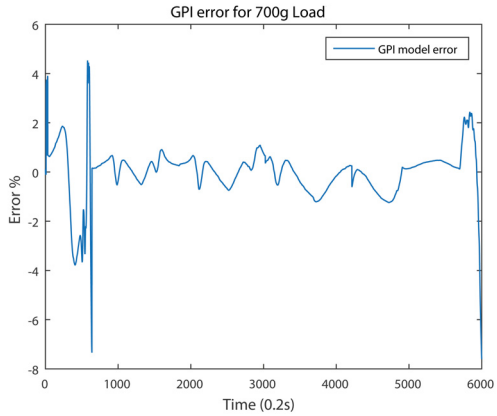

Figure 4.22: GPI model error at 700g load.

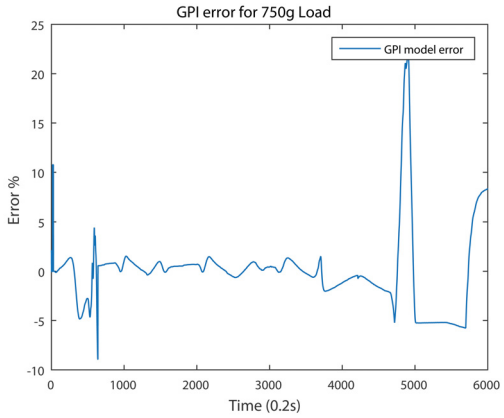

Figure 4.23: GPI model error at 750g load.

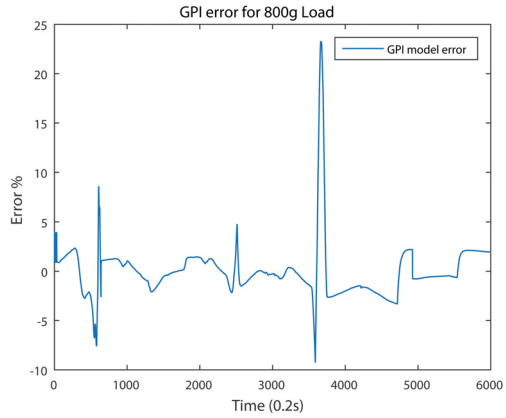

Figure 4.24: GPI model error at 800g load.

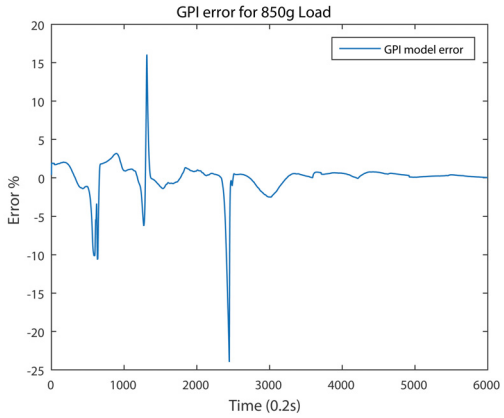

Figure 4.25: GPI model error at 850g load.

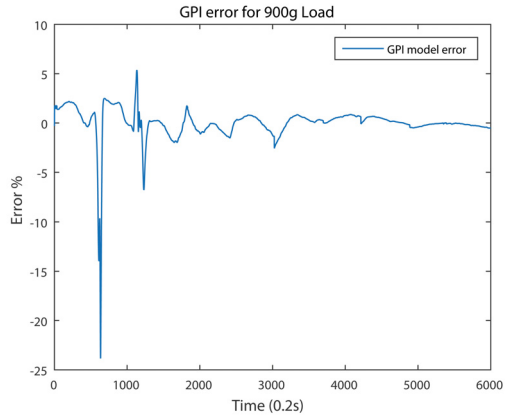

Figure 4.26: GPI model error at 900g load.

Figure 4.27: GPI model error at 950g load.

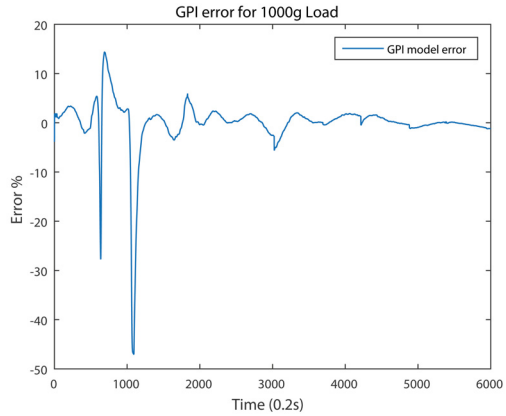

Figure 4.28: GPI model error at 1000g load.

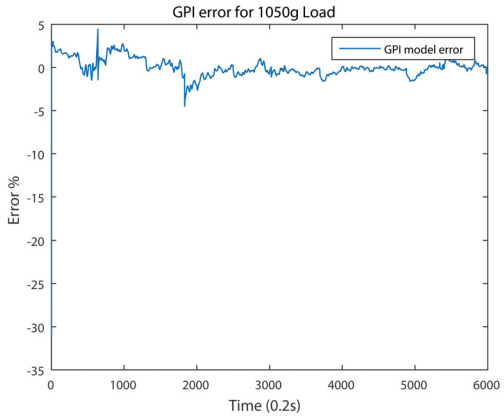

Figure 4.29: GPI model error at 1050g load.

Table 4.4: GPI model errors statistic (%).

Load	Maximum	Minimum	Mean	Standard Deviation	Range
650g	6.4709	-59.2030	-0.0319	1.3744	4.3718
700g	4.5316	-7.6045	-0.0219	1.0996	3.7954
750g	21.8413	-8.9377	-0.0134	3.8888	3.9046
800g	23.2674	-9.2745	-0.0027	2.8997	4.0012
850g	16.0427	-23.9761	-0.0145	2.3525	4.0850
900g	5.3527	-23.8491	-0.0054	1.7454	2.7587
950g	8.2147	-41.9782	-0.0084	2.9082	2.0483
1000g	14.3719	-47.0678	0.0061	5.2829	0.9896
1050g	4.5108	-31.0766	0.0000	1.0745	0.4883

From Figures 4.21 to 4.29 shown the GPI model errors are mainly fall below 5%. Generally, the GPI model errors have a standard deviation of less than 3% as observed in Table 4.4. These verify that the GPI model is capable of predicting the Nitinol hysteresis nonlinear behavior.

4.2 Stress-Dependent Generalized Prandtl-Ishlinskii Shape Memory Alloy Hysteresis Model

The GPI hysteresis modeling approach has shown to be effective in modeling the Nitinol hysteresis nonlinearity at various stress conditions. However, the multiple GPI models at discrete stress points cannot be utilized to predict the Nitinol hysteresis with a continual change of stress. The GPI models developed have to be combined into a single model as stress-dependent generalized Prandtl-Ishlinskii (SD-GPI) model that can predict the Nitinol hysteresis with the temperature and stress as inputs. The SD-GPI is very important for prediction of the Nitinol hysteresis in the antagonistic wrist configuration. This is because

the stress on the SMA is continually changing during the operation of the wrist joint. Furthermore, the Nitinols are operating in the superelastic condition to provide large strain to move the wrist joint. Manipulating the Nitinol in the superelastic condition will be dealing with the Nitinol hysteresis that is highly affected by the stress as observed in Figure 3.6.

From the best of the author's knowledge, there is no prior information on SD-GPI model development for SMA. There is a paper published in 2011 about the SD-GPI for the giant magnetostrictive actuator by [95]. In [95], the GPI density function as per Equation 3.23 is modified to incorporate the stress component to form a stress-dependent density function. The stress-dependent density function is then fit to the experimentally measured data. However, the fitted stress-dependent density function was not shown in the paper. Another researcher [96] did study the stress-dependent property of the Nitinol at the crystal level. However, the study did not result in any phenological model. Other literature on stress-dependent are stress-dependent Presiach model [97] and stress-dependent Prandtl-Ishlinskii model [98] developed for prediction of magnetostrictive actuator hysteresis. Meanwhile, stress-dependent hysteresis based on Helmholtz and Gibbs energy relations is developed for ferroelectric materials [99]. Thus, a SD-GPI model with temperature and stress as inputs was developed as follows.

4.2.1 Stress-Dependent Generalized Prandtl-Ishlinskii SMA Hysteresis Model Development

To develop the SD-GPI model, the influence of the stress applied to the Nitinol and the changes in its hysteresis behavior are firstly studied. The study found that the stress above the critical stress generates the superelastic hysteresis behavior that has a significant change in the memory part of the GPI model. The memory part of the GPI model is governed by the play operator envelops $\gamma_r(T)$, $\gamma_l(T)$ and the density function as per Equation 3.23. Figures 4.1 and 4.2 show the model parameters variation for the envelope function and the density function under different stress conditions. However, based on the GPI model parameters, a

clear relation between the parameters at different stress levels cannot be established. Further investigation found an agreement between the experimental data in Figure 3.6 and the claim in [3], [40] and [96] that the increase of stress applied on the SMA caused the transition temperature to shift higher. Knowing that the memory part of the GPI model is governed by the play operator envelops $\gamma_r(T)$, $\gamma_l(T)$, the stress is proposed to be incorporated in the play operator envelope functions. The parameters a_i and b_i $(i = 0, 1, 2, 3)$ are replaced with quadratic functions of the applied load. The parameters a_i, and b_i can be written as Equations 4.4 and 4.5

$$a_i = s_{ai0}m^2 + s_{ai1}m + s_{ai2} \tag{4.4}$$

and

$$b_i = s_{bi0}m^2 + s_{bi1}m + s_{bi2}, \tag{4.5}$$

where m is the applied load. The newly defined SD-GPI parameters can be denoted as s_{aij} and s_{bij} for $j = 0, 1, 2$ and $i = 0, 1, 2, 3$. Thus, Equation 4.1 can be further written as the SD-GPI model in Equation 4.6.

$$y_{p\gamma}(t) = p_0\gamma(T) + \sum_{j=1}^{n} p(r_j)F^{\gamma}_{lr_j}[T, \sigma](t), \tag{4.6}$$

where σ is the stress applied on the Nitinol and $y_{p\gamma}(t)$ is the elongation.

4.2.2 Stress-Dependent Generalized Prandtl-Ishlinskii Model Parameters Identification

In Tables 4.1 to 4.3, a step change in the GPI parameters d_0, d_1 and d_2 is observed between 800g load and 850g load. Thus, the SD-GPI model for the loads from 650g to 1050g is proposed to divide into two sections with each having their parameters and joint at 800g load. The first section is for the loads ranging from 650g to 800g and denotes as SD-GPI parameters 1 and the second section is for the loads ranging from 800g to 1050g and denotes as SD-GPI parameters 2. Using the curve fit tool in Matlab, the initial points of s_{aij} and s_{bij}

are obtained from the GPI model parameters with quadratic fitting. Initial points for c_i, d_i, ρ, τ and c are selected from GPI model parameters at 800g load. A total of 35 initial points are substituted into Matlab function lsqcurvefit() to obtain the best-fitted SD-GPI model. The SD-GPI model parameters are identified based on the the lowest least square errors, as shown in Tables 4.5 and 4.6.

Table 4.5: SD-GPI model parameters s_{aij} and s_{bij}.

Parameter	650-800	800-1050	Parameter	650-800	800-1050
a_{00}	-297.1181	8269.0048	b_{00}	-114.4758	-165.5890
a_{01}	537.0467	-12074.7618	b_{01}	192.5613	224.5043
a_{02}	-234.6254	4427.7566	b_{02}	-77.5850	-52.6058
a_{10}	-10.1853	-15.9337	b_{10}	9.0089	-2.0600
a_{11}	18.3751	23.0744	b_{11}	-21.8423	8.5123
a_{12}	-7.9515	-8.1009	b_{12}	13.0035	-4.1568
a_{20}	786.6742	849.6684	b_{20}	-96.4131	-157.3013
a_{21}	-1424.8980	-1229.1119	b_{21}	318.5139	40.1835
a_{22}	619.8951	427.4553	b_{22}	-229.9297	30.5354
a_{30}	-295.6842	6755.6422	b_{30}	-105.1643	-173.1184
a_{31}	529.9694	-9800.7740	b_{31}	173.0695	267.5202
a_{32}	-206.7026	3594.6662	b_{32}	-45.1994	-64.2441

Table 4.6: SD-GPI model parameters c_i, d_i, ρ, τ and c.

Parameter	650-800	800-1050
c_0	-0.7419	-0.0144
c_1	-0.0851	-0.3442
c_2	4.3164	16.1925
c_3	-51.2905	0.0197
d_0	-0.8557	-0.0144
d_1	-0.0961	-0.3442
d_2	4.7624	16.1925
d_3	-51.1227	0.0197
ρ	0.2212	11.5400
τ	6.9026	30.9878
c	0.0474	0.1581

4.2.3 Stress-Dependent Generalized Prandtl-Ishlinskii Model Verification

The fitted SD-GPI model 1 for 650g to 800g load and experimental data are shown in Figures 4.30 to 4.37.

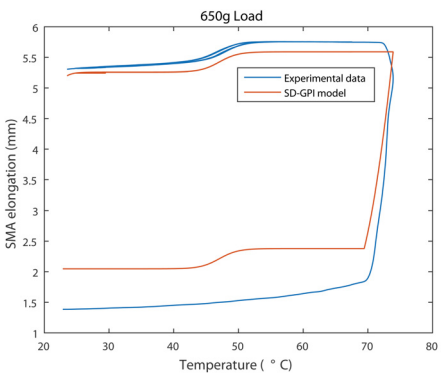

Figure 4.30: SD-GPI loop at 650g load.

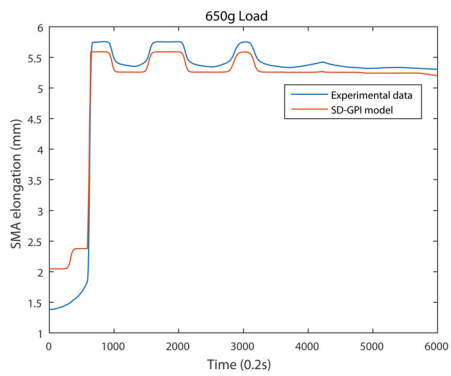

Figure 4.31: SD-GPI model at 650g load.

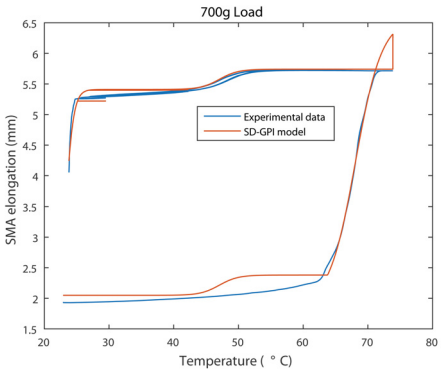

Figure 4.32: SD-GPI loop at 700g load.

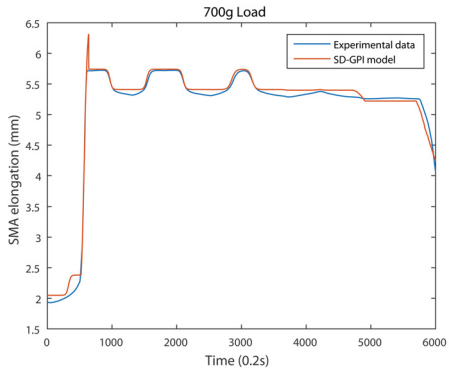

Figure 4.33: SD-GPI model at 700g load.

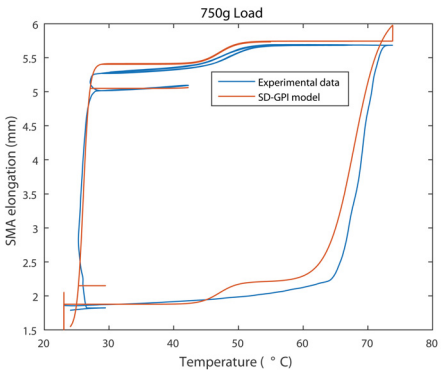

Figure 4.34: SD-GPI loop at 750g load.

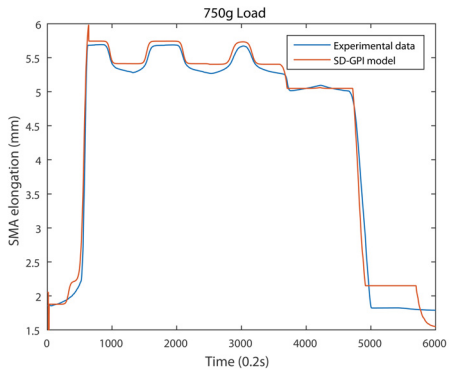

Figure 4.35: SD-GPI model at 750g load.

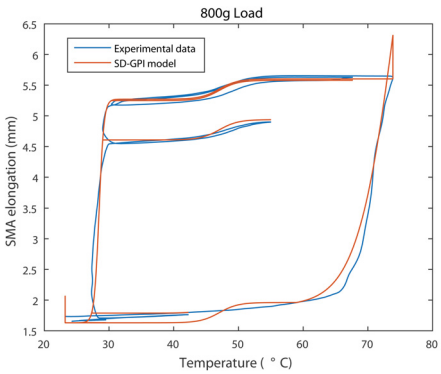

Figure 4.36: SD-GPI loop at 800g load.

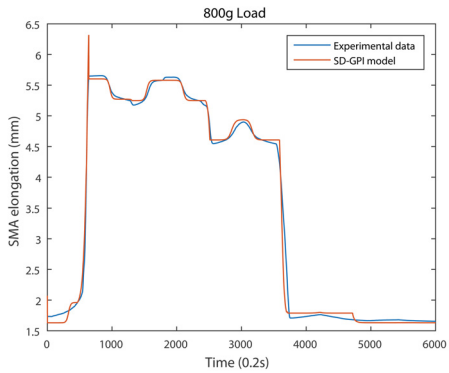

Figure 4.37: SD-GPI model at 800g load.

The fitted SD-GPI model 2 for 800g to 1050g load and experimental data are shown in Figures 4.30 to 4.37.

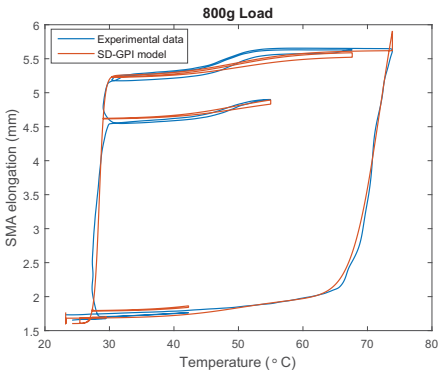

Figure 4.38: SD-GPI loop at 800g load.

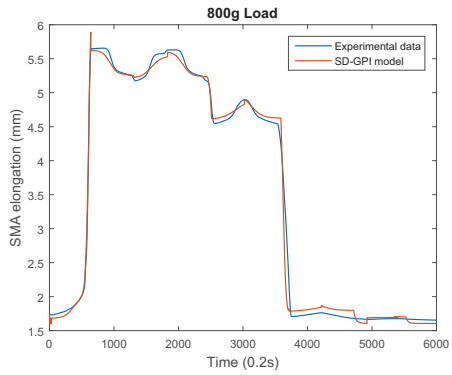

Figure 4.39: SD-GPI model at 800g load.

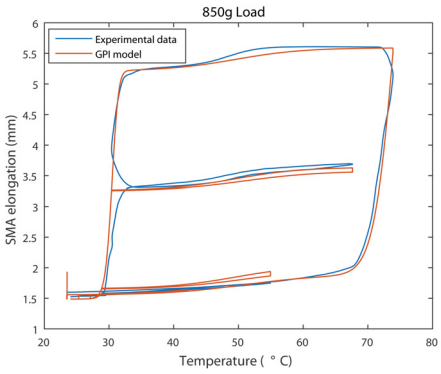

Figure 4.40: SD-GPI loop at 850g load.

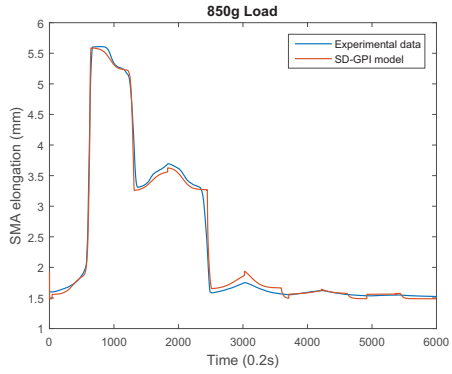

Figure 4.41: SD-GPI model at 850g load.

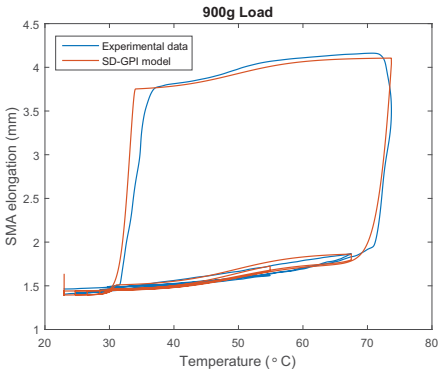

Figure 4.42: SD-GPI loop at 900g load.

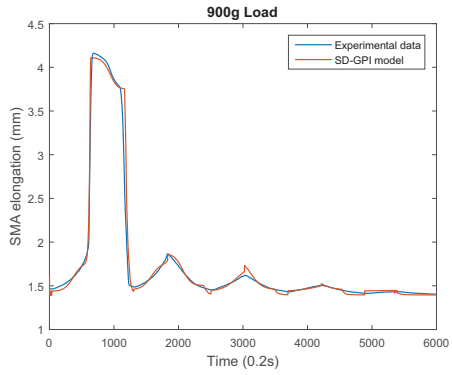

Figure 4.43: SD-GPI model at 900g load.

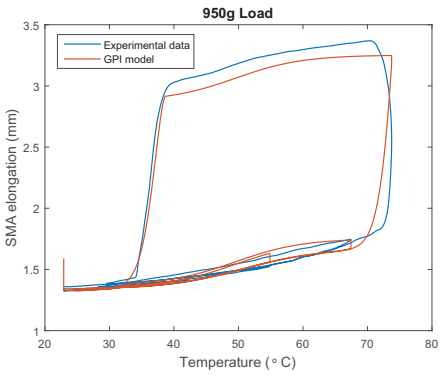

Figure 4.44: SD-GPI loop at 950g load.

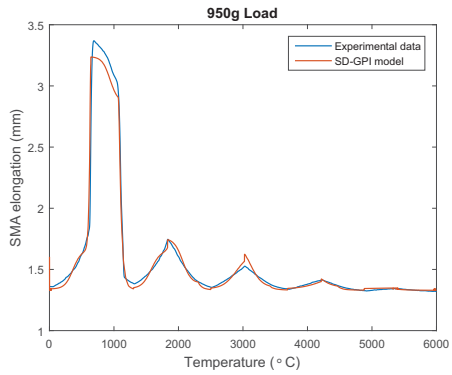

Figure 4.45: SD-GPI model at 950g load.

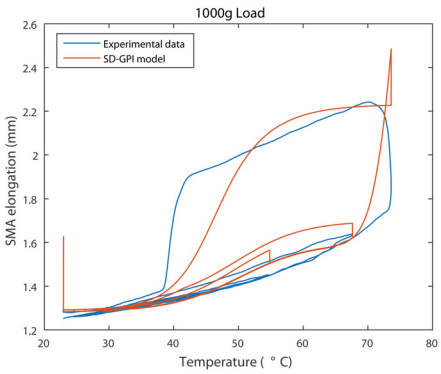

Figure 4.46: SD-GPI loop at 1000g load.

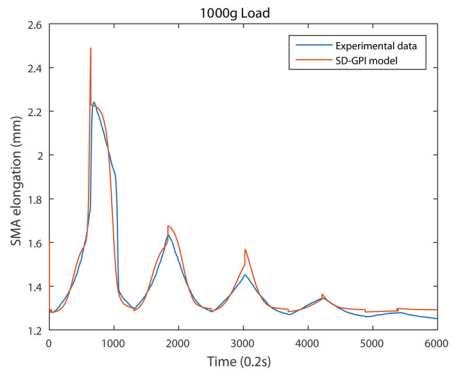

Figure 4.47: SD-GPI model at 1000g load.

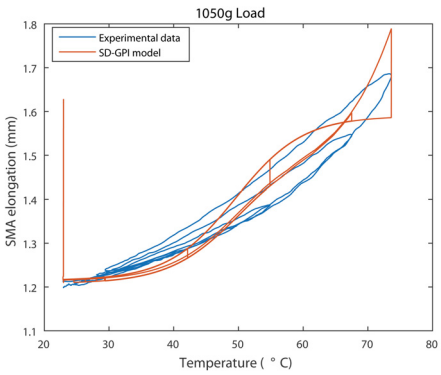

Figure 4.48: SD-GPI loop at 1050g load.

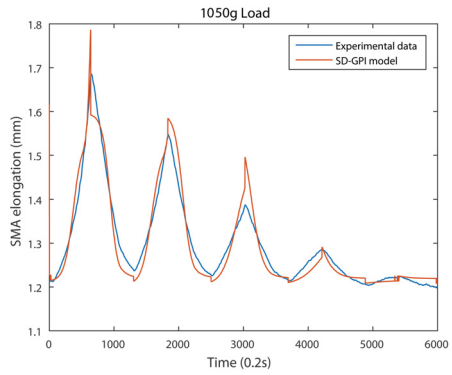

Figure 4.49: SD-GPI model at 1050g load.

The SD-GPI model errors are obtained, and the model 1 errors are shown in Figures 4.50 to 4.53.

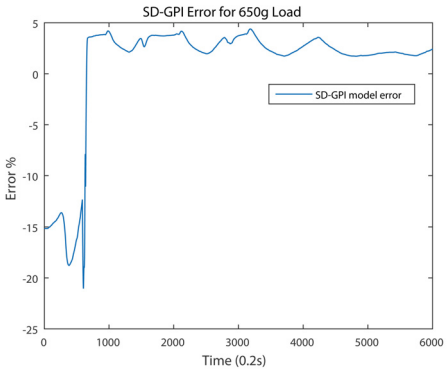

Figure 4.50: SD-GPI error at 650g load.

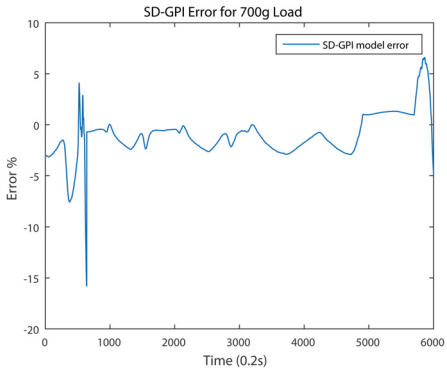

Figure 4.51: SD-GPI error at 700g load.

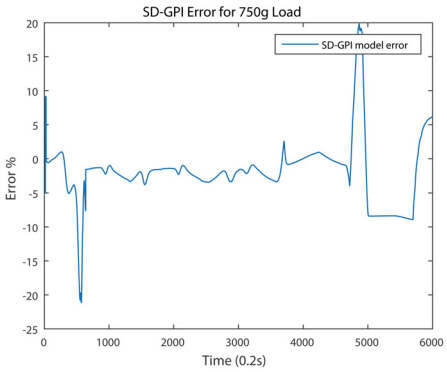

Figure 4.52: SD-GPI error at 750g load.

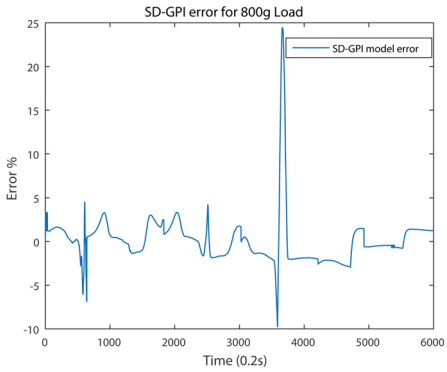

Figure 4.53: SD-GPI error at 800g load.

Meanwhile, the SD-GPI model 2 errors are shown in Figures 4.54 to 4.59.

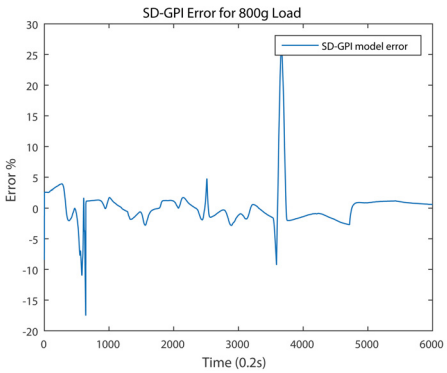

Figure 4.54: SD-GPI error at 800g load.

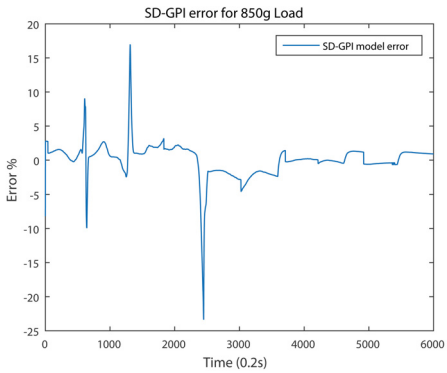

Figure 4.55: SD-GPI error at 850g load.

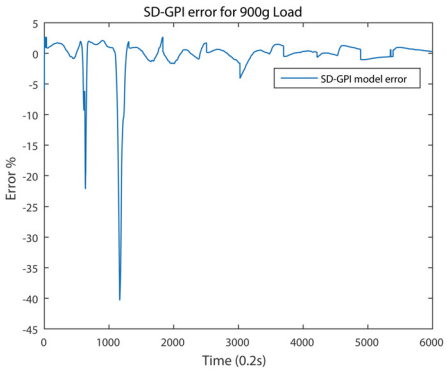

Figure 4.56: SD-GPI error at 900g load.

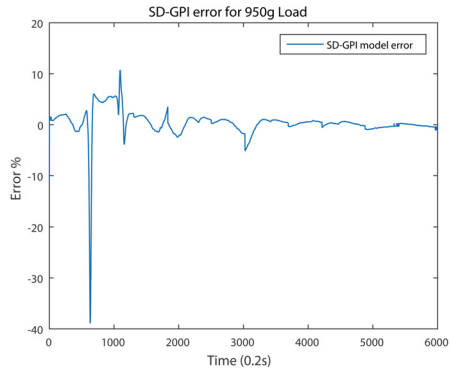

Figure 4.57: SD-GPI error at 950g load.

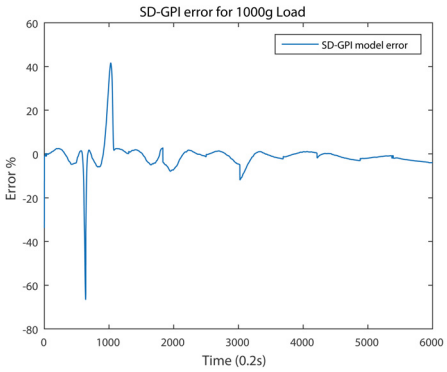

Figure 4.58: SD-GPI error at 1000g load.

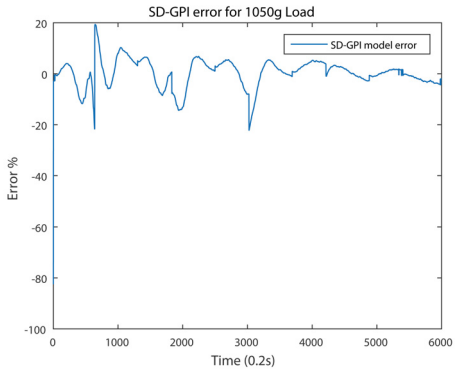

Figure 4.59: SD-GPI error at 1050g load.

The SD-GPI model errors are analyzed, and the errors statistics are shown in Tables 4.7 and 4.8.

Table 4.7: SD-GPI model 650g to 800g load error statistic (%).

Load	Maximum	Minimum	Mean	Standard Deviation	Range
650g	4.3969	-21.0483	0.7802	5.7356	4.3718
700g	6.5830	-15.8284	-1.0526	2.0920	3.7954
750g	19.8405	-21.1826	-1.9419	4.6271	3.9046
800g	25.6855	-17.5208	0.1044	3.1864	4.0012

Table 4.8: SD-GPI model 800g to 1050g error statistic (%).

Load	Maximum	Minimum	Mean	Standard Deviation	Range
800g	24.4635	-9.8012	0.1514	2.9712	4.0012
850g	16.9805	-23.3759	0.0494	2.5375	4.0850
900g	2.6978	-40.3314	-0.2996	3.5874	2.7587
950g	10.7289	-38.8960	0.3698	2.9366	2.0483
1000g	41.5960	-66.6035	-1.0516	6.1647	0.9896
1050g	19.3954	-82.4672	0.1885	5.5808	0.4883

From the statistics, the maximum and minimum values of the SD-GPI model errors are high. This only happens at the beginning of the simulation and in a very short period. Overall, the SD-GPI model can provide a prediction with errors lower than 5%. Thus, the SD-GPI models developed are verified to be capable of predicting the Nitinol hysteresis behavior.

4.3 Thermoelectric Module and SMAs Heat Flow Model

The heat flow between the Nitinol and TEM in the wrist system are illustrated in Figure 4.60.

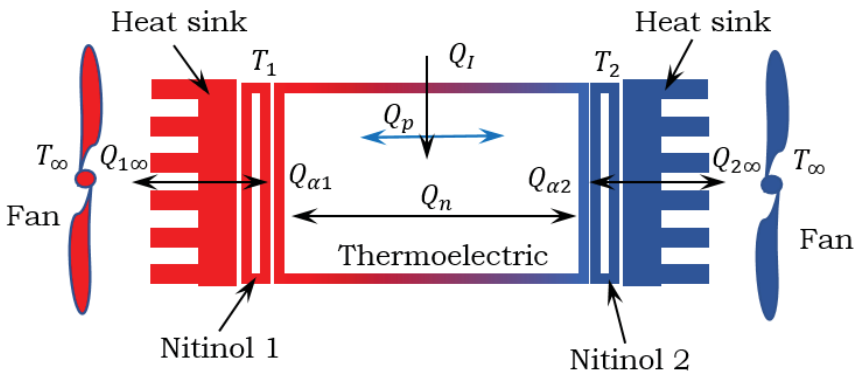

Figure 4.60: Heat flow in the TEM-SMA system.

The heat is transferred through surface convection onto the Nitinol. A thin flat bar-shaped Nitinol is ideal for this application. However, Nitinol available in the market is mainly round shaped wires. Thus, the Nitinol wire with the diameter of 0.25mm is selected to provide a large surface area over volume for fast thermal transfer. Assumption is made that the temperature variation between the TEM surface and Nitinol is small and global energy is balanced. The heat fluxes on the hot and cool Nitinol can be defined in Equations 4.7 and 4.8 as shown by [100], [101], [102] and [103].

$$\frac{dQ_{T_1}}{dt} = Q_n + Q_\tau + Q_p + Q_I + Q_\infty \tag{4.7}$$

and

$$\frac{dQ_{T_2}}{dt} = Q_n + Q_\tau + Q_p + Q_I + Q_\infty, \tag{4.8}$$

where Q_n, Q_τ, Q_p, Q_I and Q_∞ are the conduction heat flow, Thomson effect, Peltier effect, resistive heat generation and heat lost to the environment, respectively. From Equations 4.7 and 4.8, the rate of change of T_1 can be defined as

$$\rho C_p \dot{T_1} = k_T \Delta T + \alpha T_1 I - \frac{1}{2}\tau \Delta T I - \frac{1}{2} R I^2 - k_\infty (T_1 - T_\infty) \tag{4.9}$$

and similarly, rate of change of T_2 can be defined as

$$\rho C_p \dot{T_2} = k_T \Delta T + \alpha T_2 I - \frac{1}{2}\tau \Delta T I - \frac{1}{2} R I^2 - k_\infty (T_2 - T_\infty), \tag{4.10}$$

where ρ, C_p, α, τ, K_T and K_∞ are the TEM average density, TEM specific heat at constant pressure, Thomson coefficient, Peltier coefficient, thermal conductance and heat convection to the heat sink and fan, respectively. Equations 4.9 and 4.10 can be rearranged as

$$\rho C_p \dot{T_1} = [(\alpha - \frac{1}{2}\tau) T_1 + \frac{1}{2}\tau T_2)] I - (k_T + k_\infty) T_1 + k_T T_2 + \frac{1}{2} R I^2 + k_\infty T_\infty \tag{4.11}$$

and

$$\rho C_p \dot{T_2} = [(\alpha - \frac{1}{2}\tau) T_2 + \frac{1}{2}\tau T_1)] I - (k_T + k_\infty) T_2 + k_T T_1 + \frac{1}{2} R I^2 + k_\infty T_\infty. \tag{4.12}$$

Equations 4.11 and 4.12 can be further written as

$$\dot{T_1} = [(K_{\alpha\tau} T_1 + K_\tau T_2)] I - K_{T\infty} T_1 + K_T T_2 + K_R I^2 + K_\infty \tag{4.13}$$

and

$$\dot{T}_2 = [(K_{\alpha\tau}T_2 + K_\tau T_1)]I - K_{T\infty}T_2 + K_T T_1 + K_R I^2 + K_\infty, \tag{4.14}$$

where

$$\begin{aligned}
K_{\alpha\tau} &= \tfrac{2\alpha-\tau}{2\rho C_p} \\
K_\tau &= \tfrac{\tau}{2\rho C_p} \\
K_{T\infty} &= \tfrac{K_T+K_\infty}{\rho C_p} \\
K_T &= \tfrac{K_T}{\rho C_p} \\
K_R &= \tfrac{R}{2\rho C_p} \\
K_\infty &= \tfrac{K_\infty T_\infty}{\rho C_p}.
\end{aligned} \tag{4.15}$$

The model parameters can be identified experimentally. The experiment is required to verify the small variation of temperatures between the TEM surface and Nitinol, while the parameters of Equations 4.11 and 4.12 are identified via the experiment data.

4.3.1 Thermoelectric Module and SMAs Heat Flow Experimental Setup

To measure the temperature of the Nitinol wires, the average temperature on both sides of the Nitinols are acquired. Figure 4.61 shows the placement of K-type thermocouple temperature sensors to acquire the temperature of the Nitinol wires. The same arrangement is applied to both sides of the TEM, where temperature sensors 1 and 3 are placed before the SMA and temperature sensors 2 and 4 are placed after the SMA. The TEM generates excess heat from the resistance heating. To avoid over heating of the TEM, heat sinks and fans are added to both sides of the TEM. The thermal conductive paste is applied evenly and as thin as possible to improve thermal convection but not to add on too much thermal capacity.

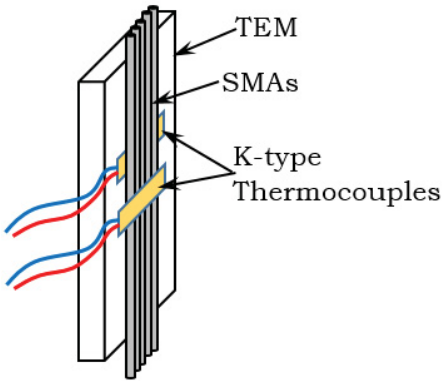

Figure 4.61: Temperature sensor placement to measure the Nitinol temperature.

The experiment setup for verifying the TEM model is shown in Figure 4.62. A 12 volts sinusoidal input signals with frequencies 1/128Hz, 1/64Hz, 1/32Hz, 1/16Hz, 1/8Hz, 1/4Hz, 1/2Hz and 1Hz are applied to the TEM, and the temperatures before and after the Nitinols are recorded via the dSPACE data acquisition system.

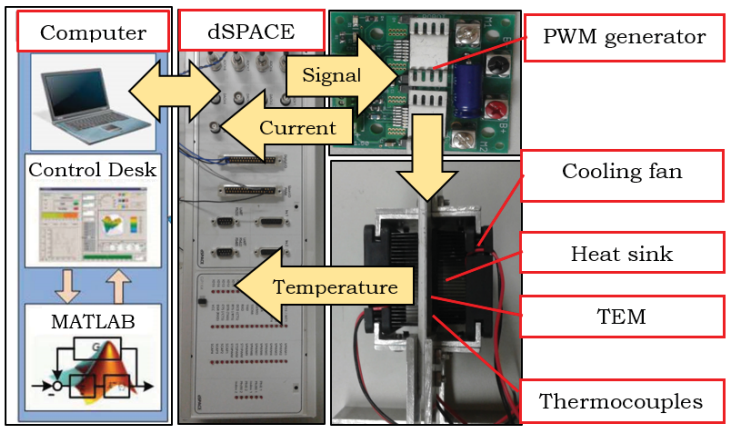

Figure 4.62: Experimental setup for TEM model verification.

Figures 4.63 to 4.78 show the Nitinols temperatures obtained from the average temperatures before and after the Nitinols.

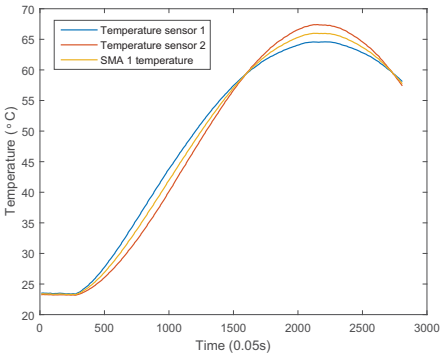

Figure 4.63: Nitinol 1 temperature at 1/128Hz.

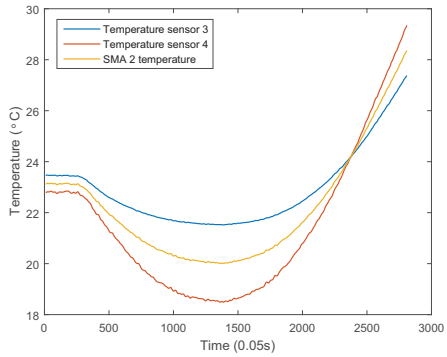

Figure 4.64: Nitinol 2 temperature at 1/128Hz.

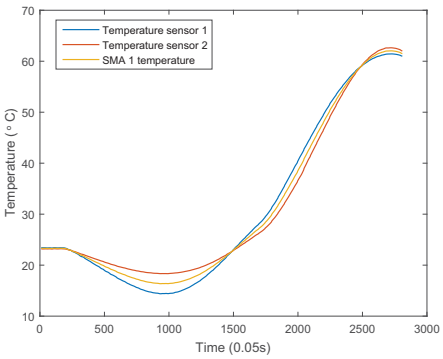

Figure 4.65: Nitinol 1 temperature at 1/64Hz.

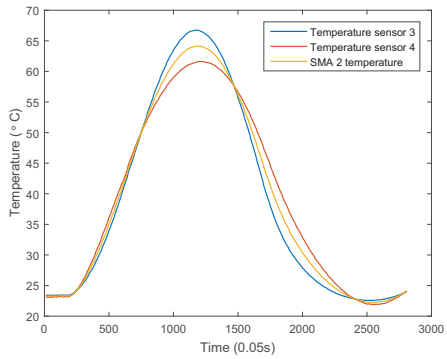

Figure 4.66: Nitinol 2 temperature at 1/64Hz.

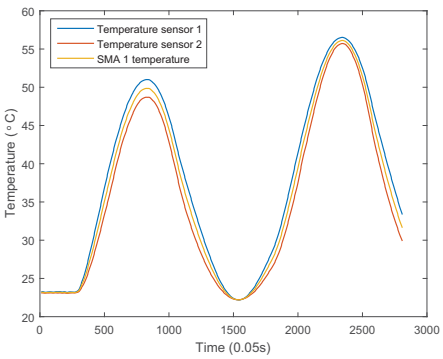

Figure 4.67: Nitinol 1 temperature at 1/32Hz.

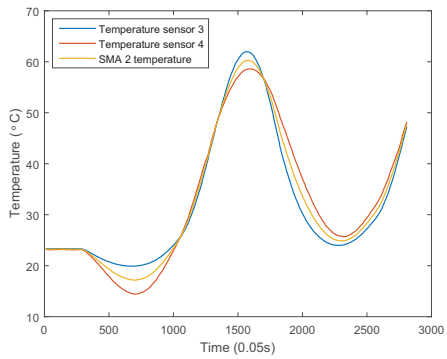

Figure 4.68: Nitinol 2 temperature at 1/32Hz.

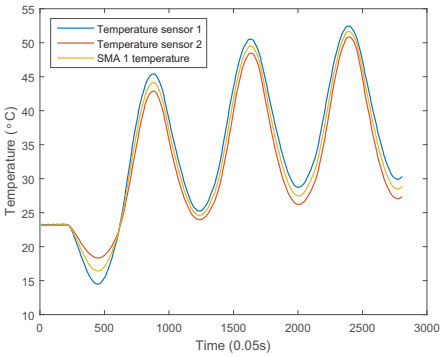

Figure 4.69: Nitinol 1 temperature at 1/16Hz.

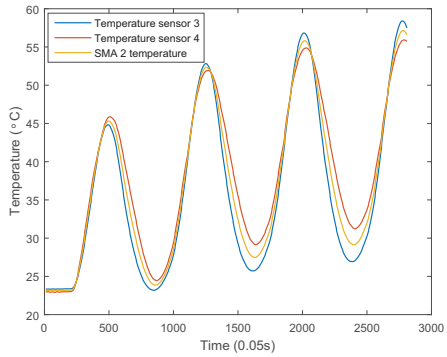

Figure 4.70: Nitinol 2 temperature at 1/16Hz.

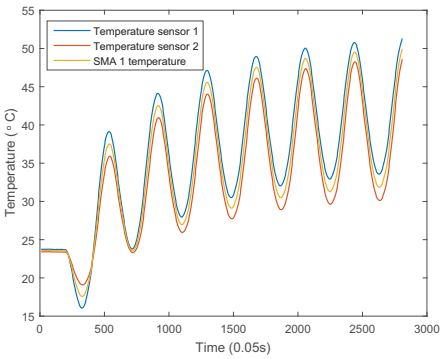

Figure 4.71: Nitinol 1 temperature at 1/8Hz.

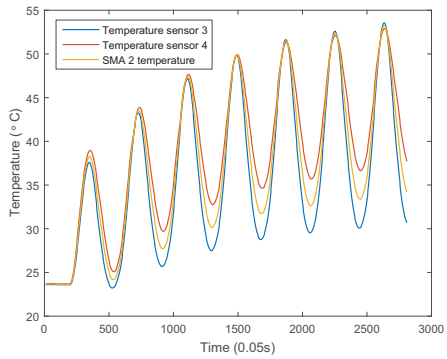

Figure 4.72: Nitinol 2 temperature at 1/8Hz.

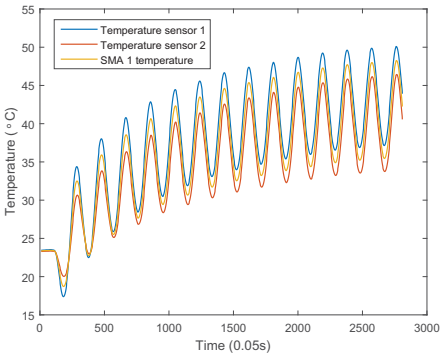

Figure 4.73: Nitinol 1 temperature at 1/4Hz.

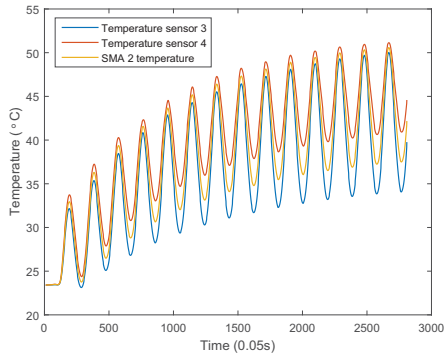

Figure 4.74: Nitinol 2 temperature at 1/4Hz.

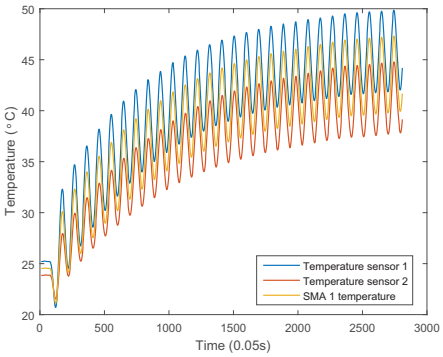

Figure 4.75: Nitinol 1 temperature at 1/2Hz.

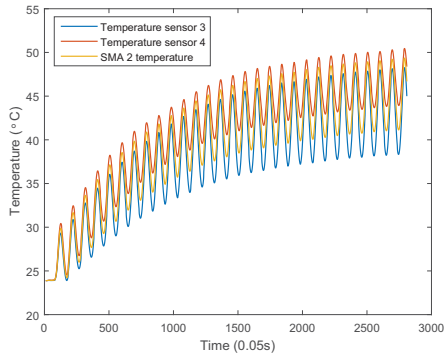

Figure 4.76: Nitinol 2 temperature at 1/2Hz.

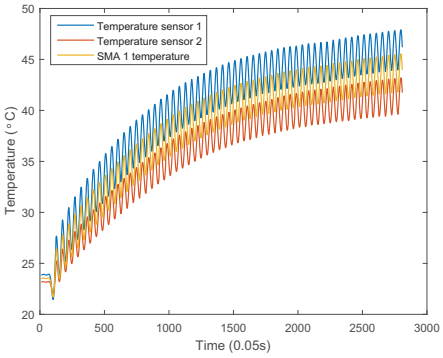

Figure 4.77: Nitinol 1 temperature at 1Hz.

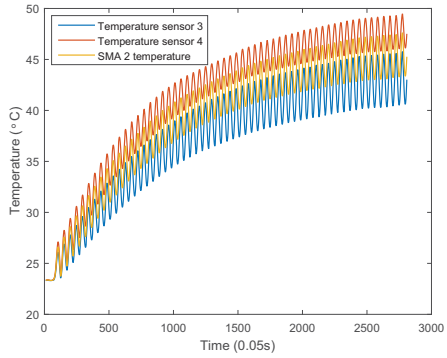

Figure 4.78: Nitinol 2 temperature at 1Hz.

4.3.2 Heat Flow Model Parameters Identification and Verification

Using Equations 4.11 and 4.12, the Runge-Kutta 4th order numerical integration is used in the Matlab lsqcurvefit() as the fitting function. All initial points values are set as 1 to obtain all the parameters in Equations 4.11 and 4.12. The best-fitted model parameters are shown in Table 4.9.

Table 4.9: TEM and SMA heat flow model parameters.

Parameters	T1	T2
$K_{\alpha\tau}$	-0.004472	0.006162
K_{τ}	-0.004207	0.003737
$K_{T\infty}$	0.052345	0.056143
K_{TC}	0.028312	0.036657
K_{I}	0.012524	0.012524
K_{∞}	0.615142	0.615142

The TEM SMA heat flow fitted models are shown in Figures 4.79 to 4.94

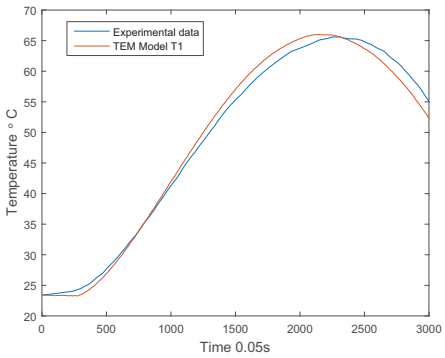

Figure 4.79: TEM SMA heat model at 1/128Hz.

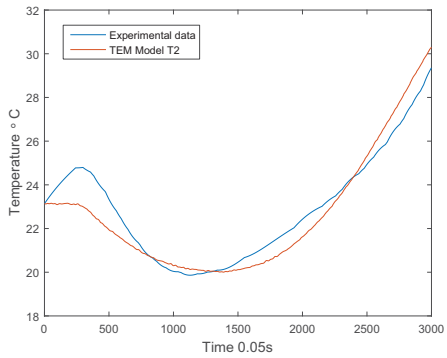

Figure 4.80: TEM SMA heat model at 1/128Hz.

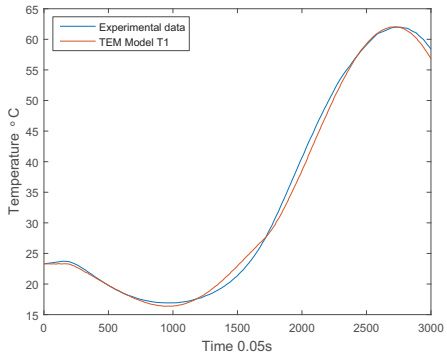

Figure 4.81: TEM SMA heat model at 1/64Hz.

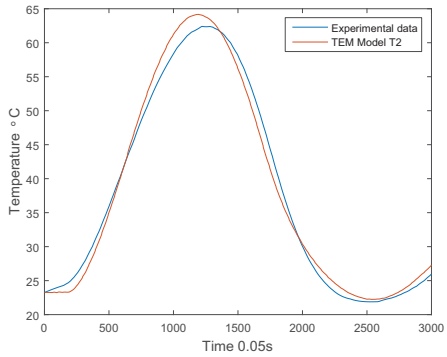

Figure 4.82: TEM SMA heat model at 1/64Hz.

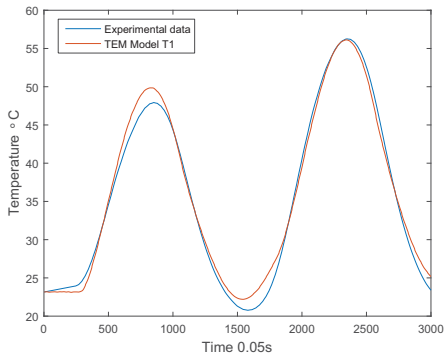

Figure 4.83: TEM SMA heat model at 1/32Hz.

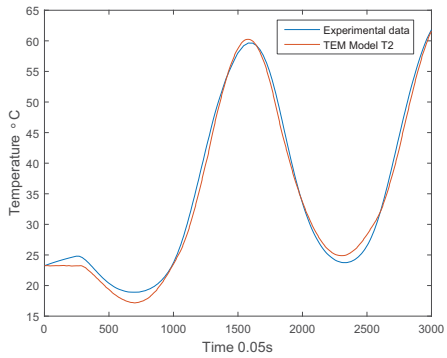

Figure 4.84: TEM SMA heat model at 1/32Hz.

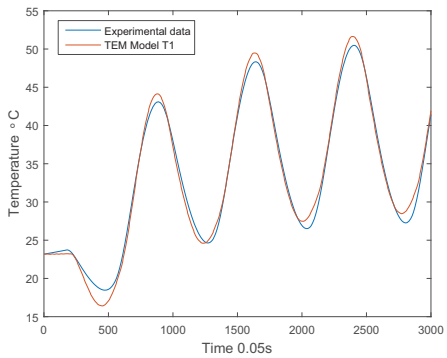

Figure 4.85: TEM SMA heat model at 1/16Hz.

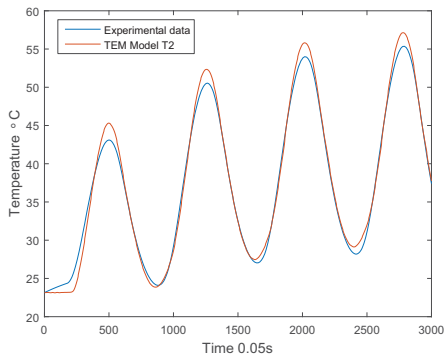

Figure 4.86: TEM SMA heat model at 1/16Hz.

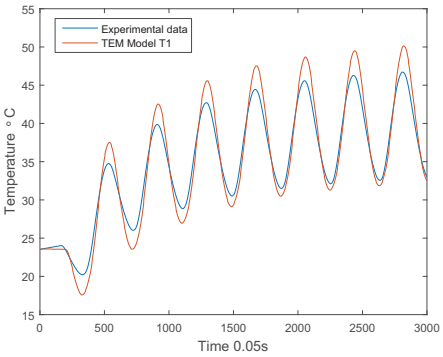

Figure 4.87: TEM SMA heat model at 1/8Hz.

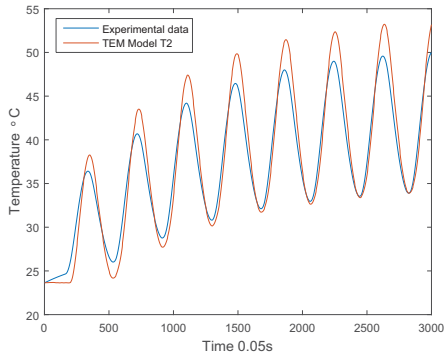

Figure 4.88: TEM SMA heat model at 1/8Hz.

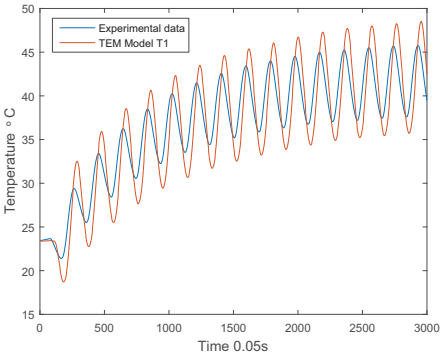

Figure 4.89: TEM SMA heat model at 1/4Hz.

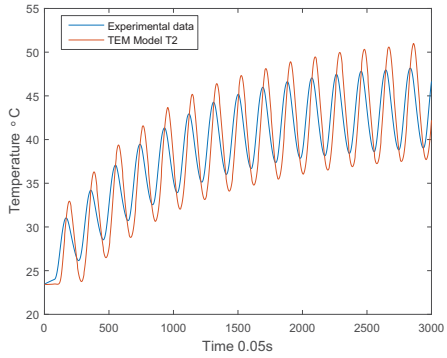

Figure 4.90: TEM SMA heat model at 1/4Hz.

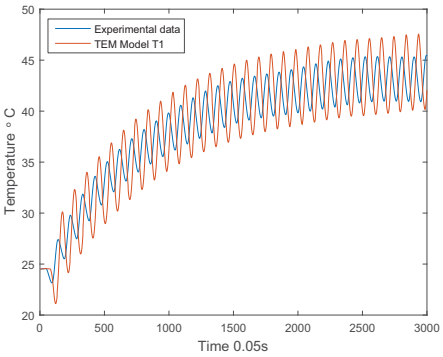

Figure 4.91: TEM SMA heat model at 1/2Hz.

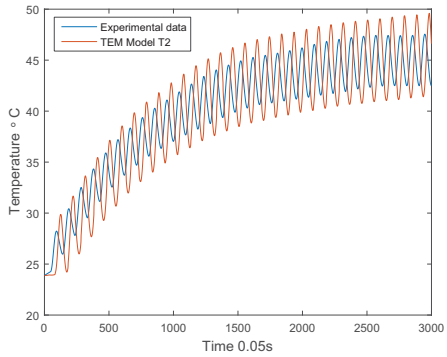

Figure 4.92: TEM SMA heat model at 1/2Hz.

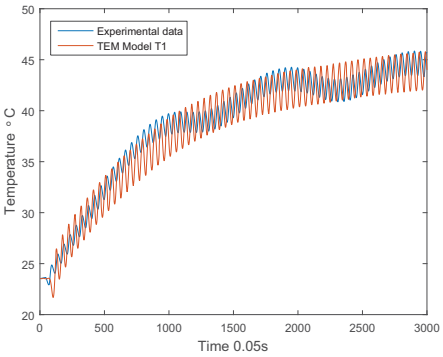

Figure 4.93: TEM SMA heat model at 1Hz.

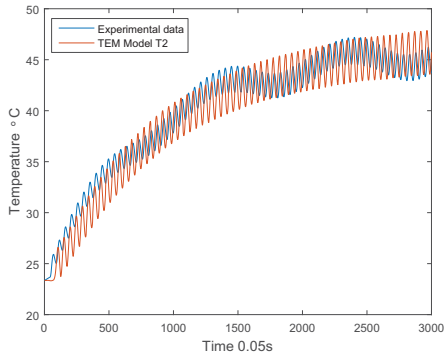

Figure 4.94: TEM SMA heat model at 1Hz.

The TEM SMA heat flow model errors are computed, and the error statistics are shown in Table 4.10.

Table 4.10: TEM and SMA heat flow model errors statistic.

Frequency	Maximum	Minimum	Mean	Standard Diviation
1/128Hz	4.4325	-6.7019	-0.2503	2.5716
1/64Hz	6.8349	-7.5688	-0.1880	3.0502
1/32Hz	5.9191	-5.4399	-0.2900	2.7860
1/16Hz	5.7159	-5.6717	0.3957	2.3225
1/8Hz	9.6616	-7.4732	0.7799	4.3393
1/4Hz	12.2255	-13.2598	-0.8758	7.4266
1/2Hz	14.0336	-14.6713	-0.3529	8.7010
1Hz	8.2108	-8.5754	-1.0697	3.8593

The error distributions of the TEM SMA heat flow models are shown in Figures 4.95 to 4.102. These figures and Table 4.10 show the model maximum error at 7.57% for frequency 1/128Hz to 1/16 Hz and a maximum error of 14.67% for frequency 1/8Hz to 1Hz. Furthermore, the errors for frequency 1/128Hz to 1/16 Hz have small standard deviation values, with mainly fall under 5%. This concludes that the TEM SMA heat flow models have good accuracy at low frequency from 1/128Hz to 1/16 Hz. However, the accuracy of the model

falls within 15% for frequency from 1/8Hz to 1Hz.

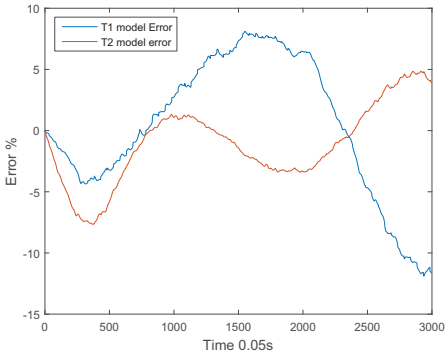

Figure 4.95: TEM SMA heat model errors at 1/128Hz.

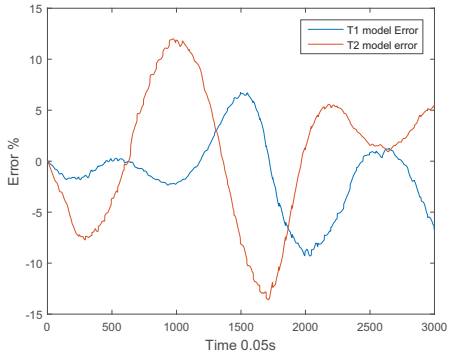

Figure 4.96: TEM SMA heat model errors at 1/64Hz.

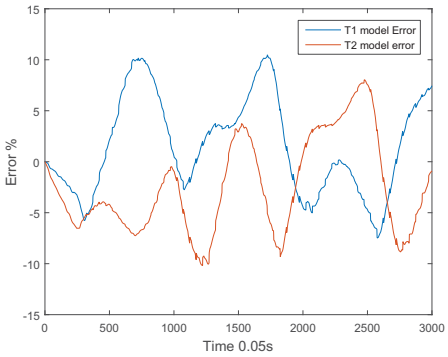

Figure 4.97: TEM SMA heat model errors at 1/32Hz.

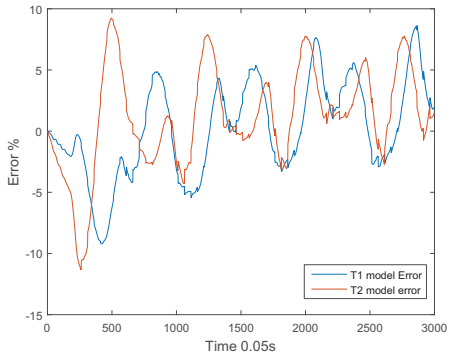

Figure 4.98: TEM SMA heat model errors at 1/16Hz.

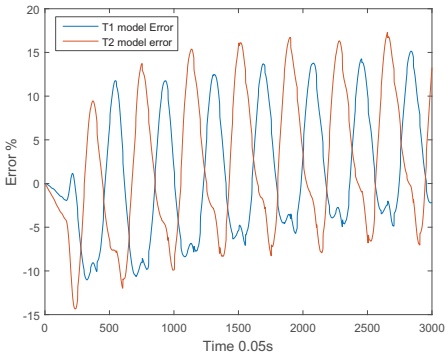

Figure 4.99: TEM SMA heat model errors at 1/8Hz.

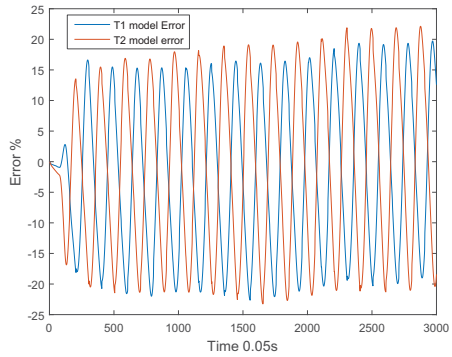

Figure 4.100: TEM SMA heat model errors at 1/4Hz.

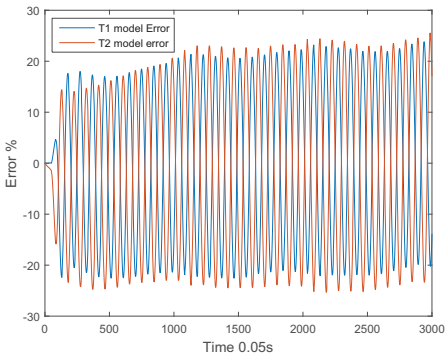

Figure 4.101: TEM SMA heat model errors at 1/2Hz.

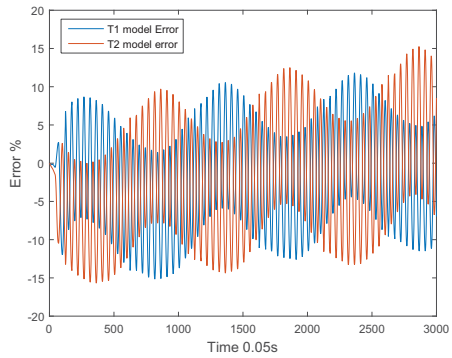

Figure 4.102: TEM SMA heat model errors at 1Hz.

4.4 Artificial Wrist joint Model

By mimicking the human wrist joint, Nitinol wires are configured in antagonistic pair by attaching one end to a pulley as opposing each other. This provides a revolute movement resembling the artificial wrist joint. The schematic drawing of the artificial wrist joint system is shown in Figure 4.103. The AM wrist joint system dynamic model can be described as

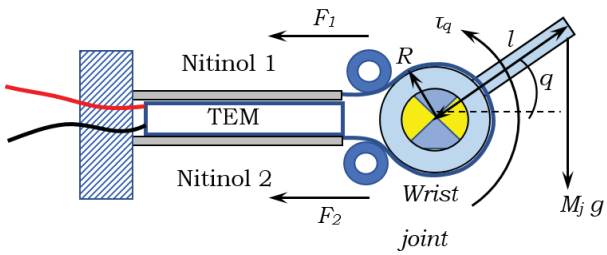

Figure 4.103: Wrist joint system schematic drawing.

Equation 4.16 [29] [30].

$$I_\omega \ddot{q} = F_1 R - F_2 R - M_j g l \cos q - \tau_f, \tag{4.16}$$

where q, I_ω, R, M_j, l, τ_f are the joint angle, joint moment inertia, pulley radius, effective joint mass, distance from the center of mass to the joint and frictional moment of joint, respectively. The frictional moment can be modeled by the coulomb-viscous model as $\tau_f = Sign(\dot{q})[M_{DF} + C_{DF}|\dot{q}|]$ if $\tau_{drv} > \tau_{sf}$ else $\tau_f = \tau_{sf}$ if $\tau_{drv} < \tau_{sf}$, where M_{DF}, C_{DF} and τ_{sf} are the dynamic friction moment, dynamic friction coefficient and static friction moment, respectively [88].

During actuation, the Nitinols pair work in opposing each other. Therefore, their strains are opposite to each other as per Equation 4.17.

$$\varepsilon_1 = -\varepsilon_2. \tag{4.17}$$

From Equation 4.16, the resultant actuation torque from the Nitinols pair can be described by

$$I_m \ddot{q} + M_e g l \cos q + \tau_f = (F_1 - F_2)R = (\sigma_1 - \sigma_2) A_{wire} r_{pulley}, \tag{4.18}$$

where σ_1 and σ_2 are the stress of Nitinol 1 and Nitinol 2, respectively; and A_{wire} is the total cross-sectional area of the Nitinol wires.

4.5 Concluding Remarks

In this chapter, the SD-GPI model for Nitinol has been developed and verified. The superelastic hysteresis loop shape is about 8 times larger than the normal hysteresis loop shape. Due to the GPI model hysteresis shape is governed by the envelop function. Thus, the SD-GPI hysteresis model is formulated by modifying the envelop function parameters into functions of stress. The development of the SD-GPI model is very important for the utilization of the Nitinol in the realization of the artificial wrist joint system. The SD-GPI provides the prediction of the Nitinol hysteretic behavior under superelastic conditions. To the best knowledge of the author, the development of stress-dependent hysteresis model of the Nitinol using invertible phenological approach including the superelastic condition is a novel work. The SD-GPI model is also verified via the error analysis with majority errors below 5%.

Following the development of SD-GPI model, the TEM SMA heat model has been adopted from researchers and modified to include the heat convection to the environment. The TEM SMA heat model parameters are obtained via least square curve fitting function in Matlab. To complete the wrist system model, the dynamic of the wrist joint system is also developed. The inverse hysteresis model of Nitinol must be obtained to mitigate Nitinol hysteresis behavior. Therefore, the next chapter will present the development of inverse hysteresis compensator and control systems.

Chapter 5

Control Development of Artificial Wrist System

The highly nonlinear hysteresis behavior of the Nitinol causes difficulty in controlling the SMA AM. This can be solved by obtaining the Nitinol temperature from the corresponding desired stress and strain. However, the numerical approach to obtain the Nitinol temperature involves heavy computational processes which could lead to a delay of the control signal. Meanwhile, the advantage of adopting the SD-GPI phenological modeling approach is that the inverse model can be analytically obtained to mitigate the hysteresis effect. Even though, the inverse compensator may result in partial mitigate of hysteresis effect and cause a residual error.

The adaptive controller is proposed to control the wrist to overcome the residual error from the inverse hysteresis compensation and the payload uncertain. The adaptive controller is developed based on the back-stepping approach. Due to the use of TEM as the heating and cooling element, a secondary feedback linearized controller as compensator is developed to linearize the input and output of the TEM. The control systems developed are verified via numerical simulations and presented in this Chapter.

5.1 Inverse-based Feedback Adaptive Control

The proposed inverse-based feedback adaptive control system consists of the inverse hysteresis compensator, the adaptive controller and the TEM linearized compensator. The overall control system is illustrated in Figure 5.1, where q is the output angle, and the subscript d denotes the desired signal.

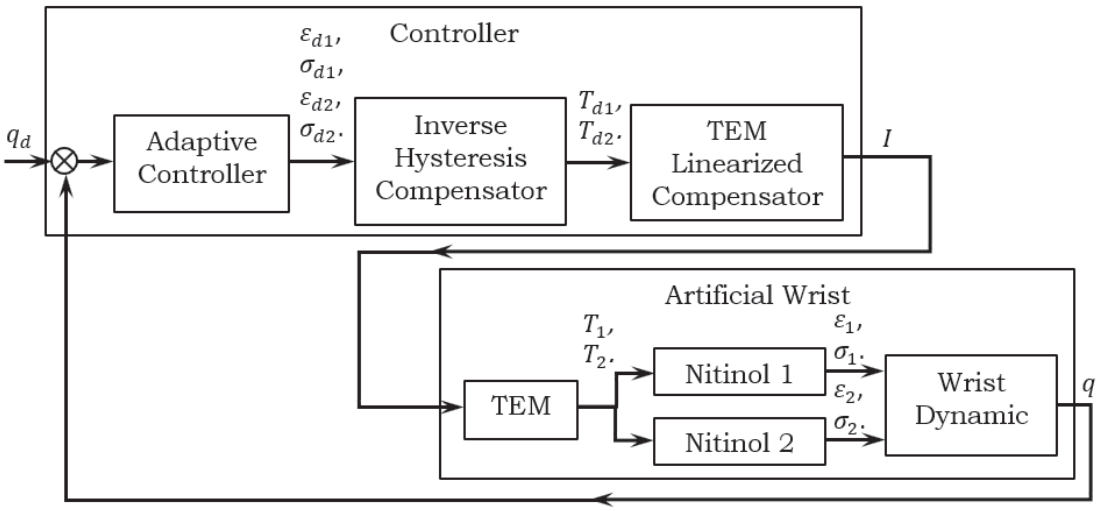

Figure 5.1: Wrist joint adaptive control system.

5.1.1 Inverse Stress-Dependent Generalized Prandtl-Ishlinksii Model

Based on the classical Prandtl-Ishlinksii hysteresis model, the continuous and rate-independent play operator was defined as Equations 5.1 and 5.4 as per [104] [105] [106], where the input $v(t)$ is represented by a space of piecewise monotone continuous function as $v(t) \in C_m[0, t_E]$, and let $0 = t_0 < t_1 < \cdots < t_N = t_E$ as a partition of $[0, t_E]$. Thus, function v is monotone at each of the sub-intervals $[t_i, t_{i+1}]$.

$$F_r[v](0) = f_r(v(0), 0) = w(0) \tag{5.1}$$

$$w(t) = F_r[v](t) = f_r(v(t), F_r[v](t_i)); \tag{5.2}$$

$$\tag{5.3}$$

for $t_i < t \leq t_{i+1}$ and $0 \leq i \leq N-1$, where

$$f_r(v, w) = max(v - r, min(v + r, w)). \tag{5.4}$$

[66], [69], [94], [104], [106], [107], [108] and others had presented the analytically inverse GPI model. Based on Equation 3.21 in Chapter 3, if the inverse envelop function $\gamma_l^{-1}, \gamma_r^{-1} : R \to R$ exists, which is similar to Equation 3.69, the inverse of the SD-GPI can be rewritten as

$$T(k) = y_{p\gamma}^{-1}[v](t) = \begin{cases} \gamma_l^{-1}(y_p[v](t)), if\ \dot{v} \geq 0 \\ \gamma_r^{-1}(y_p[v](t)), if\ \dot{v} \leq 0, \end{cases} \tag{5.5}$$

where $v = [\varepsilon_d, \sigma_d]$ is the desired input that consists of the desired strain and stress. Therefore, the inverse model can be written as

$$y_p^{-1}(t) = p_0^{-1}[\varepsilon_d, \sigma_d](t) + \int_0^R p(\hat{r}) F_{\hat{r}}[\varepsilon_d, \sigma_d] d\hat{r}. \tag{5.6}$$

Defining the inverse model in the discrete form with the input as $[\varepsilon_d, \sigma_d] \in C[0, Y]$ that having a step size of h. The discrete input is corresponding to an interval of k where $k = 0, 1, 2, ..., N = Y/h$. Thus, the discrete inverse SD-GPI model can be rewritten as Equations 5.7 and 5.8.

$$T(k) = y_{p\gamma}^{-1}[\varepsilon_d, \sigma_d](k) = \gamma^{-1}(p_0^{-1}[\varepsilon_d, \sigma_d](k) + \sum_{i=1}^{n} \hat{p}_i F_{\hat{r}_i}[\varepsilon_d, \sigma_d](k) \tag{5.7}$$

$$\gamma^{-1}[v](k) = \begin{cases} \gamma_l^{-1}([v](k)), if\ \dot{v} \geq 0 \\ \gamma_r^{-1}([v](k)), if\ \dot{v} \leq 0. \end{cases} \tag{5.8}$$

The inverse SD-GPI parameters can be analytically obtained based on the classical Prandtl-Ishlinskii model as Equations 5.9 to 5.11

$$p_0^{-1} = \frac{1}{p_0}, \tag{5.9}$$

$$\hat{r}_j = qr_j + \sum_{i=1}^{j-1} p_i(r_j - r_i), \tag{5.10}$$

$$\hat{p}_j = \frac{p_j}{(q + \sum_{i=1}^{j} p_i)(q + \sum_{i=1}^{j-1} p_i)}. \tag{5.11}$$

5.2 Inverse Stress-Dependent Generalized Prandtl-Ishlinskii Model Parameters Identification and Model Verification

The analytical inverse SD-GPI parameters obtained analytically are substituted into the inverse model for verification. Further adjustment is to ensure the accuracy of the inverse model. The adjustment is carried out by subjecting the desired input into the inverse model, and the output of the inverse model is then substituted into the SD-GPI model. The inverse model is adjusted to achieve the output from the SD-GPI to be the same as the desired input that is subjected to the inverse model. To do that, the desired linear inputs v and the compensated outputs u relationship is established as linear input-output functions at various load conditions using linear regression of the maximum and minimum points as per Equation 5.12. The load σ dependent is formulated in linear input-output functions gradient a_l and the intercept c_l as quadratic functions.

$$v = a_l u + c_l, \tag{5.12}$$

where the quadratic functions of a_l and c_l are shown in Equations 5.13 and 5.14

$$a_l = p_{a1}\sigma^2 + p_{a2}\sigma + p_{a3}, \tag{5.13}$$

$$c_l = p_{c1}\sigma^2 + p_{c2}\sigma + p_{c3}, \tag{5.14}$$

and the values of p_{ai} and p_{ci}, $i = 1, 2, 3$, are shown in Table 5.1.

Table 5.1: Linear regression parameters p_{ai} and p_{ci}.

Parameter	value	Parameter	value
p_{a1}	-0.64718	p_{c1}	9.90320
p_{a2}	0.91117	p_{c2}	-13.81200
p_{a3}	-0.23825	p_{a3}	4.58000

The desired input v and the SD-GPI parameters are used in the Matlab lsqcurvefit() function to yield the best-fitted inverse hysteresis model parameters. Overall, the inverse model parameters obtained show very small variation compared to the SD-GPI model parameters. However, there is no obvious step change of the inverse parameters through the load variation. Therefore, the inverse hysteresis model parameters are formulated as quadratic spline equations with the stress as a variable. Letting the P_{INV} as the inverse parameters, the quadratic relation based on the load can be written as

$$P_{INV} = p_{INV1}\sigma^2 + p_{INV2}\sigma + p_{INV3}. \tag{5.15}$$

The quadratic parameters for p_{INVi}, $i = 1, 2, 3$ which correspond to the load range, are shown in Tables 5.2 and 5.3.

Table 5.2: Inverse model parameters for loads range from 650g to 850g.

	650-750			750-850		
Parameter	p_{INV1}	p_{INV2}	p_{INV3}	p_{INV1}	p_{INV2}	p_{INV3}
a_0	-0.00399	0.10953	0.00000	-0.00022	0.03359	0.00000
a_1	0.00000	0.57479	0.53314	0.00000	-1.16486	1.19386
a_2	-0.00107	-0.05670	0.00000	-0.00254	-0.09409	0.00000
a_3	-0.00090	0.05202	0.00000	-0.00007	0.01778	0.00000
b_0	-0.00094	0.06662	0.00000	-0.00040	0.04015	0.00000
b_1	0.03304	0.00000	0.67651	0.04234	0.00000	0.73922
b_2	-0.00089	-0.05398	0.00000	-0.00041	-0.03745	0.00000
b_3	0.00297	-0.05430	0.00000	-0.00011	0.02124	0.00000
ρ	0.00000	-1.86374	0.76622	0.00000	-1.47130	0.87512
τ	-0.00032	0.03106	0.00000	0.00072	-0.03170	0.00000
c	0.00000	-8.85029	0.75229	0.00000	-8.85135	1.00588

Table 5.3: Inverse model parameters for loads range from 850g to 1050g.

	850-950			950-1050		
Parameter	p_{INV1}	p_{INV2}	p_{INV3}	p_{INV1}	p_{INV2}	p_{INV3}
a_0	-0.00002	0.01106	0.00000	-0.00001	0.00566	0.00000
a_1	0.00495	0.00000	0.89945	-0.02295	0.39234	0.00000
a_2	-0.00015	-0.03913	0.00000	-0.00001	-0.00564	0.00000
a_3	-0.00001	0.00922	0.00000	-0.00001	0.00565	0.00000
b_0	-0.00020	0.00000	0.95011	0.00000	-0.30509	1.05000
b_1	1.29363	0.00000	0.53020	0.00839	0.00000	0.99879
b_2	-0.00147	-0.07631	0.00000	-0.00673	-0.17647	0.00000
b_3	-0.01268	0.48855	0.00000	-0.00526	0.00000	1.05976
ρ	0.00000	0.22752	0.89063	0.01325	0.00000	0.99954
τ	-0.00041	0.04044	0.00000	-0.00186	0.09778	0.00000
c	0.00000	-7.49261	1.00053	0.00000	0.35634	0.99684

Figures 5.2 to 5.19 show the numerical simulation results of the Nitinol hysteresis loop compensator and the inverse compensated output.

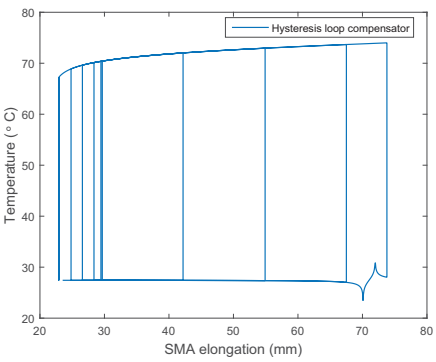

Figure 5.2: Hysteresis loop compensator at 650g load.

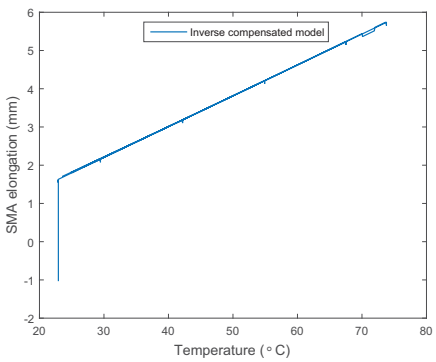

Figure 5.3: Inverse compensated result at 650g load.

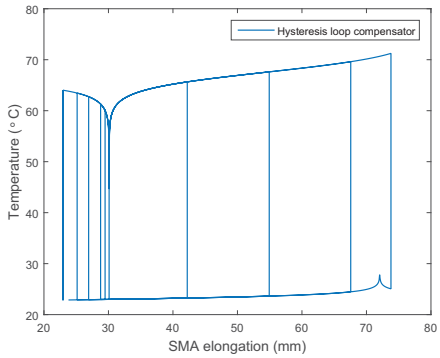

Figure 5.4: Hysteresis loop compensator at 700g load.

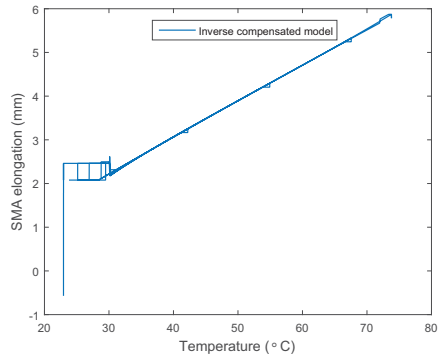

Figure 5.5: Inverse compensated result at 700g load.

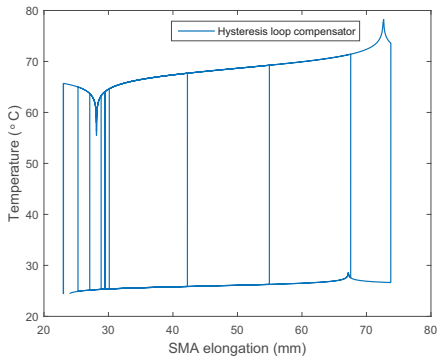

Figure 5.6: Hysteresis loop compensator at 750g load.

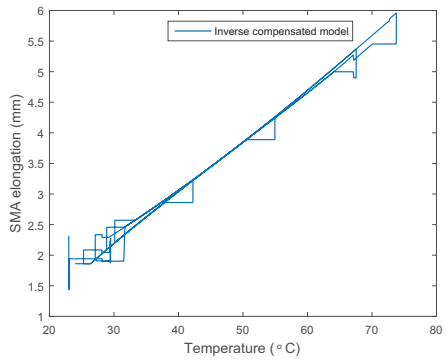

Figure 5.7: Inverse compensated result at 750g load.

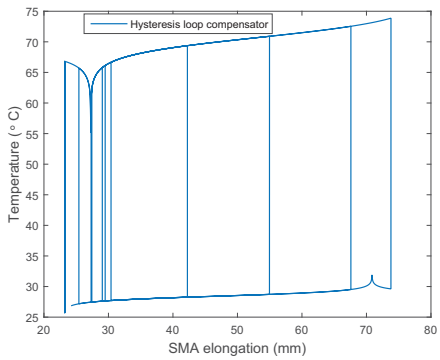

Figure 5.8: Hysteresis loop compensator at 800g load.

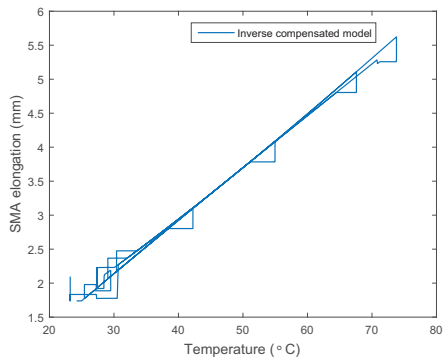

Figure 5.9: Inverse compensated result at 800g load.

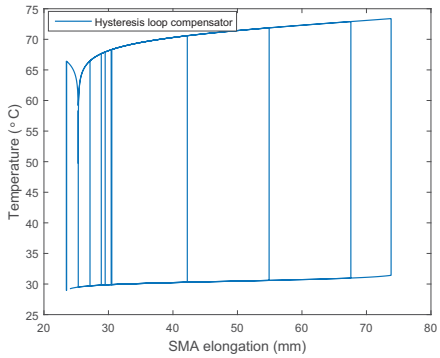

Figure 5.10: Hysteresis loop compensator at 850g load.

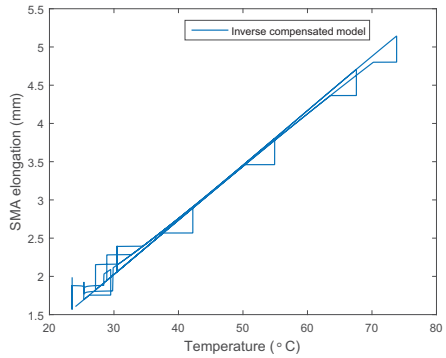

Figure 5.11: Inverse compensated result at 850g load.

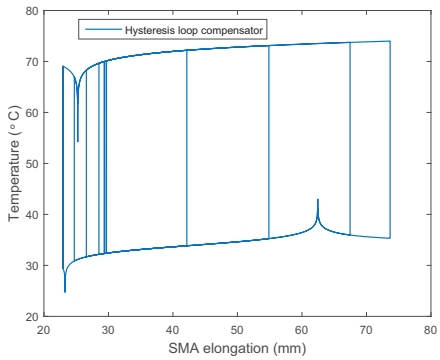

Figure 5.12: Hysteresis loop compensator at 900g load.

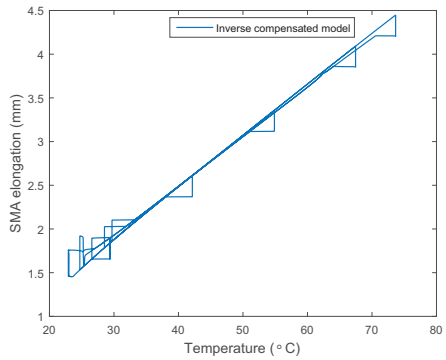

Figure 5.13: Inverse compensated result at 900g load.

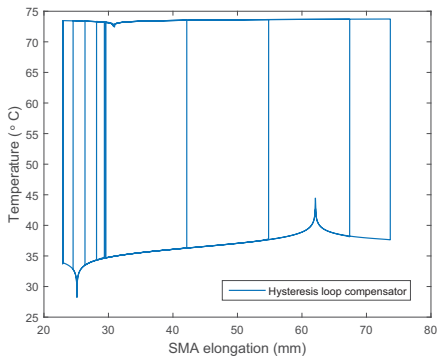

Figure 5.14: Hysteresis loop compensator at 950g load.

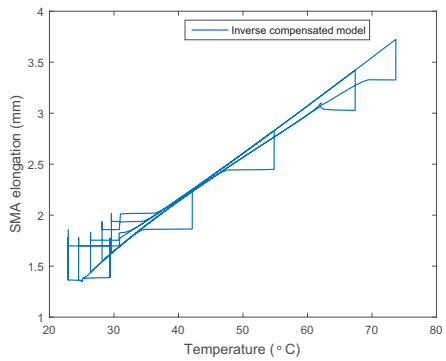

Figure 5.15: Inverse compensated result at 950g load.

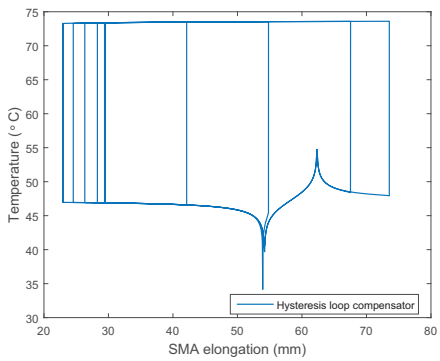

Figure 5.16: Hysteresis loop compensator at 1000g load.

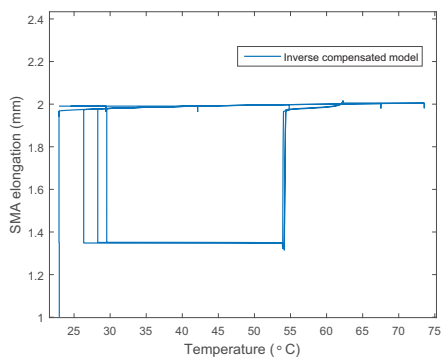

Figure 5.17: Inverse compensated result at 1000g load.

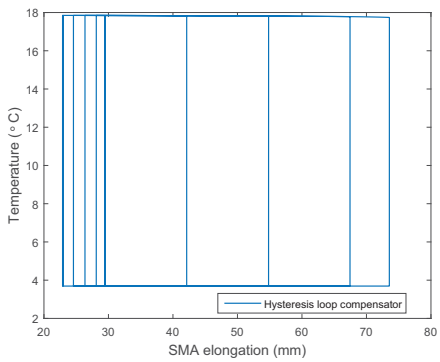

Figure 5.18: Hysteresis loop compensator at 1050g load.

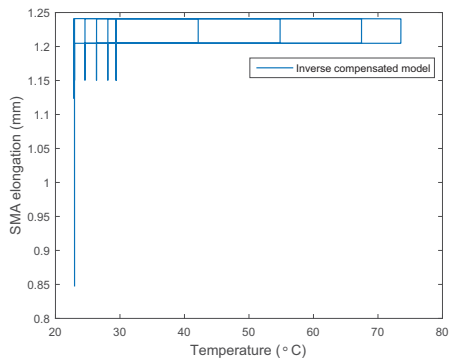

Figure 5.19: Inverse compensated result at 1050g load.

The simulation results show that the Nitinol inverse hysteresis compensator has provided a good compensation with small residual errors for hysteresis at loads from 650g to 950g. However, the inverse compensation shows large residual errors at loads from 1000g to 1050g.

5.2.1 Inverse Compensation Error

The wrist system error needs to be formulated for the implementation of model-based adaptive control. However, the actual compensator residual error is unable to be formulated. Therefore, an estimation of the error is formulated to predict the error. In [109] [110] [111]

[112] the inverse compensator error $e(t)$ can be derived as

$$\begin{aligned} e &= v - u = v - y_{p\gamma} \circ \hat{y}_{p\gamma}^{-1}(t) \\ &= (1 - \eta'(0))v(t) - \int_0^\infty \eta''(r) R_r[v](t) dr, \end{aligned} \tag{5.16}$$

where $\hat{y}_{p\gamma}^{-1}[v](t) = \hat{p}_0^{-1}(0)v(t) + \int_0^\infty (\hat{q}^{-1})''(s) F_s[v](t) ds$ is the estimated inverse compensator and using the composition corollary, $y_m \circ \hat{y}_M^{-1}(t) = \eta'(0)v(t) + \int_0^\infty \eta''(r) F_r[v](t) dr$ in [109], the sum of play operators $\int_0^\infty \eta''(r) R_r[v](t) dr$ can be written in the form of stop operator as Equations 5.17 and 5.18 to settle the unbounded condition in the control development.

$$F_r[v](t) = v - E_r[v](t), \tag{5.17}$$

where $E_r[v](t)$ is the stop operator as

$$\begin{aligned} E_r(0) &= e_r(v(0) - \omega_{-1}), \\ E_r(t) &= e_r(v(t) - v(t_i) + E_r[v](t_i)), \end{aligned} \tag{5.18}$$

where for $t_i < t \leq t_{i+1}$,$0 \leq i < N - 1$,

$$e_r(v) = min(r, max(-r, v)), \tag{5.19}$$

and ω_{-1} is the initial value. By replacing the play operator as stop operator, the inverse compensator error can be defined as Equation 5.20.

$$e = [1 - \eta'(0) - \int_0^\infty \eta''(r) dr] v(t) + \int_0^\infty \eta''(r) E_r[v](t) dr. \tag{5.20}$$

Equation 5.20 is further simplified to the form of

$$e \triangleq (1 - X_0)v(t) + d[v](t), \tag{5.21}$$

where $X_0 = \eta'(0) + \int_0^\infty \eta''(r) dr$ and $d[v](t) = \int_0^\infty \eta''(r) E_r[v](t) dr$. In [113] authors showed that the boundness of $d[v](t)$ can be achieved as $|d[v](t)| \leq D$ with D as a bounded constant. Thus, if the inverse compensator error is a bounded uncertainty, it is therefore can be eliminated by the adaptive controller.

5.2.2 Back-stepping Adaptive Control Design

Besides the compensator error, dealing with the uncertain load carried by the hand is also one of the causes of implementing the adaptive controller in the wrist. The adaptive control is developed using back-stepping approach. First, the inverse compensated output is expressed as

$$u_i(t) = X_0 v_i(t) - d[v_i](t), \tag{5.22}$$

where the subscript $i = 1, 2$ represents the Nitinol 1 and 2. Based on Equation 4.18, assuming the friction is small, the dynamic system can be defined in the state as

$$\begin{aligned} \dot{x}_1 &= \dot{q} \\ \dot{x}_2 &= \ddot{q} = \Delta F \tfrac{R}{I_\omega} - \tfrac{M_e g l}{I_\omega} cos(q) - \tfrac{\tau_f(\dot{q})}{I_\omega} \\ &= \phi\theta + \tfrac{R}{I_\omega}[(\beta_{01} v_1(t) - d[v_1](t)) - (\beta_{02} v_2(t) - d[v_2](t))], \end{aligned} \tag{5.23}$$

where $\theta = M_e$ is the uncertainty and $\phi = \frac{glcos(q)}{I_\omega}$ is the coefficient. The force difference ΔF is contributed by the Nitinol 1 and Nitinol 2. Using the desired angular joint movement q_d, the system tracking errors can be defined as

$$\begin{aligned} z_1 &= q - q_d \\ z_2 &= \dot{q} - \dot{q}_d - \alpha_1 \\ \alpha_1 &= -C_1 z_1, \end{aligned} \tag{5.24}$$

where $\beta_{01} = b_1 X_0$, $\beta_{02} = b_2 X_0$, $d_{b1}[v_{c1}](t) = b \cdot d[v_{c1}](t)$ and $d_{b2}[v_{c2}](t) = b \cdot d[v_{c2}](t)$. Meanwhile $D_{b1} = b \cdot D_1$ and $D_{b2} = b \cdot D_2$ denote the boundness of $d_{b1}[v_{c1}](t)$ and $d_{b2}[v_{c2}](t)$, respectively. θ, β_{01}, β_{02}, D_{b1} and D_{b2} are unknown parameters. Estimators are derived and used online to eliminate the uncertain errors. The $\hat{\theta}$, $\hat{\delta}_1$ $\hat{\delta}_2$, $\hat{D}_{b1}$ and $\hat{D}_{b2}$ denote the estimated values. The errors of the estimated values are derived as the true values minus the estimated values and

are written as

$$\begin{aligned}
\tilde{\theta} &= \theta - \hat{\theta}, \\
\tilde{\beta}_{01} &= \beta_{01} - \hat{\beta}_{01}, \\
\tilde{\beta}_{02} &= \beta_{02} - \hat{\beta}_{02}, \\
\tilde{D}_{b1} &= D_{b1} - \hat{D}_{b1}, \\
\tilde{D}_{b2} &= D_{b2} - \hat{D}_{b2},
\end{aligned} \tag{5.25}$$

where β_{01} and β_{02} in Equation 5.25 also can be written as Equation 5.26

$$\begin{aligned}
\tfrac{\beta_{01}}{\hat{\beta}_{01}} &= \tfrac{\tilde{\beta}_{01}}{\hat{\beta}_{01}} + 1, \\
\tfrac{\beta_{02}}{\hat{\beta}_{02}} &= \tfrac{\tilde{\beta}_{02}}{\hat{\beta}_{02}} + 1.
\end{aligned} \tag{5.26}$$

The following Lyapunov candidate is considered

$$V_1 = \frac{1}{2} z_1^2 \tag{5.27}$$

and the time derivative yields

$$\begin{aligned}
\dot{V}_1 &= z_1 \dot{z}_1 \\
&= z_1 (z_2 + \alpha_1) \\
&= -C_1 z_1^2 + z_1 z_2.
\end{aligned} \tag{5.28}$$

Considering the Lyapunov candidate for z_2

$$V_2 = V_1 + \frac{1}{2} z_2^2, \tag{5.29}$$

the time derivative yields

$$\begin{aligned}
\dot{V}_2 &= \dot{V}_1 + z_2 \dot{z}_2 \\
&= -C_1 z_1^2 + z_1 z_2 + z_2 \dot{z}_2.
\end{aligned} \tag{5.30}$$

Using Equation 5.23, $\dot{z}_2$ also can be written as

$$\begin{aligned}\dot{z}_2 &= \ddot{q} - \ddot{q}_d - \dot{\alpha}_1 \\ &= \tfrac{R}{I_\omega}\beta_{01}v_1(t) - \tfrac{R}{I_\omega}\beta_{02}v_2(t) - \tfrac{R}{I_\omega}d_{b1}[v_1](t) \\ &\quad + \tfrac{R}{I_\omega}d_{b2}[v_2](t) - \phi\theta - \ddot{q}_d - \dot{\alpha}_1,\end{aligned} \tag{5.31}$$

and proposing the adaptive controller obtains

$$\begin{aligned}v_1(t) &= \tfrac{I_\omega}{2R}\tfrac{1}{\hat{\beta}_{01}}v_{1c}(t), \\ v_{1c}(t) &= -C_2z_2 - z_1 + \dot{\alpha} + \ddot{q}_d + \phi\hat{\theta} - 2sgn(z_2)\hat{D}_{b1}, \\ v_2(t) &= -\tfrac{I_\omega}{2R}\tfrac{1}{\hat{\beta}_{02}}v_{2c}(t), \\ v_{2c}(t) &= -C_2z_2 - z_1 + \dot{\alpha} + \ddot{q}_d + \phi\hat{\theta} - 2sgn(z_2)\hat{D}_{b2}.\end{aligned} \tag{5.32}$$

With the proposed control input as per Equations 5.32 and 5.26, $\dot{z}_2$ can be redefined as

$$\begin{aligned}\dot{z}_2 &= -C_2z_2 - z_1 - \phi\tilde{\theta} - \tfrac{R}{I_\omega}d_{b1}[v_1](t) + \tfrac{R}{I_\omega}d_{b2}[v_2](t) \\ &\quad + \tfrac{\tilde{\beta}_{01}}{2\hat{\beta}_{01}}(v_{1c}(t)) + \tfrac{\tilde{\beta}_{02}}{2\hat{\beta}_{02}}(v_{2c}(t)) - sgn(z_2)\hat{D}_{b1} - sgn(z_2)\hat{D}_{b2}.\end{aligned} \tag{5.33}$$

Defining a new lyapunov candidate as

$$V_3 = V_2 + \frac{1}{2\Gamma_a}\tilde{\theta}^2 + \frac{1}{2\Gamma_{b1}}\tilde{\beta}_{01}^2 + \frac{1}{2\Gamma_{b2}}\tilde{\beta}_{02}^2 + \frac{1}{2\Gamma_{D1}}\tilde{D}_{b1}^2 + \frac{1}{2\Gamma_{D2}}\tilde{D}_{b2}^2, \tag{5.34}$$

the time derivative of V_3 yields

$$\begin{aligned}\dot{V}_3 &= \dot{V}_2 + \tfrac{1}{\Gamma_a}\tilde{\theta}\dot{\hat{\theta}} + \tfrac{1}{\Gamma_{b1}}\tilde{\beta}_{01}\dot{\hat{\beta}}_{01} + \tfrac{1}{\Gamma_{b2}}\tilde{\beta}_{02}\dot{\hat{\beta}}_{02} + \tfrac{1}{\Gamma_{D1}}\tilde{D}_{b1}\dot{\hat{D}}_{b1} + \tfrac{1}{2\Gamma_{D2}}\tilde{D}_{b2}\dot{\hat{D}}_{b1} \\ &= -C_1z_1^2 + z_1z_2 + z_2\dot{z}_2 + \tfrac{1}{\Gamma_a}\tilde{\theta}\dot{\hat{\theta}} + \tfrac{1}{\Gamma_{b1}}\tilde{\beta}_{01}\dot{\hat{\beta}}_{01} + \tfrac{1}{\Gamma_{b2}}\tilde{\beta}_{02}\dot{\hat{\beta}}_{02} + \tfrac{1}{\Gamma_{D1}}\tilde{D}_{b1}\dot{\hat{D}}_{b1} + \tfrac{1}{\Gamma_{D2}}\tilde{D}_{b2}\dot{\hat{D}}_{b1}.\end{aligned} \tag{5.35}$$

Substituting Equation 5.33 into 5.36 yields

$$
\begin{aligned}
\dot{V}_3 &= -C_1 z_1^2 - C_2 z_2^2 + \tfrac{\tilde{\theta}}{\Gamma_a}(\dot{\hat{\theta}} - z_2 \Gamma_a \phi) \\
&\quad + \tfrac{\tilde{\beta}_{01}}{\Gamma_{b1}}\big(\dot{\hat{\beta}}_{01} + \tfrac{\Gamma_{01}}{2\hat{\beta}_{01}} z_2 v_{1c}(t)\big) + \tfrac{\tilde{\beta}_{02}}{\Gamma_{b2}}\big(\dot{\hat{\beta}}_{02} + \tfrac{\Gamma_{02}}{2\hat{\beta}_{02}} z_2 v_{2c}(t)\big) \\
&\quad + \tfrac{1}{\Gamma_{d1}} \tilde{D}_{b1} \dot{\hat{D}}_{b1} - |z_2| \hat{D}_{b1} - z_2 \tfrac{R}{I_\omega} d_{b1}[v_1](t) \\
&\quad + \tfrac{1}{\Gamma_{d2}} \tilde{D}_{b2} \dot{\hat{D}}_{b2} + |z_2| \hat{D}_{b2} + z_2 \tfrac{R}{I_\omega} d_{b2}[v_2](t) \\
&\leq -C_1 z_1^2 - C_2 z_2^2 + \tfrac{\tilde{\theta}}{\Gamma_a}(\dot{\hat{\theta}} - z_2 \Gamma_a \phi) \\
&\quad + \tfrac{\tilde{\beta}_{01}}{\Gamma_{b1}}\big(\dot{\hat{\beta}}_{01} + \tfrac{\Gamma_{01}}{2\hat{\beta}_{01}} z_2 v_{1c}(t)\big) + \tfrac{\tilde{\beta}_{02}}{\Gamma_{b2}}\big(\dot{\hat{\beta}}_{02} + \tfrac{\Gamma_{02}}{2\hat{\beta}_{02}} z_2 v_{2c}(t)\big) \\
&\quad + \tfrac{1}{\Gamma_{d1}} \tilde{D}_{b1} \dot{\hat{D}}_{b1} - |z_2| \tilde{D}_{b1} - |z_2| |\tfrac{R}{I_\omega} d_{b1}[v_1](t)| \\
&\quad + \tfrac{1}{\Gamma_{d2}} \tilde{D}_{b2} \dot{\hat{D}}_{b2} + |z_2| \tilde{D}_{b2} + |z_2| |\tfrac{R}{I_\omega} d_{b2}[v_2](t)| \\
&\leq -C_1 z_1^2 - C_2 z_2^2 + \tfrac{\tilde{\theta}}{\Gamma_a}(\dot{\hat{\theta}} - z_2 \Gamma_a \phi) \\
&\quad + \tfrac{\tilde{\beta}_{01}}{\Gamma_{b1}}\big(\dot{\hat{\beta}}_{01} + \tfrac{\Gamma_{01}}{2\hat{\beta}_{01}} z_2 v_{1c}(t)\big) + \tfrac{\tilde{\beta}_{02}}{\Gamma_{b2}}\big(\dot{\hat{\beta}}_{02} + \tfrac{\Gamma_{02}}{2\hat{\beta}_{02}} z_2 v_{2c}(t)\big) \\
&\quad + \tfrac{1}{\Gamma_{d1}} \tilde{D}_{b1} (\dot{\hat{D}}_{b1} - |z_2| \Gamma_{d1}) \\
&\quad + \tfrac{1}{\Gamma_{d2}} \tilde{D}_{b2} (\dot{\hat{D}}_{b2} + |z_2| \Gamma_{d2}) \\
\dot{V}_3 &\leq -C_1 z_1^2 - C_2 z_2^2.
\end{aligned}
\tag{5.36}
$$

Set the adaptive laws as

$$
\begin{aligned}
\dot{\hat{\theta}} &= \Gamma_a z_2 \phi, \\
\dot{\hat{\beta}}_{01} &= -\tfrac{\Gamma_{b1}}{2\hat{\beta}_{01}} z_2 v_{1c}(t), \\
\dot{\hat{\beta}}_{02} &= -\tfrac{\Gamma_{b2}}{2\hat{\beta}_{02}} z_2 v_{2c}(t), \\
\dot{\hat{D}}_{b1} &= \Gamma_{D1} |z_2|, \\
\dot{\hat{D}}_{b2} &= -\Gamma_{D2} |z_2|.
\end{aligned}
\tag{5.37}
$$

Equation 5.36 shows that $V(t)$ is not increasing. This indicates that all z, $\hat{\theta}$, $\hat{\delta}_1$, $\hat{\delta}_2$, $\hat{D}_{b1}$ and $\hat{D}_{b2}$ are bounded. According to the Lasalle-Yoshizawa theorem, this condition will result in the $z_i \to 0 (i = 1, 2)$ as time $t \to \infty$. This also means that $q(t) \to q_d(t)$ as $t \to \infty$.

The adaptive controller simulation is carried out using Matlab Simulink. A fixed load of 1Kg with a distance of 0.09m away from the joint is used as the simulation environment. The model parameters used in the simulation are shown in Table 5.4.

Table 5.4: Model parameters used in the simulation.

Model Parameters	Value	Unit
Distance of mass center to joint	$l = 0.9 \times 10^{-1}$	m
Joint moment inertia	$I_\omega = 1.04346 \times 10^{-4}$	Kgm^2
Gravity	$g = 9.81$	ms^{-2}
Sprocket radius	$R = 0.75 \times 10^{-3}$	m

The input signal is a sinusoidal function of $q_d = 0.524sin(0.1t)$. The actual error of the inverse hysteresis compensator can only be obtained by measuring the hardware. For simulation purposed, the hysteresis effect is assumed to be mitigated. Thus, only the adaptive law of $\dot{\hat{\theta}} = \Gamma_a z_2 \phi$ and the control parameters C_1 and C_2 are utilized. Figures 5.20 and 5.21 show the direct control conceptual design and simulation setup using Matlab Simulink software, respectively. The control parameters are tuned to achieve the best control performance and recorded in Table 5.5. Figure 5.22 is the simulation result that shows the ability of the adaptive controller to track the desired input.

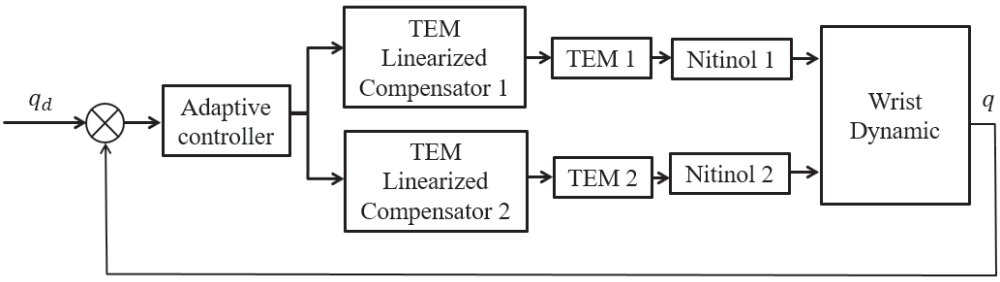

Figure 5.20: Direct Adaptive controller conceptual design.

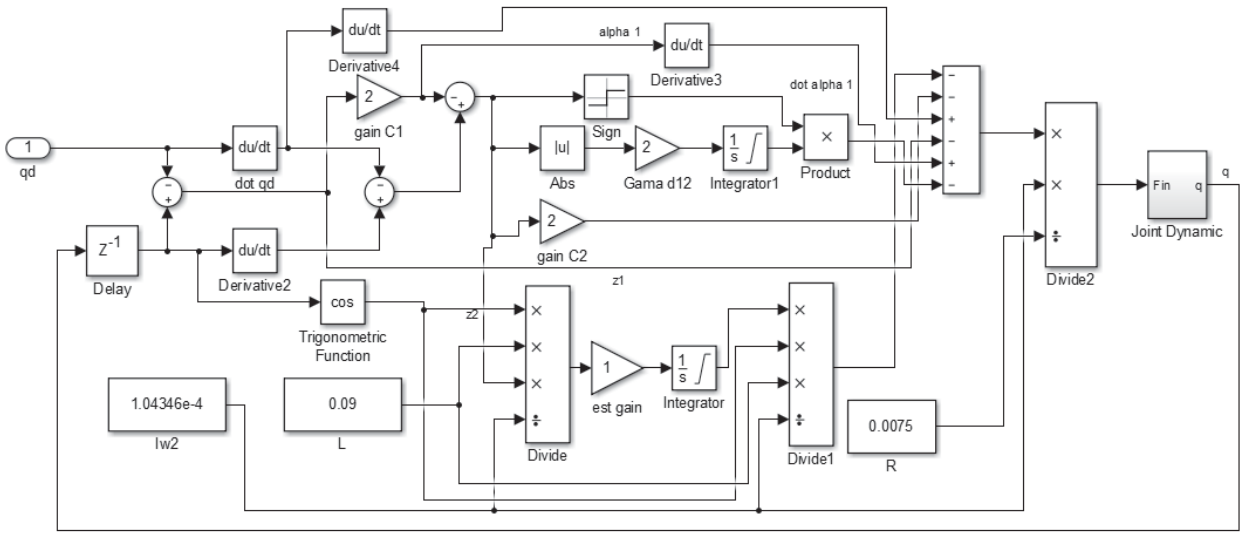

Figure 5.21: Adaptive controller simulation using Matlab Simulink.

Table 5.5: Adaptive controller parameters.

Adaptive Controller Parameters
$C_1 = 2$
$C_2 = 2$
$\Gamma_a = 1$

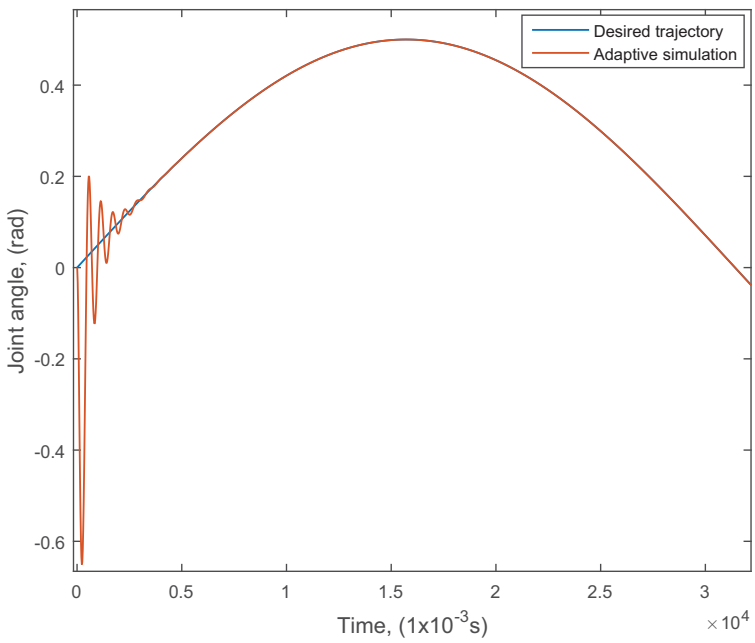

Figure 5.22: Adaptive controller simulation result.

Thermoelectric Feedback Linearized Compensator

The adaptive controller provides the temperature needed to drive the Nitinol to track the desired angular position. Using the feedback linearized control approach, a compensator is developed for the TEM to track the desired temperature generated from the adaptive controller. From Equations 4.13 and 4.14, the state equation of the TEM-SMA can be written as

$$\begin{bmatrix} \dot{T}_1 \\ \dot{T}_2 \end{bmatrix} = \begin{bmatrix} -(k_T + k_\infty & k_t \\ k_t & -(k_T + k_\infty \end{bmatrix} \begin{bmatrix} T_1 \\ T_2 \end{bmatrix} + \begin{bmatrix} (\alpha_2 - \frac{\tau}{2})T_2 + \frac{\tau T_1}{2} & \frac{R_I I}{2} \\ (\alpha_1 - \frac{\tau}{2})T_1 + \frac{\tau T_2}{2} & \frac{R_I I}{2} \end{bmatrix} \begin{bmatrix} I \\ I \end{bmatrix} + \begin{bmatrix} k_\infty T_\infty \\ k_\infty T_\infty \end{bmatrix} \tag{5.38}$$

$$y = \begin{bmatrix} T_1 \\ T_2 \end{bmatrix}$$

and the time derivative of the output can be defined as

$$\dot{y} = \begin{bmatrix} \dot{T}_1 \\ \dot{T}_2 \end{bmatrix}. \tag{5.39}$$

Substituting Equation 5.38 into Equation 5.39 can yield

$$\dot{y} = \begin{bmatrix} -(k_T + k_\infty) & k_t \\ k_t & -(k_T + k_\infty) \end{bmatrix} \begin{bmatrix} T_1 \\ T_2 \end{bmatrix} + \begin{bmatrix} (\alpha_2 - \frac{\tau}{2})T_2 + \frac{\tau T_1}{2} & \frac{R_I I}{2} \\ (\alpha_1 - \frac{\tau}{2})T_1 + \frac{\tau T_2}{2} & \frac{R_I I}{2} \end{bmatrix} \begin{bmatrix} I \\ I \end{bmatrix} + \begin{bmatrix} k_\infty T_\infty \\ k_\infty T_\infty \end{bmatrix}. \tag{5.40}$$

By choosing the input as Equation 5.43, Equation 5.40 can be written as

$$\dot{y} = \begin{bmatrix} T_{1d} - T_1 \\ T_{2d} - T_2 \end{bmatrix} + \begin{bmatrix} \dot{T}_{1d} \\ \dot{T}_{2d} \end{bmatrix}, \tag{5.41}$$

which can be simplified to Equation 5.42

$$\begin{bmatrix} \dot{T}_{1d} - \dot{T}_1 \\ \dot{T}_{2d} - \dot{T}_2 \end{bmatrix} + \begin{bmatrix} T_{1d} - T_1 \\ T_{2d} - T_2 \end{bmatrix} = 0. \tag{5.42}$$

This shows the close loop tracking error $\dot{e}+e = 0$ is an exponentially stable error dynamic. For an initial error $e(0) = \dot{e} = 0$, then $e(t) \equiv 0, \forall t \geq 0$. This shows the controller achieves perfect tracking, otherwise the error $e(t)$ converges to zero exponentially.

$$\begin{aligned} \begin{bmatrix} I \\ I \end{bmatrix} = \begin{bmatrix} (\alpha_2 - \frac{\tau}{2})T_2 + \frac{\tau T_1}{2} & \frac{R_I I}{2} \\ (\alpha_1 - \frac{\tau}{2})T_1 + \frac{\tau T_2}{2} & \frac{R_I I}{2} \end{bmatrix}^{-1} - \Bigg\{ \begin{bmatrix} -(k_T + k_\infty) & k_t \\ k_t & -(k_T + k_\infty) \end{bmatrix} \begin{bmatrix} T_1 \\ T_2 \end{bmatrix} \\ - \begin{bmatrix} T_{1d} - T_1 \\ T_{2d} - T_2 \end{bmatrix} - \begin{bmatrix} \dot{T}_{1d} \\ \dot{T}_{2d} \end{bmatrix} + \begin{bmatrix} k_\infty T_\infty \\ k_\infty T_\infty \end{bmatrix} \Bigg\}. \end{aligned} \tag{5.43}$$

Rewrite Equation 5.43 as

$$\begin{aligned} &\begin{bmatrix} \frac{1}{2}R_I \\ \frac{1}{2}R_I \end{bmatrix} I^2 + \begin{bmatrix} (\alpha_2 - \frac{\tau}{2})T_2 + \frac{\tau T_1}{2} \\ (\alpha_1 - \frac{\tau}{2})T_1 + \frac{\tau T_2}{2} \end{bmatrix} I \\ &+ \begin{bmatrix} -T_1(k_T + k_\infty) + k_T T_2 - T_1 + T_{1d} - \dot{T}_{1d} + k_\infty T_\infty \\ -T_2(k_T + k_\infty) + k_T T_1 - T_2 + T_{2d} - \dot{T}_{2d} + k_\infty T_\infty \end{bmatrix} = 0, \end{aligned} \tag{5.44}$$

where Equation 5.44 is in the form of quadratic as Equation 5.45

$$\mathbf{A}I^2 + \mathbf{B}I + \mathbf{C} = 0. \tag{5.45}$$

Finding the quadratic roots for the input current, I, yields

$$\begin{bmatrix} I_1 \\ I_2 \end{bmatrix} = \begin{bmatrix} \frac{-b_1 \pm \sqrt{b_1^2 - 4ac_1}}{2a} \\ \frac{-b_2 \pm \sqrt{b_2^2 - 4ac_2}}{2a} \end{bmatrix} \tag{5.46}$$

where $a_1 = a_2 = \frac{1}{2}R_I$, $b_1 = (\alpha_2 - \frac{\tau}{2})T_2 + \frac{\tau T_1}{2}$, $b_2 = (\alpha_1 - \frac{\tau}{2})T_1 + \frac{\tau T_2}{2}$, $c_1 = -T_1(k_T + k_\infty) + k_T T_2 - T_1 + T_{1d} - \dot{T}_{1d} + k_\infty T_\infty$ and $c_2 = -T_2(k_T + k_\infty) + k_T T_1 - T_2 + T_{2d} - \dot{T}_{2d} + k_\infty T_\infty$. In Equation 5.46, I_1 and I_2 are corresponded to T_1 and T_2, respectively. The two current I_1 and I_2 are summed as per Equation 5.47 to form a single control input I_i to the TEM as shown in Figure 5.23.

$$I_i = h_1 I_1 + h_2 I_2, \tag{5.47}$$

where h_1 and h_2 are the control weights for the T_1 and T_2, respectively.

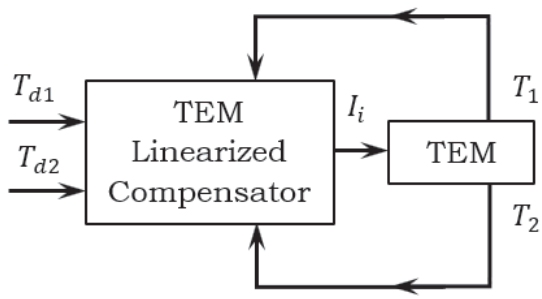

Figure 5.23: Schematic diagram of the single input current to control both sides temperatures for the TEM.

With using the parameters in Chapter 4, Table 4.9, the simulation of the TEM controller has been conducted with Matlab Simulink. The inputs are step function and sinusoidal

function with $T_{di} = 50 + 30sin(0.1t + (i-1)\pi)$, where $i = 1, 2$. Both the control weights are set as $h_1 = 1$ and $h_2 = 1$. The simulation results are shown in Figures 5.24 and 5.25.

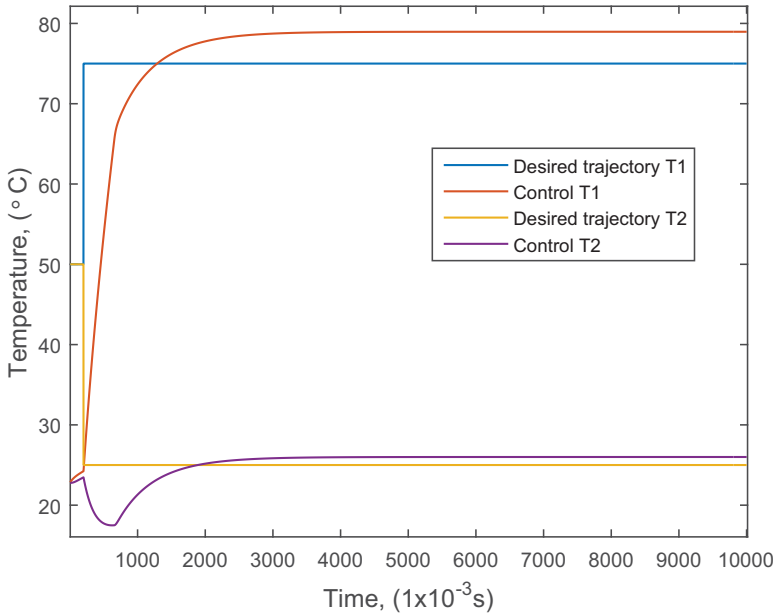

Figure 5.24: TEM control simulation with step inputs.

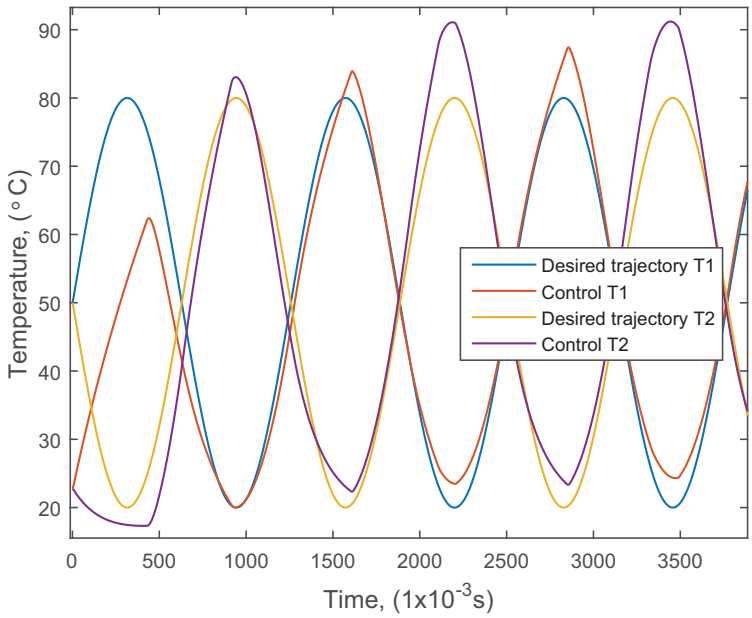

Figure 5.25: TEM control simulation with sinusoidal inputs.

Both Figures 5.24 and 5.25 show steady state like errors. The errors are due to the use of single input in controlling two outputs. The control signal is generated by adding the two feedback signals. When the two feedbacks cause errors in an opposite sign and at the same magnitude, the sum of the errors becomes zero, but the errors are not zero. The control weights are changed to only control the temperature at one side of the TEM. As a result, only the temperature T_1 is controlled when setting the $h_2 = 0$. Thus, two controllers and two layers of TEM are needed to provide heat control for the SMA. The schematic diagram of the system is shown in Figure 5.26. The T_1' and T_2' are not in used. The simulation results using two layers TEM to generate temperatures T_1 and T_2 for the Nitinols pair are shown in Figures 5.27 and 5.28.

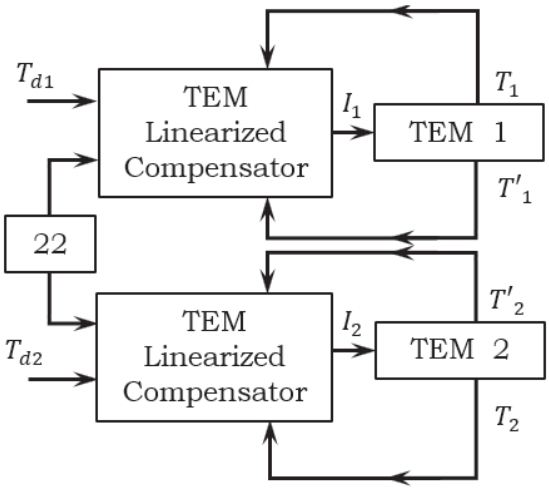

Figure 5.26: Two layers of TEM control system schematic diagram.

The simulation results of the two layers TEM system in Figures 5.27 and 5.28 show good tracking of the desired temperatures by the TEM with response to both the desired inputs of a step function and sinusoidal function, respectively.

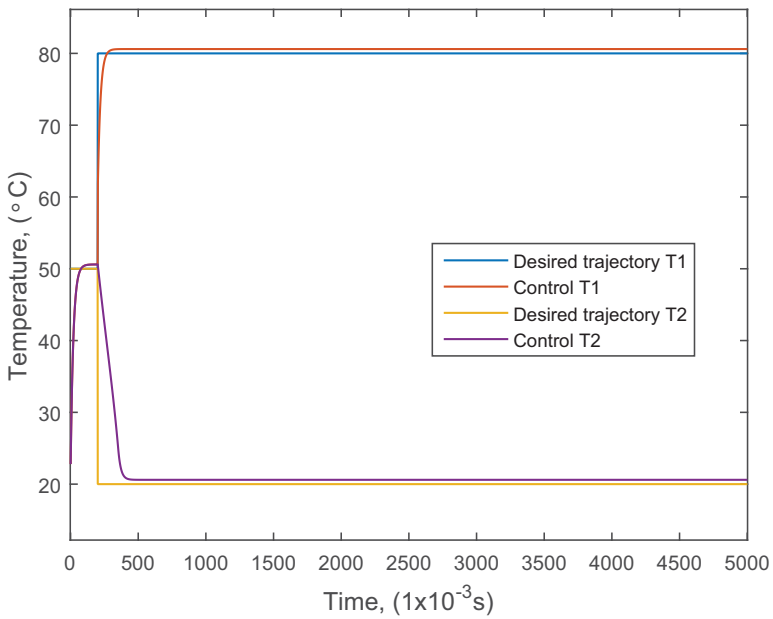

Figure 5.27: Double layers TEM control simulation with step inputs.

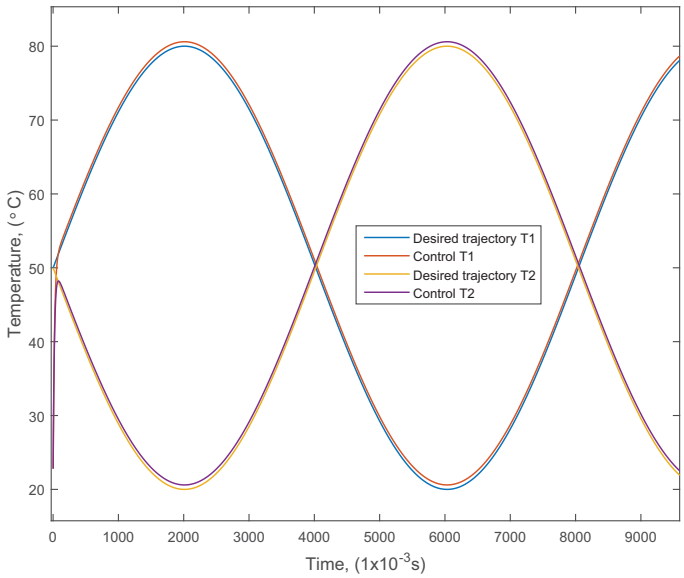

Figure 5.28: Double layers TEM control simulation with sinusoidal inputs.

Due to the TEM compensator controller limitation, the original plan has been revised from using both sides to one side only of the TEM in manipulating the Nitinols heat. Therefore, two controllers are used to control two layers of TEM to supply the temperatures for the Nitinols.

5.3 Concluding Remarks

This Chapter compiles all the controls development for the artificial wrist system. The inverse SD-GPI compensator is used in the controller design to eliminate the hysteresis effect. The global stability of the closed-loop tracking system developed using the prescribed adaptive control approach is verified through Matlab simulation.

The controller design is also extended to the development of an effective controller to track the desired temperature produced by the adaptive controller. A compensator is developed using feedback linearized approach to linearize the TEM input-output. However, due to the

single input, it is unable to control two outputs at the same time. Two layers of TEM are proposed to control the Nitinols temperatures. The proposed two layers of TEM show good performance for tracking the desired temperatures via the simulation.

Chapter 6

Experiment

The completed artificial wrist joint system is shown in Chapter 2, and Figure 2.3 is setup for the experiment. The experiment is designed to investigate the wrist joint functional target as per Chapter 1. The target is to achieve a rotation angle of 60°, the rotation speed of 5° per second, tracking capability of less than 15% tracking error and load capacity of 1Kg at 0.09m from the joint axis. The inverse-based adaptive control, direct adaptive control and PID control systems are implemented to study the tracking capability. Meanwhile, the load capacity is reduced to 0.6Kg at 0.09m from the joint axis due to the physical constraint in the design that was discussed in Chapter 2.

6.1 Artificial Wrist Experiment Platform Setup

The detail information of the experimental platform materials is itemized as follows. The completed experimental setup is shown in Figure 6.2.

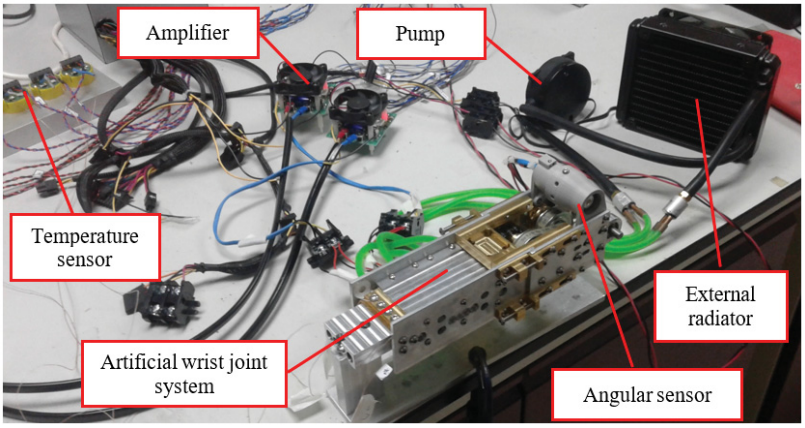

Figure 6.1: Artificial Wrist joint.

- The AMs with each made of 140 Nitinol wires of 0.25mm diameter, produced by Fort Wayne Metals are used in actuating the wrist joint.
- The H-bridge, 20A, 5V to 28V power amplifier model: RB-Rop-05 amplifies the pulse width modulation signals to drive the TEMs.
- The precision potentiometer from Bourns with ±1% 145KΩ is used to feedback the angular position.
- Four high heat pumping TEMs series: UT15,200,F2,4040 from Laird Technology are employed to heat and cool the Nitinols, two TEMs per layer for each side of the Nitinol.
- Four K-type thermocouple temperature sensors (Brand: Omega, Model: 5TC-TT-K-40-36) with 0.08mm diameter wires and TX93A temperature transmitters are used to detect the Nitinols temperatures and the TEMs temperatures.
- The GameStorm, model MaelStom 120T liquid cooling system and 65mm diameter, 12V cooling fan is used as an active cooling system for the TEMs.
- The dSPACE control board model: DS1104 provides 16-bits ADC input channels and DAC output channels. The input channels are connected to the angular displacement sensor and temperature sensors to record the signals. The output channels are

connected to two power amplifiers to drive the TEMs for heating and cooling of the Nitinols.

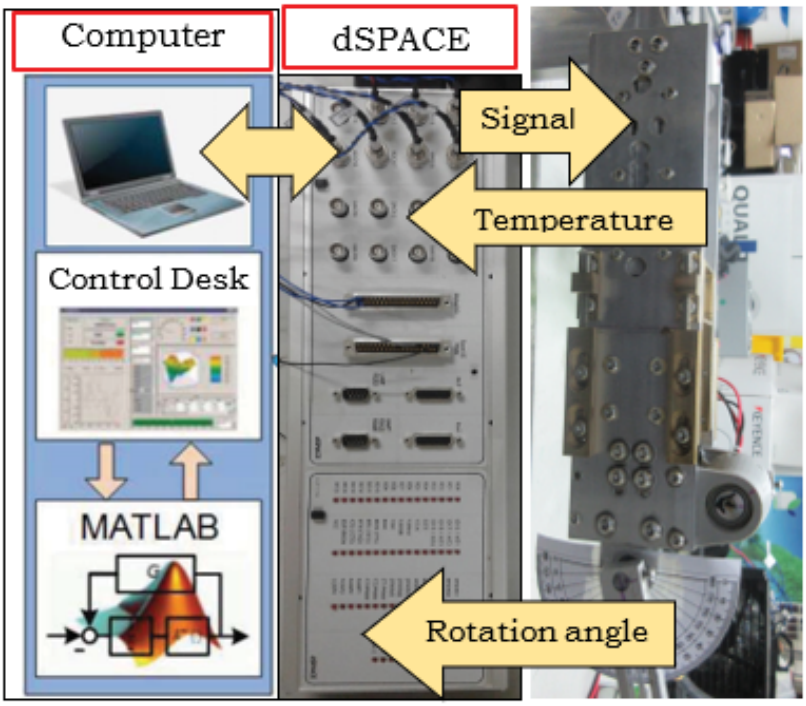

Figure 6.2: Wrist joint system experimental setup.

To achieve an angular velocity of 5° per second which is equivalent to 0.0873 rad per second, the input signal frequency is set as 0.1rad per second that is slightly higher than the required velocity. Sinusoidal desired angle $q_d = 0.524 + 0.524sin(0.1t)$ input with an amplitude of ±0.524rad (±30° total of 60°) is subject to the system. The experiment is repeated with loads from 100g to 600g using the inverse based adaptive controller, direct adaptive controller and PID controller. The direct adaptive controller and PID controller are developed for comparison purposes. The control programs are developed using Matlab Simulink. The PID conceptual design and schematic diagram are shown in Figures 6.3 and 6.4, respectively. The inverse-based adaptive controller conceptual design and schematic diagram are shown in Figures 6.5 and 6.6, respectively. For the direct adaptive controller, the controller developed in the controller simulation as per Figure 5.21 is used. The PID

controller is slightly modified by multiplying the proportional error with the error rate. This is to eliminate the delayed error rate when the error is zero.

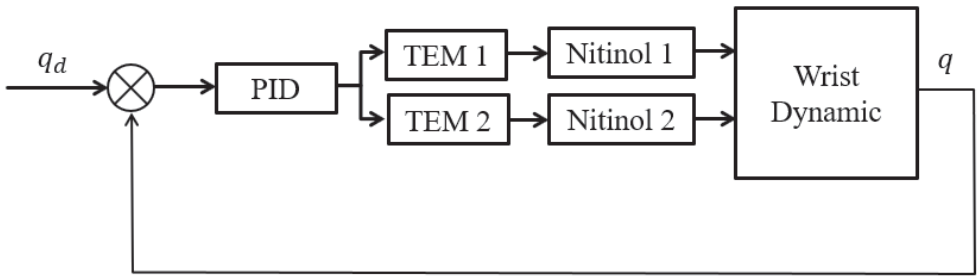

Figure 6.3: PID controller conceptual design.

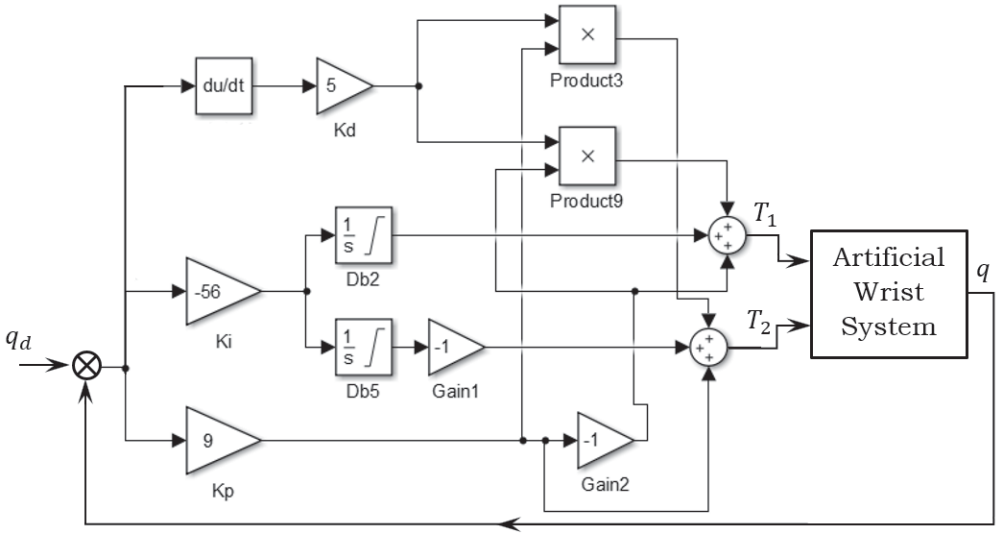

Figure 6.4: PID controller system.

The inverse-based adaptive controller is built according to Chapter 5, Equations 5.32 and 5.37. The inverse model parameters in Tables 5.2 and 5.3 are used in the inverse compensator.

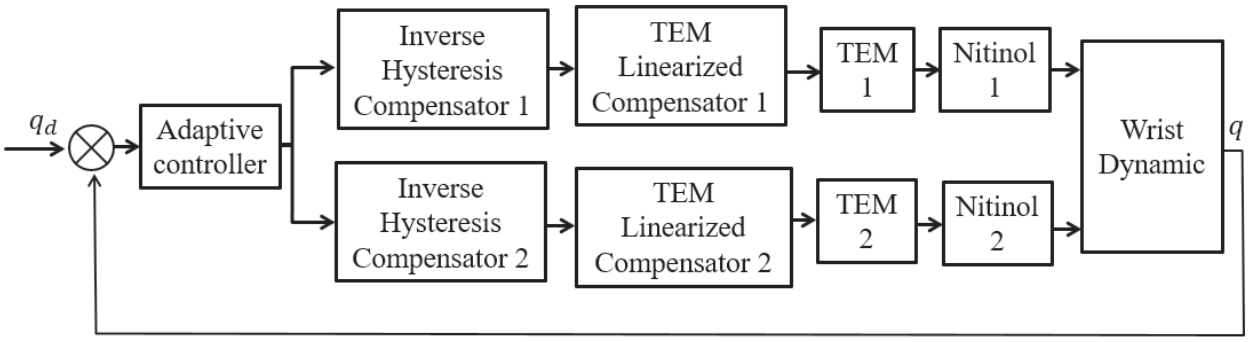

Figure 6.5: Inverse-based controller conceptual design.

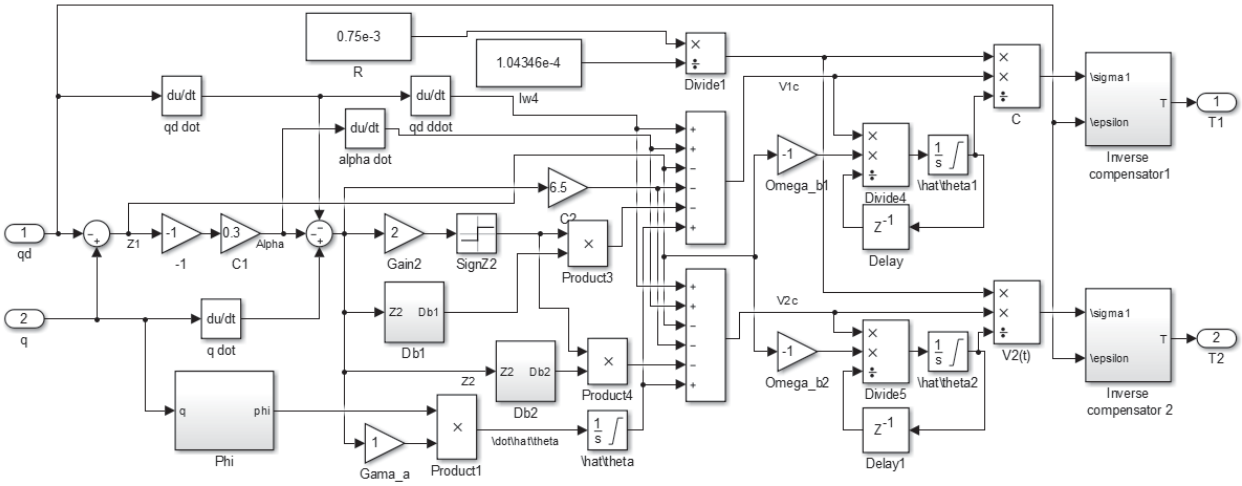

Figure 6.6: Inverse-based controller system.

All the controllers are tuned to the lowest error. The best-tuned parameters are recorded in Table 6.1. The wrist angle results from various control systems are recorded for analysis.

Table 6.1: Artificial wrist control parameters.

Inverse based adaptive	Direct adaptive	PID
$C_1 = 3$	$C_1 = 3$	$K_p = 9$
$C_2 = 6.5$	$C_2 = 5.5$	$K_i = 56$
$\Gamma_a = 0.01$	$\Gamma_a = 0.05$	$K_d = 5$
$\Gamma_{b1} = 0.05$		
$\Gamma_{b2} = 0.05$		
$\Gamma_{D1} = 0.01$		
$\Gamma_{D2} = 0.01$		

6.2 Experimental Result

Figures 6.7 to 6.9 show the experimental results of the inverse based adaptive control, direct adaptive control and PID control system performances in tracking the input signal.

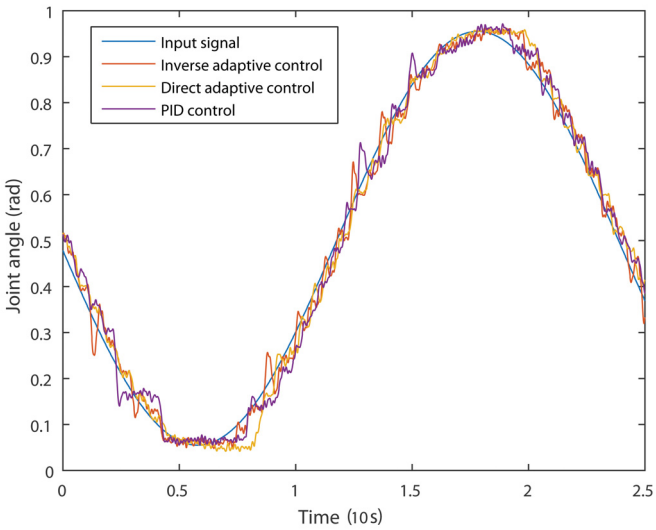

Figure 6.7: Wrist joint experimental result for inverse adaptive control, direct adaptive control and PID control system at load 100g.

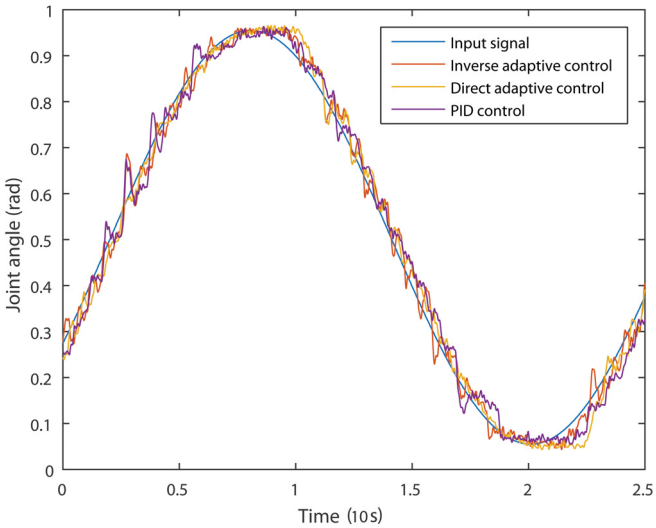

Figure 6.8: Wrist joint experimental result for inverse adaptive control, direct adaptive control and PID control system at load 200g.

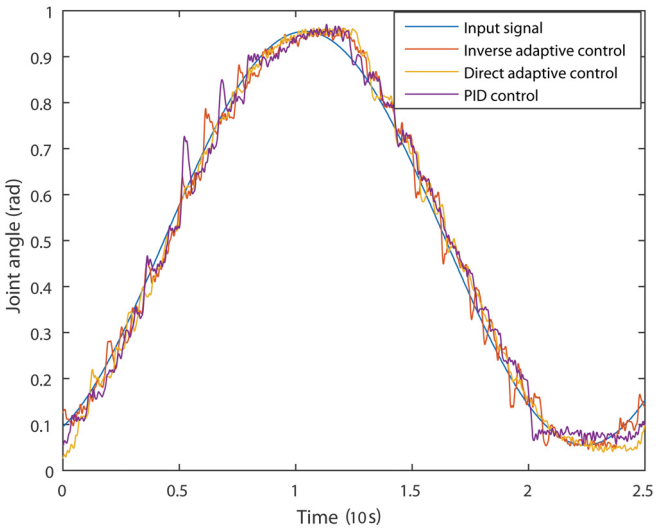

Figure 6.9: Wrist joint experimental result for inverse adaptive control, direct adaptive control and PID control system at load 300g.

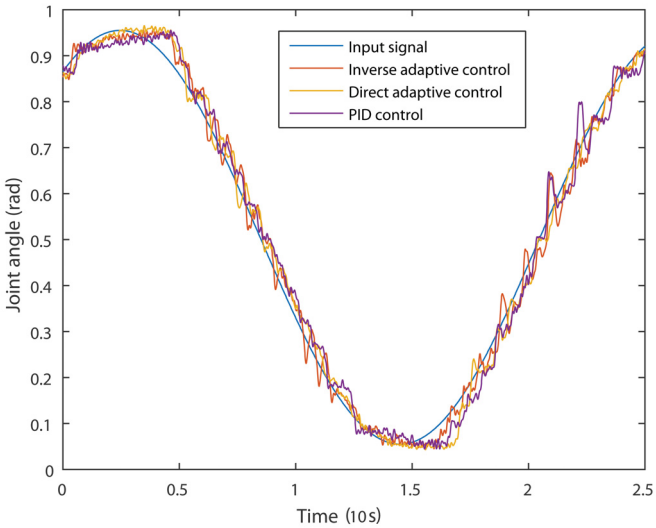

Figure 6.10: Wrist joint experimental result for inverse adaptive control, direct adaptive control and PID control system at load 400g.

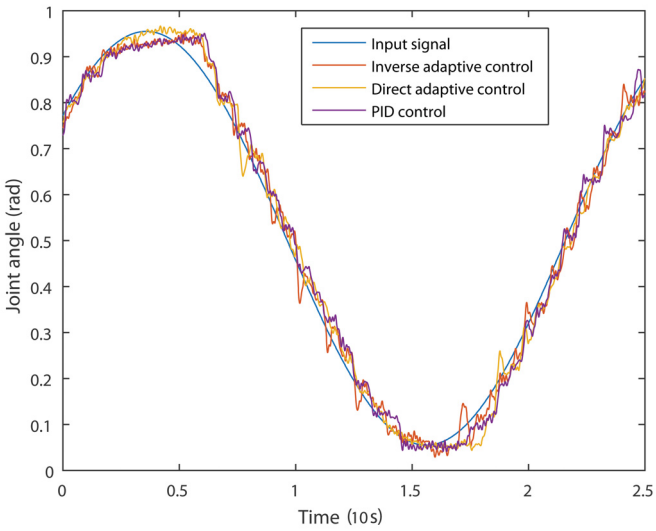

Figure 6.11: Wrist joint experimental result for inverse adaptive control, direct adaptive control and PID control system at load 500g.

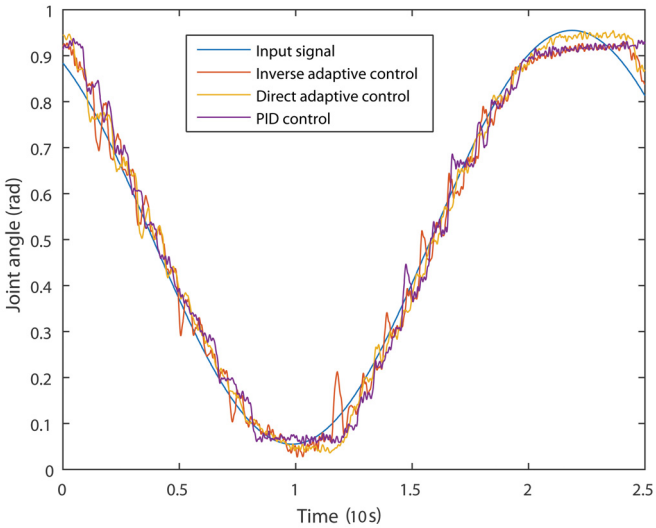

Figure 6.12: Wrist joint experimental result for inverse adaptive control, direct adaptive control and PID control system at load 600g.

The recorded experimental results are analyzed for the percentage of tracking errors. Figures 6.13 to 6.18 show the error comparison for the inverse adaptive control, direct adaptive control and PID control systems for loads from 100g to 600g.

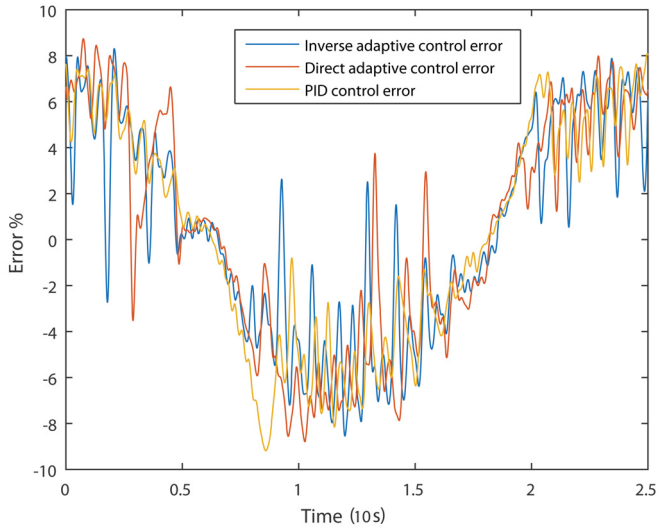

Figure 6.13: Inverse adaptive control, direct adaptive control system and PID control system error at load 100g.

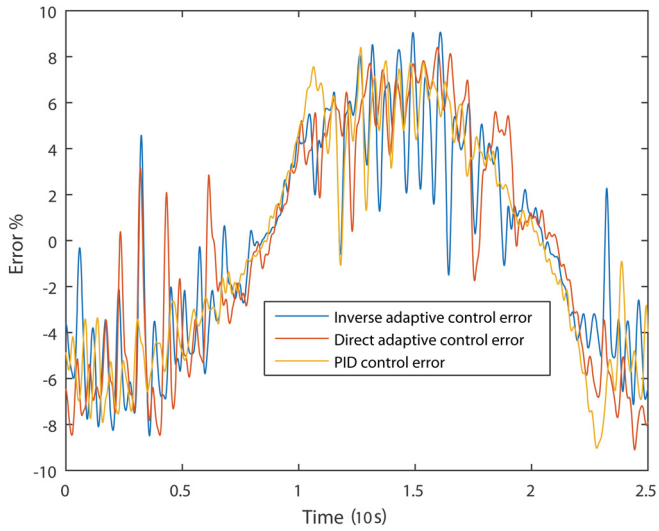

Figure 6.14: Inverse adaptive control, direct adaptive control system and PID control system error at load 200g.

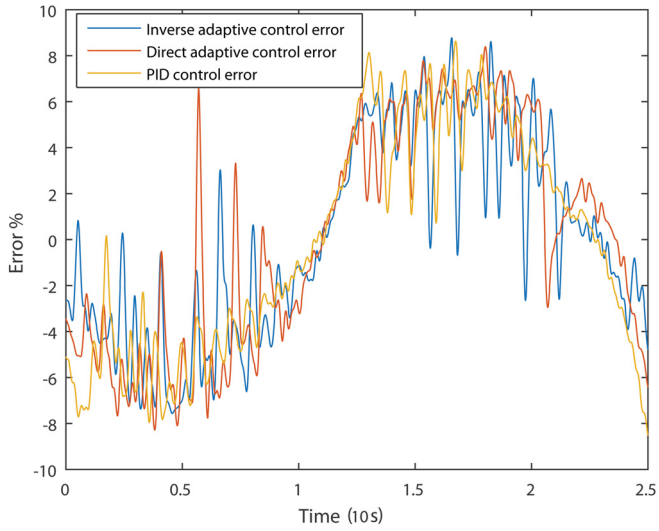

Figure 6.15: Inverse adaptive control, direct adaptive control system and PID control system error at load 300g.

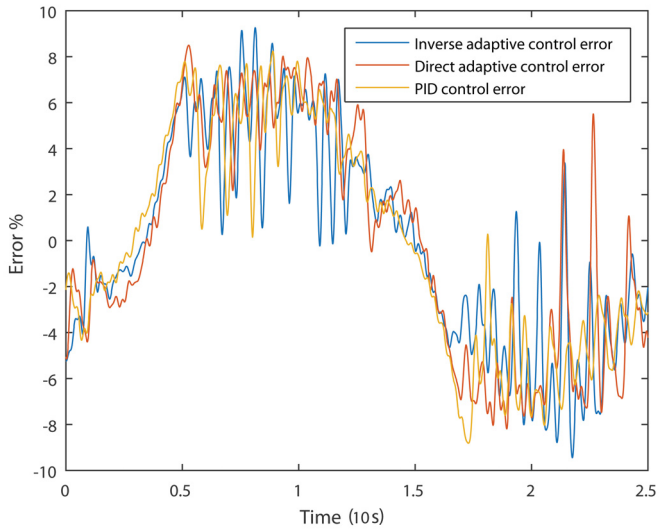

Figure 6.16: Inverse adaptive control, direct adaptive control system and PID control system error at load 400g.

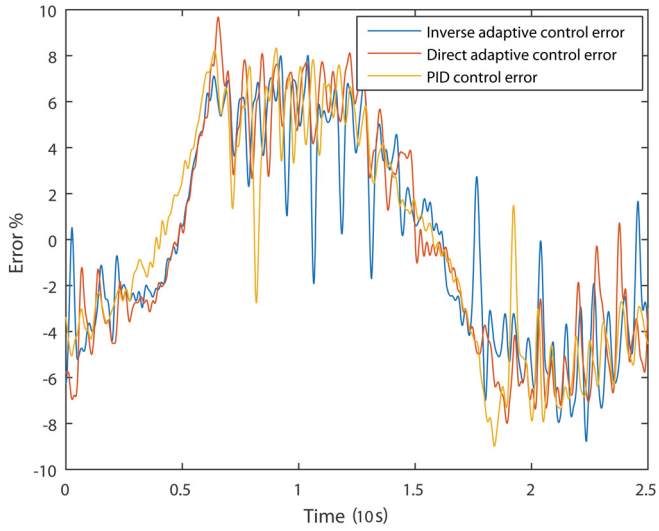

Figure 6.17: Inverse adaptive control, direct adaptive control system and PID control system error at load 500g.

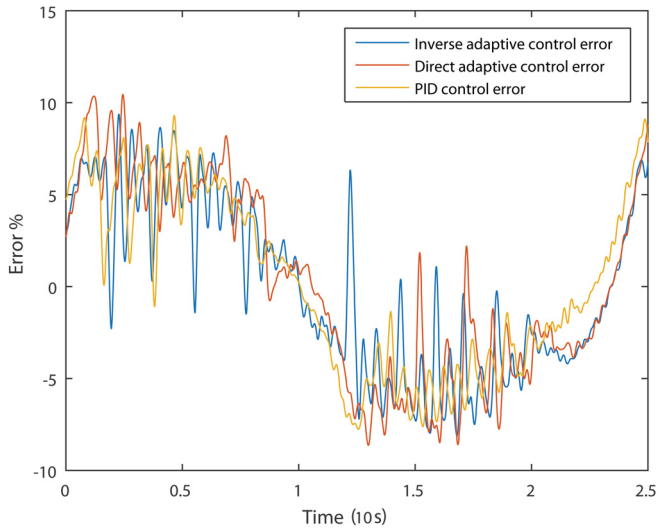

Figure 6.18: Inverse adaptive control, direct adaptive control system and PID control system error at load 600g.

6.3 Discussion of Results

The experiment results show the wrist system can achieve rotation angle of 60° for all controllers with loads ranging from 100g to 600g. The wrist system also achieves a rotation speed of 5° per second. This fulfills the movement and velocity requirement. The wrist shows the capability to lift loads to 600g, at the required movement range and velocity. The initial requirement of the 1Kg load is not achieved here due to TEM constraint. This can be overcome by custom-made TEM or Nitinol wires with a larger diameter.

The control objective is to achieve the tracking errors smaller than 15%. All the controllers achieve the control objective. The analysis of the errors from each control system is shown in Table 6.2. The inverse-based and direct adaptive controllers show errors with a small fluctuation of the maximum values between 8.5 to 9.5% for loads ranging from 100g to 600g. Meanwhile, the PID controller shows errors with maximum values between 8.4 to 10.4% and exhibits a trend of increase from load 400g to 600g. This clearly shows the PID controller limitation in handling load uncertainty. Meanwhile, the inverse-based and the direct adaptive controllers have shown the ability to adapt to the load change and maintain a small fluctuation for the error maximum values at all the loads.

For the total absolute error, the same amount of absolute error is summed for each of the controllers for a full cycle of wrist movement. The result of the inverse adaptive controller shows the smallest total absolute error, followed by the direct adaptive controller, and lastly the PID controller. The inverse-based adaptive controller shows the ability to mitigate the hysteresis effect and gives good control over the loads ranging from 100g to 500g with a total absolute error in between 93,200% to 97,900%. The total absolute error increases slightly at load 600g to 103,654%; this could be due to the limit of the Nitinol to handle the load. The direct adaptive controller shows stable absolute error within the range of 104,000% to 107,800%. Meanwhile, the PID controller is in the range of 105,600% to 109,700% for loads 100g to 500g, and with an increase to 115,075% at load 600g. This again shows the limitation of the PID controller in handling system with uncertain loads.

The maximum error values of the inverse-based adaptive controller show no significant superiority compared to the direct adaptive controller. However, in the total absolute error, the inverse-based controller is about 10% better than the direct adaptive controller at all loads except 3.85% better at 600g load. It is surprising that the direct adaptive controller has shown performance that is close to the inverse-based controller. From the literature, direct control does not show a performance close to the inverse based adaptive controller. The observation suggests that it could be due to the antagonistic system where one side of the Nitinol is cooling while the other side of the Nitinol is heating. The opposite heat reaction for the antagonist pair of Nitinols compensates each other and overcomes the lagging caused by the hysteresis behavior. However, further investigation is needed to verify this explanation.

Table 6.2: Control system error analysis.

Load	Inverse adaptive max (%)	Direct adaptive max (%)	PID max (%)	Inverse adaptive total absolute error (%)	Direct adaptive total absolute error (%)	PID total absolute error (%)
100g	8.54	9.18	8.79	97,878	107,393	108,585
200g	9.06	9.04	9.10	95,826	106,605	109,721
300g	8.77	8.63	8.39	93,181	105,752	105,643
400g	9.45	8.81	8.50	95,723	103,996	110,471
500g	8.78	8.99	9.68	97,147	105,755	109,712
600g	9.37	9.30	10.44	103,654	107,800	115,075

It is found that the liquid heat sink system is effective to remove excess heat from the TEMs. This suggests that a self-locking mechanism can be created during the operation of the wrist, where insulation layers are placed on the outer side of the Nitinols to avoid heat loss. With the reduced heat loss, only small amounts of electrical energy are needed to maintain the temperatures of the Nitinols, and same for the torque at the joint. This

mechanism is synonymous to the worm gear system that provides locking capability when the joint stays in the fixed position. The self-locking ability is very useful especially when holding the joint at a fixed position. Remarkably, the liquid cooling mechanism which inspired by the natural thermoregulation in mammals is successfully applied in wrist joint system.

6.4 Concluding Remarks

In this chapter, the TEM antagonistically driven SMA wrist joint experimental platform has been successfully developed. Experiments have been conducted to verify the system. The inverse-based adaptive control system, direct adaptive control system and PID control system are applied to study the effectiveness of each control approach in controlling the highly nonlinear hysteresis system. The inverse based control system is found superior compared to the other two controllers. Although the direct controller is not as good as the inverse based adaptive controller, the direct adaptive controller shows acceptable performance in the experimental results.

Chapter 7

Conclusions and Future Work

Smart material such as SMA is still underutilized due to its highly nonlinear and hysteretic behaviors. Although many explorations have been conducted, most of the research aimed only to understand the material properties. In this research, the exploration not only targets to understand the SMA better but also aims to an application. The application involves the use of TEM to antagonistically drive the SMA as functioning AM to actuate the artificial wrist joint system.

In this research, there are three main achievements. The first is the design and implementation of the liquid heat removal system with an external radiator, that mimics the natural heat regulation system in humans and mammals. The second achievement is the development of the stress-dependent hysteresis model based on the Generalized Prandlt-Ishlinskii modelling approach. The modeling also includes the prediction of superelastic behavior of the Nitinol and its inverse model. The third achievement includes the adaptive controller developed for the antagonist configuration of the AM system using the back-stepping method; the output linearized control system developed for the TEM to track the desired temperature; and the mechanical clamping system for holding 140 Nitinol wires to form the AM. These achievements have contribute to the advancement of the SMA application in realizing the AM system.

7.1 Concluding Remarks

The SMA is a solid state actuator that has large force over its weight and effective strain for practical applications. However, it has limited usage due to its highly nonlinear and hysteresis behaviors, especially when the hysteresis is also affected by the loading stress. The stress-dependent hysteresis behavior has been left poorly explored. Therefore, in this research, the stress-dependent hysteresis is first studied. Initial experiments on 0.25 mm diameter Nitinol #6 wire exhibit the superelastic behavior that provides large recoverable strain from 700g to 850g loads for 20°C to 76°C. This finding is in agreement with many other research, but it was poorly explained and applied in practical usage. This initial finding has led to the main key knowledge of this research, where it is the foundation for the development of stress-dependent hysteresis model for describing the superelastic behavior.

Before the initial experiment, a literature search was conducted. The search covers literature in the areas of SMA working principle, hysteresis modeling and control of the SMA with the direction towards realizing the artificial wrist joint. The study of the literature has laid down the basic foundation of this research. In the literature study, two main discoveries emerge and become the main momentum of the research. The first discovery is that the stress-dependent hysteresis of the SMA was first investigated in the earlier times. However, due to the limitation of the mathematical model, it was unable to be used in the control development. Invertible phonological hysteresis was later introduced in describing the SMA hysteretic behavior. The invertible phonological hysteresis models are effectively applied in the control system due to its invertibility. Despite that, the investigation of the SMA stress-dependent hysteresis is poorly conducted using the invertible phonological hysteresis models. The second discovery is a subset of the first discovery, where the adoption of hysteresis modeling method has a significant impact on the control development. Phenological invertible hysteresis model has provided direct access to the phenological predictions for describing the SMA hysteresis phenomena. The controller developed based on this information can exponentially drive the tracking error toward zero.

Based on the discoveries in the literature, the Nitinol stress dependent hysteresis model is developed based on the GPI phenological approach. First, the GPI model parameters at each load are fitted to the experimental data using Matlab function. Then, by regressing the parameters of the GPI models at different loads with the applied load as the variable, the SD-GPI is formulated and verified. Meanwhile, the TEM model is developed based on the heat balance theory, and the model parameters are identified using experimental data and Range-Kutta fourth order differential equation. Following the TEM model, the dynamic model of the wrist joint is also developed. At this point, all the necessary models for the TEM antagonist driven SMA wrist joint have been developed and verified.

Due to the highly nonlinear hysteretic behavior of the Nitinol, inverse based control is proposed. Therefore, the SD-GPI inverse hysteresis compensator is developed to assist the controller in mitigating the hysteresis effect. The inverse compensator can compensate most of the hysteresis effect except at loads from 1.0Kgf and above. Thus, the compensator error is formulated and overcome by the controller. By defining the inverse hysteresis compensator error and the wrist dynamic model, the adaptive back-stepping control approach is applied to develop the inverse based adaptive controller for the TEM antagonistically driven SMA wrist joint. As the Nitinol is not directly controlled by the adaptive controller, feedback linearizes perfect control system is developed as a compensator to linearize the TEM system. However, the feedback linearized controller for the TEM is only able to control one side of the temperature at one time. Thus, two layers of TEMs are setup to control the antagonist pair of Nitinols. With this system, the temperatures of the Nitinols pair have been successfully controlled in the simulation.

With all the systems verified mathematically, the physical realization is executed. Due to the limitation of the TEM surface area, a prototype unit of the wrist joint with a lower output torque is proposed to verify the wrist joint system. To remove heat between the two layers of TEMs, liquid heat sink system that inspired by nature is designed and modified from commercially available computer liquid heat sink system. The design of the wrist joint mechanical system is completed, and all parts are fabricated. Based on the superelastic

behavior learnt from the initial investigation, the pre-load condition is calibrated. An experimental platform comprising the wrist joint and necessary instrument is setup. An input signal with a frequency of 0.1rad/s and amplitude of ±0.524rad (±30° total of 60°) are subjected to the wrist joint system, and the results are collected. The control results show the inverse-based adaptive controller and the direct adaptive controller achieved tracking error of less than 10%. However, the inverse based controller shows a total tracking error 10% smaller than the direct adaptive controller. Meanwhile, the PID controller performance is not as good as the two controllers and shows an increase of errors when load increases.

Based on the objectives of this dissertation, the SD-GPI has been achieved with the errors generally below 5% and the adaptive control system has been developed for the wrist joint system with the tracking error of less than 10%. Other requirements for the wrist joint as the rotation angle of 60°, the rotation speed of 5° per second and tracking capability of less than 15% tracking error also have been achieved. The load capacity of 1Kg at 0.09m from the joint axis is achieved at 0.6Kg. Therefore, with these results, it is concluded that the TEM antagonistically driven SMA actuator for artificial muscle resembling wrist joint has been successfully achieved.

7.2 Recommendations for Future Work

Based on the current state of findings in this dissertation research, the following research topics are proposed for future research.

- Designing the mechanical transmission system to minimize the size of the bulky transmission system. At the same time exploring the use of a flat bar instead of round wire Nitinol.
- Exploring the relationship between the hysteresis model parameters at varying load conditions. Deriving a phonological model that includes the stress in the loading function.

- Increasing the response speed of the Nitinol actuated AM toward the response speed of natural muscle.

Bibliography

[1] K. Kuribayashi, "Millimeter-sized joint actuator using a shape memory alloy," *Sensors and Actuators*, vol. 20, no. 1-2, pp. 57–64, 1989.

[2] J. A. Shaw and S. Kyriakides, "Thermomechanical aspects of niti," *Journal of the Mechanics and Physics of Solids*, vol. 43, no. 8, pp. 1243–1281, 1995.

[3] C. Liang and C. Rogers, "One-dimensional thermomechanical constitutive relations for shape memory materials," *Journal of Intelligent Material Systems and Structures*, vol. 1, no. 2, pp. 207–234, 1990.

[4] K. K. Ahn and N. B. Kha, "Internal model control for shape memory alloy actuators using fuzzy based preisach model," *Sensors and Actuators A: Physical*, vol. 136, no. 2, pp. 730–741, 2007.

[5] M. M. Khan and D. C. Lagoudas, "Modeling of shape memory alloy pseudoelastic spring elements using preisach model for passive vibration isolation," in *SPIE's 9th Annual International Symposium on Smart Structures and Materials*, pp. 336–347, International Society for Optics and Photonics, 2002.

[6] M. Al Janaideh, Y. Feng, S. Rakheja, Y. Tan, and C.-Y. Su, "Generalized prandtl-ishlinskii hysteresis: Modeling and robust control for smart actuators," in *Proceedings of the 48th IEEE Conference on Decision and Control, 2009 held jointly with the 2009 28th Chinese Control Conference 2009.*, pp. 7279–7284, 2009.

[7] L. Riccardi, D. Naso, H. Janocha, and B. Turchiano, "A precise positioning actuator based on feedback-controlled magnetic shape memory alloys," *Mechatronics*, vol. 22, no. 5, pp. 568–576, 2012.

[8] M. R. Zakerzadeh and H. Sayyaadi, "Experimental comparison of some phenomenological hysteresis models in characterizing hysteresis behavior of shape memory alloy actuators," *Journal of Intelligent Material Systems and Structures*, pp. 1287–1309, 2012.

[9] G. Song, V. Chaudhry, and C. Batur, "Precision tracking control of shape memory alloy actuators using neural networks and a sliding-mode based robust controller," *Smart Materials and Structures*, vol. 12, no. 2, pp. 223–231, 2003.

[10] K. Tanaka, T. Hayashi, Y. Itoh, and H. Tobushi, "Analysis of thermomechanical behavior of shape memory alloys," *Mechanics of Materials*, vol. 13, no. 3, pp. 207–215, 1992.

[11] K. Ikuta, M. Tsukamoto, and S. Hirose, "Mathematical model and experimental verification of shape memory alloy for designing micro actuator," in *[1991] Proceedings. IEEE Micro Electro Mechanical Systems*, pp. 103–108, 1991.

[12] I. Müller and S. Seelecke, "Thermodynamic aspects of shape memory alloys," *Mathematical and Computer Modelling*, vol. 34, no. 12, pp. 1307–1355, 2001.

[13] S. M. Dutta and F. H. Ghorbel, "Differential hysteresis modeling of a shape memory alloy wire actuator," *IEEE/ASME Transactions on Mechatronics*, vol. 10, no. 2, pp. 189–197, 2005.

[14] O. Rediniotis, L. Wilson, D. C. Lagoudas, and M. Khan, "Development of a shape-memory-alloy actuated biomimetic hydrofoil," *Journal of Intelligent Material Systems and Structures*, vol. 13, no. 1, pp. 35–49, 2002.

[15] K. Xing, Y. Wang, Q. Zhu, and H. Zhou, "Modeling and control of mckibben artificial muscle enhanced with echo state networks," *Control Engineering Practice*, vol. 20, no. 5, pp. 477–488, 2012.

[16] D. Sun, B. Yan, B. Han, Y. Song, and X. Zhang, "Vibration characteristic simulation of a pneumatic artificial muscle damping seat," *Journal of Low Frequency Noise, Vibration and Active Control*, vol. 35, no. 1, pp. 39–51, 2016.

[17] J. Li, Z. Ji, X. Shi, F. You, F. Fu, R. Liu, J. Xia, N. Wang, J. Bai, Z. Wang, *et al.*, "Design and optimization of multi-class series-parallel linear electromagnetic array artificial muscle," *Bio-Medical Materials and Engineering*, vol. 24, no. 1, pp. 549–555, 2014.

[18] K. J. Kim and M. Shahinpoor, "A novel method of manufacturing three-dimensional ionic polymer–metal composites (ipmcs) biomimetic sensors, actuators and artificial muscles," *Polymer*, vol. 43, no. 3, pp. 797–802, 2002.

[19] B. Bhandari, G.-Y. Lee, and S.-H. Ahn, "A review on ipmc material as actuators and sensors: fabrications, characteristics and applications," *International Journal of Precision Engineering and Manufacturing*, vol. 13, no. 1, pp. 141–163, 2012.

[20] M. F. Barsky, D. Lindner, and R. Claus, "Robot gripper control system using pvdf piezoelectric sensors," *IEEE transactions on Ultrasonics, Ferroelectrics, and Frequency Control*, vol. 36, no. 1, pp. 129–134, 1989.

[21] P. Brochu and Q. Pei, "Advances in dielectric elastomers for actuators and artificial muscles," *Macromolecular Rapid Communications*, vol. 31, no. 1, pp. 10–36, 2010.

[22] W. Li, B. Belmont, and A. Shih, "Design and manufacture of polyvinyl chloride (pvc) tissue mimicking material for needle insertion," *Procedia Manufacturing*, vol. 1, pp. 866–878, 2015.

[23] Z. Zhakypov, J.-L. Huang, and J. Paik, "A novel torsional shape memory alloy actuator: Modeling, characterization, and control," *IEEE Robotics & Automation Magazine*, vol. 23, no. 3, pp. 65–74, 2016.

[24] J.-J. Zhang, Y.-H. Yin, and J.-Y. Zhu, "Electrical resistivity-based study of self-sensing properties for shape memory alloy-actuated artificial muscle," *Sensors*, vol. 13, no. 10, pp. 12958–12974, 2013.

[25] M. H. Elahinia, M. Ahmadian, and H. Ashrafiuon, "Design of a kalman filter for rotary shape memory alloy actuators," *Smart Materials and Structures*, vol. 13, no. 4, pp. 691–697, 2004.

[26] R. Romano and E. A. Tannuri, "Modeling, control and experimental validation of a novel actuator based on shape memory alloys," *Mechatronics*, vol. 19, no. 7, pp. 1169–1177, 2009.

[27] L. U. Odhner and H. H. Asada, "Sensorless temperature estimation and control of shape memory alloy actuators using thermoelectric devices," *IEEE/ASME Transactions on Mechatronics*, vol. 11, no. 2, pp. 139–144, 2006.

[28] K. K. Şafak and G. G. Adams, "Modeling and simulation of an artificial muscle and its application to biomimetic robot posture control," *Robotics and Autonomous Systems*, vol. 41, no. 4, pp. 225–243, 2002.

[29] M. H. Elahinia and H. Ashrafiuon, "Nonlinear control of a shape memory alloy actuated manipulator," *Journal of Vibration and Acoustics*, vol. 124, no. 4, pp. 566–575, 2002.

[30] M. Moallem and V. Tabrizi, "Tracking control of an antagonistic shape memory alloy actuator pair," *IEEE Transactions on Control Systems Technology*, vol. 17, no. 1, pp. 184–190, 2009.

[31] M. R. Zakerzadeh and H. Sayyaadi, "Deflection control of sma-actuated beam-like structures in nonlinear large deformation mode," *American Journal of Computational and Applied Mathematics*, vol. 4, no. 5, pp. 167–185, 2014.

[32] A. Price, A. Edgerton, C. Cocaud, H. Naguib, and A. Jnifene, "A study on the thermo-mechanical properties of shape memory alloys-based actuators used in artificial muscles," *Journal of Intelligent Material Systems and Structures*, vol. 18, no. 1, pp. 11–18, 2007.

[33] M. Sreekumar, M. Singaperumal, T. Nagarajan, M. Zoppi, and R. Molfino, "Recent advances in nonlinear control technologies for shape memory alloy actuators," *Journal of Zhejiang University SCIENCE A*, vol. 8, no. 5, pp. 818–829, 2007.

[34] A. Khandelwal and V. Buravalla, "Models for shape memory alloy behavior: an overview of modeling approaches," *The International Journal of Structural Changes in Solids*, vol. 1, no. 1, pp. 111–148, 2009.

[35] W. Huang, "On the selection of shape memory alloys for actuators," *Materials & design*, vol. 23, no. 1, pp. 11–19, 2002.

[36] J. M. Jani, M. Leary, A. Subic, and M. A. Gibson, "A review of shape memory alloy research, applications and opportunities," *Materials & Design*, vol. 56, pp. 1078–1113, 2014.

[37] W. J. Buehler and R. C. Wiley, "Nickel-base alloys," Mar. 23 1965. US Patent 3,174,851.

[38] A. Paiva and M. A. Savi, "An overview of constitutive models for shape memory alloys," *Mathematical Problems in Engineering*, vol. 2006, 2006.

[39] M. J. Mosley and C. Mavroidis, "Experimental nonlinear dynamics of a shape memory alloy wire bundle actuator," *Transactions-American Society of Mechanical Engineers Journal of Dynamic Systems Measurement and Control*, vol. 123, no. 1, pp. 103–112, 2001.

[40] C. Liang and C. Rogers, "Design of shape memory alloy actuators," *Journal of Mechanical Design*, vol. 114, no. 2, pp. 223–230, 1992.

[41] L. Brinson, "One-dimensional constitutive behavior of shape memory alloys: thermomechanical derivation with non-constant material functions and redefined martensite internal variable," *Journal of Intelligent Material Systems and Structures*, vol. 4, no. 2, pp. 229–242, 1993.

[42] J. A. Shaw, "Simulations of localized thermo-mechanical behavior in a niti shape memory alloy," *International Journal of Plasticity*, vol. 16, no. 5, pp. 541–562, 2000.

[43] E. A. Williams, G. Shaw, and M. Elahinia, "Control of an automotive shape memory alloy mirror actuator," *Mechatronics*, vol. 20, no. 5, pp. 527–534, 2010.

[44] K. Tanaka, S. Kobayashi, and Y. Sato, "Thermomechanics of transformation pseudoelasticity and shape memory effect in alloys," *International Journal of Plasticity*, vol. 2, no. 1, pp. 59–72, 1986.

[45] M. H. Elahinia, T. M. Seigler, D. J. Leo, and M. Ahmadian, "Nonlinear stress-based control of a rotary sma-actuated manipulator," *Journal of Intelligent Material Systems and Structures*, vol. 15, no. 6, pp. 495–508, 2004.

[46] S. M. Dutta, F. H. Ghorbel, and J. B. Dabney, "Modeling and control of a shape memory alloy actuator," in *Proceedings of the 2005 IEEE International Symposium on Intelligent Control, Mediterrean Conference on Control and Automation*, pp. 1007–1012, 2005.

[47] M. Moallem and J. Lu, "Application of shape memory alloy actuators for flexure control: theory and experiments," *IEEE/ASME Transactions on Mechatronics*, vol. 10, no. 5, pp. 495–501, 2005.

[48] K. Tanaka and S. Nagaki, "A thermomechanical description of materials with internal variables in the process of phase transitions," *Ingenieur-Archiv*, vol. 51, no. 5, pp. 287–299, 1982.

[49] K. Tanaka and R. Iwasaki, "A phenomenological theory of transformation superplasticity," *Engineering Fracture Mechanics*, vol. 21, no. 4, pp. 709–720, 1985.

[50] M. H. Elahinia and M. Ahmadian, "An enhanced sma phenomenological model: I. the shortcomings of the existing models," *Smart Materials and Structures*, vol. 14, no. 6, pp. 1297–1308, 2005.

[51] Z. Guo, H. Yu, and L.-B. Wee, "Design of a novel compliant differential shape memory alloy actuator," in *2013 IEEE/RSJ International Conference on Intelligent Robots and Systems (IROS)*, pp. 4925–4930, 2013.

[52] I. Müller, "A model for a body with shape-memory," *Archive for Rational Mechanics and Analysis*, vol. 70, no. 1, pp. 61–77, 1979.

[53] I. Müller and K. Wilmanski, "A model for phase transition in pseudoelastic bodies," *Il Nuovo Cimento B Series 11*, vol. 57, no. 2, pp. 283–318, 1980.

[54] I. Müller, "Pseudoelasticity in shape memory alloys–an extreme case of thermoelasticity," *FB9-Hermann Föttinger Institut Technical University, BERLIN, IMA preprint, Minneapolis*, pp. 1–28, 1985.

[55] M. Achenbach, T. Atanackovic, and I. Müller, "A model for memory alloys in plane strain," *International Journal of Solids and Structures*, vol. 22, no. 2, pp. 171–193, 1986.

[56] S. Seelecke and I. Muller, "Shape memory alloy actuators in smart structures: Modeling and simulation," *Applied Mechanics Reviews*, vol. 57, no. 1, pp. 23–46, 2004.

[57] J. G. Boyd and D. C. Lagoudas, "Thermomechanical response of shape memory composites," *Journal of Intelligent Material Systems and Structures*, vol. 5, no. 3, pp. 333–346, 1994.

[58] D. C. Lagoudas and Z. Ding, "Solution behavior of the transient heat transfer problem in thermoelectric shape memory alloy actuators," *SIAM Journal on Applied Mathematics*, vol. 57, no. 1, pp. 34–52, 1997.

[59] B. J. De Blonk and D. C. Lagoudas, "Actuation of elastomeric rods with embedded two-way shape memory alloy actuators," *Smart Materials and Structures*, vol. 7, no. 6, pp. 771–783, 1998.

[60] Y. Ivshin and T. J. Pence, "A thermomechanical model for a one variant shape memory material," *Journal of Intelligent Material Systems and Structures*, vol. 5, no. 4, pp. 455–473, 1994.

[61] K. K. Ahn and N. B. Kha, "Modeling and control of shape memory alloy actuators using preisach model, genetic algorithm and fuzzy logic," *Mechatronics*, vol. 18, no. 3, pp. 141–152, 2008.

[62] Y.-F. Wang, C.-Y. Su, H. Hong, and Y.-m. Hu, "Modeling and compensation for hysteresis of shape memory alloy actuators with the preisach representation," in *2007 IEEE International Conference on Control and Automation*, pp. 239–244, 2007.

[63] B. K. Nguyen and K. K. Ahn, "Feedforward control of shape memory alloy actuators using fuzzy-based inverse preisach model," *IEEE Transactions on Control Systems Technology*, vol. 17, no. 2, pp. 434–441, 2009.

[64] R. Gorbet, D. Wang, and K. Morris, "Preisach model identification of a two-wire sma actuator," in *Proceedings. 1998 IEEE International Conference on Robotics and Automation*, vol. 3, pp. 2161–2167, 1998.

[65] A. Falvo, F. Furgiuele, and C. Maletta, "Two-way shape memory effect of a ti rich niti alloy: experimental measurements and numerical simulations," *Smart Materials and Structures*, vol. 16, no. 3, pp. 771–778, 2007.

[66] M. A. Janaideh, J. Mao, S. Rakheja, W. Xie, and C.-Y. Su, "Generalized prandtl-ishlinskii hysteresis model: Hysteresis modeling and its inverse for compensation in smart actuators," in *2008 47th IEEE Conference on Decision and Control*, pp. 5182–5187, 2008.

[67] M. Al Janaideh, C.-Y. Su, and S. Rakheja, "Development of the rate-dependent prandtl–ishlinskii model for smart actuators," *Smart Materials and Structures*, vol. 17, no. 3, pp. 1–11, 2008.

[68] H. Sayyaadi, M. R. Zakerzadeh, and M. A. V. Zanjani, "Accuracy evaluation of generalized prandtl-ishlinskii model in characterizing asymmetric saturated hysteresis nonlinearity behavior of shape memory alloy actuators," *International Journal of Research and Reviews in Mechatronic Design and Simulation (IJRRMDS)*, vol. 1, 2011.

[69] H. Sayyaadi and M. R. Zakerzadeh, "Position control of shape memory alloy actuator based on the generalized prandtl–ishlinskii inverse model," *Mechatronics*, vol. 22, no. 7, pp. 945–957, 2012.

[70] M. Zakerzadeh, H. Sayyaadi, and M. V. Zanjani, "Characterizing hysteresis nonlinearity behavior of sma actuators by krasnosel'skii-pokrovskii model," *Applied Mathematics*, vol. 1, no. 1, pp. 28–38, 2011.

[71] G. Webb, L. Wilson, D. Lagoudas, and O. Rediniotis, "Adaptive control of shape memory alloy actuators for underwater biomimetic applications," *AIAA Journal*, vol. 38, no. 2, pp. 325–334, 2000.

[72] G. Webb, A. Kurdila, and D. Lagoudas, "Adaptive hysteresis model for model reference control with actuator hysteresis," *Journal of Guidance, Control, and Dynamics*, vol. 23, no. 3, pp. 459–465, 2000.

[73] G. V. Webb, D. C. Lagoudas, and A. J. Kurdila, "Hysteresis modeling of sma actuators for control applications," *Journal of Intelligent Material Systems and Structures*, vol. 9, no. 6, pp. 432–448, 1998.

[74] M. Zhou, S. Wang, and W. Gao, "Hysteresis modeling of magnetic shape memory alloy actuator based on krasnosel'skii-pokrovskii model," *The Scientific World Journal*, vol. 2013, 2013.

[75] M. Zhou, Q. Zhang, and J. Wang, "Feedforward-feedback hybrid control for magnetic shape memory alloy actuators based on the krasnosel'skii-pokrovskii model," *PloS One*, vol. 9, no. 5, p. e97086, 2014.

[76] P. Junker and K. Hackl, "A thermo-mechanically coupled field model for shape memory alloys," *Continuum Mechanics and Thermodynamics*, vol. 26, no. 6, pp. 859–877, 2014.

[77] J. A. Shaw, "A thermomechanical model for a 1-d shape memory alloy wire with propagating instabilities," *International Journal of Solids and Structures*, vol. 39, no. 5, pp. 1275–1305, 2002.

[78] D. C. Lagoudas, Z. Bo, and M. A. Qidwai, "A unified thermodynamic constitutive model for sma and finite element analysis of active metal matrix composites," *Mechanics of Composite Materials and Structures*, vol. 3, no. 2, pp. 153–179, 1996.

[79] G. Song, V. Chaudhry, and C. Batur, "A neural network inverse model for a shape memory alloy wire actuator," *Journal of Intelligent Material Systems and Structures*, vol. 14, no. 6, pp. 371–377, 2003.

[80] A. Vitiello, G. Giorleo, and R. E. Morace, "Analysis of thermomechanical behaviour of nitinol wires with high strain rates," *Smart Materials and Structures*, vol. 14, no. 1, pp. 215–221, 2005.

[81] A. Bhattacharyya, D. Lagoudas, Y. Wang, and V. Kinra, "On the role of thermoelectric heat transfer in the design of sma actuators: theoretical modeling and experiment," *Smart Materials and Structures*, vol. 4, no. 4, pp. 252–263, 1995.

[82] C. Mavroidis, "Development of advanced actuators using shape memory alloys and electrorheological fluids," *Journal of Research in Nondestructive Evaluation*, vol. 14, no. 1, pp. 1–32, 2002.

[83] H. Ashrafiuon, M. Eshraghi, and M. H. Elahinia, "Position control of a three-link shape memory alloy actuated robot," *Journal of Intelligent Material Systems and Structures*, vol. 17, no. 5, pp. 381–392, 2006.

[84] V. Bundhoo, E. Haslam, B. Birch, and E. J. Park, "A shape memory alloy-based tendon-driven actuation system for biomimetic artificial fingers, part i: design and evaluation," *Robotica*, vol. 27, no. 1, pp. 131–146, 2009.

[85] G. Gilardi, E. Haslam, V. Bundhoo, and E. J. Park, "A shape memory alloy based tendon-driven actuation system for biomimetic artificial fingers, part ii: modelling and control," *Robotica*, vol. 28, no. 5, pp. 675–687, 2010.

[86] J. Colorado, A. Barrientos, C. Rossi, J. Bahlman, and K. Breuer, "Corrigendum: Biomechanics of smart wings in a bat robot: morphing wings using sma actuators," *Bioinspir & Biomim*, vol. 3, no. 3, 2013.

[87] Y. Tanaka and A. Yamada, "A rotary actuator using shape memory alloy for a robot-analysis of the response with load," in *Proceedings IROS'91: IEEE/RSJ International Workshop on Intelligent Robots and Systems' 91*, pp. 1163–1168, 1991.

[88] J. Ko, M. B. Jun, G. Gilardi, E. Haslam, and E. J. Park, "Fuzzy pwm-pid control of cocontracting antagonistic shape memory alloy muscle pairs in an artificial finger," *Mechatronics*, vol. 21, no. 7, pp. 1190–1202, 2011.

[89] N. B. Kha and K. K. Ahn, "Position control of shape memory alloy actuators by using self tuning fuzzy pid controller," in *2006 1ST IEEE Conference on Industrial Electronics and Applications*, pp. 1–5, 2006.

[90] A. Hadi, A. Yousefi-Koma, M. Elahinia, M. Moghaddam, and A. Ghazavi, "A shape memory alloy spring-based actuator with stiffness and position controllability," *Proceedings of the Institution of Mechanical Engineers, Part I: Journal of Systems and Control Engineering*, vol. 225, no. 7, pp. 902–917, 2011.

[91] S. Majima, K. Kodama, and T. Hasegawa, "Modeling of shape memory alloy actuator and tracking control system with the model," *IEEE Transactions on Control Systems Technology*, vol. 9, no. 1, pp. 54–59, 2001.

[92] Y. Feng, C. A. Rabbath, H. Hong, M. Al Janaideh, and C.-Y. Su, "Robust control for shape memory alloy micro-actuators based flap positioning system," in *Proceedings of the 2010 American Control Conference*, pp. 4181–4186, 2010.

[93] L. Brinson and M. Huang, "Simplifications and comparisons of shape memory alloy constitutive models," *Journal of Intelligent Material Systems and Structures*, vol. 7, no. 1, pp. 108–114, 1996.

[94] M. Al Janaideh, S. Rakheja, and C.-Y. Su, "A generalized prandtl–ishlinskii model for characterizing the hysteresis and saturation nonlinearities of smart actuators," *Smart Materials and Structures*, vol. 18, no. 4, pp. 045001–1–045001–9, 2009.

[95] Z. Zhang, Q. Chen, J. Mao, and Z. Wang, "A generalized stress-dependent prandtl-ishlinskii model and its adaptive inverse compensation with model reference for gma," in *8th Asian Control Conference (ASCC), 2011*, pp. 535–540, 2011.

[96] R. Hamilton, H. Sehitoglu, Y. Chumlyakov, and H. Maier, "Stress dependence of the hysteresis in single crystal niti alloys," *Acta Materialia*, vol. 52, no. 11, pp. 3383–3402, 2004.

[97] A. Bergqvist and G. Engdahl, "A stress-dependent magnetic preisach hysteresis model," *IEEE Transactions on Magnetics*, vol. 27, no. 6, pp. 4796–4798, 1991.

[98] Z. Zhang, J. Mao, and W. Chen, "Stress-dependent hysteresis modeling and tracking control of giant magnetostrictive actuator for periodic reference input," *IFAC Proceedings Volumes*, vol. 41, no. 2, pp. 2288–2293, 2008.

[99] B. L. Ball, R. C. Smith, S.-J. Kim, and S. Seelecke, "A stress-dependent hysteresis model for ferroelectric materials," *Journal of Intelligent Material Systems and Structures*, vol. 18, no. 1, pp. 69–88, 2007.

[100] B. Huang and C. Duang, "System dynamic model and temperature control of a thermoelectric cooler," *International Journal of Refrigeration*, vol. 23, no. 3, pp. 197–207, 2000.

[101] G. Fraisse, J. Ramousse, D. Sgorlon, and C. Goupil, "Comparison of different modeling approaches for thermoelectric elements," *Energy Conversion and Management*, vol. 65, pp. 351–356, 2013.

[102] S. Shaojing and Q. Qin, "Temperature control of thermoelectric cooler based on adaptive nn-pid," in *International Conference on Electrical and Control Engineering (ICECE), 2010*, pp. 2245–2248, 2010.

[103] M. Guiatni, A. Drif, and A. Kheddar, "Thermoelectric modules: Recursive non-linear arma modeling, identification and robust control," in *33rd Annual Conference of the IEEE Industrial Electronics Society, 2007. IECON 2007.*, pp. 568–573, 2007.

[104] M. A. Janaideh, *Generalized Prandtl-Ishlinskii hysteresis model and its analytical inverse for compensation of hysteresis in smart actuators.* PhD thesis, Concordia University, 2009.

[105] M. Al Janaideh, Y. Feng, S. Rakheja, C.-Y. Su, and C. A. Rabbath, "Hysteresis compensation for smart actuators using inverse generalized prandtl-ishlinskii model," in *2009 American Control Conference*, pp. 307–312, 2009.

[106] M. Al Janaideh, S. Rakheja, J. Mao, and C.-Y. Su, "Inverse generalized asymmetric prandtl-ishlinskii model for compensation of hysteresis nonlinearities in smart actuators," in *2009 International Conference on Networking, Sensing and Control*, pp. 834–839, 2009.

[107] M. Al Janaideh, C.-Y. Su, and S. Rakheja, "Compensation of symmetric and asymmetric hysteresis nonlinearities in smart actuators with a generalized prandtl-ishlinskii presentation," in *2010 IEEE/ASME International Conference on Advanced Intelligent Mechatronics*, pp. 890–895, 2010.

[108] J. Zhang, E. Merced, N. Sepúlveda, and X. Tan, "Modeling and inverse compensation of hysteresis in vanadium dioxide using an extended generalized prandtl–ishlinskii model," *Smart Materials and Structures*, vol. 23, no. 12, p. 125017–125026, 2014.

[109] S. Liu, C. Y. Su, and Z. Li, "Robust adaptive inverse control of a class of nonlinear systems with prandtl-ishlinskii hysteresis model," *IEEE Transactions on Automatic Control*, vol. 59, no. 8, pp. 2170–2175, 2014.

[110] S. Liu and C.-Y. Su, "Adaptive inverse output feedback control of uncertain systems preceded with hysteresis actuators," *IFAC Proceedings Volumes*, vol. 47, no. 3, pp. 7196–7201, 2014.

[111] Y. Feng, C.-Y. Su, and H. Hong, "Universal construction of robust adaptive control laws for a class of nonlinear systems preceded by generalized prandtl-ishlinskii representation," in *3rd IEEE Conference on Industrial Electronics and Applications, 2008. ICIEA 2008*, pp. 153–158, 2008.

[112] S. Liu, Z. Li, and C.-Y. Su, "Robust adaptive control of a class of nonlinear system with an asymmetric shifted prandtl-ishlinskii hysteresis model," in *International Conference on Advanced Mechatronic Systems (ICAMechS), 2012*, pp. 217–222, 2012.

[113] Q. Wang and C.-Y. Su, "Robust adaptive control of a class of nonlinear systems including actuator hysteresis with prandtl–ishlinskii presentations," *Automatica*, vol. 42, no. 5, pp. 859–867, 2006.